UNIVERSITY OF SOUTHAMPTON

FACULTY OF PHYSICAL SCIENCES AND ENGINEERING

Optoelectronics Research Centre

Pulse-Shaping Assisted Nonlinear Optical Signal Generation in Fibres

by

Xin Yang

Thesis for the degree of Doctor of Philosophy

September 2013

UNIVERSITY OF SOUTHAMPTON

ABSTRACT

FACULTY OF PHYSICAL SCIENCES AND ENGINEERING
Optoelectronics Research Centre

Doctor of Philosophy

PULSE-SHAPING ASSISTED NONLINEAR OPTICAL SIGNAL GENERATION IN FIBRES

by Xin Yang

This thesis investigates pulse-shaping assisted nonlinear optical signal generation in fibers. A linear pulse shaping stage is included in nonlinear fibre optic systems to achieve flexible and precise control over the characteristics of the output signal.

The nonlinear generation of broadband spectra with desired characteristics is demonstrated as a first application of this technique. The key feature is that the linear filtering stage is placed prior to the nonlinear broadening stage in the system. A numerical simulation procedure is established to find the appropriate transfer functions of the programmable pulse shaper based on the backward propagation in a fibre. Consequently, an adaptive pulse shaping system exploiting evolutionary algorithms is built and employed to facilitate automatic convergence to the desired spectrum. The nonlinear generation of ultra-flat broadband spectra with different bandwidths is demonstrated. Additionally, the generation of broadband spectra with symmetric and linear edges exhibiting slopes of different steepness is also presented.

As a second application of this technique, the linear filtering stage is incorporated into the cavity of a passively mode-locked erbium-doped fibre ring laser (EFRL). The aim here is to achieve flexible and precise control over the temporal waveforms of the laser pulses. In order to find the appropriate laser configuration which allows for the manipulation of the characteristics of the laser pulses through intra-cavity spectral filtering, both all-anomalous dispersion and all-normal dispersion cavities are numerically studied. The influence of intra-cavity amplitude filtering and net dispersion on the characteristics of laser pulses in a passively mode-locked dispersion-managed (DM) EFRL is experimentally demonstrated.

Contents

List of Figures

List of Tables

Declaration of Authorship

I, Xin Yang , declare that the thesis entitled *Pulse-Shaping Assisted Nonlinear Optical Signal Generation in Fibres* and the work presented in the thesis are both my own, and have been generated by me as the result of my own original research. I confirm that:

- this work was done wholly or mainly while in candidature for a research degree at this University;
- where any part of this thesis has previously been submitted for a degree or any other qualification at this University or any other institution, this has been clearly stated;
- where I have consulted the published work of others, this is always clearly attributed;
- where I have quoted from the work of others, the source is always given. With the exception of such quotations, this thesis is entirely my own work;
- I have acknowledged all main sources of help;
- where the thesis is based on work done by myself jointly with others, I have made clear exactly what was done by others and what I have contributed myself;
- parts of this work have been published as: See *List of Publications*

Signed:.....

Date:.....

Acknowledgements

Almost four years in ORC, not long, also not short. It has become an indelible imprint on my memory. It is a period of my life full of the sweets and the bitters. I have really enjoyed it and it has been great. It is hard for me to express all my passion of thanksgiving in such a short page, but I would like to take this opportunity to thank a few people to whom I feel particularly indebted.

Without any doubt, the top scorer is my supervisor, Professor Periklis Petropoulos. I would always remember how he taught me to do research hand by hand. He was always patient to me no matter how silly a mistake I have made in my work. He kept his door open to me whenever I need some guidance and assistance from him. He always encouraged me to move forward in my research and made me feel that he would always stand at my back to support me. I feel very fortunate to have been guided and supervised by such a wonderful person.

I would like to give a big thank you to Professor David Richardson. Although he is very busy, he always provided me with very inspiring feedback every time I knocked on his door. I am also impressed by his ability to handle all his working load effectively. He is a person that I should always learn from.

I have also found it very rewarding to work with Dr. Kamal Hammani. He is in the similar age as me. But I learnt a lot from him. We had a lot of useful discussion on the work on passively mode-locked fiber ring lasers. His talent led us to obtain the knowledge about the lasers with much deeper insight.

I have also enjoyed working with Dr. Radan Slavik and Dr. Francesca Parmigiani. They helped me with a lot of practical issues in the lab. They are nice people and always ready to help. I would like also to say thank you to Dr. Sheng Liu, Dr. Joseph Kakande, Mr. Liam Jones, Mr. Mohamed Ettabib, Mr. David Wu and Mr. Victor Rancano. They were my companions in the lab. We have had a plenty of useful discussion.

I would like to thank Mrs. Eveline Smith. She helped me to settle down in the ORC. She had done a wonderful administrative work. She was always ready to provide me with visa support letters, enrolment letters and so on.

Finally, it would be the great support from my family. The ever lasting trust and confidence from my wife, Ying Jiang, is always my driving force in my life. She also keeps encouraging me and calming me down whenever I felt frustrated. I feel also indebted with my parents and my parents-in-law. The support they gave to me is of immense value. They never put extra pressure on me and always help me resolve every tiny issues in my life.

Nomenclature

AOM	Acoustic-Optic Modulator
APM	Additive-Pulse Mode-Locking
ASE	Amplified Spontaneous Emission
CMA	Covariance Matrix Adaptation
DCF	Dispersion Compensating Fiber
DFWM	Dissipative Four-Wave-Mixing
DM	Dispersion-Managed
DS	Dissipative Solitons
EA	Evolutionary Algorithm
EDF	Erbium Doped Fiber
EDFA	Erbium Doped Fiber Amplifier
EFRL	Er-doped Fiber Ring Laser
EP	Evolutionary Programming
ERGO	Erbium Glass Oscillator
ES	Evolution Strategy
ESA	Electrical Spectrum Analyzer
FFT	Fast Fourier Transform
FROG	Frequency Resolved Optical Gating
FWHM	Full Width at Half Maximum
GA	Genetic Algorithm
GS	Gerchberg-Saxton Algorithm
GVD	Group Velocity Dispersion
HNLF	Highly Nonlinear Fiber
ISSFM	Inverse Split-Step Fourier Method
ITO	Indium Tin Oxide
KIT	Karlsruhe Institute of Technology
LC	Liquid Crystal
LCM	Liquid Crystal Modulator
LCOS	Liquid Crystal on Silicon
LPFGs	Long Period Fiber Gratings
MF	Misfit Factor
MLL	Mode-Locked Laser

NALM	Nonlinear Amplifying Loop
ND	Net Dispersion
NLSE	Nonlinear Schrödinger Equation
NPR	Nonlinear Polarization Rotation
OFDM	Orthogonal Frequency Division Multiplexing
OSA	Optical Spectrum Analyzer
OSNR	Optical Signal to Noise Ratio
OSO	Optical Sampling Oscilloscope
PCF	Photonic Crystal Fiber
PD	Photodiode
RF	Radio Frequency
RIN	Relative Intensity Noise
SDS	Stretched Dissipative Solitons
SMF	Single-Mode Fiber
SLM	Spatial Light Modulator
SPIDER	Spectral Phase Interferometry for Direct Electric-field Reconstruction
SPM	Self-Phase Modulation
SSFBGs	Superstructured Fiber Bragg Gratings
SSFM	Split-Step Fourier Method
SS	Self-Similar
TBP	Time-Bandwidth Product
TUB	Technical University of Berlin
WDM	Wavelength Division Multiplexing
W/S	Finisar Waveshaper

Chapter 1

Introduction

1.1 Research Area and Motivation

The field of nonlinear fibre optics has been an active research area and thus has been rapidly growing over the last 25 years [1, 2, 3]. In the 1990s, the driving force in this area was the advent of low-loss rare-earth doped silica fibres [4], such as the erbium doped fibre (EDF), which subsequently facilitated the emergence of fibre amplifiers. Erbium doped fibre amplifiers (EDFAs) are widely used in the current optical fibre communication systems and have revolutionised the design of the system. They allow for the propagation of optical signals over thousands of kilometers of fibre as they can amplify signals in the C-band (1530 - 1565 nm), where the propagation loss in silica is minimum. EDFAs provide high gains of up to around $60dB$ [5] and their noise figure can be designed to be as low as $3.1dB$ [6] which is close to the quantum limit of $3dB$. By increasing the erbium concentration, they can be also operated in the L-band (1565 - 1625 nm) [7].

From the late 1990s, the focus of research in the field of nonlinear fibre optics switched to the design and fabrication of several kinds of new fibres with nonlinear coefficient γ larger than $10W^{-1}km^{-1}$. These fibres are referred to as highly nonlinear fibres (HNLF). A simple way to increase the nonlinearity in a silica fibre is to reduce its core diameter. This method would eventually be limited by the loss related to the mode confinement of the fibre [8]. The development of microstructured fibres [9], especially photonic crystal fibres (PCF) [10] provided a flexible way of enhancing the nonlinearity in a fibre. The prominent feature in the structure of these fibres is that a solid core is surrounded by a cladding full of air holes. For a PCF with multiple rings of periodic air holes in the cladding, its effective area and dispersive properties depend on the air-hole diameter and the hole-to-hole spacing [11]. Consequently, by adjusting the design parameters, such a PCF can have relatively high nonlinearity and specific dispersive properties. Combined with EDFAs, one of the most important applications of HNLFs is the generation of broadband spectra spanning several tens or even hundreds of nanometers [12, 13, 11].

In a nonlinear fibre optic system, which aims at the generation of a broadband spectrum, it is often desirable to achieve precise and flexible control over the characteristics of the generated spectrum. For example, in communications, an ultra-flat broadband spectrum is highly demanded in optical orthogonal frequency division multiplexing (OFDM) systems to be used as the source of sub-carriers. Unfortunately, it is not possible to nonlinearly generate a strictly flat-top spectrum with conventional Gaussian or hyperbolic secant pulses. The reason is that the nonlinear propagation of these kinds of pulses in a fibre always ends up with a broadened spectrum with ripples on the top, unless special care has been taken in the design of the dispersion profile. Pulses with other temporal shapes have therefore been investigated for the nonlinear generation of flat-top spectra generation.

In 2000, M. E. Fermann et al. [14] demonstrated that a relatively smooth SPM-broadened spectrum could be generated by the nonlinear propagation of parabolic pulses in a normal dispersion fibre. Following that, a vast amount of research has been devoted to parabolic pulse generation. There are mainly two ways to generate parabolic pulses, as reported in the literature. One of the approaches is the nonlinear formation based on tailoring the fibre dispersion profile as reported in [15, 16]. The other approach is linear spectral filtering of a conventional pulsed laser source using superstructured fibre Bragg gratings (SSFBGs) as demonstrated in [17].

Utilizing the concept of the SSFBG based pulse shaping process, P. Almeida et al. [18] reported the generation of flat spectra with sharp edges through SPM in a conventional commercial highly nonlinear dispersion shifted fibre by shaping the pulses generated by a laser into a suitable waveform before nonlinear broadening. This waveform was calculated by solving the nonlinear Schrödinger equation (NLSE) in the backward direction using the desired flat-top spectrum as the target. In the actual experiment, a spectrum exhibiting ripples up to $\sim 1.5dB$ on the top was achieved.

The approach of flat-top spectrum generation described in this thesis inherits the idea reported in [18]. But instead of using a purpose-built special SSFBG, the pre-shaping of optical pulses is carried out by a commercial programmable pulse shaper. This filter is much more flexible than a SSFBG due to its ability of reconfiguration. As will be shown in this thesis, it can be incorporated with an adaptive pulse system to guarantee the quality of the generated spectrum. Thus, in this thesis, I aim at the generation of a broadband spectrum exhibiting ripples less than $1dB$ on the top.

An EDF can be also used as the gain medium in fibre lasers. It provides broad gain bandwidths. Thus, the fibre laser allows for the generation of ultra-fast pulses over a wide range of wavelength. Passively mode-locked erbium-doped fibre ring lasers (EFRL) have been widely explored for soliton generation with sub-picosecond pulse duration [19, 20, 21]. In the field of signal processing in optical telecommunication systems, saw-tooth pulses, rectangular pulses and parabolic pulses are required for the retiming of signals. They are normally generated from soliton lasers through an extra spectral filtering stage. It would be interesting if the rectangular or triangular pulses could be

generated directly from a laser. In this way, their power could be adjusted without the need for an external amplifier according to the requirements of applications. Therefore, in this thesis, I investigate the possibility of such an idea by including a programmable optical filter inside the ring cavity of a passively mode-locked EFRL.

1.2 Contribution to Knowledge

The objectives of the work reported in this thesis have been to study the pulse-shaping assisted nonlinear signal generation in fibres. The main results achieved by the end of the study are outlined below:

- A numerical simulation procedure based on inverse split-step Fourier method (ISSFM) to find out the appropriate transfer function of the pulse shaper for pulse-shaping assisted nonlinear broadening. This procedure was orally presented in CLEO-Europe 2011 [22] and published in Journal of Lightwave Technology [23].
- Generation of a $12nm$ wide flat-top spectrum based on adaptive pulse shaping. The experimental results were orally presented in ECOC 2011 [24] and published in Journal of Lightwave Technology [23].
- Generation of an ultra-flat frequency comb covering the full-C band based on adaptive pulse shaping and characterisation of the noise characteristics of the generated comb. The experimental results were orally presented in OFC 2012 [25] and published in IEEE Photonics Technology Letters [26]. They also contributed towards the demonstration of system experiments that were published in [27].
- Numerical and experimental demonstrations of the generation of broadband spectrum with symmetric and linear edges.
- Numerical studies of the influence of the intra-cavity adaptive pulse shaping in passively mode-locked EFRLs with different cavity configurations.
- Experimental investigation of the influence of intra-cavity amplitude shaping and manipulation of net dispersion on the characteristics of laser pulses in a dispersion-managed (DM) passively mode-locked EFRL. This work was orally presented in CLEO US 2013 [28].

1.3 Layout of the Thesis

The thesis is organised in eight chapters. Chapter 2 provides the theoretical background of the work. The chapter starts with the derivation of the Nonlinear Schrödinger

Equation (NLSE), which is the equation governing the pulse propagation in a nonlinear dispersive fibre. Subsequently, the effects of GVD and SPM on the pulse propagation in a fibre are presented. Then, the split-step Fourier method (SSFM) and inverse SSFM (ISSFM) are described as numerical tools to solve the NLSE in either the forward or the backward directions of pulse propagation in the fibre. Since pulse shaping is the key technique for the experimental work, its general principle and various technologies for implementing it are presented, especially the technology of liquid crystal on silicon (LCOS).

Chapter 3 introduces the adaptive pulse shaping system. The general principle of the system is described. The evolutionary algorithm is reviewed in detail, which allows an understanding of how an adaptive system works. Then, the evolution strategy (ES), which has been selected as the optimization algorithm in my adaptive system, is described in detail. As an application, an arbitrary spectral synthesis is presented. It is designed for the nonlinear generation of broadband spectra with user-defined characteristics.

Chapter 4 describes the nonlinear generation of a flat-top spectrum based on the technique of pulse-shaping assisted nonlinear broadening. A numerical simulation procedure is first established to obtain the transfer function for the programmable optical filter, which is placed prior to the nonlinear broadening stage. The quality of the generated spectrum based on the numerically calculated transfer function reveals the uncertainties in the system. The arbitrary spectral synthesis, described in Chapter 3, is then employed to overcome the limitation imposed by the uncertainties and consequently improve the quality of the generated spectrum. Then the power of the pulses at the input end of the HNLF is increased with the aim to generate ultra-flat frequency comb covering the full C-band. Furthermore, the noise characteristics of the generated frequency comb is measured. At the end of the chapter, a joint experiment between the Karlsruhe Institute of Technology (KIT) and the ORC is presented as an application of the generated frequency comb.

Chapter 5 presents the generation of a broadband spectrum with symmetric and linear edges based on the adaptive pulse shaping assisted nonlinear broadening. It is investigated through both numerical simulations and experiments. The influence of the slopes of the edges of the target spectrum and the fibre parameters on the performance of the arbitrary spectral synthesis is studied.

Chapter 6 reviews the passively mode-locked EFRL. The description starts from the principle of mode-locking, followed by various passive mode-locking techniques and the pulse shaping mechanisms in different types of laser cavities. Then, it reports the numerical simulation for the passively mode-locked EFRL. The aim of the numerical simulation is to find out the appropriate laser configuration, which allows for the manipulation of the characteristics of the laser pulses through intra-cavity spectral filtering. Both all-anomalous dispersion and all-normal dispersion cavities are studied.

Chapter 7 describes the experimental work on a dispersion-managed (DM) passively

mode-locked EFRL. Mode-locking is based on the nonlinear polarization rotation (NPR) in the fibre. The cavity consists of a dispersion compensating fibre (DCF), a single-mode fibre (SMF) and an erbium doped fibre (EDF) as the gain medium. The most prominent feature is the inclusion of a programmable optical filter in the cavity. The influence of intra-cavity amplitude shaping on the characteristics of the laser pulses is investigated through filters with different bandwidths. The filter shapes are Gaussian, third-order super-Gaussian and sinc square function. The impact of net dispersion of the cavity on the characteristics of the laser pulses is also studied by the spectral phase shaping in the programmable optical filter.

The thesis concludes with Chapter 8, where I highlight the key results and point out possible future directions of the work.

Chapter 2

Background

2.1 Introduction

The discussion in this chapter focuses on the background knowledge required in the simulations and experiments described in the following chapters of this thesis. As the basis for the understanding of the behaviour of optical short pulses in optical fibres, the classical pulse propagation theory is briefly covered. The derivation of the well-known Nonlinear Schrödinger Equation (NLSE) is presented. Linear dispersion and nonlinear refraction are described, followed by the description of the Split Step Fourier Method (SSFM), which is a widely used numerical method to calculate the solution of the NLSE. The basic principle of pulse shaping, which is the overarching technique used in all the experimental work reported in this thesis, is thoroughly described. The working principle of pulse shaping devices is introduced, especially for the liquid crystal on silicon (LCOS) programmable filter, which is selected here for its reconfigurable features and fine spectral resolution. As a means of improving the quality of the shaped signal, the applications of the adaptive pulse shaping are presented.

2.2 Pulse Propagation Theory

The propagation of a picosecond pulse inside a nonlinear dispersive fibre can be predicted by analysing the combined effects of group velocity dispersion (GVD) and self-phase modulation (SPM). Solving the NLSE using the SSFM is a common way to study the evolution of both the pulse shapes and optical spectra in the fibre.

2.2.1 Nonlinear Schrödinger Equation

NLSE governs the picosecond pulse propagation inside the nonlinear dispersive fibre. The derivation of NLSE starts from the wave equation as expressed in Equation 2.1 [29]:

$$\nabla^2\vec{E} - \frac{1}{c^2}\frac{\partial^2\vec{E}}{\partial t^2} = \mu_0\frac{\partial^2\vec{P}_L}{\partial t^2} + \mu_0\frac{\partial^2\vec{P}_{NL}}{\partial t^2}, \tag{2.1}$$

where $\vec{E}$ is the electric field, while $\vec{P}_L$ and $\vec{P}_{NL}$ are the linear and nonlinear parts of the induced polarization, respectively.

In order to solve this equation, the necessary assumptions are following: (a) $\vec{P}_{NL}$ is treated as small perturbation to $\vec{P}_L$. (b) The polarization state of the optical field is assumed to be maintained along the fibre length. As a result, the scalar approach is applicable. (c) The pulse propagating inside the fibre, centred at ω_0 is assumed to have a spectral width $\Delta\omega$ such that $\Delta\omega/\omega_0 << 1$ [29].

By introducing the slowly varying envelop approximation [30], $\vec{E}$, $\vec{P}_L$ and $\vec{P}_{NL}$ could be expressed in Equations 2.2, 2.3 and 2.4:

$$\vec{E}\left(\vec{r},t\right) = \frac{1}{2}\hat{x}[E\left(\vec{r},t\right)exp\left(-i\omega_0 t\right) + c.c], \tag{2.2}$$

$$\vec{P}_L\left(\vec{r},t\right) = \frac{1}{2}\hat{x}[P_L\left(\vec{r},t\right)exp\left(-i\omega_0 t\right) + c.c], \tag{2.3}$$

$$\vec{P}_{NL}\left(\vec{r},t\right) = \frac{1}{2}\hat{x}[P_{NL}\left(\vec{r},t\right)exp\left(-i\omega_0 t\right) + c.c], \tag{2.4}$$

where $\hat{x}$ is the polarization unit vector, $E\left(\vec{r},t\right)$ is a slowly varying function of time. $P_L\left(\vec{r},t\right)$ and $P_{NL}\left(\vec{r},t\right)$ are related to $E\left(\vec{r},t\right)$ in the form

$$P_L\left(\vec{r},t\right) = \epsilon_0\int_{-\infty}^{\infty}\chi_{xx}^{(1)}E\left(\vec{r},t'\right)exp[-i\omega_0\left(t-t'\right)]dt', \tag{2.5}$$

$$P_{NL}\left(\vec{r},t\right) \approx \epsilon_0\epsilon_{NL}E\left(\vec{r},t\right), \tag{2.6}$$

where the nonlinear contribution to the dielectric constant is defined as

$$\epsilon_{NL} = \frac{3}{4}\chi_{xxxx}^{(3)}|E\left(\vec{r},t\right)|^2. \tag{2.7}$$

It is more convenient to obtain the wave equation for $E\left(\vec{r},t\right)$ in the Fourier domain. The Fourier transform $\tilde{E}\left(\vec{r},\omega-\omega_0\right)$ of $E\left(\vec{r},t\right)$ is defined as

$$\tilde{E}\left(\vec{r},\omega-\omega_0\right) = \int_{-\infty}^{\infty}E\left(\vec{r},t\right)exp[i\left(\omega-\omega_0\right)t]dt. \tag{2.8}$$

By substituting Equations 2.2 - 2.4 into Equation 2.8, $\tilde{E}\left(\vec{r},\omega-\omega_0\right)$ is found to satisfy the Helmholtz equation

$$\nabla^2\tilde{E} + \epsilon\left(\omega\right)k_0^2\tilde{E} = 0, \tag{2.9}$$

where $k_0 = \omega/c$ and

$$\epsilon(\omega) = 1 + \tilde{\chi}^{(1)}_{xx} + \epsilon_{NL} \tag{2.10}$$

is the dielectric constant, which could be used to define the intensity dependent refractive index $\tilde{n}$ and absorption coefficient $\tilde{\alpha}$ expressed in Equation 2.11.

$$\tilde{n} = n + n_2|E|^2, \quad \tilde{\alpha} = \alpha + \alpha_2|E|^2 \tag{2.11}$$

where n and α represent the linear refractive index and the linear absorption coefficient of the fibre, respectively. Using $\epsilon = (\tilde{n} + i\alpha/2k_0)^2$ together with Equations 2.7 and 2.10, the nonlinear-index coefficient n_2 and the two-photon absorption coefficient α_2 is given by

$$n_2 = \frac{3}{8n} Re\left(\chi^{(3)}_{xxxx}\right), \quad \alpha_2 = \frac{3\omega_0}{4nc} Im\left(\chi^{(3)}_{xxxx}\right). \tag{2.12}$$

Generally speaking, α_2 is relative small for silica fibres and often ignored, and n_2 is a measure of fibre nonlinearity.

Equation 2.9 could be solved by using the method of separation of variables [31]. The solution is assumed to be in the form

$$\tilde{E}(\vec{r}, \omega - \omega_0) = F(x, y)\, \tilde{A}(z, \omega - \omega_0)\, exp(i\beta_0 z), \tag{2.13}$$

where $F(x, y)$ is the modal distribution, $\tilde{A}(z, \omega - \omega_0)$ is a slowly varying function of z, and β_0 is the wave number. The equations for $F(x, y)$ and $\tilde{A}(z, \omega)$ are obtained from Equation 2.9 as below:

$$\frac{\partial^2 F}{\partial x^2} + \frac{\partial^2 F}{\partial y^2} + [\epsilon(\omega) k_0^2 - \tilde{\beta}^2]F = 0, \tag{2.14}$$

$$2i\beta_0 \frac{\partial \tilde{A}}{\partial z} + \left(\tilde{\beta}^2 - \beta_0^2\right)\tilde{A} = 0. \tag{2.15}$$

The dielectric constant in Equation 2.14 could be approximated by

$$\epsilon = (n + \Delta n)^2 \approx n^2 + 2n\Delta n, \tag{2.16}$$

where Δn is a small perturbation expressed by

$$\Delta n = n_2|E|^2 + \frac{i\alpha}{2k_0}. \tag{2.17}$$

By solving Equation 2.14 using first-order perturbation theory [32], the eigenvalue $\tilde{\beta}$ becomes

$$\tilde{\beta}(\omega) = \beta(\omega) + \Delta\beta, \tag{2.18}$$

where

$$\Delta\beta = \frac{k_0 \iint_{-\infty}^{\infty} \Delta n |F(x, y)|^2 dxdy}{\iint_{-\infty}^{\infty} |F(x, y)|^2 dxdy}. \tag{2.19}$$

In this way, Equation 2.15 evolves into the following expression

$$\frac{\partial \tilde{A}}{\partial z} = i[\beta(\omega) + \Delta\beta - \beta_0]\tilde{A}. \tag{2.20}$$

The physical meaning of Equation 2.20 is that as the pulses propagate down the fibre, the induced phase shift for each spectral component within the pulse envelope is both frequency and intensity dependent.

The propagation equation for $A(z,t)$ can be obtained by taking the inverse Fourier transform of Equation 2.20. Here, it is necessary to expand $\beta(\omega)$ in a Taylor series respect to the carrier frequency ω_0 as

$$\beta(\omega) = \beta_0 + (\omega - \omega_0)\beta_1 + \frac{1}{2}(\omega - \omega_0)^2\beta_2 + \frac{1}{6}(\omega - \omega_0)^3\beta_3 + \cdots, \tag{2.21}$$

where

$$\beta_m = \left(\frac{d^m\beta}{d\omega^m}\right)_{\omega=\omega_0} \qquad (m = 1, 2, \ldots). \tag{2.22}$$

Due to the assumption that the pulse bandwidth is very small compared to the carrier optical frequency, the third and higher-order terms in Equation 2.21 can be considered negligible.

As a result, the equation for $A(z,t)$ is

$$\frac{\partial A}{\partial z} = -\beta_1\frac{\partial A}{\partial t} - \frac{i\beta_2}{2}\frac{\partial^2 A}{\partial t^2} + \frac{\alpha}{2}A + i\Delta\beta A. \tag{2.23}$$

From the expression of $\Delta\beta$, it is clear that the term $i\Delta\beta A$ includes the effect of fibre loss and nonlinearity. By using Equations 2.17 and 2.19, Equation 2.23 becomes

$$\frac{\partial A}{\partial z} + \beta_1\frac{\partial A}{\partial t} + \frac{i\beta_2}{2}\frac{\partial^2 A}{\partial t^2} - \frac{\alpha}{2}A = i\gamma|A|^2A, \tag{2.24}$$

where the nonlinear parameter γ is defined as

$$\gamma = \frac{n_2\omega_0}{cA_{eff}}. \tag{2.25}$$

The parameter A_{eff} is known as the effective core area and defined as

$$A_{eff} = \frac{\left(\iint_{-\infty}^{\infty}|F(x,y)|^2dxdy\right)^2}{\iint_{-\infty}^{\infty}|F(x,y)|^4dxdy}. \tag{2.26}$$

Equation 2.24 is known as the nonlinear Schrödinger equation (NLSE) which governs the propagation of picosecond pulses in a nonlinear dispersive fibre. It includes the effects of fibre loss through α, chromatic dispersion through β_2, and fibre nonlinearity through γ.

By introducing a retarded frame, which is a frame of reference moving together with the

pulse at the group velocity v_g, the following transformation is made to Equation 2.24.

$$T = t - z/v_g \equiv t - \beta_1 z \tag{2.27}$$

After the transformation, Equation 2.24 becomes

$$i\frac{\partial A}{\partial z} - \frac{i\alpha}{2}A - \frac{\beta_2}{2}\frac{\partial^2 A}{\partial T^2} + \gamma|A|^2 A = 0. \tag{2.28}$$

Since the time window is moving together with the pulse in the retarded time frame, the NLSE can be solved without changing the time window size as z becomes large.

2.2.2 Pulse Behaviour in Different Propagation Regimes

The general behaviour of picosecond pulses propagating inside the nonlinear dispersive fibre could be described using either Equation 2.24 or Equation 2.28. In order to explicitly investigate the effects of linear dispersion and nonlinear refraction on the propagation, it is instructive to study the behaviour of picosecond pulses in different propagation regimes.

In the first instance, it is essential to categorize the pulse propagation in the fibre with respect to the dominant effect in each case. Depending on the quantitative relation between the initial pulse width T_0 and peak power P_0 of the picosecond pulses at the input end of the fibre, either the dispersive or the nonlinear effect dominates the pulse propagation along the fibre.

It is useful to introduce a time scale τ normalized to T_0 and amplitude U normalized to $\sqrt{P_0}$ for the following analysis as shown in Equation 2.29 and Equation 2.30 [33]:

$$\tau = \frac{T}{T_0} = \frac{t - z/v_g}{T_0}, \tag{2.29}$$

$$A(z,\tau) = \sqrt{P_0} exp(-\alpha z/2)\, U(z,\tau). \tag{2.30}$$

By using Equation 2.28 to Equation 2.30, $U(z,\tau)$ is found to satisfy

$$i\frac{\partial U}{\partial z} = \frac{sgn(\beta_2)}{2L_D}\frac{\partial^2 U}{\partial \tau^2} - \frac{exp(-\alpha z)}{L_{NL}}|U|^2 U, \tag{2.31}$$

where $sgn(\beta_2) = \pm 1$ depending on the sign of β_2 and

$$L_D = \frac{T_0^2}{|\beta_2|}, \quad L_{NL} = \frac{1}{\gamma P_0}, \tag{2.32}$$

L_D and L_{NL} are known as dispersion length and nonlinear length respectively, which are two very important length scales in the pulse propagation analysis. The relative importance of GVD and SPM on the pulse propagation could be represented by a parameter

N, which is defined in Equation 2.33:

$$N^2 = \frac{L_D}{L_{NL}} = \frac{\gamma P_0 T_0^2}{|\beta_2|}. \tag{2.33}$$

In the theory of optical fibre solitons, the parameter N is also referred to as soliton order. The energy of a N^{th} order soliton is N^2 times higher than that of a fundamental soliton.
Depending on the relation between fibre length L , dispersion length L_D and nonlinear length L_{NL}, the pulses evolve quite differently along the fibre for different values of N. There are four interesting regimes for characterizing the pulse behaviour.

- Regime 1: $L << L_D$ and $L << L_{NL}$, neither GVD nor SPM dominate the pulse propagation.
- Regime 2: $L << L_{NL}$ but $L \sim L_D$, $N << 1$, GVD dominates the pulse propagation.
- Regime 3: $L << L_D$ but $L \sim L_{NL}$, $N >> 1$, SPM dominates the pulse propagation.
- Regime 4: $L \geq L_D$ and $L \geq L_{NL}$, $N \sim 1$, both GVD and SPM play an important role in the pulse propagation, the pulse propagates under the control of the interaction between GVD and SPM.

2.2.2.1 Distortion Free Propagation Regime

In the first regime in the above list, the pulse experiences distortion-free propagation as neither GVD nor SPM play a significant role in the pulse propagation. This can be easily derived from Equation 2.31, as both of the terms on the right-hand side of the equation can be neglected. Thus, $U(z, \tau) = U(0, \tau)$, i.e. the pulses maintain both their temporal shape and spectrum during the propagation. The fibre plays a passive role by reducing the pulse energy because of the loss.

2.2.2.2 GVD Dominated Propagation Regime

When the pulses propagate in the second regime, the fibre can be treated as a linear medium. Dispersion, however, has a dominant role in the pulse propagation. The most significant dispersive phenomenon is GVD [34]. The equation which describes the effects

of GVD could be derived by setting $\gamma = 0$ and $\alpha = 0$ in Equation 2.28. The normalized intensity $U(z,T)$ is expressed as

$$U(z,T) = \frac{1}{2\pi}\int_{-\infty}^{\infty} \tilde{U}(0,\omega)\, exp\left(\frac{i}{2}\beta_2\omega^2 z - i\omega T\right) d\omega, \tag{2.34}$$

where $\tilde{U}(0,\omega)$ is the Fourier transform of the incident field at $z = 0$. From Equation 2.34, it is clear that GVD induces a phase shift for each spectral component of the pulse, which is dependent on both the frequency and the propagation distance. GVD does not distort the pulse spectrum, since it does not generate any new frequencies. But it affects the pulse shape due to the induced phase change.

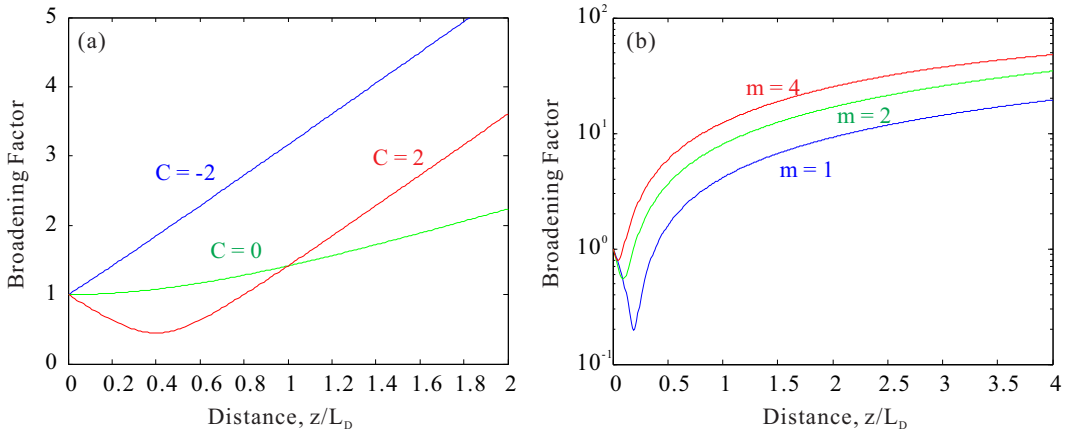

Figure 2.1: Brodening factor as functions of distance for (a) a chirped Gaussian pulse and (b) a chirped super-Gaussian pulse ($C = 5$) propagating in the anomalous-dispersion region of a fibre. C represents the chirp parameter of Gaussian pulse. m represents the order of super-Gaussian pulse.

The explicit effect of GVD can be conveniently demonstrated through an investigation of the propagation of Gaussian pulses inside a fibre. Take an unchirped Gaussian pulse as a first example. The pulse broadens and a linear chirp is imposed upon it during its propagation. However, if the Gaussian pulse is initially chirped, the GVD effect can either broaden or compress the pulse depending on the sign of the product of the GVD parameter β_2 and the chirp parameter C (which is the second order derivative of the temporal phase of a pulse respect to the time). Figure 2.1a demonstrates the broadening factor as a function of the distance for a chirped Gaussian pulse propagating in the anomalous-dispersion region of the fibre. It can be seen that when $\beta_2 C > 0$, the pulse broadens much faster than an unchirped pulse, since the induced chirp contributes to the input chirp. The situation is different for $\beta_2 C < 0$. The pulse is compressed initially and then broadened after a minimum width has been reached. The reason is that the GVD induced chirp and the input chirp cancel out each other because of their different signs. A super-Gaussian pulse of order m can be considered as an additional example to

reveal the impact of the steepness of the pulse edges on the GVD induced pulse broadening. Figure 2.1b shows the broadening factor as a function of the distance for positively chirped super-Gaussian pulses of various orders in the anomalous-dispersion region of a fibre. A higher-order super-Gaussian pulse with sharp leading and trailing edges has a much wider spectrum. The GVD induced phase change of a spectral component is proportional to its separation from the central frequency. As a result, a wider spectrum results in a faster rate of broadening.

2.2.2.3 SPM Dominated Propagation Regime

In the third propagation regime, nonlinear effects dominate the propagation of picosecond pulses. SPM is the most fundamental nonlinear effect to be explored here [35]. As the nonlinear effect in the optical fibre originates from the intensity dependence of the refractive index, the fibre loss cannot be ignored while investigating the pulse propagation in this regime. The pulse behaviour under SPM can be predicted when it is possible to apply the limit $\beta_2 = 0$ to Equation 2.31. The normalized intensity $U(L,T)$ is expressed by Equation 2.35:

$$U(L,T) = U(0,T)\, exp[i\phi_{NL}(L,T)], \tag{2.35}$$

where $U(0,T)$ is the incident field at $z = 0$ and

$$\phi_{NL}(L,T) = |U(0,T)|^2 (L_{eff}/L_{NL}). \tag{2.36}$$

The effective length L_{eff} for a fibre of length L is defined as

$$L_{eff} = [1 - exp(-\alpha L)]/\alpha. \tag{2.37}$$

From Equation 2.35, it is clear that SPM alone does not change the pulse shape during the propagation. Equation 2.36 shows that the nonlinear phase shift ϕ_{NL} induced by SPM is intensity dependent. The maximum phase shift ϕ_{max} occurs at the pulse centre. As $|U(0,0)|^2 = 1$, the maximum phase shift ϕ_{max} is given by

$$\phi_{max} = L_{eff}/L_{NL} = \gamma P_0 L_{eff}. \tag{2.38}$$

So L_{NL} is the effective propagation distance at which $\phi_{max} = 1$.
From Equation 2.36, it is also seen that the nonlinear phase shift ϕ_{NL} is also time dependent, which implies that the instantaneous frequency differs across the pulse. Meanwhile, the intensity dependence of ϕ_{NL} leads to continuously generated new frequency components during the pulse propagation in the fibre. As a consequence, SPM induces spectral broadening without distorting the pulse shape.

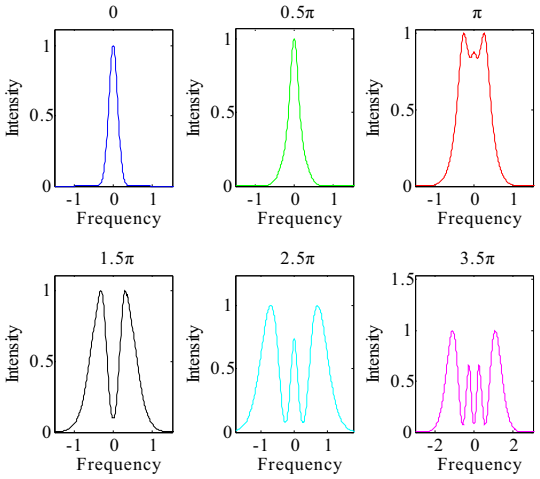

Figure 2.2: SPM-broadened spectra for an unchirped Gaussian pulse. Spectra are labelled by the maximum nonlinear phase shift ϕ_{max}.

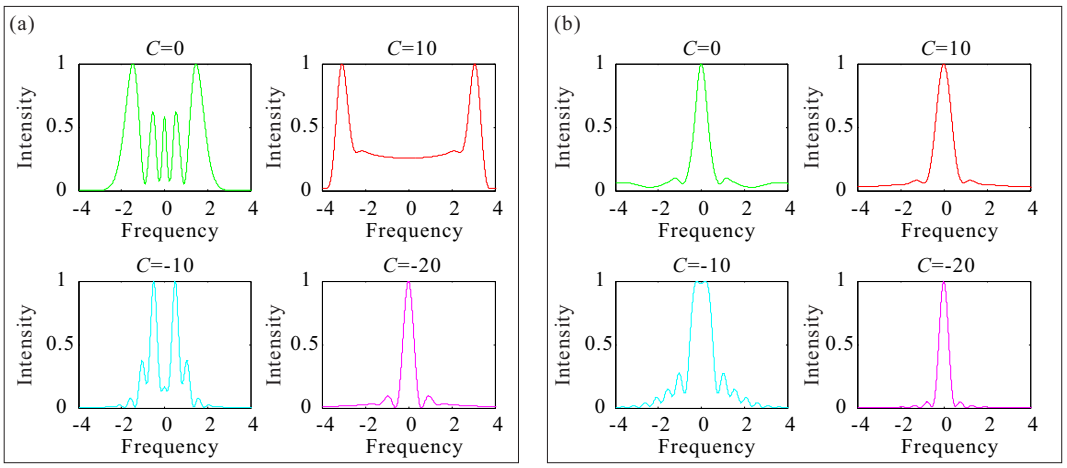

Figure 2.3: Comparison of SPM-broadened spectra for (a) Gaussian pulses and (b) Third-order super-Gaussian pulses for four values of chirp parameter C when $\phi_{max} = 4.5\pi$.

The effect of SPM can be once again readily studied by an investigation of the propagation of Gaussian pulses inside a fibre. Typically, the SPM-induced broadened spectrum is oscillatory over the entire frequency range and consists of many peaks. As shown in Figure 2.2, the number of peaks depends on ϕ_{max} and increases with it. From Figure 2.3a, it can be seen that the initial chirp on the Gaussian pulse plays a similar role as in the GVD-induced pulse broadening. Figure 2.3b demonstrates that the SPM-induced spectrum of a third-order super-Gaussian pulse with sharp edges also has a number of sidelobes, but keeps the energy remaining in the central peak of the pulse. The features of the SPM-induce spectrum strongly depends on the pulse shape.

2.2.2.4 GVD & SPM Dominated Propagation Regime

The picosecond pulse propagation is governed by both GVD and SPM in the fourth regime [36]. Figure 2.4 demonstrates the evolution of the pulse shape and its optical spectrum for an initially unchirped Gaussian pulse in the normal dispersion region with $N = 1$ and $\alpha = 0$. The pulse broadens much faster than the GVD-only scenario (Section 2.2.2.2). This can be explained by noting that SPM generates red-shifted frequency components near the leading edge and blue-shifted frequency components near the trailing edge. In the normal-dispersion region, the red components travel faster than the blue components. Thus, SPM leads to enhanced pulse broadening rate. On the other hand, the SPM-induced nonlinear phase shift reduces as compared to the SPM-only scenario, in which the pulse shape keeps unchanged (Section 2.2.2.3). For $z/L_D = 5$, a two-peak spectrum is expected in the SPM-only scenario. The single-spectrum shown in Figure 2.4b means that the nonlinear phase shift is now less than π because of the pulse broadening.

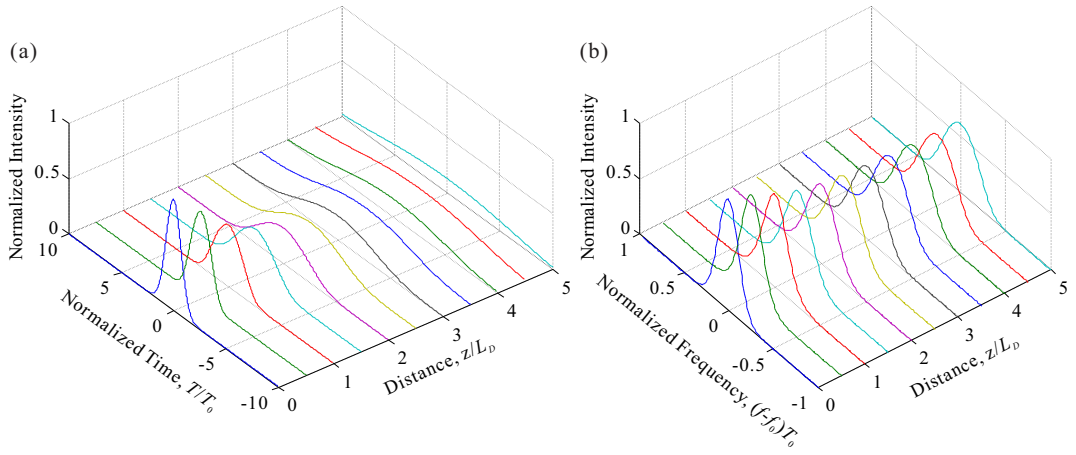

Figure 2.4: Evolution of (a) pulse shapes and (b) optical spectra over a distance of $5L_D$ for an initially unchirped Gaussian pulse in the normal dispersion region for $N = 1$.

Figure 2.5 shows the evolution of the pulse shape and optical spectrum under the same conditions as in Figure 2.4 but for the sign of β_2, which is opposite in this case. In the anomalous dispersion region, the pulse broadens at a much lower rate as compared to the GVD dominated scenario (Section 2.2.2.2). Meanwhile, the spectrum becomes narrower rather than wider as seen in the SPM dominated scenario (Section 2.2.2.3). This is because the GVD-induced chirp and SPM-induced chirp cancel each other in the central portion of the Gaussian pulse. It can be anticipated that a chirp-free pulse can be maintained under the combined effects of GVD and SPM in the anomalous dispersion region. In this scenario, if the input pulse is chosen to be an unchirped hyperbolic secant pulse, both its shape and spectrum do not change during the propagation. This is a fundamental soliton, the discovery of which and its study in the context of optical fibre

communication date back to 1973 [37].

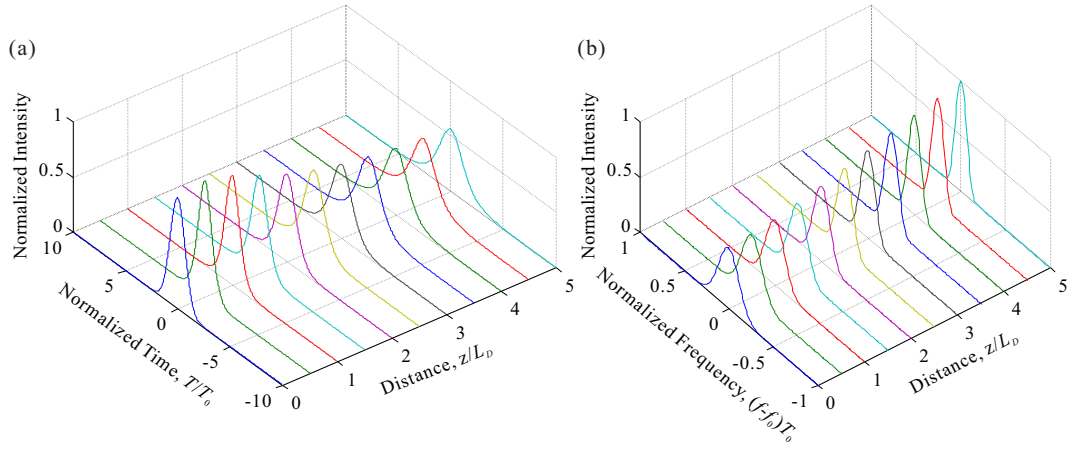

Figure 2.5: Evolution of (a) pulse shapes and (b) optical spectra over a distance of $5L_D$ for an initially unchirped Gaussian pulse in the anomalous dispersion region for $N = 1$.

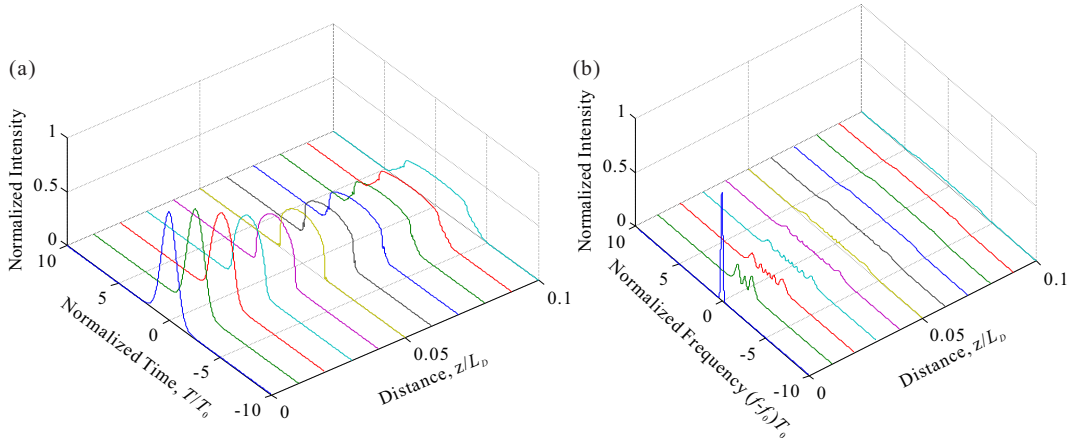

Figure 2.6: Evolution of (a) pulse shapes and (b) optical spectra over a distance of $0.1L_D$ for an initially unchirped Gaussian pulse in normal dispersion region for $N = 30$.

The evolution of pulse shapes and optical spectra of an initially unchirped Gaussian pulse in the normal dispersion region with $N = 30$ and $\alpha = 0$ is considered in Figure 2.6. The behaviour of the pulse is different from the observation in Figure 2.4. The pulses experience a phenomenon termed optical wave breaking, which happens in the normal dispersion region for large N values. A distinct feature of this effect is the rapid oscillatory structure near the pulse edges accompanied by sidelobes in the spectrum. Also, the GVD modifies the multipeak central portion of the spectrum. This happens because the combination of the GVD-induced chirp and the SPM-induced chirp is nonlinear. Different parts of the pulse propagate at different speeds. In the normal dispersion region, the red-shifted light near the leading edge travels faster and overtakes the unshifted light in

the forward tail of the pulse, while the blue-shifted light near the trailing edge does the opposite. The oscillations at the pulse edges are a result of the interference between the two frequencies co-existing in the same instance. Optical wave breaking cannot happen in the anomalous dispersion region because the red-shifted light near the leading edge cannot overtake the faster forward tail. This statement can be appreciated by simulating the evolution of pulse shapes and optical spectra in the anomalous dispersion region with the same value of N, shown in Figure 2.7. As shown in Figure 2.7a, after a certain distance of propagation, the inner parts compress whereas the outer parts of the pulse broaden. This is different from the pulse behaviour in Figure 2.6a, where the inner parts expand more rapidly than the outer parts. As a result, in the anomalous dispersion region, short optical pulses experience pedestal formation rather than wave breaking. As shown in Figure 2.7b, the acquired pedestals in the time domain lead to many more peaks in the spectrum as compared with Figure 2.6b [38].

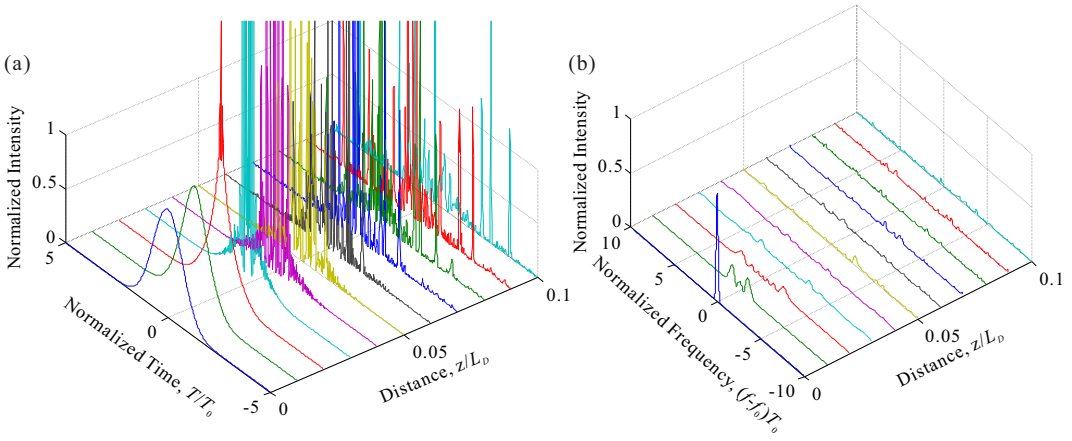

Figure 2.7: Evolution of (a) pulse shapes and (b) optical spectra over a distance of $0.1L_D$ for an initially unchirped Gaussian pulse in anomalous dispersion region for $N = 30$.

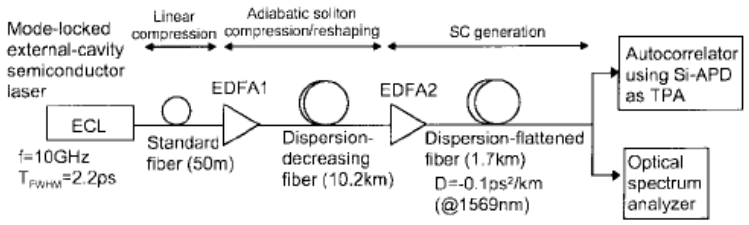

Figure 2.8: Experimental setup for SC generation reported by Y. Takushima et al [39]. ©1998 IEEE

Since both the pulse shapes and the optical spectra generated in the normal dispersion regime are much smoother, a large amount of work on nonlinear spectral broadening in

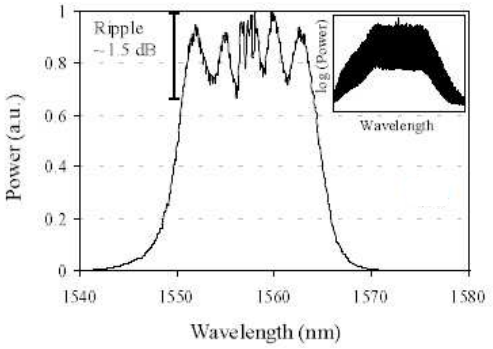

Figure 2.9: Flat spectrum generation by P. Almeida et al. through SSFBG based pulse pre-shaping [18]. ©2005 IEEE

this region is described in the literature. The common objective of the works reviewed below was to improve the spectral flatness of the broadband spectrum. Since SPM induces a perfect linear chirp on the parabolic pulses, they remain parabolic in shape and lead to a spectrally flat spectrum whilst propagating within the normal dispersion region of a nonlinear fibre [40]. Based on this concept, F. Parmigiani et al. [17] obtained a flat SPM-induced spectrum with a $3dB$ bandwidth of $29nm$ and ripples of around $3dB$ on the top through the propagation of parabolic pulses in a HNLF. Benefiting from the particular dispersion and nonlinearity design of a normal dispersion photonic crystal fibre (PCF) used for the spectral broadening, L. Hooper et al. [41] achieved a $800nm$ SPM-induced spectrum with ripples of up to $5dB$. The achieved spectrum was around three times broader as compared to the spectrum generated from the same length conventional single mode fibre by using the same input pulse. Through further tailoring of the spectrum achieved by parabolic pulse propagation in the normal dispersion region of a HNLF, M. Clarke et al. [42] generated a flat-top spectrum with a $3dB$ bandwidth of $20nm$ with ripples of up to around $3dB$ on the top. Y. Takushima et al. [39] reported the generation of a flat supercontinuum (SC) over $140nm$ wide with ripples of up to around $5dB$ on the top by using semiconductor laser based pulse sources. As shown in Figure 2.8, the most crucial design of their system was the use of a dispersion-flattened fibre having a small normal GVD which was separated from the pulse compression/reshaping section. This approach can be considered as the first demonstration of the pulse pre-shaping enhanced SC generation. With pulse pre-shaping performed by superstructured fibre Bragg gratings which can be treated as a linear filter, as shown in Figure 2.9, P. Almeida et al. [18] generated a flat spectrum with maximum $1.5dB$ ripples on the top over a $3dB$ bandwidth of $13nm$ through the propagation inside the normal dispersion region of a commercial HNLF. It was reported that the flatness of the generated spectrum has the potential to be further improved by optimizing the linear filter design. With the employment of evolutionary algorithms, K. Kashiwagi et al. [43] generated a spectrum with 3dB spectral peaks and a $20dB$ bandwidth of $118nm$ in the normal dispersion region of a dispersion flattened fibre. They precisely controlled the pulse synthesizer through genetic algorithms (GA). The combination of fitness functions in

GA enhanced the suppression of the background noise and consequently improved the flatness of the generated spectrum.

2.2.3 Numerical Method

As a nonlinear partial differential equation, the NLSE (Equation 2.4 or Equation 2.8) generally does not have analytic solutions. Therefore, a numerical approach is required to model the picosecond pulse propagation in optical fibres. The split-step Fourier method (SSFM) is a widely used numerical method to compute the pulse at the output of a fibre if its characteristics at the fibre input are known [44]. However, the opposite operation can also be envisaged, which is referred to as the inverse split-step Fourier method (ISSFM) [45].

2.2.3.1 Split-Step Fourier Method

The basic concept of SSFM is to assume that the dispersive and nonlinear effects can be considered to act independently over each short section of distance h inside the fibre. This parameter h is called the step size in SSFM. Mathematically,

$$A\left(z+h,T\right) \approx exp\left(h\hat{D}\right) exp\left(h\hat{N}\right) A\left(z,T\right), \tag{2.39}$$

where

$$\hat{D} = -\frac{i\beta_2}{2}\frac{\partial^2}{\partial T^2}, \tag{2.40}$$

$$\hat{N} = i\gamma|A|^2. \tag{2.41}$$

The exponential operator $exp\left(h\hat{D}\right)$ can be performed in the Fourier domain as

$$exp\left(h\hat{D}\right) B\left(z,T\right) = F_T^{-1} exp[h\hat{D}\left(i\omega\right)] F_T B\left(z,T\right), \tag{2.42}$$

where F_T represents the Fourier-transform, $\hat{D}\left(i\omega\right)$ is obtained from Equation 2.40 by replacing $\partial/\partial T$ by $i\omega$, where ω is the angular frequency in the Fourier domain.
In order to achieve more accurate results, the procedure in Equation 2.42 is replaced by

$$A\left(z+h,T\right) = exp\left(\frac{h}{2}\hat{D}\right) exp\left(h\hat{N}\right) \left(\frac{h}{2}\hat{D}\right) A\left(z,T\right), \tag{2.43}$$

or

$$A\left(z+h,T\right) = exp\left(\frac{h}{2}\hat{N}\right) exp\left(h\hat{D}\right) exp\left(\frac{h}{2}\hat{N}\right) A\left(z,T\right). \tag{2.44}$$

There are various selection criteria of h in the literature. The figure of merit of each criterion is the computational cost for a certain level of global accuracy. Some typical selection criteria of h for optical fibre communication systems can be found in [46].

2.2.3.2 Inverse Split-Step Fourier Method

It is possible to calculate the input waveform that gives rise to a known pulse at the output of the fibre by removing the nonlinear and dispersive effects one step at a time. This is the basic concept of the inverse split-step Fourier method (ISSFM). Mathematically, ISSFM can be expressed as

$$A\left(z-h,T\right)=exp\left(-\frac{h}{2}\hat{D}\right)exp\left(-h\hat{N}\right)exp\left(-\frac{h}{2}\hat{D}\right)A\left(z,T\right). \tag{2.45}$$

The ISSFM is useful in specific cases when some of the characteristics of the desired input pulses are uncertain, even completely unknown. Once the characteristics of the desired input pulses are calculated using the ISSFM, the pulse shaping techniques, introduced in the next section, can be used to transform the conventional Gaussian or hyperbolic secant pulse shapes to the shapes determined by the calculation.

2.3 Pulse Shaping Techniques

The generation of arbitrary and user-defined waveforms with precisely controlled characteristics in both phase and amplitude is important for all the experimental work described in this thesis. The technique of pulse shaping in the spectral domain fulfils this requirement. In this section, pulse shaping is thoroughly investigated from its fundamental concepts to its applications.

2.3.1 Fundamental Concept of Pulse Shaping

The pulse shaping techniques discussed here are based on the linear, time-invariant filter, which is a well-known concept in electrical signal processing. Linear filtering could be described in either time or frequency domain.
In the time domain, the filter is represented by its impulse response $h\left(t\right)$. The output electrical field $E_{out}\left(t\right)$ of the linear filter is the convolution of the input electrical field $E_{in}\left(t\right)$ and the filter impulse response $h\left(t\right)$. Mathematically, this can be expressed as

$$E_{out}\left(t\right)=E_{in}\left(t\right)*h\left(t\right)=\int E_{in}\left(t'\right)h\left(t-t'\right)dt', \tag{2.46}$$

where $*$ denotes convolution. From Equation 2.46, it is easy to conclude that if the input electrical field of the linear filter is a delta function, then the output electrical field is simply the filter's impulse response. As a result, if the input pulse is short enough, the task of generating an output pulse with an arbitrary shape is equivalent to designing a linear filter with an impulse response that resembles the output shape.
In the frequency domain, the filter is characterized by its frequency response $H(\omega)$. The Fourier transform $\tilde{E}_{out}(\omega)$ of the output electrical field is the product of the Fourier transform $\tilde{E}_{in}(\omega)$ of the input electrical field and the frequency response $H(\omega)$. This quantitative relation can be expressed as

$$\tilde{E}_{out}(\omega) = \tilde{E}_{in}(\omega) H(\omega) . \tag{2.47}$$

In Equation 2.47, $\tilde{E}_{out}(\omega)$, $\tilde{E}_{in}(\omega)$ and $H(\omega)$ are the Fourier transforms of $E_{out}(t)$, $E_{in}(t)$ and $h(t)$, respectively. Since the Fourier transform of the delta function is the unity function, the output spectrum of a delta input pulse is simply the frequency response of the linear filter. As the implementation of multiplication is much more straightforward than convolution, it is usually preferable to perform the filter design in the frequency domain.

2.3.2 Pulse Shaping Devices

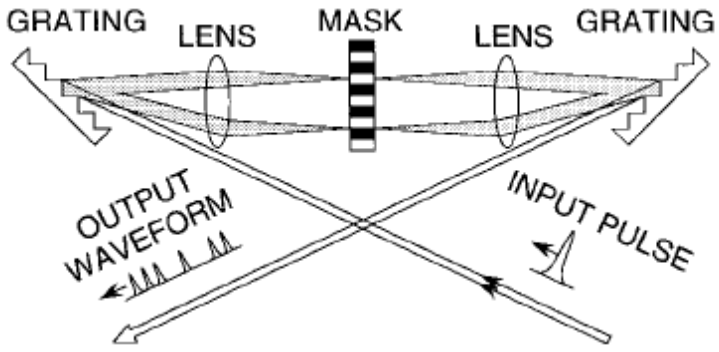

Figure 2.10: Configuration of basic pulse shaping apparatus [47]. ©1998 IEEE

Perhaps the most widely known pulse shaping apparatus is the one shown in Figure 2.10. As described by A. Weiner [47, 48, 49], this basic apparatus consists of a pair of diffraction gratings and lenses, and a phase and amplitude mask. The pair of diffraction gratings and lenses is configured as a zero dispersion pulse compressor. This configuration ensures that the output pulse is identical to the input pulse if there is no pulse shaping mask.
The frequency components of the input pulse are angle dispersed by the first grating, and then focused to small diffraction limited spots at the back focal plane of the first lens. Due to the spatial Fourier transform performed by the first lens, the frequency

components are spatially separated along one dimension. The spatially dispersed frequency components on the back focal plane are manipulated by the spatially patterned phase and amplitude mask (or a spatial light modulator, SLM) located there. The shaped pulse is obtained after the recombination of all the frequency components by the second grating and lens. The mask used in the configuration could be either fixed or programmable.

The fixed shaping masks can provide excellent shaping quality, but can only perform binary phase modulation. Their other drawback is of course that for every new application of the apparatus, an individually designed mask needs to be fabricated.

The programmable SLM is capable of generating continuous phase control for the pulse shaping process. Based on the same configuration as demonstrated in Figure 2.10, two common techniques are discussed here. In the first technique, the liquid crystal modulator (LCM) arrays are used to replace the fixed mask in the configuration. Detailed information on LCM based programmable pulse shapers can be found in [50, 51, 52]. The amplitude and phase control of the dispersed frequency components are achieved by the refractive index change of the liquid crystal induced by the applied electric field. Since the LCM requires vertical polarization, while the efficient diffraction of the grating needs horizontal polarization, the LCM is sandwiched by two half wave plates in the configuration. In the second technique, an acousto-optic modulator (AOM) is used as a programmable mask in the configuration. The basic concept of AOM based programmable pulse shapers can be found in [53, 54]. A piezoelectric transducer in the AOM converts the radio frequency (RF) voltage signal applied to the AOM crystal into a travelling acoustic wave. The travelling acoustic wave leads to a refractive index grating through the photo-elastic effect. Depending on the waveform of the RF signal, the dispersed frequency components could be either phase or amplitude modified.

Superstructured fibre Bragg gratings (SSFBGs) can also be used as spectral filters which allow for both amplitude and phase shaping. Their operation once again relies on the linear filtering in the spectral domain. But the mechanism of changing the spectral amplitude and phase of the input pulse is different. In a SSFBG, the refractive index profile is not uniform in amplitude or/and phase across its length. If the relative changes of its refractive index are small enough to allow the incident light to penetrate the full length of the device, it is termed as weak SSFBG. In a weak SSFBG, the whole grating structure has a equal contribution to the reflected light. Then the impulse response $h(t)$ of a SSFBG has the same envelope as the spatial refractive index modulation profile $A(x)$ which is used to write the grating. The conversion from space to time can be calculated via $t = 2xn/c$, where n is the refractive index of the fibre core. Thus, with well defined input and output pulse characteristics, a SSFBG can be designed and fabricated to satisfy the required shaping process. The advantages of SSFBGs over LCM or AOM are: Firstly, they can be readily integrated in optic fibre systems. Secondly, they are less lossy, simple and cheap. But they are static components and are not reconfigurable

[55, 56]. As reviewed in [57, 58], several optical telecommunication systems have employed SSFBG based pulse shaper to obtain pulses with specific characteristics desired in each system. Some typical applications include: saw-tooth pulses generation for robust and high performance time domain add-drop multiplexing [59, 60, 61], rectangular [62, 63, 64] and parabolic [65] pulses generation for all fibre based pulse retiming.
Long period fibre gratings (LPFGs) have also been used as pulse shaping devices. Unlike the previously described pulse shaping devices, the LPFG filters shape the pulses in the temporal domain based on the technique of temporal coherence synthesis. In this technique, the general principle is the constructive interference of time-delayed replicas of a transform-limited pulse, which leads to the superposition of the temporal waveform of the time-delayed individual pulses. The relative time delay among the different pulse replicas determines the pulse shapes synthesized at the output of such a device [66]. In practice, this technique was reported to be implemented by an all-fibre Mach-Zehnder interferometer consisting of two cascaded LPFGs [67]. In this configuration, the first LPFG splits the input pulse energy into two parts. These two parts propagate in the core mode and one of the cladding modes respectively at different speeds until they reach the second LPFG. In this second LPFG, the two modes interfere coherently. Since both of the interfering signals propagate inside a single piece of the fibre, the operation of this device is robust in terms of the temperature sensitivity. Both stable flat-top [68] and parabolic [67] optical pulses can be generated using such a device.

2.3.3 Description of the LCOS Shaping Filter

Besides the pulse shaping devices described in the previous section, the Liquid Crystal on Silicon (LCOS) technique was studied for pulse shaping in recent years. In this section, the LCOS technique and the pulse shaper based on it are reviewed.

Figure 2.11: Schematic of LCOS Structure [69]. ©2006 IEEE

The LCOS technique was first demonstrated by G. Baxter in 2005 [69]. It is a display technique which combines liquid crystal (LC) and semiconductor technologies. As shown in Figure 2.11, in the LCOS structure, the liquid crystal is placed in between an ITO-coated (ITO: Indium Tin Oxide) top glass and an active matrix backplane. As stated by K. Johnson in 1993 [70], the LCOS can be employed to control the phase of the light reflected from each pixel. The switching element based on the technology of LCOS is the heart of a commercial programmable pulse shaper, Finisar Waveshaper (W/S). The W/S provides unique capabilities for the independent control of the spectral amplitude

and phase of short optical pulses.

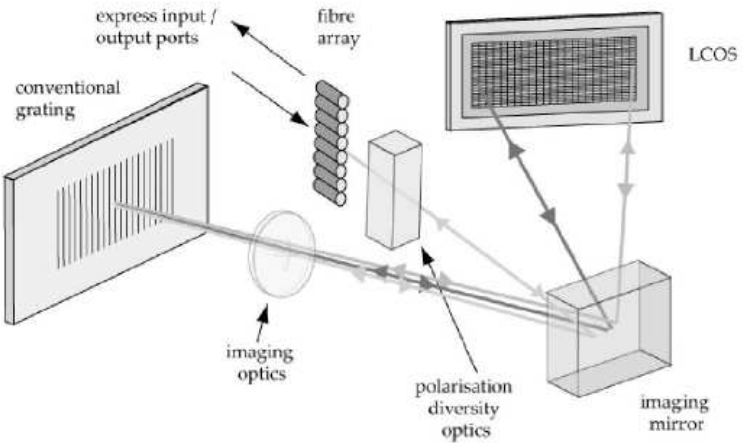

Figure 2.12: Waveshaper Optical Design [69]. ©2006 IEEE

The optical design of the W/S is shown in Figure 2.12. The W/S provides integrated switching and optical power control by incorporating polarization diversity, control of mode size and 4-f wavelength optical imaging in the dispersive axis of the LCOS. When light passes from the fibre array, the polarization diversity optics separates the two orthogonal polarization states and aligns them to be in the high efficiency s-state of the diffraction grating. Then, the imaging optics reflects the light to the grating. The grating makes the light angularly dispersed and reflects it back to the cylindrical mirror which redirects the separated frequency (wavelength) components to different channels on the LCOS. The beam-steering image on the LCOS makes the path of every wavelength channel reflected to a particular port of the fibre array. Phase control of every wavelength channel is achieved by the phase image applied on the LCOS. The optical power control for every wavelength channel is implemented by setting the grating pattern on the LCOS to split the light into two paths. Then, one of them is directed to the output fibre, while the unwanted power is directed to a dump location in the W/S. This is a significant difference to the conventional LCM based programmable pulse shaper mentioned in Section 2.3.2, where the wavelength dependent attenuation is achieved by polarization dependent deflection or displacement.

The W/S available in our laboratory is operated in C band. It has a maximum filter bandwidth of $5THz$ ($40nm$ @$1550nm$). The resolution of the frequency setting in the W/S is $1GHz$. For the optical power control, the W/S controls the attenuation in the range of 0 to $35dB$ with a resolution of $0.1dB$. For the spectral phase control, the effective range is from 0 to 2π.

Before actually employing the W/S for the research work reported in the following chapters of this thesis, I first characterised its attenuation response using the experimental setup shown in Figure 2.13. The amplified spontaneous emission (ASE) source from an erbium doped fibre amplifier (EDFA) was used as the broadband source which covered

the wavelength range from $1540nm$ to $1560nm$ in the characterization. The first measurement was carried out when no attenuation and phase change was applied on the input signal by the W/S. Consequently, the insertion loss of the W/S was measured under this test. In a second measurement, I applied a repeated attenuation profile in the range of $0-25dB$ in steps of $0.1dB$ and measured the optical response at the output when no phase change was applied.

Figure 2.13: Experimental setup for W/S attenuation response characterization.

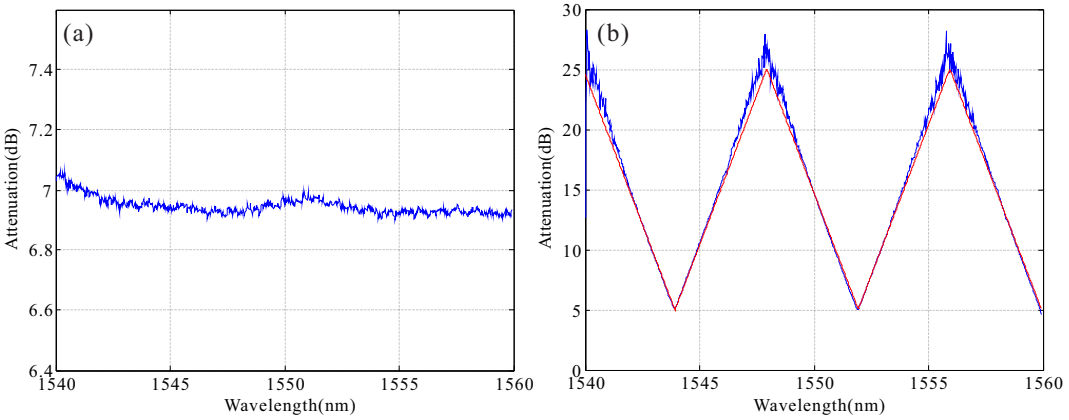

Figure 2.14: Attenuation response of the W/S. (a) The insertion loss of W/S measured when no attenuation and phase change was applied. (b) The attenuation response of the W/S with a repeated attenuation profile.

From the characterization results shown in Figure 2.14, it is easy to conclude that the insertion loss of the W/S for each frequency component is around $7dB$. The response of the W/S for small values of attenuation was much more precise than its response for large values. This indicates that the W/S requires calibration before being used to shape pulses which are required to have accurately controlled characteristics.
Since it is not straightforward to accurately measure the spectral phase of an optical pulse, the group delay of the W/S was measured to deduce the spectral phase response of the W/S. This is because the group delay is the first derivative of the spectral phase with respect to the angular frequency. The principle and experimental setup of the group delay measurement can be found in [71]. The spectral phase response of the W/S was also measured when no attenuation or phase change was programmed on the W/S. The purpose of this test was to find out the dispersion induced by the instrument itself. The group delay measurement result and its linear fitting are shown in Figure 2.15. The measurement indicated that the W/S itself induced a group delay of $0.25ps/nm$.

Although it was quite small, it still needs to be compensated for in any application requiring precise spectral phase control.

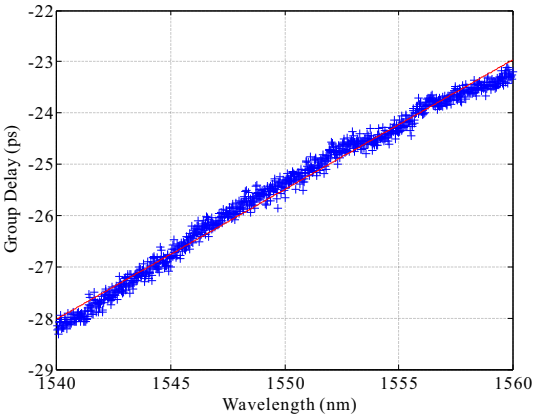

Figure 2.15: The group delay measurement of the W/S when no attenuation and phase change was applied.

2.3.4 Adaptive Pulse Shaping

The pulse shaping technologies described in Section 2.3 provide the capability to harness short optical pulses. In practice, the precision of the pulse shaping process is mainly limited by both an incomplete knowledge of the input laser source characteristics and any imperfections in the pulse shaping apparatus, eg. the introduction of residual dispersion. Both these drawbacks are almost impossible to compensate for manually. Because of this, it is often necessary to bring in adaptive pulse shaping processes to overcome these difficulties.

Evolutionary algorithms are embedded into the pulse shaping process by receiving information from the experiment and using it as the feedback to update the transfer function of a programmable shaper. There are a large number of demonstrations on this approach in the literature.

T. Baumert et al. reported a femtosecond pulse compression process in 1997 [72]. A pulse shaper based on a LCM was used to recompress the pulse broadened by a SF10-rod with the aid of evolutionary strategy (ES) with additional crossover procedure. The intensity of the second harmonic signal of the recompressed pulse was utilized as the feedback in the algorithm. Without any prior knowledge of the input pulse, the algorithm successfully drove the pulse shaper to compress the input pulse into a nearly transform limited pulse.

The authors of the previous work only modified the spectral phase of the pulse to eliminate the dispersion induced pulse broadening. The first adaptive real-time femtosecond

pulse shaping process that acted both on the spectral intensity and the phase was reported by D. Meshulach et al. in 1998 [73]. The cross correlation measurement of the output pulse was used as the feedback to evaluate the properly designed cost function in a simulated annealing algorithm. They managed to obtain the target pulse from the LCM based pulse shaper without requiring any optimisation of the input pulse.
In 2001, D. Zeidler et al. [74] thoroughly demonstrated adaptive femtosecond pulse compression with the assistance of ES. The validity and efficiency of the algorithm was investigated through both simulation and experiment. They also revealed some methods to design the search space and determine the dimension of individuals. This work could be treated as a useful guideline for the pulse shaping process with evolutionary algorithms.
Some works are devoted to speeding up the convergence of the adaptive pulse shaping system. In 2002, A. Rundquist et al. [75] numerically and experimentally demonstrated the performance of the Gerchberg-Saxton (GS) algorithm in phase-only pulse shaping. The GS algorithm iterates the phase function by connecting the input pulse spectrum and temporal intensity profile of the target pulse with a one-dimensional fast Fourier transform (FFT). So the algorithm converges much faster than conventional evolutionary algorithms and is independent of the number of phase points.
In 2003, R. Mizoguchi et al. [76] proposed a thinning out method to improve the convergence time of the genetic algorithm (GA) used in a programmable SLM based pulse shaping system. In this method, the GA does not optimize the condition of all the pixels in the SLM, but only optimizes every N^{th} pixel, where $N = 1,\ 2,\ 4,\ 8,\ 16$. The condition of the remaining pixels was interpolated. They experimentally proved that the convergent value of the optimization was not affected if the value of N was appropriately chosen.
The pulse propagation could also be optimized by the adaptive pulse shaping process. F. G. Omenetto and et al. [77] reported successful pulse propagation in a single mode fibre keeping its original characteristics through simulation. A pulse shaper was used at the input of the fibre to pre-shape the pulse. The transfer function of the pulse shaper was optimized by the GA in which the characteristics of the pulses at the output end of the fibre were used as the feedback. This method provided the capability to evolve towards the optimum field when the theoretical prediction is difficult and the experimental conditions are not consistent.

2.4 Conclusion and Discussion

This chapter provides a review of the theories needed to understand the work described in the rest of this thesis. In Section 2.2, the NLSE, which is fundamental in order to understand the nonlinear pulse propagation in an optical fibre, was firstly derived.

Then, the effects of GVD and SPM were thoroughly described to demonstrate how the pulse behaviour is affected in the different dispersion regimes. The numerical method employed to solve the NLSE is a tool that has been used to simulate the optical fibre systems described in the following chapters. The pulse shaping technique discussed in Section 2.3 is the technique employed in all the experiments reported in the rest of this thesis.

Chapter 3

Adaptive Pulse Shaping System

3.1 Introduction

Chapter 2 reviewed prior art, where it was demonstrated that the combination of a pulse shaping system with an adaptive mechanism is beneficial in improving the quality of the shaped signal. In this chapter, the principle of adaptive pulse shaping is thoroughly described, showing how it is able to minimize the differences between the signal after shaping and the target signal. The chapter starts with a description of the main building blocks of adaptive pulse shaping, followed by a description of the general principle of the evolutionary algorithm, which governs the optimization process in an adaptive system. The evolution strategy (ES), which is the optimization algorithm selected to be implemented in my experiments, is introduced in detail. At the end of the chapter, I introduce the basic configuration of what I call an arbitrary spectral synthesis system, which is an extension of the general adaptive pulse shaping system including a nonlinear broadening stage.

3.2 General Principles of Adaptive Pulse Shaping

The aim of an adaptive pulse shaping system is to compare the characteristics of a shaped pulse with those of a target pulse and then gradually minimize the differences between the two [72]. Figure 3.1 schematically shows the configuration of a typical adaptive pulse shaping system. The pulse source is normally a mode-locked laser (MLL) emitting a train of pulses, the temporal shape of which is normally either Gaussian or secant hyperbolic. Due to the fact that no new frequencies can be generated in the linear pulse shaping process, the spectral bandwidth is the most important parameter for the pulsed source. The pulse shaper is the key element in a pulse shaping system. It can be

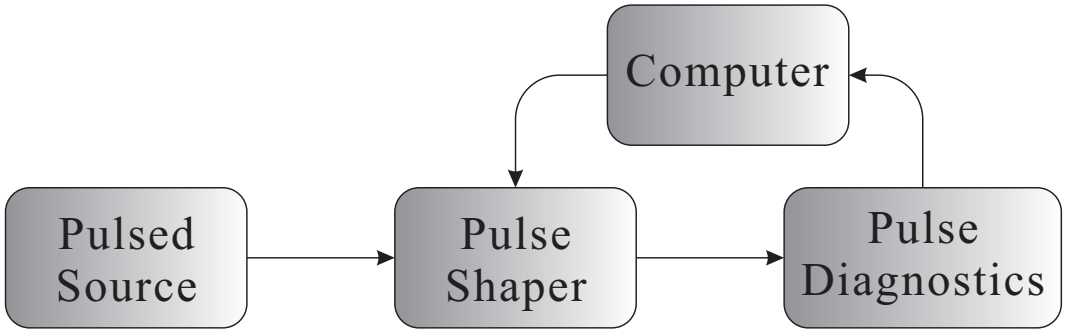

Figure 3.1: Blockdiagram of an adaptive pulse shaping system.

any device which is capable of altering the spectral amplitude and phase of an incident light beam, such as a fibre Bragg grating [55] or a spatial light modulator based on liquid crystal [50]. In the case of an adaptive pulse shaping system, the pulse shaper is additionally required to be programmable and reconfigurable. Another important component of an adaptive pulse shaping system is the pulse diagnostics. There are various techniques to assess the pulse characteristics. Typically, an optical spectrum analyser (OSA) is a common device to obtain the spectrum of a pulse. In the time domain, short pulse shapes can be directly measured by an optical sampling oscilloscope (OSO). The drawback of these two simple and straightforward measurements is that the phase information of the pulse is lost. For the acquisition of the full pulse characteristics, techniques such as either frequency resolved optical gating (FROG) [78], or spectral phase interferometry for direct electric-field reconstruction (SPIDER) [79] are available and widely used. The choice of the most suitable technique to use in the adaptive system readily depends on the objectives of the experiments. Finally, a computer is an indispensable element in an adaptive pulse shaping system. It is the host of the optimization algorithm and communicates with both the devices for pulse characterization and the pulse shaper through its interfaces, thus forming a close feedback loop.

All of the hardware of an adaptive pulse shaping system works under the control of a dedicated optimization algorithm. For any optimization algorithm, a feedback signal is essential as it leads the evolution of the system parameters which are being optimized. In an adaptive pulse shaping system, the comparison between the measurement results of the pulse diagnostics and the characteristics of the target pulse is quantized to be used as the feedback signal. Consequently, the transfer function fed into the programmable pulse shaper is optimized according to it. The optimization process is terminated when the feedback signal indicates that the quality of the shaped pulse reaches the requirement of the experiment.

An adaptive pulse shaping system exhibit several attractive features. Firstly, it allows automatic convergence to a target pulse. Secondly, the adverse impact on the shaped pulse of the various uncertainties in the system can be minimized. Finally, it provides a route towards an intelligent experimental system with limited human intervention,

which is an efficient way to conduct and collect results from a complex experiment involving a large amount of devices and instruments.

3.3 Evolutionary Algorithms

Evolutionary algorithms (EAs), which will be thoroughly reviewed in this section, are common tools for adaptive pulse shaping. They are global optimization algorithms which mimic the biological evolution process. Individuals with robust gene qualities will survive the natural selection and produce offsprings for the next generation.

3.3.1 The Generic Blockdiagram

As reviewed in Section 2.3.4, by incorporating an adaptive system, the quality of the shaped signal obtained after the pulse shaping can be significantly improved. An adaptive system is governed by the evolutionary algorithms (EAs). In the following sections, the general principle of the EA is cohesively reviewed and elaborated.

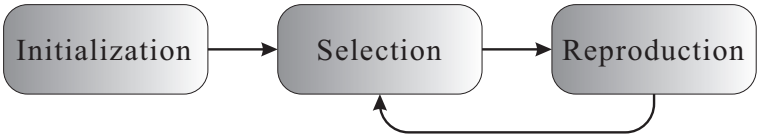

Figure 3.2: The generic blockdiagram of an evolutionary algorithm.

Figure 3.2 shows the generic blockdiagram for an evolutionary algorithm (EA) [80, 81, 82]. In general, an EA starts with the initialization, followed by an iterative loop of selection and reproduction. At the stage of initialization, an EA must specify the representations of the candidates and then the population sizes of both the parent and the offspring candidates. At the stage of selection, the first task is to specify the form of the objective function, the value of which is referred to as the fitness value of the candidates generated in an EA. It is also the criterion for the evaluation of the candidates. Then the EA must determine the mechanism to select the eligible parent candidates for the production of offspring candidates and subsequently the survival candidates for the next generation. The stage of reproduction also plays an important role in an EA, since it determines how the offspring candidates are produced in each generation. It directly affects the robustness of an EA. In addition to these major stages, a stopping condition is essential to an EA since it provides the criterion to terminate it. In the following discussion of this section, each stage is introduced in detail.

3.3.1.1 Initialization

In the stage of initialization, the representation of candidates is the first issue to be resolved. It can be treated as the genome of a candidate, and each element of the representation is the gene of a candidate. According to [81, 82], there are two kinds of representations. In the first one, a candidate is represented by its visible physical features. Consequently, it is referred to as *phenotype* and the search space is named *phenotype space*. The second one is referred to as *genotype*, in which the genetic makeup is used to represent a candidate and the search space is named *genotype space*. The connection between these two kinds of representations is established by a mapping or coding function. With respect to the design of the coding function, the easiest way could be to follow the requirement of a particular algorithm being selected. Alternatively, the coding function can be avoided by directly using the *phenotype* to represent a candidate. There is no general answer to the question of which one of the two representations is better. In practice, more straightforward and problem-related representation is preferred.
Once the representation of a candidate is fixed, the next task in the stage of initialization is to determine the population sizes of the parents and the offsprings, which are usually kept constant in an EA. As the parent population is the basis for the generation of new search points, its size can be viewed as the degree of parallel searches that an EA supports. There is a critical number for the parent population size, by which an EA can always converge to the global optimum. When the parent population size is too small, an EA is often trapped by a local optimum. An unnecessarily large parent population size does not benefit the search for the global optimum, but can only reduce the speed of convergence of an EA.
The offspring population size plays a significantly different role in an EA. It indicates the willingness of an EA to keep the current parent population as the basis for the generation of a new search point without including any newly generated high quality offspring candidates in the parent population. If the offspring population size is too small, the candidates in the current parent population are prematurely removed before they can even be offered an opportunity to generate any offspring candidates. Consequently, an EA experiences a premature reduction of the diversity in the parent population and then it more likely converges to a local optimum.

3.3.1.2 Selection

The design of the objective function, which provides the formula to calculate the fitness value of a candidate, is the first problem to be faced when an EA enters the stage of selection. In general, as shown in Figure 3.3, there are two kinds of objective functions. One of them is linear, while the other is nonlinear. For a linear objective function (Figure 3.3a), the optimum can be always found at the boundaries of the search space

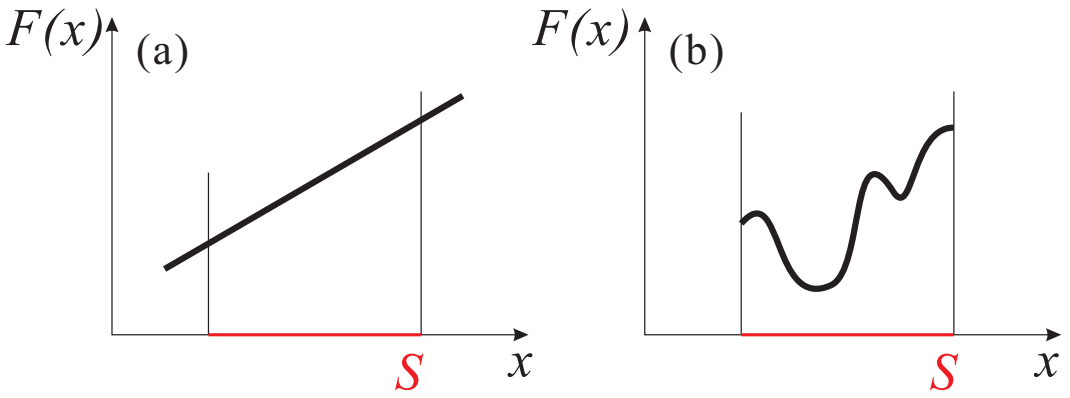

Figure 3.3: (a) Linear objective function and (b) nonlinear objective function for an EA. S represents the search space. x represents the search point. $F(x)$ represents the fitness value of the corresponding search point.

and the local optimum is the global optimum as well. The situation is different for a nonlinear objective function (Figure 3.3b), the optima are not necessarily located at the boundaries and instead they can be attained anywhere in the search space. Meanwhile, the global optimum exists together with several local optima and consequently the objective function exhibits a multi-peak structure. The objective function in an EA is often nonlinear as the problem requiring optimisation is often complex. Then, an EA must determine its selection mechanisms.
In general, the parent population size m is maintained in an EA. This is achieved by repeating the following two steps:

- n offspring candidates are generated using the current parent population as the source, and then
- the population size is reduced from $m + n$ to m.

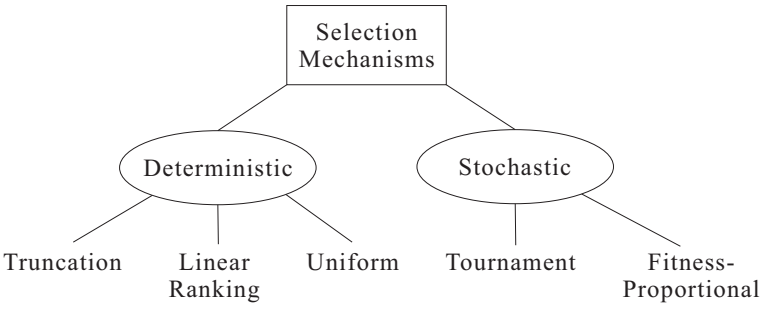

Figure 3.4: Categories of selection mechanisms in EA

In both of these two steps, a selection process is required to pick up a subset of candidates from the entire population. In the first step, a certain number of candidates in the current parent population is selected to produce the n offspring candidates. In the second step, m candidates are selected to be the parent population of the next generation. As shown in Figure 3.4, the two basic categories of selection mechanisms are

deterministic and *stochastic* [82].
In the category of deterministic selection, a fixed number is assigned to each candidate in the population, which indicates the number of times a candidate will be selected. Three commonly used deterministic selection mechanisms are: truncation, linear ranking and uniform selection. By contrast, in the category of stochastic selection, it is a fixed probability p_i of being chosen that is assigned to each candidate. As a result, after k selections have been made, each candidate will be selected $k * p_i$ times on average. However, the actual number of times a candidate is selected can be largely different from this expectation since the selection is made by randomly sampling the given probability distribution. Typical stochastic selection mechanisms are tournament selection and fitness-proportional selection.
There are differences in the performance of the EAs, depending on the selection process that has been adopted. A deterministic selection mechanism forces the candidate in the population to be selected at least once. This does not happen in a stochastic selection mechanism. As it is basically a statistical sampling process, the subset of candidates being selected can and frequently does deviate considerably from the expected ones. In the worst case, the best candidate in the population may never get chosen, but the worst one may have been selected a number of times. Therefore, it appears that there is no reason to implement the stochastic selection in an EA. However, it is demanded in some occasions. When an EA is trapped at a local optimum, the stochastic selection can act as a perturbation to help the EA escape from the trapping. Consequently, the robustness of an EA is improved.
Comparing to whether the implemented selection mechanism is deterministic or stochastic, it is more important to understand how a specific selection mechanism influences the evolution direction in an EA, which is termed the selection pressure [82]. Since the evolution direction depends on how the selection mechanism selects the survival candidates, it is equivalent to investigating how a particular selection mechanism distributes selection probability over the selection pool. Since most selection mechanisms are based on the fitness value, it is convenient to compare different selection mechanisms if the selection pool is sorted from top to bottom by decreasing fitness values.
Based on the study presented in [82], an EA with truncation selection converges much faster than an EA with the other two deterministic selection mechanisms. This is because the focus of search is greatly narrowed to several candidates ranked at the top of the selection pool. Thus, the selection pressure is strong in such an EA. The selection probabilities are assigned across the entire selection pool in an EA with either linear or uniform selection. In an EA with linear ranking, the probability of a candidate to be selected is proportional to its position in the ranking. The convergence speed to the optimum slows down as the selection pressure is weaker. An EA with uniform selection has the weakest selection pressure. As a result, it requires much longer time to converge to an optimum, which is more likely to be a local one. The selection pressure provided by the two stochastic selection mechanisms is generally weaker than the truncation but

stronger than the uniform selection. The tournament selection provides similar selection pressure to linear ranking. The ranking of selection mechanisms from weakest to strongest is:

- uniform
- fitness-proportional
- linear ranking and tournament selection
- truncation

It is then relevant to discuss how a selection mechanism can be chosen in the design process of an EA. The basic rule here is that the compounding selection pressure cannot be too high to prevent an EA from converging too fast to a local optimum. As a result, one of the selection mechanisms is generally required to be the uniform selection in an EA. The overall selection can be in turn adjusted by fixing one of the mechanisms to be uniform and choosing the other one from non-uniform mechanisms.

3.3.1.3 Reproduction

The stage of reproduction in an EA is responsible for the generation of offspring candidates. Distinguished by the number of parent candidates involved in the process, there are two basic classes of reproductive mechanisms: mutation of a single parent candidate and recombination of multiple parent candidates.
In the classic one-parent mutation reproductive mechanism, the offspring candidate is generated simply by copying the parent candidate and then applying variation over a portion of genes in the genome of the candidate. The amount of variations is determined by the number of genes being modified and the amount they are modified, by which is also termed the step size of the mutation and quantified as the distance between the candidates before and after the mutation in the search space.
In the case of multiple parent candidates, recombination is the reproductive mechanism. Here, the situation of two parent candidates is used as an example to explain how recombination produces offspring candidates. Under the recombination mechanism, the genome of an offspring candidate consists of subsets of genomes from both parents which are reassembled dynamically. The traditional operator here is crossover, in which several crossover points are selected first and then the subsets of genomes from the two parents are gathered into the genome of an offspring candidate alternatively at the crossover points. More details about the crossover operator can be found in [83, 84, 85].
Which one is better between crossover and mutation? As in the case of representation of candidates and selection category, there is no certain answer to this question. According

to [82], both crossover and mutation have their own advantages and drawbacks. Since crossover only exchanges genes between the two parent candidates, it does not create any new genes. The offspring candidates produced by crossover are the vertices of a N-dimensional rectangle defined by the parent candidates in the search space. Mutation, by contrast, keeps generating new genes, but because it is varying continuously, it cannot take large single step, which the crossover would be able to achieve. The choice between them is problem-related. It is worth pointing out that the choice between them also depends on the selection mechanism implemented in an EA. The rule here is that the combined effects of selection and reproduction mechanisms in an EA is required to make sure that the EA can gradually converge to the global optimum.

3.3.1.4 Stopping Criteria

The final part in an EA relates to the stopping criterion which is discussed here. Ideally, an EA is expected to stop when it finds the optimum solution. In some search problems with constraints applied to the search space, it is easy to know that an optimum has been reached. But for more general global search problems without any constraints, it is not possible to know that for sure. Normally, an EA is terminated based on the convergence of the algorithm, the quality of the best candidate encountered during the search, or the consumed computational effort.
Convergence means that there are no further changes occurring in the population. This can be detected by monitoring the evolution curve of the fitness value of the candidates from each generation. The convergence is reached once the curve is flattened out. Alternatively, there is either a pre-defined threshold for the fitness value of the candidate indicating acceptable quality or a computational budget. An EA is stopped as long as either of them is reached. The goal here is to make sure that an EA is able to find the global optimum within a certain amount of computational time.

3.3.2 Major Evolutionary Algorithm Approaches

There are three major approaches of implementing an EA: *Genetic Algorithm* (GA), *Evolutionary Programming* (EP) and *Evolution Strategy* (ES). In this section, they will firstly be introduced and then, following the structure of the presentation so far, they will be compared with respect to the following: the representation method of candidates, the selection operator and the reproduction operator. A comprehensive overview of all these algorithms can be found in [80].

3.3.2.1 Genetic Algorithm

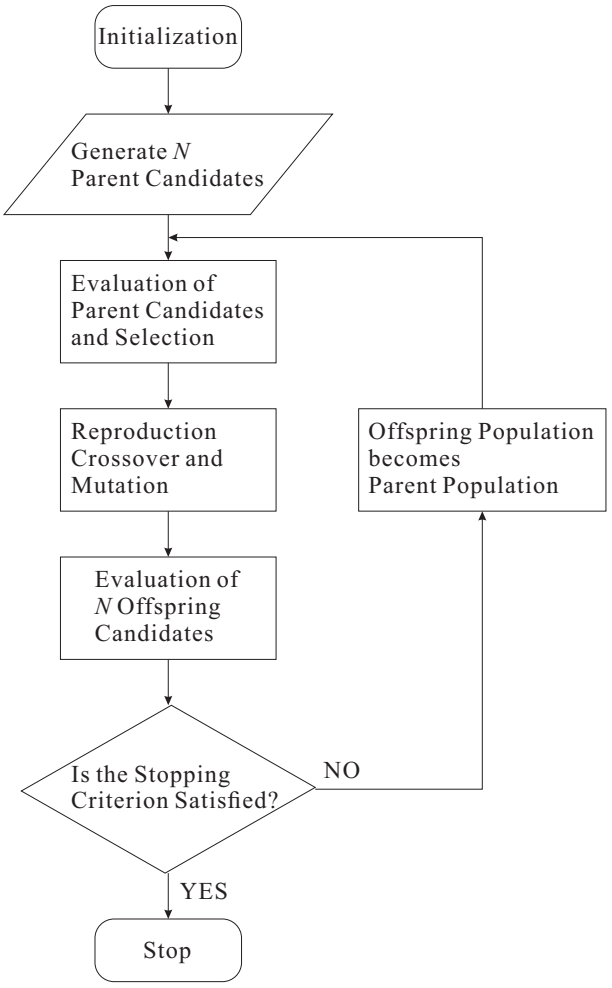

Figure 3.5: Flow chart of a GA.

GA has a long traceable history of more than half a century. It was invented by Holland in 1962 [86]. In 1975, it was used as an algorithm for parameter optimization by K. DeJong [87] for the first time. The general principle of the GA can be found in the flow chart Figure 3.5. It is worth noting that a large amount of modifications have been applied to the original GA to meet the requirement of specific optimization problems.
In a GA, the candidates are always represented in genotype. This means that a coding function is required to produce the corresponding binary strings for the candidates. Once a parent population with size N is generated, the parent candidates are evaluated using the objective function. Subsequently, the parent candidates used for the generation of offspring candidates is chosen based on the fitness-proportional selection mechanism. The better parent candidates contribute more to the genomes of offspring candidates. In the reproduction process, as normally the population size is fixed in a GA, N offspring candidates are generated step by step through both crossover and mutation. As long as the stopping criterion is not reached, the current offspring population

becomes the parent population for the next generation and the entire procedure repeats.

3.3.2.2 Evolutionary Programming

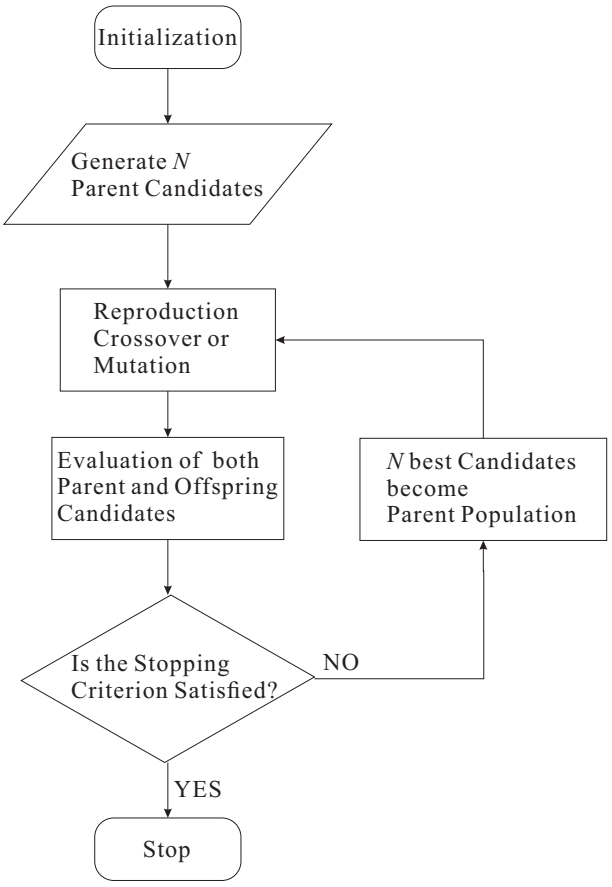

Figure 3.6: Flow chart of an EP.

EP was initially developed for artificial intelligence applications by Fogel in early 1960s [88, 89]. The general principle of EP is shown in Figure 3.6.
In an EP, the representation of candidates is phenotype, in which a coding function is avoided. In the initialization stage, N parent candidates are generated. In the reproduction process, through either a mutation or crossover operator, each of the current parent candidates generates exactly one offspring candidate. Then the parent and offspring populations are merged together to form a single population of size $2N$ and which is sorted according to their fitness value. The selection mechanism used here is truncation. In order to fix the parent population size, the N best candidates are selected to be the parent candidates for the next generation. The algorithm terminates once the stopping criterion is satisfied.

3.3.2.3 Evolution Strategy

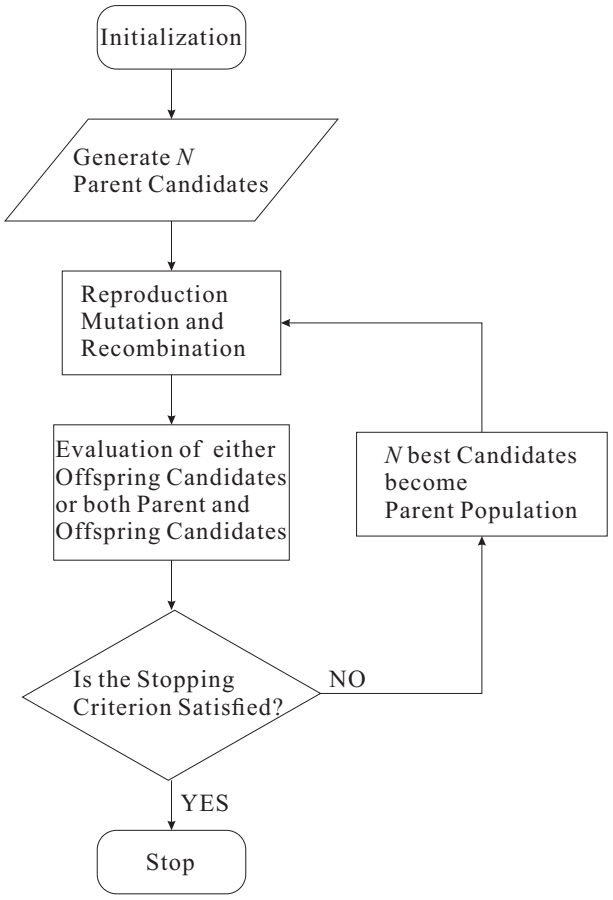

Figure 3.7: Flow chart of an ES.

ES was initially designed to solve complicated discrete and continuous parameter optimization problems and is applied mainly in experimental works. Compared to GA and EP, it has many more branches available to choose from according to the practical requirements of the experiments. It has been consequently selected for the experimental work described in this thesis. The basic flow chart of ES is shown in Figure 3.7.
In an ES, the candidates are represented as vectors of real numbers, i.e., they are represented in phenotype. Again, in the initialization stage, a parent population of size N is generated. In the reproduction process, a mutation operator is firstly used to generate $M(M \geq N)$ offspring candidates. Depending on the particular branch of ES being used, either the offspring population of size M or a merged population of both parent and offspring candidates of size $M + N$ are evaluated and sorted out. By using the truncation selection, top N candidates are selected to be parent candidates for the next generation. The algorithm is terminated when the stopping criterion is reached. A detailed description of ES will be given in Section 3.4.

3.4 Evolution Strategy

The evolution strategy (ES) is one of the main variations of evolutionary algorithms. The origins of ES dates back to 1960s in Germany. It was invented by Rechenberg and Schwefel in their theses [90, 91] at the Technical University of Berlin (TUB). Comprehensive reviews of ES could be found in references [92, 93].

3.4.1 Basic Principle of the Evolution Strategy

The ES follows the generic structure of an evolutionary algorithm consisting of initialization and an iterative loop of selection and reproduction, as described in Section 3.3.1. Apart from that, there are several distinct features in the ES. Firstly, the candidates are usually represented in phenotype, i.e., vectors of real numbers. This implies that no coding process is required in the ES. Secondly, the reproduction process of the ES is completed by mutation, in which random numbers with a zero-mean Gaussian distribution are generated and updated. Consequently, the ES is a stochastic search algorithm. The standard deviation σ of the Gaussian distribution plays an important role in the mutation process as it can ultimately affect the performance of the algorithm. It is therefore termed the "strategy parameter" and updated in a fashion that depends on the specific ES. Finally, the ES is designed for the minimization of a nonlinear objective function, as defined in Section 3.3.1.2. This nonlinear objective function is also called "fitness function" in the ES. All the candidates are evaluated according to the fitness function and sorted out based on the corresponding fitness value. Distinguished by the eligibility of the parent candidates for the selection of the candidates that will become the new parents in the following generation, there are two categories of ES that are considered here [93].

The first category is named $(\mu+\lambda)$-ES [93]. In each generation of the ES in this category, $\lambda(\lambda \geq 1)$ offspring candidates are generated from μ parent candidates. The μ parent candidates for the next generation are the best out of both the parent and the offspring candidates in the current generation. A typical ES in this category is the two-membered ES, which I have selected for my work.

The second category of evolution strategies is called (μ, λ)-ES [93]. In each generation of the ES in this category, $\lambda(\lambda \geq \mu)$ offspring candidates are generated from the μ parent candidates. Only the λ offspring candidates are eligible to be considered and the best μ candidates out of them are selected to be the parent candidates for the next generation. I have chosen the covariance matrix adaptation (CMA) ES, which is a variation of (μ, λ)-ES, for use in my work.

3.4.2 The Two-Membered Evolution Strategy

Step 0: Initialization

Create an n-dimensional Euclidean Search Space

The initial parent candidate: $X_{parent}^{(0)} = \left\{ x_i^{(0)}, i = 1,2,\ldots,n \right\}^T, x_i^{(0)} \in R$

Step 1: Mutation

Generate an offspring candidate from the parent candidate in generation t through

$$X_{offspring}^{(t)} = X_{parent}^{(t)} + Z^{(t)}$$

where $x_{offspring,i}^{(t)} = x_{parent,i}^{(t)} + z_i^{(t)}, z_i^{(t)} \in N\left(0, \sigma_t^2\right) i = 1,2,\ldots,n$

Step 2: Selection

Select the parent candidate for the next generation t+1 from the parent candidate in iteration t and its offspring

$$X_{parent}^{(t+1)} = \begin{cases} X_{offspring}^{(t)}, F\left(X_{offspring}^{(t)}\right) \leq F\left(X_{parent}^{(t)}\right) \\ X_{parent}^{(t)}, otherwise \end{cases}$$

where, $F(X)$ is the fitness function
Increase t to t+1, repeat step 1 and step 2 until the termination rule is hold

Figure 3.8: The basic algorithm for the two-membered ES.

Figure 3.8 mathematically shows the basic algorithm of the two-membered ES for a minimization problem. At the beginning of the optimization process, the search space is initialized to be an n-dimensional Euclidean space. This means that the candidates X generated in the optimization process are arrays of n elements. Depending on the requirements of users, the parent candidate X_{parent} in the first generation can be initialized to either an array of zero or a user-specified array. Then, in the mutation process of each generation (Step 1 in Figure 3.8), an offspring candidate $X_{offspring}$ is generated by adding a zero-mean Gaussian distributed array Z with a standard deviation of $\sigma^{(t)}$ to the parent candidate. The standard deviation $\sigma^{(t)}$ is the strategy parameter of the two-membered ES. In the step of selection (Step 2 in Figure 3.8), both the parent candidate X_{parent} and the offspring candidate $X_{offspring}$ are eligible for the selection of the parent candidate in the next generation. By comparing the fitness values $F(X)$ of these two candidates, the one with the smaller value is selected. The algorithm is terminated when the fitness value converges to a pre-determined threshold, or the maximum number of generations has been reached.

The self-adaptation of the strategy parameter $\sigma^{(t)}$ is important in the ES. The one-fifth rule introduced in [93] is specially designed for the two-membered ES. In the programming procedure shown in Figure 3.9, the strategy parameter $\sigma^{(t)}$ is initially kept constant

1. Run the two-membered ES for m generations with σ_t keeps constant.
2. Calculate the success probability P_s within these m generations.
3. Update σ_t according to the following rules.

$$\sigma_{t,new} = \begin{cases} \sigma_t / a, P_s > 1/5 \\ \sigma_t \cdot a, P_s < 1/5 \\ \sigma_t, P_s = 1/5 \end{cases}$$

4. Repeat 1 to 3 until the algorithm is terminated

Figure 3.9: The programming procedure of the one-fifth rule.

for m generations. In these m generations, as long as the offspring candidate is selected as the parent candidate for the next generation, the current generation is marked as a success generation. Consequently, a quantity named as success probability P_s is defined as the ratio between the number of the successful generations and m. The value of $\sigma^{(t)}$ for the next m generations is adapted according to the value of P_s. If P_s is larger than $1/5$, $\sigma^{(t)}$ must be increased, otherwise, $\sigma^{(t)}$ must be decreased. The adaptation of $\sigma^{(t)}$ is scaled by a coefficient a ($a < 1$) and its reciprocal. The optimal value of the coefficient a is related to the fitness function to be optimized, the freedom of the search space n and the number of generations to be tested m. If n is large enough, m is chosen to be equal to n. As suggested by Schwefel in his thesis [94], in this situation, the value of a is recommended in the range of [0.85 1).

The two-membered ES is expected to be efficient as its strategy is simple. Meanwhile, its drawback is the risk of being stuck at a local minimum as it can only explore a fraction of the whole search space.

3.4.3 The Covariance Matrix Adaptation Evolution Strategy

Compared with the two-membered ES, the CMA-ES has a much more complex strategy allowing the exploration of a much broader search space. As a result, it has a much higher probability of finding the global minimum but a lower efficiency. A detailed description of the CMA-ES can be found in [95].

The basic algorithm of the CMA-ES is schematically shown in Figure 3.10. The step of initialization is the same as in the two-membered ES. The search space is once again an n-dimensional Euclidean space. The parent candidate X_{parent} in the first generation is once more either an array of zero or a user-specified array. The differences between the two algorithms start to emerge in the iterative loop. In addition to the two steps of mutation and selection which are present in the two-membered ES, CMA-ES includes the additional step of recombination. In the mutation process of each generation of the CMA-ES, λ offspring candidates $X_{offspring}$ are generated by adding an array Z which is Gaussian distributed with zero mean and a standard deviation of $\sigma^{(t)}$ to the parent

Step 0: Initialization

Create an n-dimensional Euclidean Search Space

The initial parent candidate: $X_{parent}^{(0)} = \{x_i^{(0)}, i = 1,2,\ldots,n\}^T, x_i^{(0)} \in R$

Step 1: Mutation

Generate λ offspring candidates from the parent candidate in generation t through

$$X_{offspring}^{(t)} = X_{parent}^{(t)} + Z^{(t)}$$

where $x_{offspring,i}^{(t)} = x_{parent,i}^{(t)} + z_i^{(t)}, z_i^{(t)} \in N\left(0,\sigma_t^{\,2}\right) i = 1,2,\ldots,n$

Step 2: Selection

Select and sort out the best μ out from λ offspring candidates according to their fitness values

Step 3: Recombination

Increase t to t+1, the parent candidate for generation t+1 is achieved from a weighted average process of the selected μ offspring candidates from generation t

$$X_{parent}^{(t+1)} = \frac{1}{\sum_{j=1}^{\mu} w_j} \sum_{j=1}^{\mu} w_j X_{j:\lambda:offspring}^{(t)} \qquad w_j = \ln\left(\frac{\lambda+1}{2}\right) - \ln(j)$$

where, w_i is the weight, $X_{j:\lambda:offspring}^{(t)}$ denotes the jth best offspring candidate in generation t

Repeat Step 1 to Step 3 until the termination rule is hold

Figure 3.10: The basic algorithm for the CMA-ES.

candidate X_{parent} and repeating this procedure λ times. The value of $\sigma^{(t)}$, which is the strategy parameter, keeps unchanged in the generation. Then in the step of selection, only the λ offspring candidates $X_{offspring}$ are sorted out according to their fitness values. The best μ out of them are selected to enter the recombination process. The values of μ and λ are determined according to Equation 3.1 and Equation 3.2 [95]:

$$\lambda = 4 + \lfloor 3ln(n) \rfloor . \tag{3.1}$$

$$\mu = \lfloor \lambda/2 \rfloor . \tag{3.2}$$

In the step of recombination, the parent candidate X_{parent} for the next generation is generated through a weighted average process of the best μ candidates, in which the candidate with the smallest fitness value is awarded the largest weight. This is a unique way to generate the parent candidate X_{parent}. It keeps the optimization process evolving towards the optimum direction. The rule of termination of the algorithm is the same as in the two-membered ES except that it is monitoring the convergence of the minimum of the λ fitness values in each generation.

CMA-ES belongs to the general category of the $(1, \lambda)$-ES. The common means for the self-adaptation of the strategy parameter $\sigma^{(t)}$ in $(1, \lambda)$-ES variations and the generation of a new parent candidate are shown in Equations 3.3 and 3.4.

$$\sigma^{(t+1)} = \sigma^{(t)} exp(\xi), \tag{3.3}$$

$$x^{(t+1)} = x^{(t)} + \sigma^{(t+1)} z^{(t)}, \tag{3.4}$$

where ξ is a random number and represents the mutation strength of $\sigma^{(t)}$, $z^{(t)}$ is a Gaussian distributed vector with zero-mean and a variance of 1. The importance of the mutation strength ξ can be observed from Equations 3.3 and 3.4. It first directly determines the difference between $\sigma^{(t+1)}$ and $\sigma^{(t)}$, which is referred to as the change rate. Subsequently, the selection difference of $x^{(t)}$, which is the difference between $x^{(t+1)}$ and $x^{(t)}$ depends on the mutation strength as well. From a large amount of theoretical studies made to seek for the optimum mutation strength $\sigma^{(t)}$ [92, 96], it is found that the mutation strength that leads to an optimum change rate is usually not in accordance with the mutation strength that gives rise to a suitable selection difference. Generally speaking, the mutation strength required for the optimum change rate is weaker than the one for the suitable selection difference. The process of derandomization is employed here to resolve this misalignment in a way that the dependence of the change rate of $\sigma^{(t)}$ on the mutation strength ξ is eliminated [95].

In the CMA-ES, the process of derandomization takes effects on the self-adaptation of the strategy parameter $\sigma^{(t)}$ [95]. Equations 3.5 and 3.6 demonstrate the way to update $\sigma^{(t)}$ and generate the new candidate under the derandomization.

$$\sigma^{(t+1)} = \sigma^{(t)} exp(\frac{||z^{(t)}|| - E[||N(0,1)||]}{d}), \tag{3.5}$$

$$x^{(t+1)} = x^{(t)} + \sigma^{(t)} z^{(t)}, \tag{3.6}$$

where $||\cdot||$ is used to denote the length of a vector. $(||z^{(t)}|| - E[||N(0,1)||])/d$ replaces ξ in Equation 3.3, where $E[||N(0,1)||]$ is the expectation of $||z^{(t)}||$ under random selection, $d \geq 1$ is a damping parameter to control the change rate of $\sigma^{(t)}$. This means that the step length $||z^{(t)}||$ for the mutation on the object being optimized is used to change $\sigma^{(t)}$. The strategy parameter $\sigma^{(t)}$ is then increased if $||z^{(t)}||$ is larger than expected. In the opposite way, it is decreased.

An optimization process should be evaluated after several generations, rather than a single step. Thus, the self-adaptation of the strategy parameter is also worth to be designed based on the record of the selection information over a number of generations in the optimization process. In the CMA-ES, the quantity of evolution path $p^{(t)}$, which shows the correlation between single steps, is used to update the strategy parameter $\sigma^{(t)}$ together with the derandomization process. The iterative method to calculate the

evolution path is named cumulation and shown in Equation 3.7 [95]:

$$p^{(t+1)} = (1-c)p^{(t)} + \sqrt{c(2-c)}z^{(t+1)}, \tag{3.7}$$

where $p^{(t)}$ presents the evolution path for the generation t and $p^{(0)} = 0$, c is a normalization factor within the range from 0 to 1. Mathematically, the evolution path for the next generation is the normalized vector summation of the evolution path of the current generation and the mutation vector of the next generation. If $c = 1$, there is no cumulation. After about $1/c$ generations, the original information contained in $p^{(t)}$ is reduced by a factor of $1/e = 0.37$. This means c^{-1} is the number of generations being summarized in the current evolution path. Finally, the strategy parameter $\sigma^{(t)}$ is updated according to Equation 3.8 [95].

$$\sigma^{(t+1)} = \sigma^{(t)} \cdot exp(\frac{1}{d} \cdot \frac{||p^{(t+1)}|| - E[||N(0,1)||]}{E[||N(0,1)||]}) \tag{3.8}$$

In conclusion, the CMA-ES is a robust optimization algorithm. In the CMA-ES, by generating a large number of offspring candidates in each generation, a broader search space can be explored during the optimization process. The weighted recombination, in which the best offspring candidate is rewarded with the largest weight, ensures that the optimization process continues to move towards the optimum direction. Additionally, the CMA-ES has the capability of escaping from local minima due to the self-adaptation transition of the step size based on derandomization and cumulation.

3.5 Arbitrary Spectral Synthesis: System Configuration

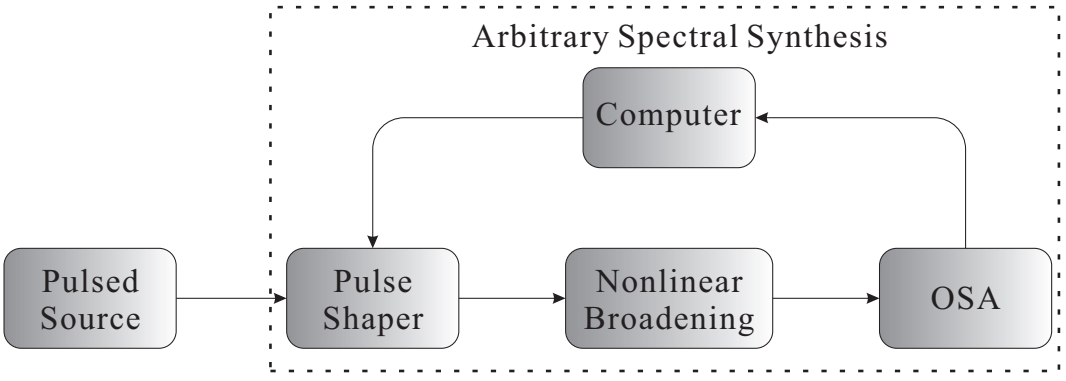

Figure 3.11: Configuration of arbitrary nonlinear spectrum generation based on pulse pre-shaping. OSA: Optical Spectrum Analyser.

The adaptive pulse shaping system shown in Figure 3.1 can be extended to include some other components between the pulse shaper and the pulse diagnostics. As reported in

[77], a single mode fibre (SMF) was included in the system and then the transfer function of the pulse shaper was optimized using the characteristics of the pulses at the output of the SMF as the feedback signal. In the simulation, the pulses at the output of the SMF maintained the characteristics of the original pulses, such as peak power and pulse width.

In this project, I designed an arbitrary spectral synthesis system for the nonlinear generation of broadband spectra with desired spectral shapes. The configuration of this system is shown in Figure 3.11. A nonlinear broadening stage (typically an amplifier and a highly nonlinear fibre) is employed in the system. Rather than measuring the characteristics of the pulse directly after the pulse shaper, the characteristics of the pulses after nonlinear propagation in the highly nonlinear fibre (HNLF) are used as the feedback signal to dynamically adjust the transfer function fed into the pulse shaper. As the focus point is on the spectrum of the generated signal, an OSA measurement is sufficient to be used as the pulse diagnostic adopted in the system. The difference between the measured spectrum U_{meas} and the target spectrum U_{target} is quantified by the misfit function MF defined in Equation 3.9.

$$MF^2 = \int (U_{meas} - U_{target})^2 d\omega \Big/ \int U_{meas}^2 d\omega \tag{3.9}$$

Depending on the requirements of the experiment with regard to the quality of the generated spectrum, the optimization algorithm in the system can be either the two-membered ES or the CMA-ES. The calculation time of the optimisation process depends on the sweeping time of the OSA, the computational speed of the computer and the transition time between different transfer functions of the pulse shaper. Among them, the sweeping time of the OSA depends readily on the bandwidth of the target spectrum. The target spectrum for the arbitrary spectral synthesis is required to be physically reasonable. Otherwise, the adaptive pulse shaping system is not able to reach a solution.

3.6 Conclusion and Discussion

This chapter has described the general principles of adaptive pulse shaping, including the necessary building blocks and some of its distinct features. A brief overview of the evolutionary algorithm which facilitates the adaptive pulse shaping system, was given in Section 3.3. The use of such algorithms has been crucial for the nonlinear spectrum generation described in Chapters 4 and 5, as well as for the modelling work of EFRLs in Chapter 6. Then, the ES algorithms that I have used in my work were thoroughly described. Two variations of the ES, the two-membered ES and the CMA-ES, were considered and have been described in detail. I have finally introduced the arbitrary spectral synthesis system which I have developed in my project work, and the detailed

implementation and applications of which are described in the following chapter. In the following chapter, I demonstrate the nonlinear generation of ultra-flat broadband spectra. The reason why an arbitrary spectral synthesis system with adaptive pulse shaping is necessary in the experiment is revealed first. Then the implementation and the effect on quality of the generated spectrum is illustrated.

Chapter 4

Generation of Flat-Top Spectrum

4.1 Introduction

As the techniques for generating and detecting signals become ever more complex in modern communication systems the need to develop more sophisticated methods for harnessing both linear and nonlinear effects in optical fibres emerges. Kerr effects in optical fibres have been widely used in the literature for a variety of applications, including the spectral broadening of pulsed laser signals using self-phase modulation (SPM), often in combination with other nonlinear effects. The generated broadband spectra can be useful in a variety of applications in optical communications. For example, they can be sliced to generate several wavelength division multiplexing (WDM) channels from a single laser source [97]. More recently, they have also been used to generate subcarriers for optical orthogonal frequency division multiplexing (OFDM) systems [98]. All of these applications ideally require the generation of spectra with accurately controlled shapes and bandwidths.

Recent developments in optical fibre technology have allowed significant advances in the tailoring of nonlinearly generated broadband spectra. Specially designed microstructured fibres offering suitable dispersion and nonlinear characteristics have been extensively used to generate smooth broadband spectra. In a recent example, an SPM-induced $800nm$ wide spectrum with $\sim 5dB$ ripples was generated in a photonic crystal fibre offering appropriately engineered nonlinear and dispersive properties [41]. On the other hand, rather than relying on the special characteristics of the highly nonlinear fibre (HNLF), one could directly shape the broadened spectrum by applying filtering after the nonlinear propagation [42]. However, this technique is rather power inefficient, since it can only remove portions of power through filtering, from a signal which has previously been amplified in order to give rise to nonlinear effects in the HNLF. Moreover, the bandwidth is also limited by the capabilities of the shaper itself. A more power efficient technique would be to shape the spectrum prior to the nonlinear element (and amplifier) and to rely on the nonlinear generation itself to directly generate the desired

spectrum. This technique also potentially allows at the same time for the generation and manipulation of light over a spectral range that greatly exceeds the operating bandwidth of the pulse shaper itself. This concept was previously used for the generation of a $15nm$ flat spectrum with power fluctuations of $\sim 1.5dB$ starting from a laser source emitting $1.8ps$ soliton pulses (with a corresponding $3dB$ spectral bandwidth of $2.5nm$) at a repetition rate of $10GHz$ [18].

There are two approaches to the implementation of this technique. The first one is referred to as inverse propagation approach, and is based on the calculation of the exact pulse shape which, after nonlinear propagation, yields the desired output spectrum. For a nonlinear element with given characteristics, this can be achieved using backward propagation calculations based on the inverse split-step Fourier method (ISSFM). Once the desired input pulse shape to the nonlinear medium is known, then a filter which allows precise shaping (in both amplitude and phase) of the incident pulse (generated directly from the seed pulse source) is required. This approach had previously been employed in [18]. Alternatively, the arbitrary spectral synthesis presented in Section 3.5 can be applied and is consequently referred to as an adaptive approach. The transfer function of the pulse shaper is dynamically adjusted by using the difference between the generated spectrum and the target spectrum as the feedback signal.

In the following section, a proof-of-principle experiment to nonlinearly generate a $\sim 12nm$ wide ultra-flat spectrum is presented. Both the inverse propagation approach and the adaptive approach have been used in the experiments. The description begins with the inverse propagation approach, in which the numerical simulation used to calculate the required waveform and subsequently the transfer function fed into the pulse shaper are described in the first instance. Through the associated experiment, it is shown that substantial discrepancies were obtained between the generated and the target spectrum, thus highlighting the limitations of this approach. In order to overcome the adverse impact of these limitations, the adaptive approach is used next so as to improve the quality of the generated spectrum. It is demonstrated that the quality of the generated spectrum is significantly improved when the adaptive approach is in place. Encouraged by the good outcome from the proof-of-principle experiment, an ultra-flat frequency comb covering the full C-band is generated relying completely on the capability of the optimization algorithm without any initial estimation of the transfer function. In order to further examine the quality of the generated frequency comb, the noise characteristics are measured and compared to those of the mode-locked laser used as the seed source. Finally, the experimental results are summarized and further discussed.

4.2 Proof-of-Principle Experiment: Nonlinear Generation of a 12nm Wide Flat-top Spectrum

In this section, the nonlinear generation of a $\sim 12nm$ wide ultra-flat spectrum based on pulse shaping applied prior to the nonlinear broadening is demonstrated as the proof-of-principle experiment of my technique. The target spectrum is firstly generated through the inverse propagation approach. A numerical simulation procedure is established to seek for the appropriate transfer function of the pulse shaper. The deviation of the generated spectrum from the target spectrum reveals the limitations of the inverse propagation approach. Then, the adaptive approach is employed to improve the quality of the generated spectrum.

4.2.1 Inverse Propagation Approach

4.2.1.1 Numerical Simulations

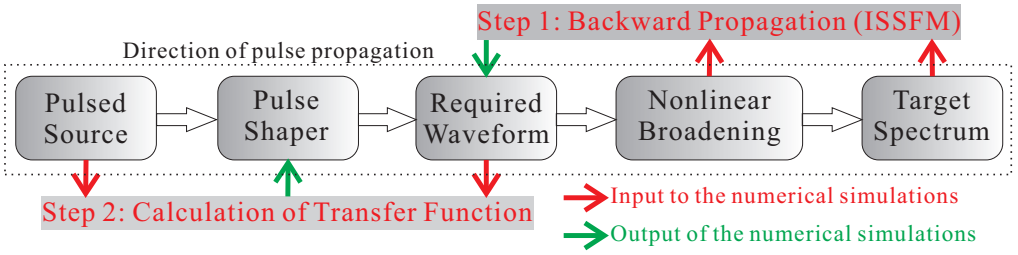

Figure 4.1: Schematic of the nonlinear generation of desired spectrum and the associated numerical simulation procedure.

Figure 4.1 shows the schematic of the methodology followed for the nonlinear generation of an ultra-flat broadened spectrum using inverse propagation approach. The pulsed laser source, normally a mode-locked laser (MLL), was firstly passed through a pulse shaper. The pulse shaper was to shape the pulses into a waveform which would evolve into the desired spectrum after propagating into a nonlinear medium, eg. an HNLF.
A simulation procedure was devised in order to calculate a transfer function suitable for this purpose. As shown in Figure 4.1, this simulation procedure followed two steps: in the first step, the characteristics of the target spectrum were defined. The ISSFM was then employed to calculate the waveform required at the input of the HNLF with its parameters. In the second step, prior knowledge of the pulse characteristics generated by the MLL enabled the calculation of the transfer function which needed to be fed into the programmable filter.
The target spectrum was chosen to have a third-order super-Gaussian shape. In order to avoid demanding the generation of ultrashort pulses from the MLL, I allowed the output

pulses to be linearly chirped. Then for sufficiently large chirp values, the waveform corresponding to this target spectrum was

$$u_{target}(t) = exp\{-0.5 \times [(t/T_0)^6 + iC(t/T_0)^2]\} \tag{4.1}$$

where T_0 and C represented the half-width (at 1/e-intensity point) and the chirp parameter of the pulse, respectively. The pulsed laser source used in the following discussion was a $9.9532GHz$ MLL generating almost transform-limited Gaussian pulses centred at $1550nm$ with a full width at half maximum (FWHM) of $2ps$ and a $3dB$ bandwidth of $\sim 2.5nm$. Figure 4.2 shows the measured temporal and spectral profiles of these pulses and compares them with the numerical profiles I assumed when designing the transfer function. For all the calculations, the signal average power at the output of the system was assumed to be $0.5W$, a power level readily provided by several telecommunication erbium doped fibre amplifiers (EDFA).

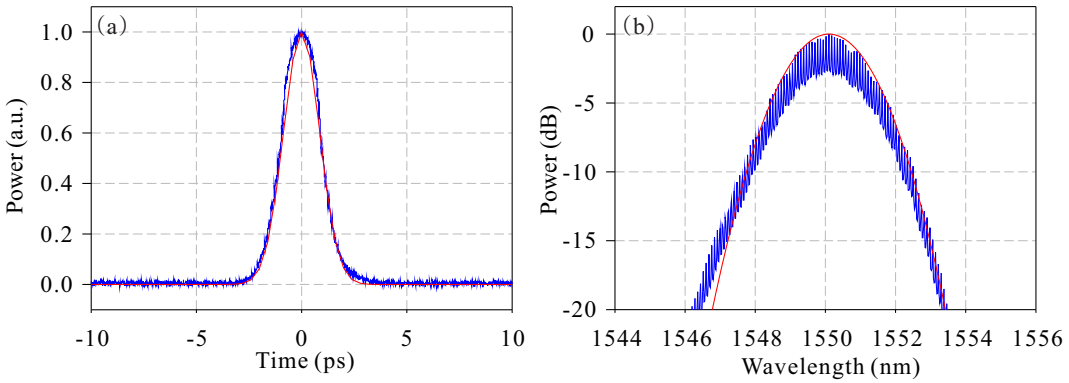

Figure 4.2: Measured (blue) and simulated characteristics (red) of the MLL pulses. (a) Temporal profile (measured with an optical sampling oscilloscope), and (b) spectral trace (resolution bandwidth = 0.02nm).

Length	$1km$
Dispersion Parameter @$1550nm$	$-1.7ps/nm \cdot km$
Dispersion Slope @$1550nm$	$0.0023ps/nm^2 \cdot km$
Nonlinear Coefficient	$18/W/km$
Loss	$2.13dB/km$

Table 4.1: HNLF Parameters

The exact bandwidth and shape of the target spectrum then clearly depended on the combination of T_0 and C. Consequently, in the simulation, I defined a group of target spectra by varying the value of T_0 from $8.5ps$ to $26.5ps$ and the value of C from 10 to 100. The value ranges of T_0 and C ensured that the target spectrum had the shape of a third-order Gaussian function. Taking the HNLF parameters shown in Table 4.1 into account (which correspond to a fibre which was available in our lab), the required waveforms at the input of the HNLF could be calculated from the ISSFM for each target

spectrum with a unique combination of T_0 and C.
It can be expected that only a subset of the waveforms obtained from the ISSFM calculations could be implemented with our available pulse source. Since the spectral pulse shaping is a passive linear process in which new frequency components cannot be generated, the root mean square bandwidth of the shaped waveform $\Delta\lambda^{rms}_{shaped}$ needed to be narrower than that of the original MLL pulse $\Delta\lambda^{rms}_{MLL}$, i.e.,

$$R^{shaped}_{\lambda}(T_0, C) = \Delta\lambda^{rms}_{shaped}/\Delta\lambda^{rms}_{MLL} < 1 \tag{4.2}$$

where $R^{shaped}_{\lambda}(T_0, C)$ represents the ratio between $\Delta\lambda^{rms}_{shaped}$ and $\Delta\lambda^{rms}_{MLL}$.
Additionally, after pulse shaping, the adjacent pulses should not overlap with each other in the time domain. As the MLL pulses had a duty cycle of 0.02, the temporal root mean square width of the shaped waveform $\Delta\tau^{rms}_{shaped}$ could not be larger than 50 times the root mean square width of the original MLL pulses $\Delta\tau^{rms}_{MLL}$. In order to completely avoid any interference at the wings between the adjacent pulses after shaping, $\Delta\tau^{rms}_{shaped}$ was further restricted to be less than 10 times shorter than $\Delta\tau^{rms}_{MLL}$, i.e.,

$$R^{shaped}_{\tau}(T_0, C) = \Delta\tau^{rms}_{shaped}/\Delta\tau^{rms}_{MLL} < 10 \tag{4.3}$$

where $R^{shaped}_{\tau}(T_0, C)$ represents the ratio between $\Delta\tau^{rms}_{shaped}$ and $\Delta\tau^{rms}_{MLL}$.

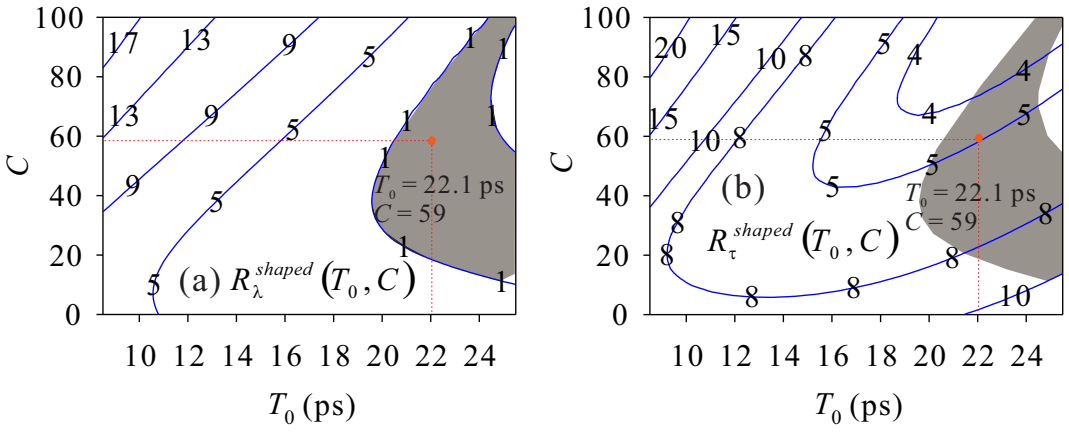

Figure 4.3: Simulation results for pulses with an average power of $0.5W$. (a) Contour plot of the ratio of spectral widths between shaped and MLL pulses. (b) Contour plot of the ratio of temporal widths between shaped and MLL pulses. The shadowed areas on the plots represent the space where feasible solutions are located. The solution examined experimentally is marked on the plots.

Since they are functions of the shaped waveform, the two ratios defined in Equation 4.2 and Equation 4.3 are also functions of T_0 and C, and they can be plotted on contour plots against these two parameters (Figure 4.3). On each contour plot, there is an area satisfying each corresponding inequality. The intersection between these two areas, as shown in the shadowed area of Figure 4.3, is where the feasible waveforms are located.

From all the feasible waveforms, we chose the one with minimum $R_{\lambda}^{shaped}(T_0, C)$ value for the experimental demonstrations presented in the following sections. A comparison between this waveform and the assumed original MLL pulses is shown in Figure 4.4. It is worth to note that this waveform is not transform-limited, and its frequency chirp is represented by the green dashed line in Figure 4.4a. After the nonlinear propagation in the HNLF, this waveform evolves into a third-order super-Gaussian spectrum with a $3dB$ bandwidth of $11nm$ and a linearly chirp third-order super-Gaussian pulse with $T_0 = 22.1ps$ and $C = 59$.

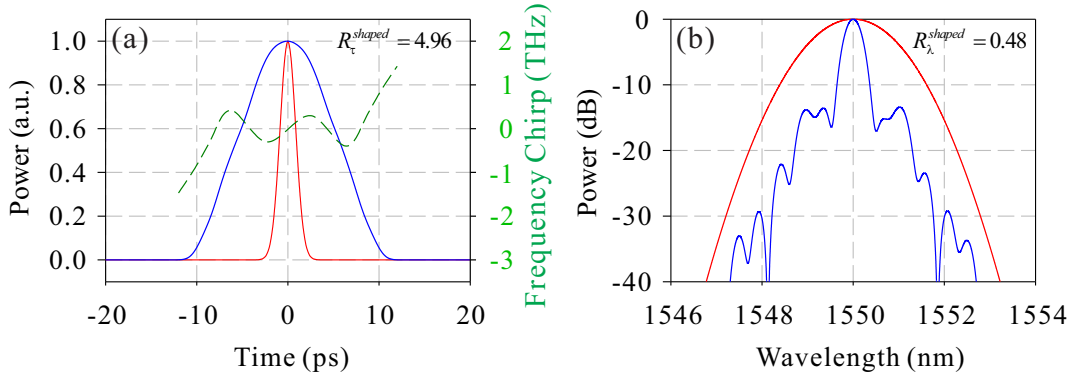

Figure 4.4: Comparison between the selected feasible waveform and MLL pulses. The red solid lines represent the MLL pulses, while the blue solid lines represent the selected feasible waveform. (a) Comparison of pulse shapes. The green dashed line represents the frequency chirp of the selected waveform. (b) Comparison of optical spectra.

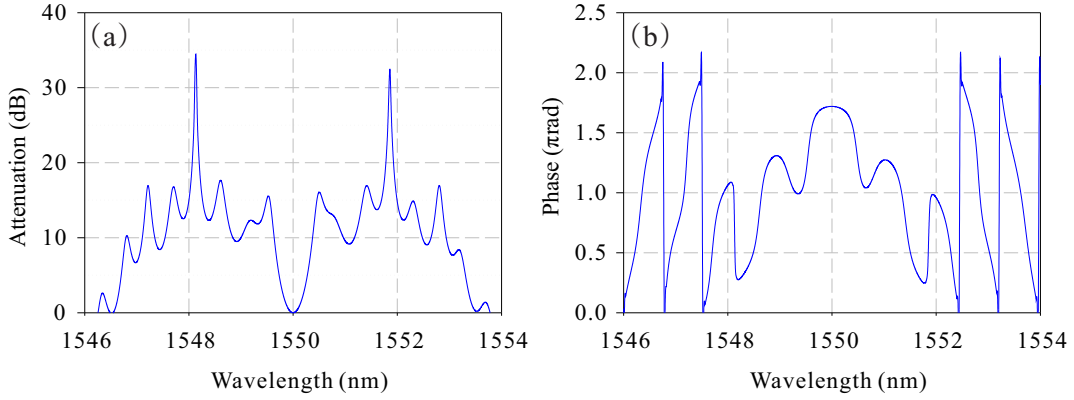

Figure 4.5: Calculated transfer function for the solution for $T_0 = 22.1ps$ and $C = 59$. (a) Attenuation profile. (b) Phase Profile.

The transfer function that needed to be programmed to the shaping filter in order to implement this waveform is shown in Figure 4.5. This was calculated by dividing the spectrum of the shaped waveform by the original MLL spectrum, and includes both the response in the amplitude and the phase.

4.2.1.2 Experimental Results

The accuracy of the transfer function obtained from the previously described numerical simulation procedure was firstly tested through the simple experimental configuration of Figure 4.6. The erbium glass oscillator (ERGO) emitted a Gaussian pulse train with a repetition rate of $\sim 9.9532 GHz$ and a FWHM of $2ps$ centred around $1550nm$. The pulses were then passed through an LCOS programmable phase and amplitude filter (Finisar Waveshaper - W/S), which was configured with the transfer function obtained from the numerical simulation procedure. At the output, the temporal waveform and spectrum of the shaped pulses were measured using an optical sampling oscilloscope (OSO) and an optical spectrum analyser (OSA), respectively. The EDFA was used at the input of the OSO to provide sufficient power for the measurement.

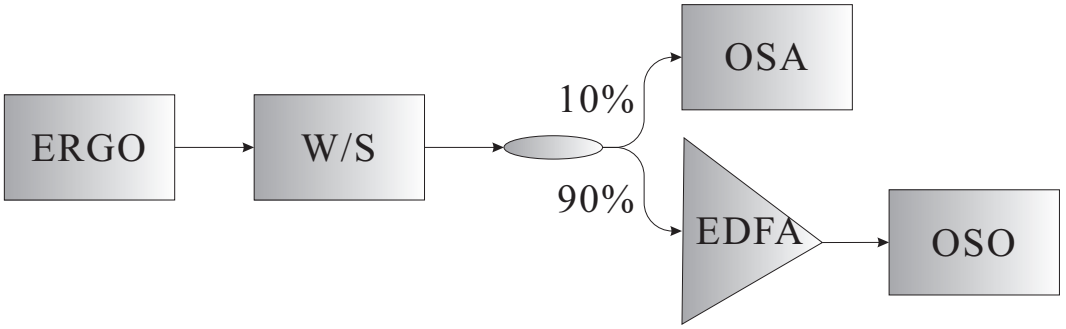

Figure 4.6: Experimental Setup for testing the transfer function obtained from numerical simulations. ERGO: Erbium Glass Oscillator. W/S: Finisar Waveshaper. EDFA: Erbium Doped Fibre Amplifier. OSA: Optical Spectrum Analyser. OSO: Optical Sampling Oscilloscope.

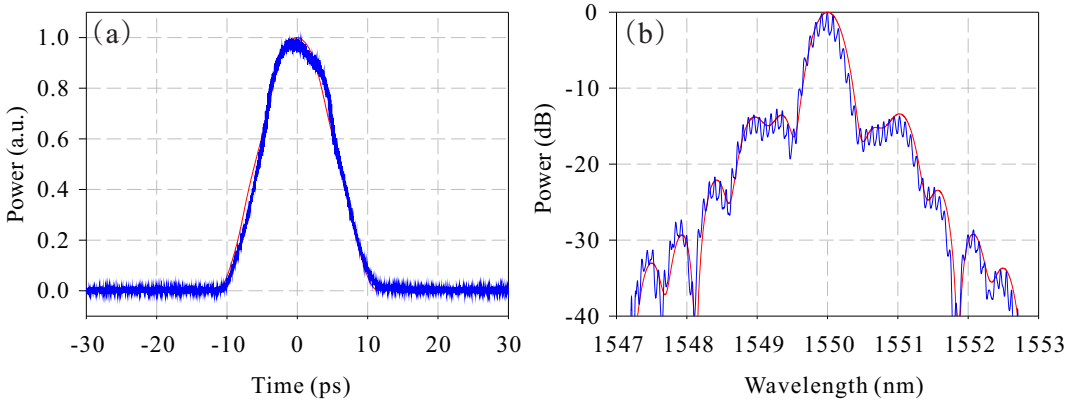

Figure 4.7: Temporal profile (a) and spectrum (b) of the shaped pulses. The red traces represent the target signals from the ISSFM calculations and the blue traces represent the profile (temporal resolution: $1ps$) and spectrum (resolution bandwidth: $0.2nm$) of the experimentally generated signals.

These measurements showed that the shaped pulses had a FWHM of $\sim 13ps$ and the

spectrum exhibited several pairs of sidelobes (Figure 4.7). In the frequency domain (Figure 4.7b), the spectrum of the shaped pulses was almost identical to the calculated spectrum. However, the spectrum phase information was missing in such a measurement. In the time domain (Figure 4.7a), small but noticeable discrepancies were observed on the temporal waveform. I assume that these deviations were originated from the inaccurate phase control in the W/S. It was then reasonable to consider to adjust the phase profile in the W/S. However, a spectral phase measurement was not straightforward. Instead, to evaluate the influence of such a small discrepancy on the nonlinearly generated broadband spectrum, the nonlinear propagation of the shaped pulses in an HNLF was monitored.

Figure 4.8 shows the experimental setup for the nonlinear propagation of the shaped pulses. This is simply an extension of the experimental setup shown in Figure 4.6. Rather than being characterized, the shaped pulses at the output of the W/S were amplified to $0.8W$ and launched into the HNLF with the parameters listed in Table 4.1. The output of the HNLF was monitored on an OSA.

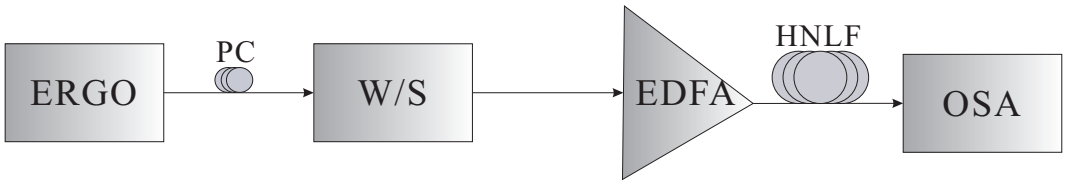

Figure 4.8: Experimental setup for the nonlinear propagation of the shaped pulse in an HNLF. PC: Polarization Controller.

In order to benchmark the flatness of the nonlinear spectrum generated from the shaped pulses, we first experimented with (unshaped) Gaussian pulses of the same power and temporal width as the pulses shown in Figure 4.7a. In this case, the spectrum at the output of the HNLF exhibited the familiar multitude of spectral peaks, typical of SPM in a normal dispersion fibre (Figure 4.9a). The spectrum obtained when the shaped pulses were used is presented in Figure 4.9b. The number of peaks on the generated spectrum was reduced. However, there was a substantial discrepancy between the generated and the target spectrum manifesting itself a spectral lobe developing at the centre of the spectrum. This observation indicated that even small discrepancies on the temporal waveform of the shaped pulses did have significant influence on the nonlinearly generated broadband spectrum.

Furthermore, the likely reasons for the observed discrepancy between the generated and target spectrum are following: (a) the actual characteristics of both the MLL pulse (in both phase and intensity) and the HNLF may not have been exactly the same as the parameters used in the numerical simulation procedure. (b) The amplifier was assumed to be strictly linear in the simulations, but it could introduce a small amount of nonlinear phase shift in practice. (c) The phase and amplitude characteristics of the W/S were not accurately calibrated.

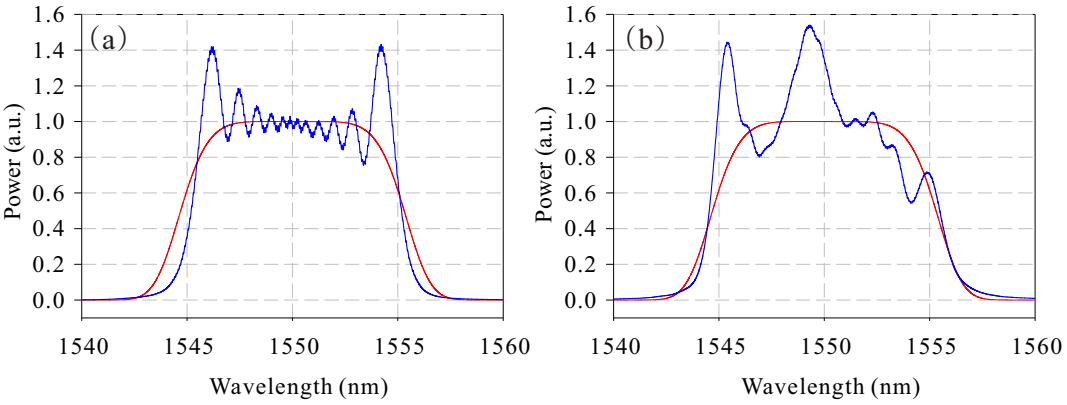

Figure 4.9: SPM spectra generated from (a) 13*ps* Gaussian pulse, (b) the waveform shown in Figure 4.7. Red traces: target spectra, blue traces: generated spectra. Resolution bandwidth: 0.5*nm*.

The limitations listed above made optimisation of the experimental procedure an extremely complex problem. It was hard to manually adjust the phase profile in the W/S so as to improve the quality of the generated spectrum. I therefore studied the application of the arbitrary spectral synthesis described in Section 3.5 as a potential solution to these issues.

4.2.2 Adaptive Approach

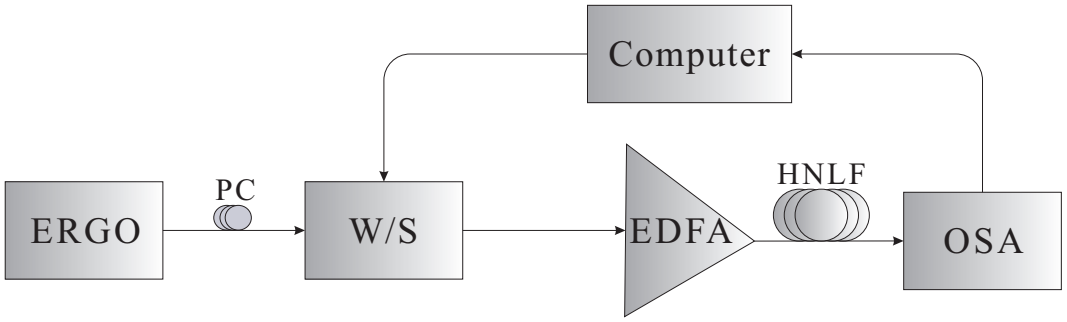

Figure 4.10: Experimental setup for the experiment including adaptive pulse shaping system.

In order to overcome the limitations revealed in the inverse propagation approach and obtain a more precisely shaped spectrum, the adaptive pulse shaping system described in Section 3.5, that controls the transfer function via a feedback mechanism with a view of optimizing the shape of the final spectrum, is employed in the experiments described in this section. The performance of the adaptive pulse shaping system is investigated when either the two-membered or the CMA-ES is adopted as the optimization algorithm in the system.

Figure 4.10 shows the experimental setup for the implementation of the adaptive pulse shaping system. It builds on the setup used in the inverse propagation approach (Figure 4.8), now including also a feedback loop. The output of the HNLF was monitored by an OSA and used as a feedback signal to the optimization algorithm which dynamically updated the filtering characteristics of the W/S. In order to achieve the pulse determined by the simulation, the transfer function obtained in the inverse propagation approach was applied into the W/S as the starting point of the optimization algorithm. The operating bandwidth of the W/S was only $8nm$.
The adaptive pulse shaping approach aimed at minimizing the difference between the generated spectrum U_{meas} and the target spectrum U_{target} by dynamically adjusting the transfer function fed into the programmable pulse shaper W/S. The misfit function MF defined in Equation 3.9 was used to quantify this difference. Since the goal here was to improve the flatness at the top of the generated spectrum (U_{meas}), evaluation of the MF function was restricted to include contributions from only wavelengths lying within the 5% bandwidth of U_{target}. In the experiment, only the phase profile of the transfer function was being optimized, since the power spectrum of the shaped signal could be accurately monitored using an OSA. The adjustment of the phase profile fed into the programmable pulse shaper was accomplished by adding a smaller perturbation represented by a weighted summation of first kind Chebyshev polynomials up to order N. The value of N represents a trade-off between the accuracy of the optimization process and its efficiency. The use of Chebyshev polynomials has the advantage that when the weights are the same for all the terms, their contribution to the entire summation is comparable. Consequently, instead of the phase profile itself, the $(N + 1)$ weights of Chebyshev polynomials became the objective of the optimization process.

4.2.2.1 Experimental Results: Two-Membered ES

The simple two-membered ES was used as the first attempt to improve the flatness at the top of the generated spectrum. A weighted summation of Chebyshev polynomials up to 20^{th} order represented the phase perturbation in the algorithm. Consequently, the two-membered ES was required to optimize 21 weights of the summation. According to the principle of the two-membered ES, these 21 weights were normally distributed with zero mean and a variance of σ, which was set to an initial value of 0.06 and updated during the optimization process.
Figure 4.11a shows the generated spectrum when the adaptive system using two-membered ES was in place. The flatness of the generated spectrum was dramatically improved relative to the result of Figure 4.9b. A spectrum exhibiting a $3dB$ bandwidth of $11nm$ with a central region of $7nm$ where the fluctuation was less than $0.5dB$ was nonlinearly generated. The MF value of this spectrum was 0.078 (for comparison the spectrum obtained when using the inverse propagation approach alone exhibited a MF value of

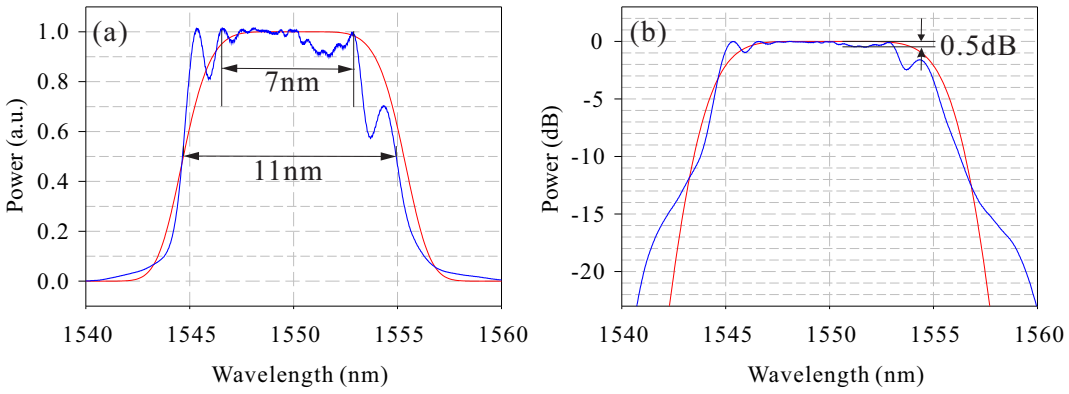

Figure 4.11: SPM spectra generated after application of the adaptive system using two-membered ES in linear (a) and logarithmic (b) scale, respectively. Red traces: target spectra, blue traces: measured spectra. Resolution bandwidth: $0.5nm$.

0.312). In order to appreciate the quality of the generated spectrum, the same trace is also presented in Figure 4.11b on a logarithmic scale.

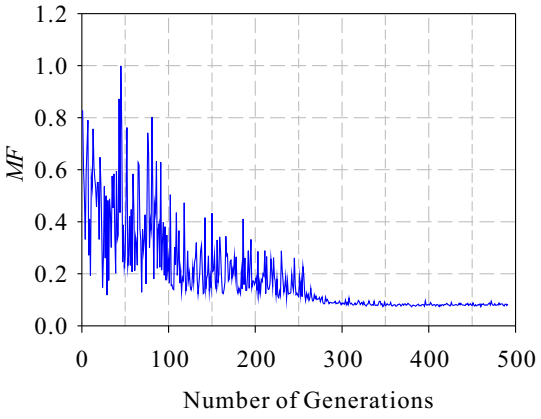

Figure 4.12: Evolution of MF value in the two-membered ES.

Finally, the value of the MF function versus the number of algorithm iterations is plotted in Figure 4.12. A ten-fold improvement in the achieved MF value was observed within 300 iterations. In the experiment, the algorithm took about $20mins$ to converge to this value.

The phase transfer function of the W/S that gave rise to this spectrum is shown in the blue trace in Figure 4.13 and compared to the numerically calculated one (red trace). Even though the differences between the two traces are only subtle, the improvement in the flatness of the resultant spectrum has been significant. This implies that the spectral phase shaping was very important for our application.

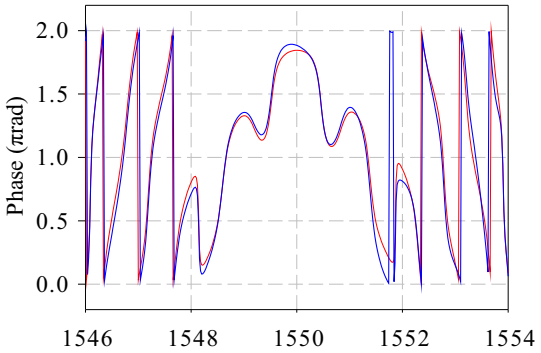

Figure 4.13: Comparison between the phase profiles fed into the W/S before and after optimization. Red trace: before optimization; blue trace: after optimization.

4.2.2.2 Experimental Results: CMA-ES

As mentioned in Section 3.4.2, the search space in the two-membered ES is limited; it is therefore likely that the search can be trapped at a local minimum. In order to explore a broader search space and search for a better result with a higher probability to correspond to the global minimum, the CMA-ES was tested.
In the experiment, only the phase profile was optimised. The phase perturbation was still represented by a weighted summation of Chebyshev polynomials up to 20^{th} order. According to principle of the CMA-ES, in each generation, 13 offspring candidates were generated and the best 6 out of them were eligible to form the parent candidate for the next generation through the weighted average process. As in the previous case, the variance σ of the normally distributed weights was also set to an initial value of 0.06.
The best spectrum achieved when the CMA-ES was employed is shown in both linear (Figure 4.14a) and logarithmic scale (Figure 4.14b). The flatness of the generated spectrum was further improved relative to the case of the two-membered ES algorithm, and a $3dB$ bandwidth of 12 nm with a central region of $8nm$ where the ripples were less than $0.5dB$ was achieved. The MF value of this spectrum was 0.041.
Figure 4.14c is a high resolution (resolution bandwidth = $0.01nm$) measurement result of this spectrum. The dense spectral lines accommodated in the spectrum can be observed. The uniform extinction ratio of the spectral lines across the entire spectrum (limited by the resolution bandwidth of the OSA) is an indication of the good coherence properties of the generated spectrum.
It is clear from Figure 4.15, that a more significant adjustment had been made to the numerically calculated initial phase profile, implying that the solution found by CMA-ES had a longer distance in the search space from the origin compared to the two-membered ES. The exploration of a broader search area provides the CMA-ES the ability to escape from being trapped in a possible local minimum during the optimization process.

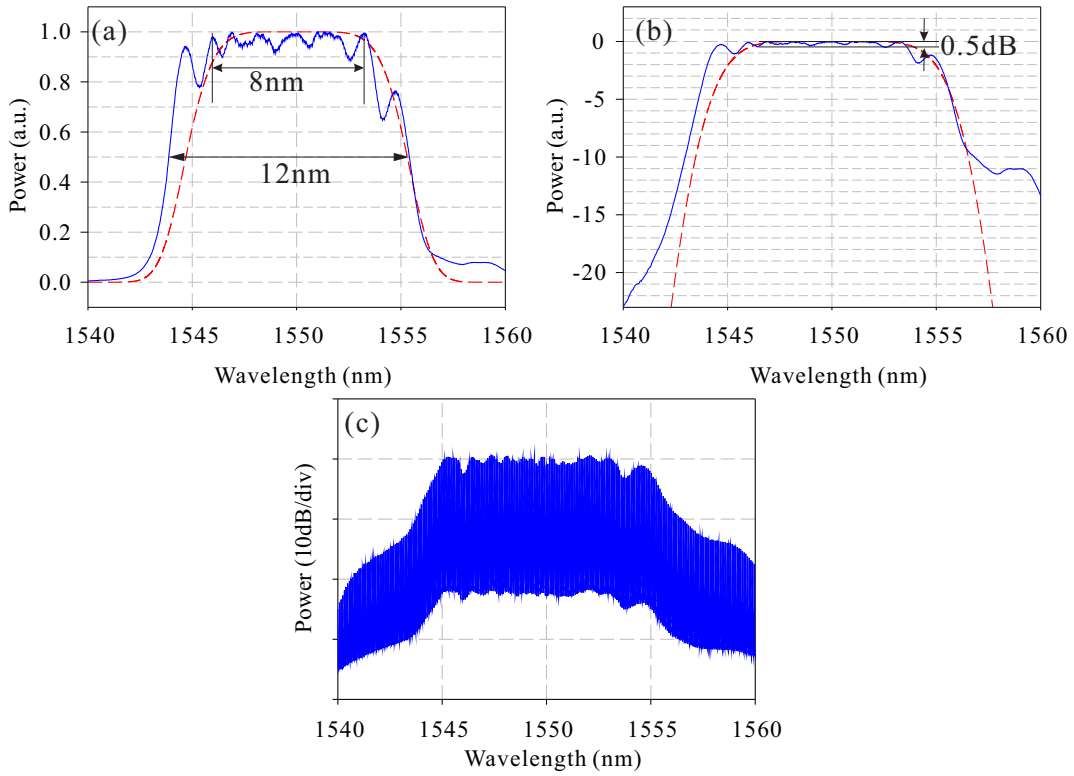

Figure 4.14: SPM spectra generated after application of the adaptive system using CMA-ES in linear (a) and logarithmic (b) scale, respectively. Red traces: target spectra, blue traces: measured spectra. Resolution bandwidth: $0.5nm$. (c) High resolution (resolution bandwidth: $0.01nm$) measurement results of the optimized spectrum with $MF = 0.041$.

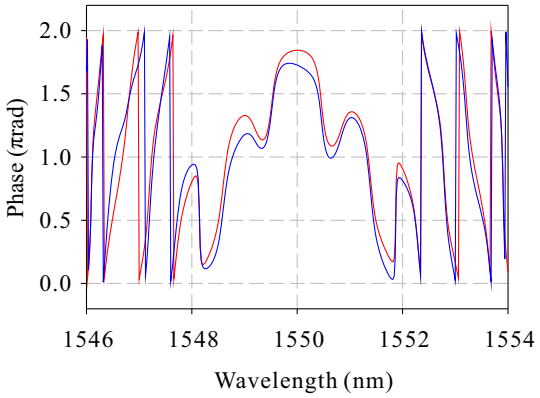

Figure 4.15: Comparison between the phase profiles fed into the W/S before and after optimization. Red trace: before optimization; blue trace: after optimization.

Figure 4.16 records the minimum MF value in each generation. A five-fold improvement in the MF value was observed within 130 generations. As there were 13 offspring candidates evaluated in each generation, the CMA-ES algorithm evaluated 1690 candidates in total. This large amount of candidates and the substantially increased complexity

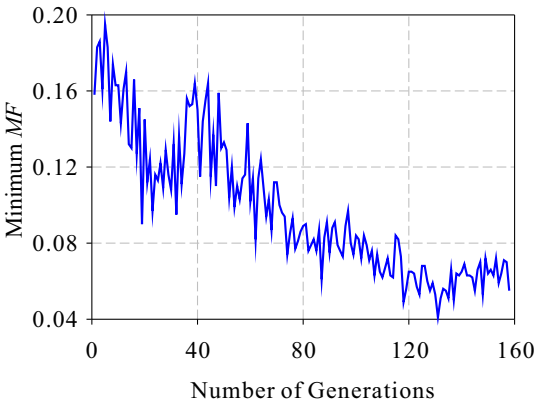

Figure 4.16: Evolution of Minimum MF value for each generation in CMA-ES.

made the algorithm more robust, but also less efficient. In the experiment, CMA-ES took about $2hours$ to reach this solution. The better result was obtained at the cost of sacrificing the efficiency of the optimization process.
In conclusion, in these proof-of-principle experiments, the nonlinear generation of a $\sim 12nm$ wide ultra-flat spectrum based on pulse shaping had been attempted in two different ways. By applying the transfer function obtained from the numerical simulations directly into the W/S, a substantial spectral lobe developed at the centre of the spectrum. An adaptive pulse shaping system significantly improved the flatness of the generated spectrum through dynamically adjusting the phase profile of the transfer function applied into the W/S. With either the two-membered ES or the CMA-ES as the optimization algorithm in the system, the fluctuations on the top of the generated spectrum was reduced to $\sim 0.5dB$. These results have demonstrated the ability of the adaptive pulse shaping system to improve the quality of the nonlinearly generated spectrum. By increasing the power at the input of the HNLF, an interesting next step would be to blindly optimize the transfer function (both in amplitude and phase) applied into the W/S and to investigate the nonlinear generation of spectra spanning several tens of nanometers.

4.3 Generation of an Ultra-flat Frequency Comb Covering the Full-C Band

In this section, building on the results from the proof-of-principle experiments, the target is to nonlinearly generate an ultra-flat frequency comb covering the full C-band, starting from the $2ps$ Gaussian pulses with a $3dB$ bandwidth of $2.5nm$. Subsequently, the noise characteristics of the generated frequency comb are measured and compared with those of the input $2ps$ Gaussian pulses.

4.3.1 Generation Process

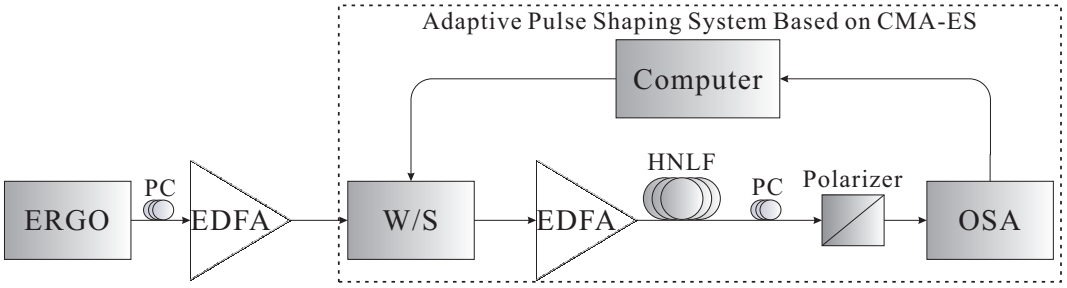

Figure 4.17: Experimental setup for the nonlinear generation of the ultra-flat broadband frequency comb.

Length	$500m$
Dispersion Parameter @1550nm	$-0.87ps/nm \cdot km$
Dispersion Slope @1550nm	$-0.0006ps/nm^2 \cdot km$
Nonlinear Coefficient	$19/W/km$
Loss	$2dB/km$

Table 4.2: Parameters of the HNLF used for the generation of ultra-flat broadband frequency comb

Figure 4.17 shows the experimental setup of the nonlinear generation of the ultra-flat broadband frequency comb. It followed a similar configuration to the experimental setup for the proof-of-principle experiment shown in Figure 4.10. The seed pulse was again the ERGO MLL emitting $2ps$ Gaussian pulses at $1550nm$ with a repetition rate of 9.9532 GHz. A pre-amplification stage was included in the system to pre-compensate for the loss of the W/S and consequently suppress the noise induced by the second EDFA. In order to achieve the generation of a broadband spectrum that can cover the full C-band, the shaped pulses were amplified to a higher power than before ($32dBm$) and launched into a HNLF with parameters as shown in Table 4.2. A polariser was placed at the output of the system to ensure that the generated frequency comb had a single polarization, as required in most applications. The output signal was eventually monitored by an OSA, and this measurement was also used to provide the feedback signal for the computer-controled adaptive pulse shaping system.

Unlike the proof-of-principle experiment, in this case, there was no attempt to calculate the optimum transfer function prior to the application of the adaptive process. Instead, the control over the quality of the generated frequency comb was completely dependent on the capability of the optimization algorithm adopted in the adaptive pulse shaping system. The CMA-ES, which is the most sophisticated of the algorithms that I have studied, was employed to control both the phase and the amplitude of the transfer function of the W/S and minimize the difference between the generated U_{meas} and the target spectrum U_{target}. The misfit function shown in Equation 3.9 was again used to quantify this difference. Since the target of this experiment was to generate an ultra-flat frequency comb covering the full C-band, the target spectrum U_{target} was simply a line

of uniform spectral density across a $40nm$ bandwidth centred at $1550nm$.
The W/S was initially programmed to be a dispersionless bandpass filter with a bandwidth of $8nm$. In the optimization process, the shaping functions of both amplitude and phase were represented, each by a weighted summation of first kind Chebyshev polynomials of 10^{th} order. Consequently, the CMA-ES optimized a vector of weights that included 22 elements. Following the principle of the CMA-ES, in the mutation process, 13 vectors of weights were generated by adding a random (Gaussian distributed) vector to the starting vector of weights. The variance of the Gaussian distributed vector was set to 0.06 initially and self-adapted during the optimization process. Subsequently, each of the corresponding 13 transfer functions was fed into the W/S and their MF values were calculated according to Equation 3.9 once the corresponding spectra were generated. The vectors of weights were ranked according to their MF values. Then, the 6 best out of the 13 vectors of weights were selected into the weighted recombination process, in which larger weights were assigned to the better vectors. The resulting vector of weights became the starting vector of weights for the next generation. The algorithm was terminated manually when an acceptable agreement between the generated U_{meas} and the target spectrum U_{target} was reached, typically when $MF < 0.2$.

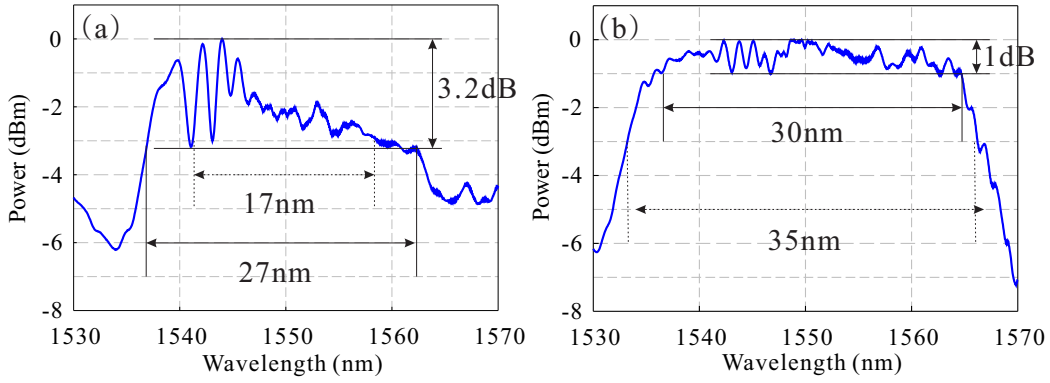

Figure 4.18: SPM spectra generated from (a) $2ps$ Gaussian pulses directly and (b) after the application of the adaptive system using the CMA-ES (resolution bandwidth: $0.2nm$).

In order to demonstrate the effectiveness of the technique, the experimentally generated spectrum at the output of the HNLF when no shaping was applied is first presented in Figure 4.18a. The spectrum exhibited a multitude of spectral peaks with large fluctuations of $3.2dB$ over a bandwidth of $27nm$. Meanwhile, the $3dB$ bandwidth was only $17nm$. We next consider the system when CMA-ES-based adaptive shaping was applied. The spectrum obtained after the CMA-ES algorithm was terminated is presented in Figure 4.18b; the trace shows a significant improvement in the spectral flatness. A $3dB$ bandwidth of $35nm$ was achieved, and the power variations over a central region of $30nm$ were less than $1dB$.
A high resolution measurement of the generated frequency comb is shown in Figure 4.19. The generated comb had the same line spacing as the source pulse; thus, there were 375

spectral lines accommodated in the $30nm$ flat region. As shown in Figure 4.19a and Figure 4.19b, the OSNR of the spectral lines within the generated frequency comb was around $20dB$ and was uniform over the entire comb. This value was actually limited by the resolution bandwidth of the OSA.

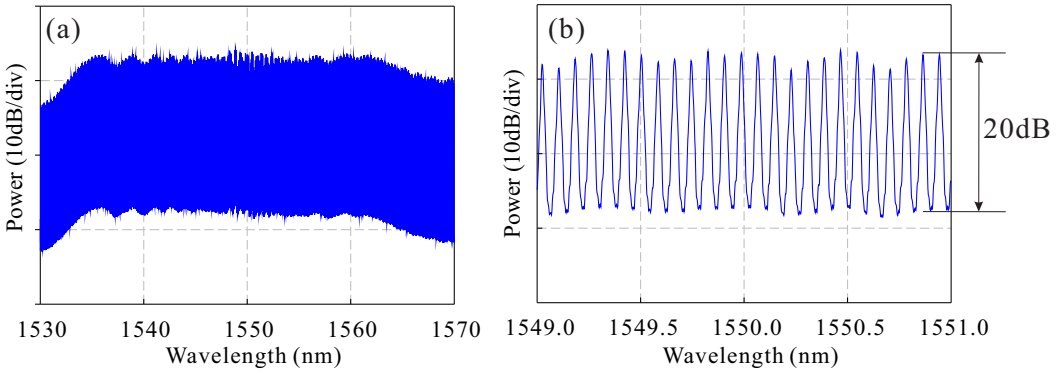

Figure 4.19: High resolution (resolution bandwidth: $0.01nm$) measurement over (a) $40nm$ and (b) $2nm$ of the generated frequency comb.

Both of the amplitude (red trace) and phase profile (blue trace) of the transfer function that gave rise to the ultra-flat frequency comb covering the full C-band are shown in Figure 4.20a. It is clear that the amplitude shaping was relatively weak, while the phase shaping was more significant. This indicates that the phase shaping played an important role in the generation process of the ultra-flat frequency comb.

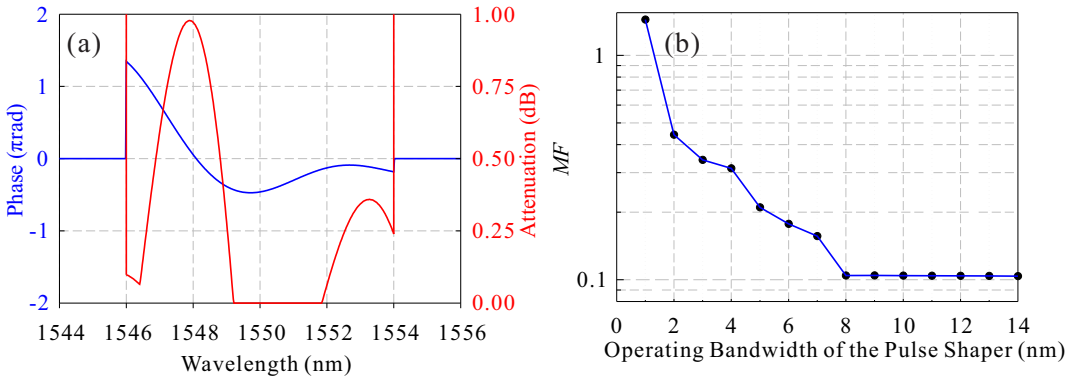

Figure 4.20: (a) The transfer function fed into the W/S after optimization. Red Trace: Amplitude Profile; Blue Trace: Phase Profile. (b) Numerical simulation result for the dependence of the MF value on the operating bandwidth of the pulse shaper.

It is worth noting that the operating bandwidth of the W/S was $8nm$ in our experiment: only a small fraction of the bandwidth of the generated frequency comb. This is an important feature of our technique, and to study it further, I simulated the experiment by setting the pulse shaper bandwidth to gradually narrower values (the signal was considered to be truncated outside the bandwidth of the pulse shaper). For each

bandwidth of the pulse shaper, the MF of the best spectrum achieved in the simulation was recorded. The graph of Figure 4.20b, which shows the MF as a function of the pulse shaper bandwidth, indicates uniform performance down to a value of $\sim 8nm$. Even narrower shaper bandwidths than this would result in a compromise in the quality of the generated spectrum. The sharp change happened at $\sim 8nm$ can be explained by the fact that the frequency components lying outside the bandwidth of $8nm$ of the MLL pulses were too weak to have any influence in the shaping process (Figure 4.4b).

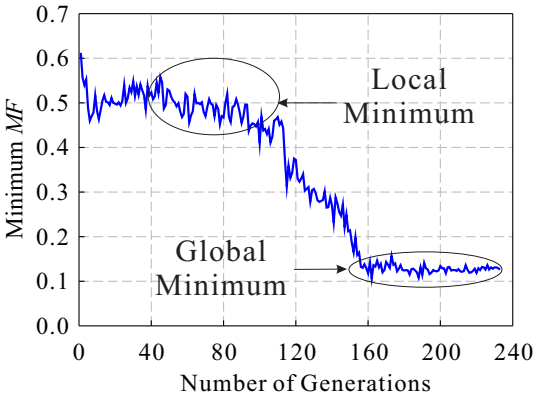

Figure 4.21: Evolution of the minimum MF value in each generation of the CMA-ES.

The evolution of the minimum MF value shown in Figure 4.21 is a typical example of the capability of the CMA-ES to escape from local minima due to the self-adaptation transition of the step size described in Section 3.4.3. The optimisation process escaped from a local minimum of around 0.5 to eventually converge to a global minimum of around 0.12 (see markings on the plot). The optimisation process took about 3hours to converge to the global minimum. The calculation time was longer than the time consumed in the experiment described in Section 4.2.2.2. This is due to the longer sweeping time of the OSA as broader spectra were being generated.

4.3.2 Noise Characteristics of the Generated Ultra-Flat Frequency Comb

The noise characteristics of a signal is always an important factor for its telecommunication applications. One of the possible applications of the generated ultra-flat frequency comb is to be used as the source of sub-carriers in an optical telecommunication system, which is designed for high bit rate modulation. It is important to ascertain the impact of both the pulse shaping and the nonlinear broadening on the noise characteristics of the pulse train. In order to measure the noise characteristics, a high resolution spectral measurement which can fully resolve each of the frequency components of a signal is required. For a signal with a GHz repetition rate, the previously described time-averaged

OSNR spectral measurement is not sufficient to meet this requirement due to the limited resolution bandwidth.

For a broadband source, the study of the dynamic, inter-modal noise is of particular interest. One of the methods to study this kind of noise is to carry out the relative intensity noise (RIN) measurement for each longitudinal mode of the spectrum [99, 100]. However, in the case of the ultra-flat frequency comb described here, it was practically not possible to isolate the individual $10GHz$ frequency lines of the generated comb because of their close spacing. Instead, both the source MLL and the generated ultra-flat frequency comb were treated as periodic pulse trains and their noise properties were characterized based on the measurements and analysis of their power spectra, as described in [101].

The output pulses of any practical MLL exhibit random changes in their profile rather than being exact periodic replicas of each other. These random changes are understood as the noise of the pulse source. The power spectrum, which is the Fourier transform of the autocorrelation function of the laser intensity, is used to determine the characteristics of the noise. In stochastic processes, the amount of random fluctuations is often characterized by the root-mean-square (rms) deviation of the noise quantity, which is given by the area of the noise spectrum. The power spectrum of a periodic pulse train can be obtained using a combination of a suitably fast photodiode (PD) and an electrical spectrum analyser (ESA). In an actual experiment only a truncated power spectrum is measured because of the bandwidth limitations imposed by the PD and/or the ESA.

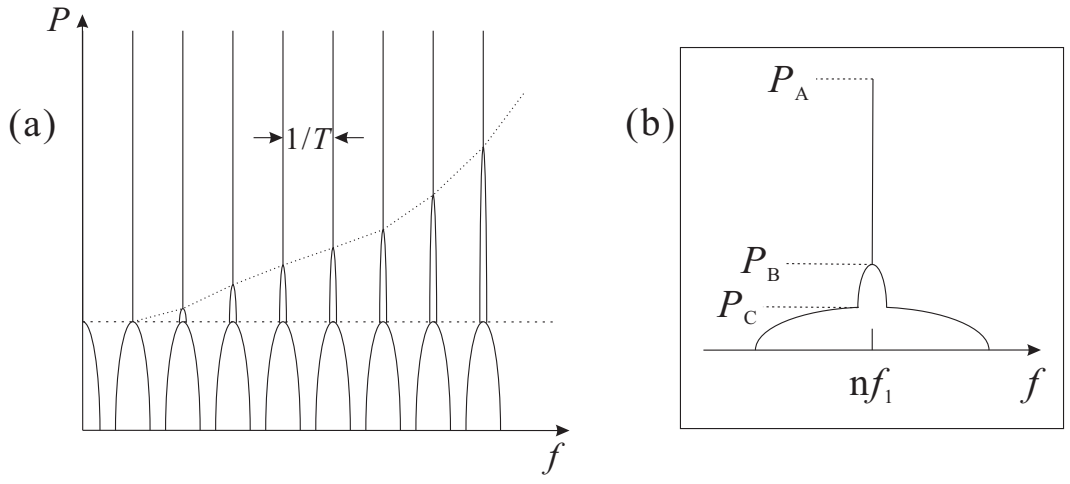

Figure 4.22: (a) Power spectrum of a pulse train obtained from the ESA measurement. The dotted line indicates the maxima of the noise bands representing amplitude noise. The dashed line marks the maxima of the narrow noise bands representing the temporal jitter. (b) Schematic illustration of the structural details for an arbitrary n^{th} order frequency component. P_A represents the power of the spike, P_B represents the power of the narrowband noise, P_C represents the power of the broadband noise band at the bottom, respectively.

For the measurement, the pulse shape was assumed to be constant, while the pulse energy and repetition time exhibited random changes. This means that there were two kinds of noise considered here. One was the fluctuation in pulse energy (amplitude noise), while the other one was the temporal jitter. Figure 4.22a sketches the power spectrum of a periodic pulse train from the ESA measurement. It is clear that there are three different contributions on each discrete line of the spectrum. The δ-function corresponds to the perfect, noise-free pulse train. The bottom broad band manifests the fluctuation of the pulse energy and it remains unchanged on each frequency component. In the middle of the spectrum, the narrow band represents the temporal jitter, the power of which is proportional to the square of the order n of the frequency component. The n^2 dependence of the temporal jitter is important as it allows for the distinction between the two kinds of noise. The fluctuation of the pulse energy can be obtained through the first order frequency component as the contribution of temporal jitter is negligible. On the other hand, the temporal jitter needs to be characterized using the high frequency components on which it plays a dominant role.

Figure 4.22b schematically illustrates the details of the structure for an arbitrary n^{th} frequency component [101]. P_A, P_B and P_C represent the powers of the δ-function, the narrowband temporal jitter and the broadband noise representing the fluctuation in the pulse energy, respectively. In order to have a quantitative characterization of the noise, it is required to obtain the following quantities through both low- and high- resolution ESA measurements: (a) the ratios of P_B/P_A and P_C/P_A, and (b) the frequency widths (FWHM) Δf of the noise bands. For each kind of noise, the time constant t_c is $1/2\pi\Delta f$. The rms value of the fluctuation of the pulse energy is calculated through the following expression

$$\Delta E/E = [(P_C/P_A)_L \Delta f_A/\Delta f_{res}]^{1/2}. \tag{4.4}$$

where $(P_C/P_A)_L$ represents the power ratio of the frequency component with lower order. The value of $(P_C/P_A)_L$ is obtained from the low resolution measurement and then transformed into its corresponding value in the high resolution measurement by multiplying the resolution bandwidth ratio. Δf_A represents the FWHM of the noise band from the low resolution measurement, while Δf_{res} represents the high resolution. The switch between the high resolution and low resolution measurement is due to the fact that the high resolution is chosen as the common reference bandwidth for a direct comparison.

From the low resolution and high resolution measurement, the fast and slow temporal jitter can be achieved, respectively. The expressions for the calculations of the rms values are shown in Equation 4.5 and Equation 4.6:

$$\Delta t'/T = (2\pi n)^{-1}[(P_C/P_A)_n \Delta f'_J/\Delta f_{res}]^{1/2}, \tag{4.5}$$

$$\Delta t/T = (2\pi n)^{-1}[(P_B/P_A)_n \Delta f_J/\Delta f_{res}]^{1/2}, \tag{4.6}$$

where $(P_C/P_A)_n$ and $(P_B/P_A)_n$ represent the power ratios of the frequency component with n^{th} order. The value of $(P_C/P_A)_n$ follows the same way in the calculation of the fluctuation of the pulse energy, while the value of $(P_B/P_A)_n$ is directly obtained from the high resolution measurement. $\Delta f'_J$ and Δf_J represent the FWHM of the fast temporal jitter and slow temporal jitter obtained from low resolution and high resolution measurements, respectively.

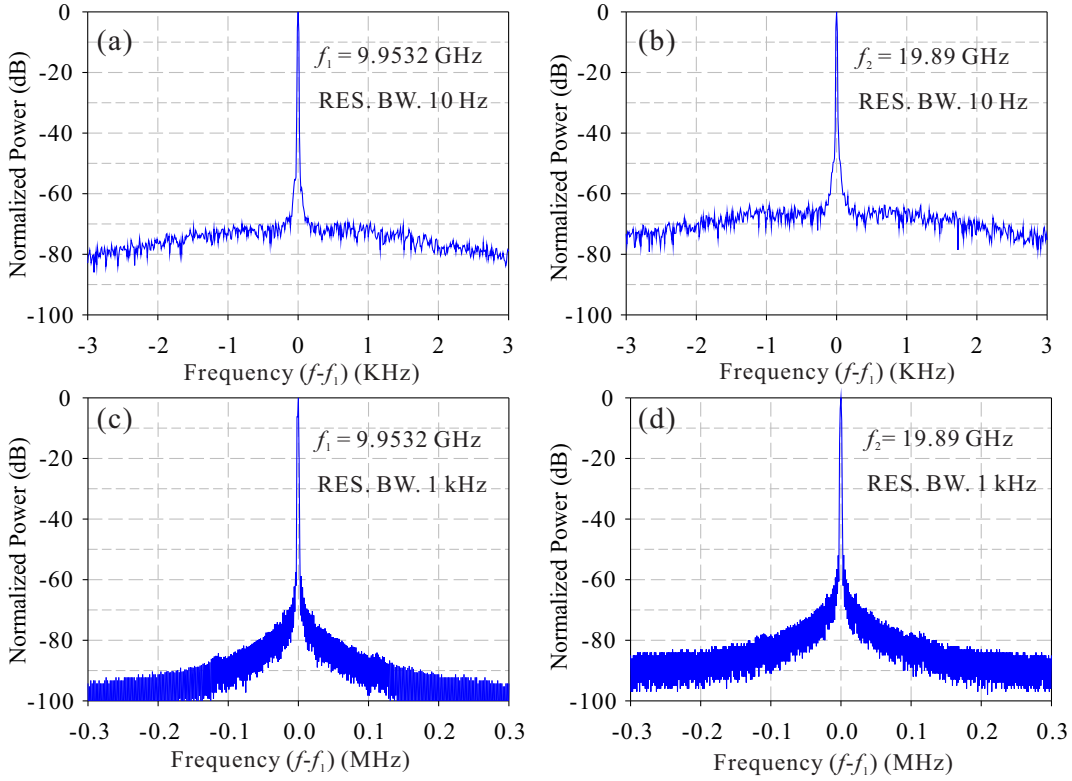

Figure 4.23: Power spectra of the first two harmonics of the ERGO laser measured with a resolution bandwidth of $10Hz$ at (a) $\sim$9.9532GHz, (b) $\sim$19.89GHz. Power spectra of the first two harmonics of the ERGO laser measured with a resolution bandwidth of $1kHz$ at (c) $\sim$9.9532GHz, (d) $\sim$19.89GHz.

In the measurement, a $10GHz$ PD was used to detect signals in the noise characterization. The ESA used in the experiment has a bandwidth of $\sim 40GHz$. Since the ERGO laser, which was the seed source MLL in the generation process of the ultra-flat frequency comb, has a repetition rate of $\sim$9.9532GHz, only the first two lines of the laser can be explicitly measured. Thus, the first two harmonics of both the signals centred $\sim$9.9532GHz and $\sim$19.89GHz were measured to calculate the parameters of the noise. The resolution bandwidths for the measurements were $10Hz$ and $1kHz$, respectively. The measurement results for the ERGO laser are shown in Figure 4.23. For the fluctuation of the pulse energy, $(P_C/P_A)_1 = 4.479 \times 10^{-8}$, $\Delta f_A = 785kHz$. For the fast temporal jitter, $(P_C/P_A)_2 = 1.758 \times 10^{-7}$, $\Delta f'_J = 82.3kHz$. For the slow temporal jitter, $(P_C/P_B)_2 = 1.349 \times 10^{-7}$, $\Delta f'_J = 670kHz$. The noise characteristics of the ERGO laser

are summarized in Table 4.3.

	rms Value	Time Constant
Pulse Energy	0.059%	$2.03\mu s$
Fast Jitter	$9.58fs$	$1.93\mu s$
Slow Energy	$69fs$	$0.143ms$

Table 4.3: The noise characteristics of the ERGO laser

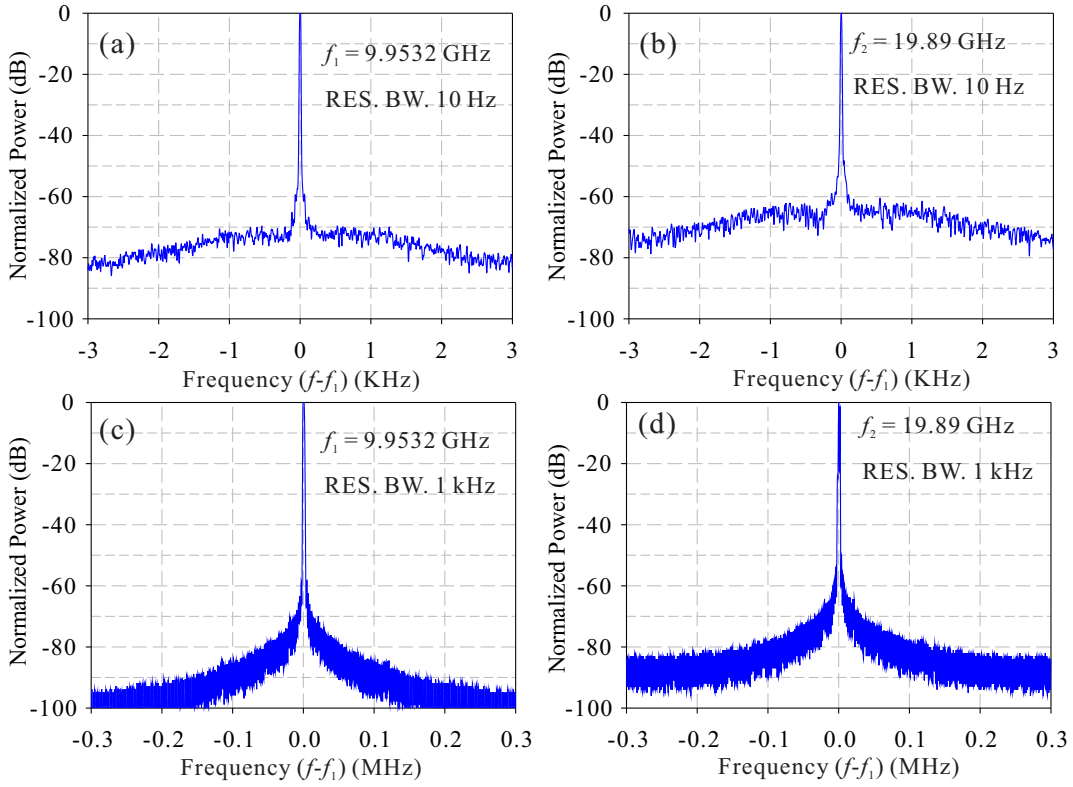

Figure 4.24: Power spectra of the first two harmonics of the generated ultra-flat frequency comb measured with a resolution bandwidth of $10Hz$ at (a) $\sim 9.9532GHz$, (b) $\sim 19.89GHz$. Power spectra of the first two harmonics of the generated ultra-flat frequency comb measured with a resolution bandwidth of $1kHz$ at (c) $\sim 9.9532GHz$, (d) $\sim 19.89GHz$.

	rms Value	Time Constant
Pulse Energy	0.059%	$3.42\mu s$
Fast Jitter	$10.8fs$	$1.97\mu s$
Slow Energy	$72fs$	$0.136ms$

Table 4.4: The noise characteristics of the generated ultra-flat frequency comb

Then the noise characteristics of the generated ultra-flat frequency comb were measured. The measurement results are shown in Figure 4.24. For the fluctuation of the pulse energy, $(P_C/P_A)_1 = 4.615 \times 10^{-8}$, $\Delta f_A = 776kHz$. For the fast temporal jitter, $(P_C/P_A)_2 = 2.275 \times 10^{-7}$, $\Delta f'_J = 80.9kHz$. For the slow temporal jitter, $(P_C/P_B)_2 = 1.24 \times 10^{-7}$, $\Delta f'_J = 703kHz$. The noise characteristics of the generated ultra-flat frequency comb are summarized in Table 4.4.
From the results summarized in Table 4.3 and Table 4.4, it is observed that the generated frequency comb had almost identical noise characteristics as the source ERGO laser. This indicates that the manipulation of the amplitude and phase of the MLL pulses by the W/S and their subsequent nonlinear spectral broadening in the normal-dispersion HNLF did not result in noticeable deterioration of the noise characteristics of the signal. Since the ERGO itself is a low-noise MLL designed for telecommunication applications, the broadened frequency comb could also be used in various telecommunication applications, such as, the source for an WDM Nyquist system. This application will be described in brief in the following section.

4.3.3 Application of the Generated Ultra-Flat Frequency Comb

In this section, I describe the experiments that used the generated ultra-flat frequency comb as the channel source in a WDM Nyquist system. The experiment is reported in [27] and was carried out jointly with researchers of the Karlsruhe Institute of Technology (KIT). This experiment demonstrated $32Tbits/s$ $16QAM$ Nyquist WDM transmission over a total length of $22km$ of SMF28 without optical dispersion compensation.
In a Nyquist WDM system, in order to achieve a high bit rate, a large number of optical carriers are required. It is also crucial to precisely control the spacing and equalize the power of neighbouring optical carriers. Consequently, an ultra-flat optical comb source, such as the previously described comb source, is highly demanded to be one of the key components for building up such a system. I used the experimental setup shown in Figure 4.17, using a $12.5GHz$ MLL this time (which was available at KIT) as the seed source, with a maximum available power of $2W$ at the input of the HNLF and generated a frequency comb exhibiting a $3dB$ bandwidth of $\sim 31nm$ and a $2dB$ bandwidth of $\sim 29nm$ (Figure 4.25). The transmission system of KIT required that the comb source should be linearly polarised. This requirement was served by the inclusion of the polariser shown in Figure 4.17. In fact, it was during the course of these joint experiments that a polariser was used in the comb generation system. Since the HNLF used in the experiment was not polarization maintaining (PM), the polarised frequency comb at the output was prone to environmentally-induced random changes of birefringence. As a result, it was seen that the generated frequency comb was fluctuating in the long term spectral measurement. Subsequently, it was not used in the experiment at the end.

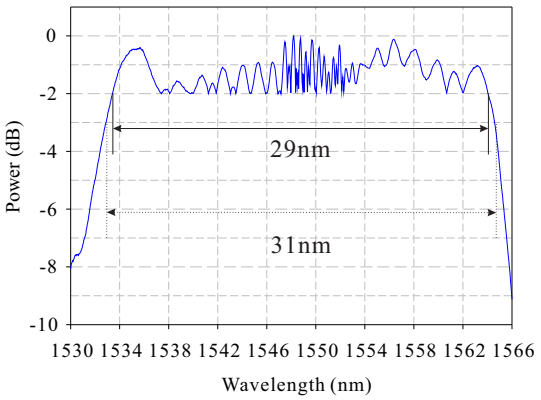

Figure 4.25: Frequency comb generated in the joint experiment in KIT.

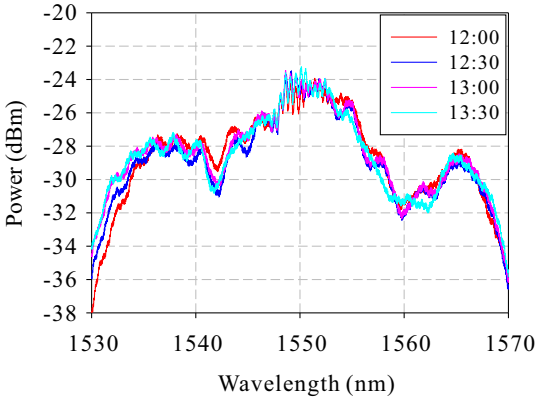

Figure 4.26: Stability measurement of the nonlinearly broadened spectrum when the HNLF was protected in an enclosure.

Following the joint experiments, I investigated the stability issue of the broadened ultra-flat frequency comb. It transpired that even simple isolation of the HNLF from the environment, by placing it inside an enclosure, was adequate to largely resolve the issue. After the protection, I performed spectral measurements over a period of 90 minutes to assess the stability of the system, and found the power variation of any of the frequency lines across the entire comb to be less than 1dB during this time (see Figure 4.26). I anticipate even better overall stability to be achieved through the use of a fully PM system.

4.4 Conclusion and Discussion

In this chapter, the generation of an ultra-flat broadband spectrum based on adaptive pulse shaping applied prior to nonlinear spectral broadening was demonstrated. With a power level of $\sim 0.8W$ at the input of the HNLF, the generated spectrum exhibited a $3dB$ bandwidth of $\sim 12nm$ and a $0.5dB$ bandwidth of $\sim 8nm$. By increasing the power level

to $\sim 2W$, the generated ultra-flat frequency comb covered the full C-band, exhibiting a $3dB$ bandwidth of $\sim 35nm$ and a $1dB$ bandwidth of $\sim 30nm$, and had a uniform OSNR of $\sim 20dB$ over its entire bandwidth. Similar noise performance was observed for both the generated frequency comb and the low-noise source MLL, indicating that the noise penalty induced by the linear pulse shaping and the nonlinear broadening on the signal is negligible.

My technique relies upon adaptively shaping the short pulses generated by a MLL into a waveform that forms the desired spectrum after nonlinear propagation in an HNLF. This approach has several advantages: Firstly, it is no longer tied directly to the characteristics of either the pulse source or the HNLF. These are only treated as parameters in the ISSFM-based simulation procedure for the calculation of the pulse shaping function. Besides, in the case of blind optimization for the generation of the ultra-flat frequency comb, they could even be neglected. Therefore in principle, without modifying the hardware of the system, I should be able to generate several different spectral shapes. Secondly, this approach is power-efficient since the shaping is carried out before amplification and nonlinear spectral broadening takes place, i.e. there is no power loss once the signal has been amplified prior to the nonlinear element. Meanwhile, the bandwidth of the nonlinearly generated spectrum depends on the power at the input of the HNLF, and not the capability of the pulse shaper, which is only required to be capable of shaping the (much narrower than the final spectrum) MLL pulses. This was demonstrated in the experiment that generated a frequency comb covering the full C-band where it was shown that it was possible to effectively control the optical spectrum over ranges that greatly exceed the operating bandwidth of the pulse shaper itself.

Another important feature of my technique is the use of adaptive pulse shaping based on ES. The difference between the generated and the target spectrum is used as a feedback parameter in order to dynamically update the transfer function fed into the pulse shaper until a satisfactory solution has been achieved. Both the two-membered ES and CMA-ES algorithms have been shown to improve the accuracy of the generated spectrum substantially. The simple strategy of the two-membered ES provides higher efficiency in terms of the number of iterations required, but also less reliability with respect to the likelihood of finding the best solution possible. On the other hand, the CMA-ES explores a much broader search space and has higher probability to reach the global minimum, albeit at the expense of a lower efficiency.

The generation of an ultra-flat broadband spectrum is only one of the applications of my technique. To explore this further, I then studied the manipulation of the edges (rather than the central portion) of the nonlinearly broadened spectrum. The nonlinear generation of spectra with a specially designed edge structure will be demonstrated in the following Chapter.

Chapter 5

Generation of Spectrum with Specially Designed Edges

5.1 Introduction

In Chapter 4, ultra-flat broadband spectra with different bandwidths have been successfully generated based on an approach, in which the adaptive pulse shaping is applied prior to the stage of nonlinear broadening. This approach is power-efficient and no longer tied directly to the characteristics of either the pulse source or the HNLF, as more conventional approaches are. The bandwidth of the spectrum generated through this approach can greatly exceed the operating bandwidth of the pulse shaper. By employing the ES as the optimization algorithm, the adaptive pulse shaping mechanism implemented in the approach has the ability to overcome the influence from the uncertainties in the system and consequently guarantee the high quality of the generated spectrum. Furthermore, the generation of an ultra-flat frequency comb covering the full-C band demonstrates that the adaptive pulse shaping mechanism exploiting the CMA-ES is robust enough to carry out blind optimization without any advanced numerical efforts to calculate the filtering characteristics required for the pulse shaper.

In this chapter, as a second application, my technique for the nonlinear generation of broadband spectrum will be adopted to control and manipulate the characteristics on the two edges of the spectrum. By using the CMA-ES based adaptive pulse shaping mechanism with blind optimization, the generation of target spectra, whose edges are symmetric and linear, will be investigated both numerically and experimentally. Consequently, the slope of the edges (rather than its top region) will be the parameters of the target spectrum looked into here. The aim of this study is to further explore the capability and flexibility of my technique.

5.2 Numerical Simulations

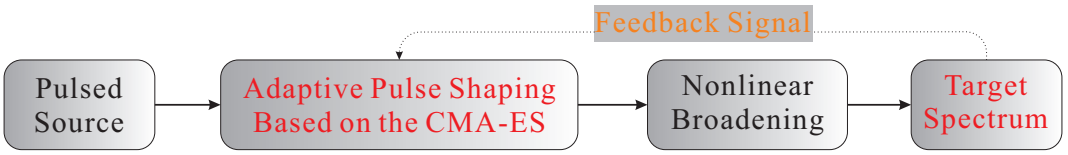

Figure 5.1: Schematic of the numerical simulation procedure of the nonlinear generation of broadband spectra with symmetric and linear edges.

In this section, I will first present a numerical simulation procedure which is designed to test the feasibility of the nonlinear generation of a broadened spectrum with symmetric and linear edges assisted by the CMA-ES based adaptive pulse shaping system. Figure 5.1 shows the schematic of the simulation. The pulsed laser source is adaptively shaped based on the feedback, which in this case is the shape of the spectral edges after nonlinear broadening.
In the simulation, the pulsed laser source was still the $9.9532GHz$ MLL emitting almost transform-limited Gaussian pulses centred at $1550nm$ with a FWHM of $2ps$ and a $3dB$ bandwidth of $\sim 2.5nm$, which was used in Chapter 4 already. In the adaptive pulse shaping mechanism, the CMA-ES was implemented in the same way as described in Section 4.3.1 to blindly optimize the transfer function in the pulse shaping process. In the nonlinear broadening stage, the amplifier was assumed to be strictly linear. In order to investigate the influence of the different HNLFs used in the system, two HNLFs, whose parameters are summarized in Table 4.1 and Table 4.2, were used for nonlinear broadening alternatively in the simulation. In the following discussion, the HNLF with parameters shown in Table 4.1 is referred to as HNLF01, while the one of Table 4.2 is referred to as HNLF02. The design of the target spectra with symmetric and linear edges will be thoroughly described in Section 5.2.1. In Section 5.2.2, for target spectra with different slopes of the edges, the simulation results in the two HNLFs including the comparison between the optimized spectrum and the target spectrum as well as the transfer function that gives rise to the optimized spectrum will be summarized.

5.2.1 Design of Target Spectrum

Although the characteristics on the edges of the generated spectrum are the objective parameters being optimized here, there is no harm to design the target spectrum to have a flat top. Together with the desired symmetric and linear edges, the target spectrum resembles the shape of an isosceles trapezium, as sketched in Figure 5.2.

In the sketch, the x- and y- axes represent the wavelength λ and the normalized power P, respectively. The bandwidth of the top flat region $\Delta\lambda_t$ ($\Delta\lambda_t = \lambda_{tl} - \lambda_{ts}$) and the

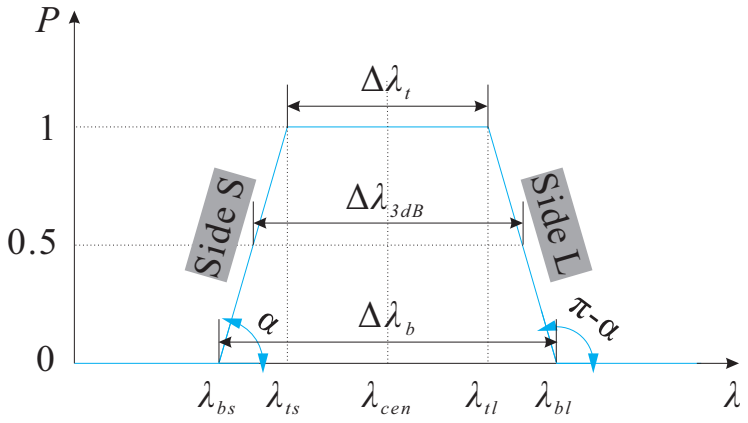

Figure 5.2: Sketch of an isosceles trapezium representing the target spectrum with symmetric and linear edges. λ_{cen} represents the central wavelength.

full bandwidth $\Delta\lambda_b$ ($\Delta\lambda_b = \lambda_{bl} - \lambda_{bs}$) of the target spectrum are the lengths of the two parallel sides of the isosceles trapezium. From the properties of the isosceles trapezium, it is obvious that the $3dB$ bandwidth $\Delta\lambda_{3dB}$ of the target spectrum is the average of $\Delta\lambda_t$ and $\Delta\lambda_b$, as shown in Equation 5.1.

$$\Delta\lambda_{3dB} = 0.5 \times (\Delta\lambda_t + \Delta\lambda_b) \tag{5.1}$$

The combination of Side S and Side L of the isosceles trapezium is the representation of the symmetric and linear edges of the target spectrum. According to the properties of the isosceles trapezium, the slopes of the two edges are the tangent of the supplementary bottom angles α and $\pi - \alpha$, and consequently opposite to each other. The geometric expressions for $tan\alpha$ and $tan(\pi - \alpha)$ are shown in Equations 5.2 and 5.3, respectively. Finally, as a function of wavelength λ, the target spectrum $P(\lambda)$ can be mathematically expressed as in Equation 5.4.

$$tan\alpha = 1/(\lambda_{ts} - \lambda_{bs}) = 2/(\Delta\lambda_b - \Delta\lambda_t) \tag{5.2}$$

$$tan(\pi - \alpha) = 1/(\lambda_{tl} - \lambda_{bl}) = -2/(\Delta\lambda_b - \Delta\lambda_t) \tag{5.3}$$

$$P(\lambda) = \begin{cases} 0 & \lambda < \lambda_{bs} \\ tan\alpha \cdot (\lambda - \lambda_{bs}) = 2(\lambda - \lambda_{bs})/(\Delta\lambda_b - \Delta\lambda_t) & \lambda_{bs} \leq \lambda \leq \lambda_{ts} \\ 1 & \lambda_{ts} < \lambda < \lambda_{tl} \\ tan(\pi - \alpha) \cdot (\lambda - \lambda_{bl}) = -2(\lambda - \lambda_{bl})/(\Delta\lambda_b - \Delta\lambda_t) & \lambda_{tl} \leq \lambda \leq \lambda_{bl} \\ 0 & \lambda > \lambda_{bl} \end{cases} \tag{5.4}$$

Following from this design, the bandwidth and the exact slopes of the edges of the target spectrum clearly depend on the values of $\Delta\lambda_b$ and $\Delta\lambda_t$. The energy of the signal is the integral of the spectrum with respect to the wavelength, i.e., the area covered by the envelope of the spectrum. Since the area of a trapezium is the product of the central

median and the height, the $3dB$ bandwidth of the target spectrum is directly proportional to the energy of the spectrum. Thus, according to Equations 5.1 - Equation 5.3, target spectra with different slopes but same energy can be defined by adjusting the values of $\Delta\lambda_b$ and $\Delta\lambda_t$ while keeping their sum constant.

5.2.2 Simulation Results

The aim of the simulation described here was to investigate the feasibility of the nonlinear generation of a target spectrum with symmetric and linear edges assisted by the CMA-ES based adaptive pulse shaping system. Using the same methodology as in Section 4.3.1, the pulse shaper was initially modelled as a dispersionless bandpass filter with a bandwidth of $8nm$. Both the attenuation and the phase profiles were expressed, each by a weighted summation of 10^{th} order first kind Chebyshev polynomials. The weights of these two polynomials were optimized simultaneously. Thus, a vector of weights with 22 elements was the objective being optimized by the CMA-ES.

	$\Delta\lambda_{3dB}$ (nm)	$\Delta\lambda_t$ (nm)	$\Delta\lambda_b$ (nm)	$tan\alpha$	$tan(\pi-\alpha)$
Target Spectrum 1	11	5	17	1/6	-1/6
Target Spectrum 2	11	8	14	1/3	-1/3

Table 5.1: Parameters of target spectra.

The parameters of the target spectra used in the simulation procedure are summarized in Table 5.1. According to the definitions of parameters in Section 5.2.1, the two target spectra have a common $3dB$ bandwidth of $11nm$. On Target Spectrum 1, the slopes of the two edges are $1/6$ and $-1/6$, respectively. While on Target Spectrum 2, they are $1/3$ and $-1/3$, respectively. In order to achieve the $3dB$ bandwidth of $11nm$, the output power of the amplification in the nonlinear broadening stage was set to be $17dBm$.
The quantity MF, defined in Equation 3.9, was once more used to quantify the agreement between the generated and the target spectrum. Since the goal here was to control and manipulate the characteristics on the edges of the generated spectrum, evaluation of the MF function was restricted to include contributions from only wavelengths lying within the range of $[\lambda_{bs}\ \lambda_{ts}]$ and $[\lambda_{tl}\ \lambda_{bl}]$. The top region of the generated spectrum was subsequently not taken into account.
The simulation results for the two target spectra when HNLF01 was used for the nonlinear broadening of the shaped pulses are shown in Figures 5.3 and 5.4. For Target Spectrum 1 with slopes of $1/6$ and $-1/6$ on the edges, the value of the MF of the optimized spectrum shown in Figure 5.3a was 0.086. From the transfer function shown in Figure 5.3b, nearly no amplitude shaping was required, and the phase shaping was relatively gentle. As the absolute value of the slopes on the edge doubled to $1/3$ for Target Spectrum 2, the performance deteriorated. The value of the MF of the optimized

spectrum shown in Figure 5.4a increased to 0.2423. The transfer function obtained in this case (Figure 5.4b) reveals that the shaper played a more active role in this case. All these observations indicate that the slopes of the edges on the target spectrum have vital influence on the performance of the blind optimization. Better performance of the adaptive pulse shaping system was observed when the target spectrum has a weaker steepness.

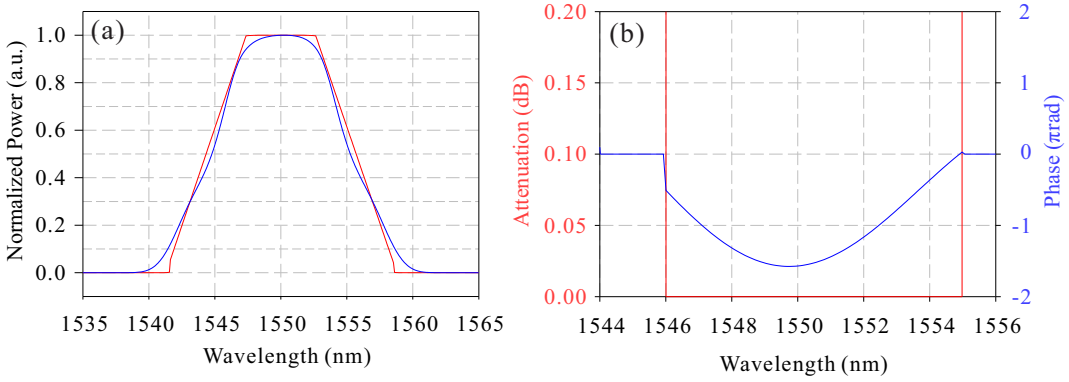

Figure 5.3: Simulation results for Target Spectrum 1 using HNLF01. (a) Comparison between the spectrum obtained after optimization and the target spectrum. Red Trace: Target spectrum. Blue Trace: Optimized spectrum. (b) The transfer function, giving rise to the optimized spectrum, obtained in the simulation. Red Trace: Attenuation Profile. Blue Trace: Phase Profile.

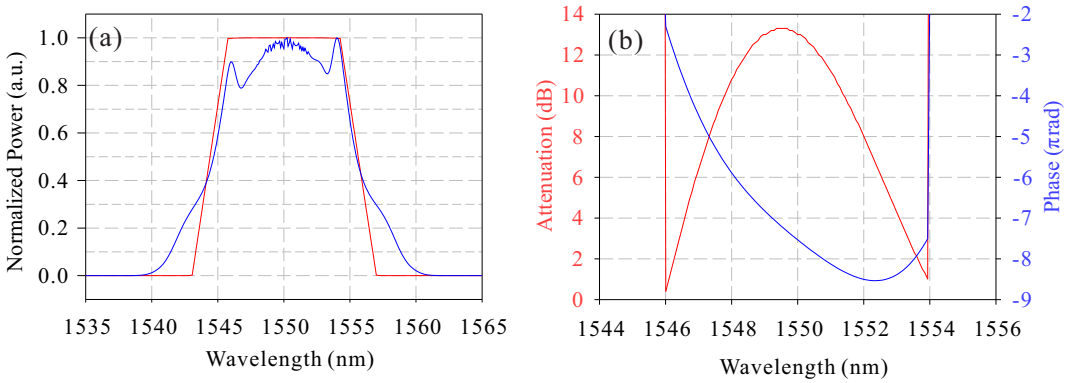

Figure 5.4: Simulation results for Target Spectrum 2 using HNLF01. (a) Comparison between the spectrum obtained after optimization and the target spectrum. Red Trace: Target spectrum. Blue Trace: Optimized spectrum. (b) The transfer function, giving rise to the optimized spectrum, obtained in the simulation. Red Trace: Attenuation Profile. Blue Trace: Phase Profile.

Similar simulations were carried out for the second fibre (HNLF02). The simulation results are shown in Figures 5.5 and 5.6. The values of MF of the optimized spectrum for the two target spectra plotted in Figures 5.5a and 5.6a were 0.0891 and 0.2492, respectively. By comparing the transfer functions shown in Figures 5.5b and 5.6b, a harder

shaping effort was once again observed for Target Spectrum 2 with stronger steepness. Despite the transfer functions obtained here having some rather different characteristics to those of 5.3b and 5.4b, the general conclusion for the performance of the adaptive pulse shaping system, when different HNLFs were considered, remain the same.

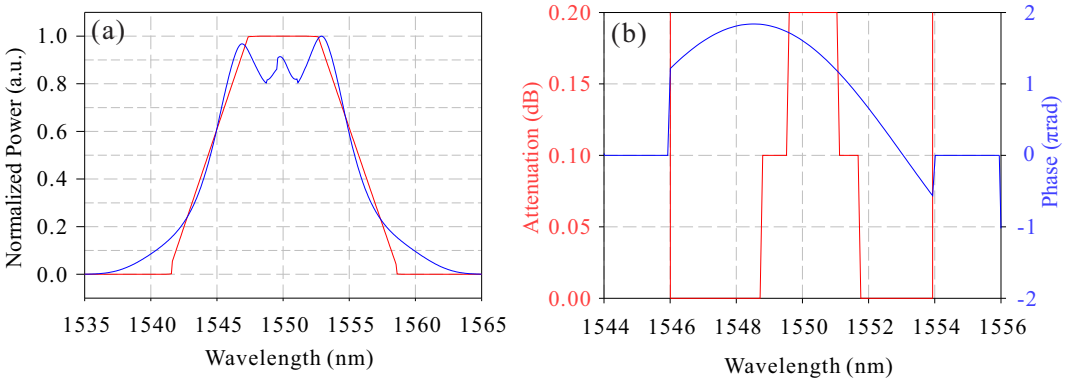

Figure 5.5: Simulation results for Target Spectrum 1 using HNLF02. (a) Comparison between the spectrum obtained after optimization and the target spectrum. Red Trace: Target spectrum. Blue Trace: Optimized spectrum. (b) The transfer function, giving rise to the optimized spectrum, obtained in the simulation. Red Trace: Attenuation Profile. Blue Trace: Phase Profile.

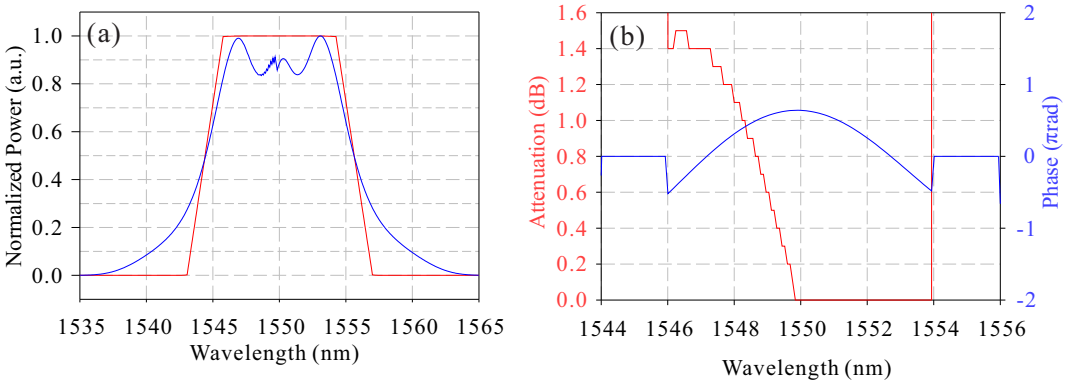

Figure 5.6: Simulation results for Target Spectrum 2 using HNLF02. (a) Comparison between the spectrum obtained after optimization and the target spectrum. Red Trace: Target spectrum. Blue Trace: Optimized spectrum. (b) The transfer function, giving rise to the optimized spectrum, obtained in the simulation. Red Trace: Attenuation Profile. Blue Trace: Phase Profile.

5.3 Experimental Results

The experimental investigation of the feasibility of nonlinear generation of target spectra with symmetric and linear edges assisted by adaptive pulse shaping exploiting the CMA-ES is described in this section.

The experimental setup used here was identical to the setup depicted in Figure 4.17 for the nonlinear generation of the ultra-flat frequency comb. The settings of the parameters of the CMA-ES employed in the adaptive pulse shaping system were the same as the setting described in Section 4.3.1 except for the target spectra which were now the spectra defined in Table 5.1. In the experiment, the shaped pulses were amplified to $20dBm$, instead of $17dBm$ that was used in the simulation, to ensure that the $3dB$ bandwidth of $11nm$ could be achieved. The discrepancy was due to the existence of losses in the system which were not taken into account in the simulation.

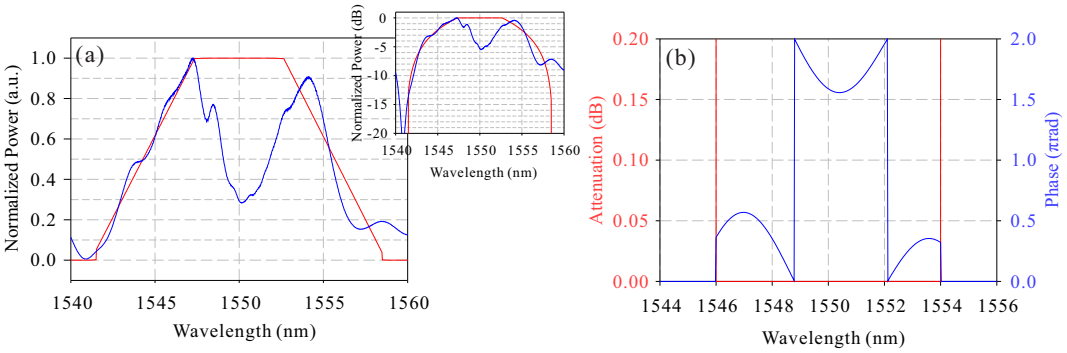

Figure 5.7: Experimental results for Target Spectrum 1 using HNLF01. (a) Comparison between the spectrum obtained after optimization and the target spectrum. Red Trace: Target spectrum. Blue Trace: Optimized spectrum. The inset shows the traces plotted in logarithmic scale. (resolution bandwidth: $0.2nm$) (b) The transfer function obtained after the optimization. Red Trace: Attenuation Profile. Blue Trace: Phase Profile.

Figures 5.7 and 5.8 present the experimental results obtained when HNLF01 was used to nonlinearly broaden the shaped pulse. When the absolute value of the slopes on the edges of the target spectra doubled from 1/6 to 1/3, the values of MF increased from 0.174 (Figure 5.7a) to 0.25 (Figure 5.8a). Meanwhile, the shaping effort became harder when the slope of the edges of the target spectra changed from 1/6 (Figure 5.7b) to 1/3 (Figure 5.8b). The conclusion that a target spectrum with weaker steepness is easier to be generated was experimentally proven.

The experimental results when HNLF02 replaced HNLF01 in the nonlinear broadening stage are shown in Figures 5.9 and 5.10. The observations were again similar to the corresponding simulation results. The values of MF were 0.124 (Figure 5.9a) and 0.138 (Figure 5.10a) for the optimized spectra in the two cases, respectively. Both the amplitude shaping and the phase shaping in the transfer function for the slope of 1/3

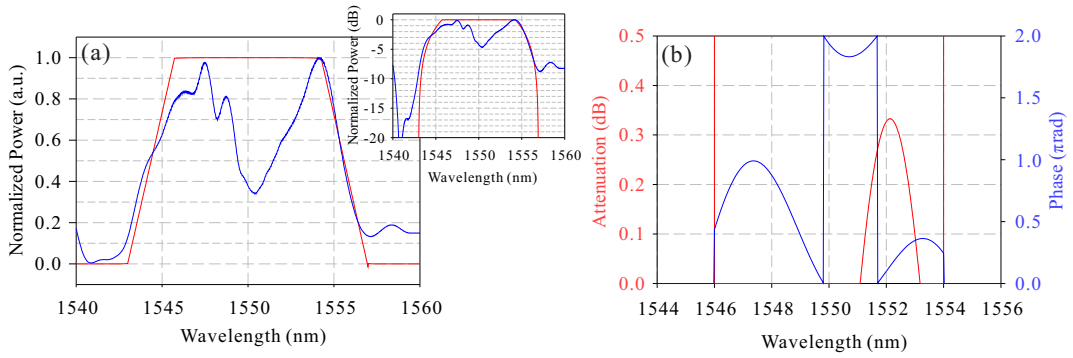

Figure 5.8: Experimental results for Target Spectrum 2 using HNLF01. (a) Comparison between the spectrum obtained after optimization and the target spectrum. Red Trace: Target spectrum. Blue Trace: Optimized spectrum. The inset shows the traces plotted in logarithmic scale. (resolution bandwidth: $0.2nm$) (b) The transfer function obtained after the optimization. Red Trace: Attenuation Profile. Blue Trace: Phase Profile.

(Figure 5.10b) were stronger than those for the slope of 1/6 (Figure 5.9b). Comparing the results from the two HNLFs, the performance of the adaptive pulse shaping system did not vary much between each other, which is in accordance with the previously described numerical observations. This experimentally proves that my technique for harnessing the nonlinear broadened spectrum is not tied directly to the fibre characteristics.

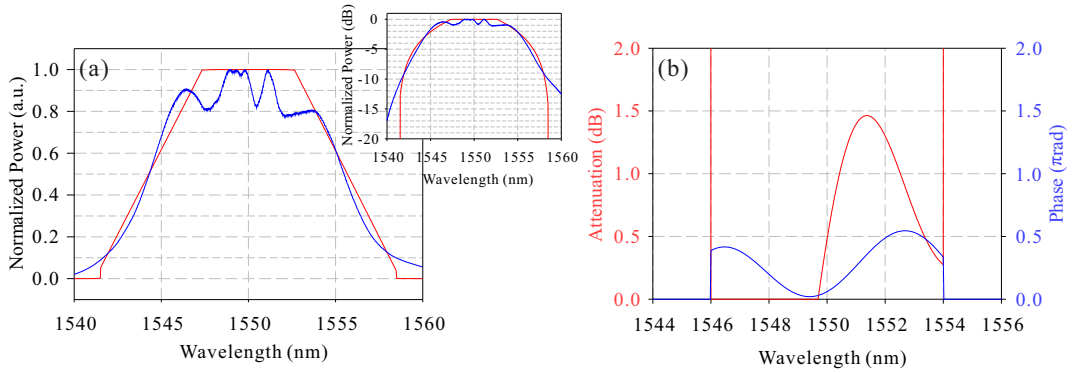

Figure 5.9: Experimental results for Target Spectrum 1 using HNLF02. (a) Comparison between the spectrum obtained after optimization and the target spectrum. Red Trace: Target spectrum. Blue Trace: Optimized spectrum. The inset shows the traces plotted in logarithmic scale. (resolution bandwidth: $0.2nm$) (b) The transfer function obtained after the optimization. Red Trace: Attenuation Profile. Blue Trace: Phase Profile.

With the aim of seeking for better solutions, the normalisation was performed at the

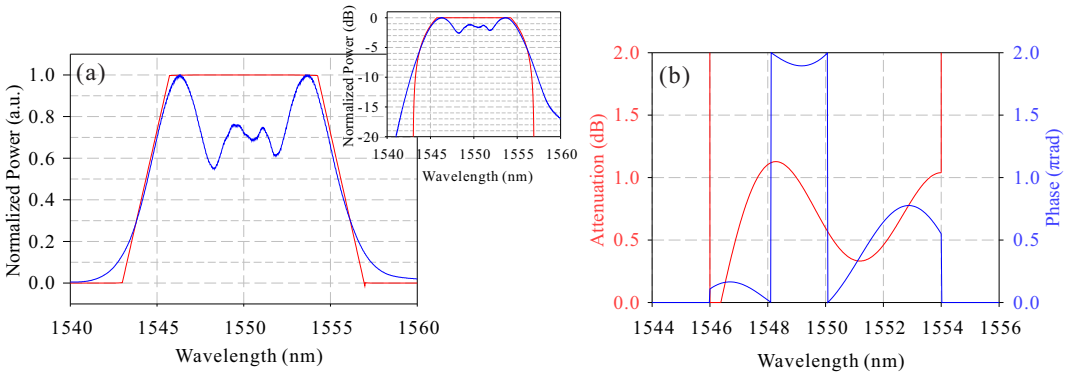

Figure 5.10: Experimental results for Target Spectrum 2 using HNLF02. (a) Comparison between the spectrum obtained after optimization and the target spectrum. Red Trace: Target spectrum. Blue Trace: Optimized spectrum. The inset shows the traces plotted in logarithmic scale. (resolution bandwidth: $0.2nm$) (b) The transfer function obtained after the optimization. Red Trace: Attenuation Profile. Blue Trace: Phase Profile.

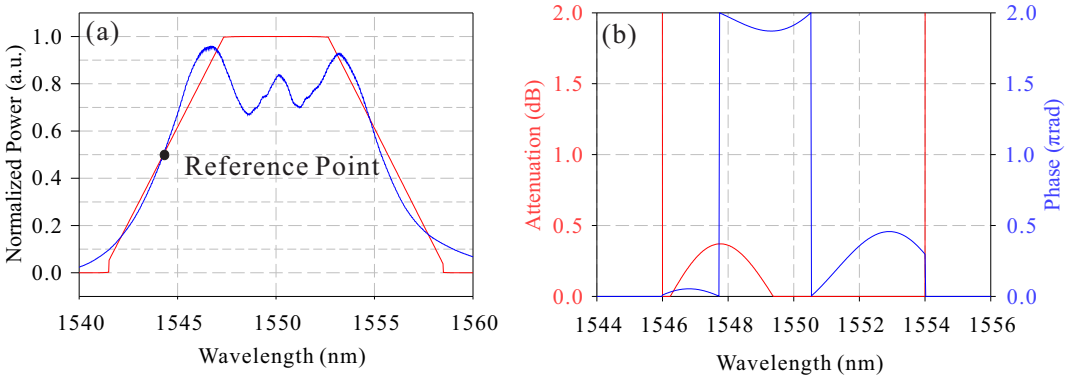

Figure 5.11: Experimental results for Target Spectrum 1 using HNLF02 with normalized to the wavelength corresponding to a power level of 0.5 on the target spectrum. (a) Comparison between the spectrum obtained after optimization and the target spectrum. Red Trace: Target spectrum. Blue Trace: Optimized spectrum. (resolution bandwidth: $0.2nm$) (b) The transfer function obtained after the optimization. Red Trace: Attenuation Profile. Blue Trace: Phase Profile.

half-power level of the spectral top of the target spectrum. The corresponding experimental results are shown in Figures 5.11 and 5.12 with the reference point marked. The values of MF were 0.121 (Figure 5.11a) and 0.297 (Figure 5.12a), respectively. Compared to the result obtained when the spectrum is normalized to its maximum, the results for the slope of 1/6 were slightly better, whereas they were worse when the slope was set to 1/3. Unlike the previous results, Figure 5.12a shows that the generated spectrum had a smaller $3dB$ bandwidth than the target spectrum with a slope of 1/3. The origin of this inconformity was the stochastic nature of the optimisation process. In the blind optimisation process, the transfer function applied into the pulse shaper was generated by the optimisation algorithm itself. When the slope was set to 1/3, coincidently at the beginning of the optimisation process, there existed a small wavelength

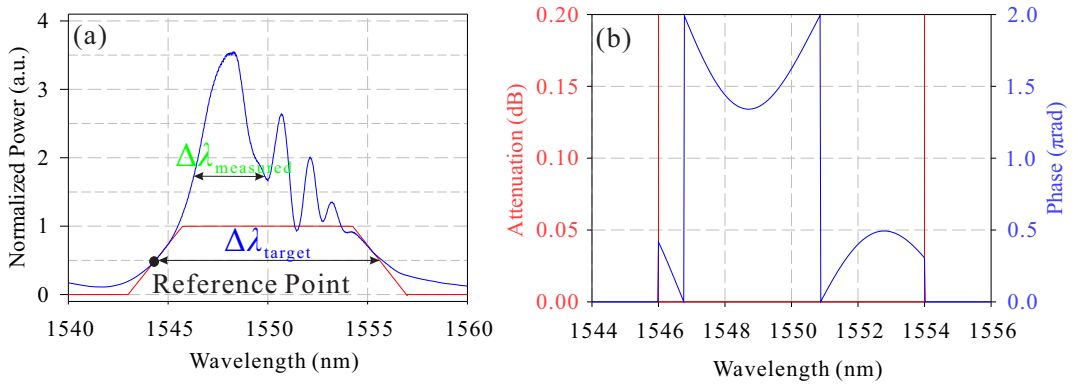

Figure 5.12: Experimental results for Target Spectrum 2 using HNLF02 with normalized to the wavelength corresponding to a power level of 0.5 on the target spectrum. (a) Comparison between the spectrum obtained after optimization and the target spectrum. Red Trace: Target spectrum. Blue Trace: Optimized spectrum. (resolution bandwidth: $0.2nm$) (b) The transfer function obtained after the optimization. Red Trace: Attenuation Profile. Blue Trace: Phase Profile.

range, in which the generated spectrum agreed well with the target spectrum. Then, the optimisation process devoted itself only to working on this part of the generated spectrum without taking its entire bandwidth into account. In the other case, such a coincidence did not occur. The optimisation process was forced to firstly make sure that the generated spectrum has a similar bandwidth to the target spectrum and then work on the characteristics of the generated spectrum.

5.4 Conclusion and Discussion

In this chapter, the use of the arbitrary spectral synthesis exploiting adaptive pulse shaping based on the CMA-ES was explored both numerically and experimentally with the aim of controlling and manipulating the characteristics of the edges of the generated spectrum. At a power level of $20dBm$ at the input of either HNLF01 or HNLF02, the generated spectrum exhibited a $3dB$ bandwidth of $11nm$ as well as symmetric and linear edges with slopes of different steepness.

Through the results from both simulation and experiments, it was observed that the performance of the arbitrary spectral synthesis technique was better when it was targeting the generation of spectra with weaker steepness. By comparing the results from the two different HNLFs both numerically and experimentally, it is proven that my technique is not tied directly to the fibre characteristics.

In both Chapter 4 and this chapter, the arbitrary spectral synthesis had been demonstrated to successfully control the characteristics on either the top or the edges of the generated spectrum. It would be an interesting next step to control the number and

the depth of the ripples in the oscillatory structure on the top of the spectrum, which is typical of SPM.

On the other hand, it is also attractive to consider the adaptive pulse shaping system separately. It has the potential to be implemented with other systems. In the next chapter, numerical simulations will be presented that explore the inclusion of the adaptive pulse shaping system into the cavity of a passively mode-locked laser and its influence on the temporal shape of the laser pulses.

Chapter 6

Numerical Study of Passively Mode-locked Fibre Ring Lasers

6.1 Introduction

In Chapters 4 and 5, I described how the adaptive pulse shaping system had been successfully employed for arbitrary spectral synthesis targeting specific features either on the top or the edges of the spectrum. In this chapter instead, I first present an overview of passively mode-locked fibre ring lasers is presented. The discussion generally covers the theory of mode-locking, a comparison between active and passive mode-locking, various techniques for achieving passive mode-locking, possible cavity configurations for passively mode-locked fibre ring lasers and their associated pulse shaping mechanisms. Then, I investigate placing the pulse shaper inside a laser cavity, giving rise to direct generation of pulses with tailored characteristics. The review of passively mode-locked fibre ring laser (EFRL) presented in Section 6.2 revealed that the temporal waveforms generated from such lasers normally have either a Gaussian, hyperbolic secant, or parabolic shape. It is then interesting to explore the potential of an intra-cavity adaptive pulse shaping system to modify the temporal shape of an EFRL output according to the shaper transfer characteristics.

Since the aim of this work is to change the temporal shape of the output pulses, the difference between the generated and target waveform will be used as the feedback signal to dynamically adjust the transfer function of the programmable filter incorporated into the cavity. As in the previous chapters, this difference will be quantified using the misfit factor (MF) defined in Equation 3.9. The simulations presented in this chapter target the generation of either triangular or rectangular shapes. The results obtained from the simulations of both all-anomalous and all-normal dispersion cavities will be summarized.

6.2 Mode-Locked Erbium-Doped Fibre Ring Lasers

The other main work reported in this thesis relates to Mode-Locked Erbium Fibre Ring Laser (EFRL). In this section, the discussion starts with a description of the theory of mode-locking, and gradually extends to mode-locking mechanisms, cavity configurations and pulse formation principles in a passively mode-locked EFRL.

6.2.1 Theory of Mode-Locking

The term "Laser" stands for "Light Amplification by Stimulated Emission of Radiation". Generally speaking, within a laser, coherent radiation of light can be generated or amplified at almost any frequency of the electromagnetic spectrum. The essential elements in a laser are: (a) a gain medium, which is able to amplify light through stimulated emission; (b) a pumping process, which is responsible for providing energy to the gain medium; and (c) an appropriate optical feedback component, which allows the beam of radiation to bounce back and forth in the formed cavity and pass through the gain medium repeatedly [102].

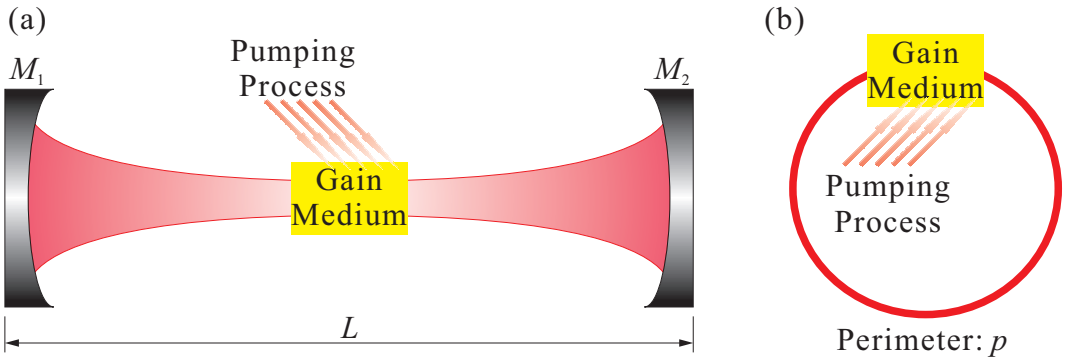

Figure 6.1: Laser cavity configuration. (a) Linear cavity of length L and (b) Ring cavity of perimeter p.

Depending on the implementation of the optical feedback, there are two common configurations of a laser cavity: linear cavity (Figure 6.1a) and ring cavity (Figure 6.1b). In a linear cavity, a pair of mirrors is placed at either end of the gain medium. The light inside the cavity reflects at the surface of each mirror and then returns to the starting position. If the separation between the two mirrors is L, the phase shift accumulated within a single round-trip is $2\omega L/c$. In the case of a ring cavity, the optical path is configured to a closed loop with a perimeter p. As a consequence, the phase shift within a single round-trip is $\omega p/c$.

In the steady state, a standing-wave is formed in the cavity. Hence, the phase shift accumulated within a single round-trip must be some integer multiple of 2π. In the

linear cavity,

$$2\omega L/c = n2\pi, \qquad n = integer. \tag{6.1}$$

A set of discrete and equally spaced frequencies given by

$$\omega = \omega_n \equiv n \times 2\pi \times \left(\frac{c}{2L}\right) \tag{6.2}$$

meets the phase condition. According to [102], these frequencies ω_n are referred to as *axial modes* or *longitudinal modes* of the laser. They are the resonant frequencies of the cavity at which exactly n half-wavelengths exist along the resonator axis between the pair of mirrors. The separation between the axial modes is $\Delta\omega_{ax} \equiv \omega_{n+1} - \omega_n = 2\pi \times \frac{c}{2L}$. In the ring cavity, the phase condition becomes $\omega p/c = n2\pi$ and subsequently, the axial modes exist at frequencies of $\omega_n = n \times 2\pi \times (c/p)$. Thus, the separation between the axial modes in the cavity is fixed, so that

$$\Delta\omega_{ax} \equiv \omega_{n+1} - \omega_n = 2\pi \times \frac{c}{p}. \tag{6.3}$$

Clearly, the number of axial modes existing in the laser cavity is limited by the bandwidth of the gain medium. Any axial mode residing outside the gain bandwidth cannot be amplified during the building up of the laser.

As shown in Figure 6.2, the temporal waveforms of the signal synthesized inside the laser cavity strongly depends on the number of axial modes as well as the relative amplitudes and phase angles between them. Figure 6.2a and Figure 6.2b show how the number of in-phase axial modes existing in the laser cavity influences the synthesized waveform. The number of axial modes in these examples is 5 and 7, respectively. The axial modes with uniform relative amplitudes and correlated phase angles give rise to a temporal waveform with the shape of the sinc square function. The pulse width and number of sub-peaks are determined by the number of axial modes excited inside the cavity. This is because the number of axial modes is equivalent to the spectral bandwidth of the square spectrum. In the remaining cases, the number of axial modes is fixed to 7. In Figure 6.2c, the axial modes are all in phase and have a Gaussian distributed amplitude profile. As expected, periodic Gaussian pulses emerge in the temporal domain. This indicates that the temporal shape of the synthesized signal depends on the envelope of the axial modes. Two examples of in-phase axial modes with randomly distributed amplitudes are shown in Figure 6.2d and Figure 6.2e. A pulse train of periodic pulses can still be obtained in the temporal domain. However, sub-pulses of an irregular background are observed between the adjacent main pulses. Due to the random amplitudes of the axial modes, the pattern of the sub-pulses varies from case to case. Finally, Figures 6.2f, 6.2g and 6.2h represent cases where a random phase profile have been applied to the spectra. Even though periodic temporal waveform are still obtained, they are markedly different than in the previous cases.
Generally, regardless of the relative amplitudes and phase angles between the various

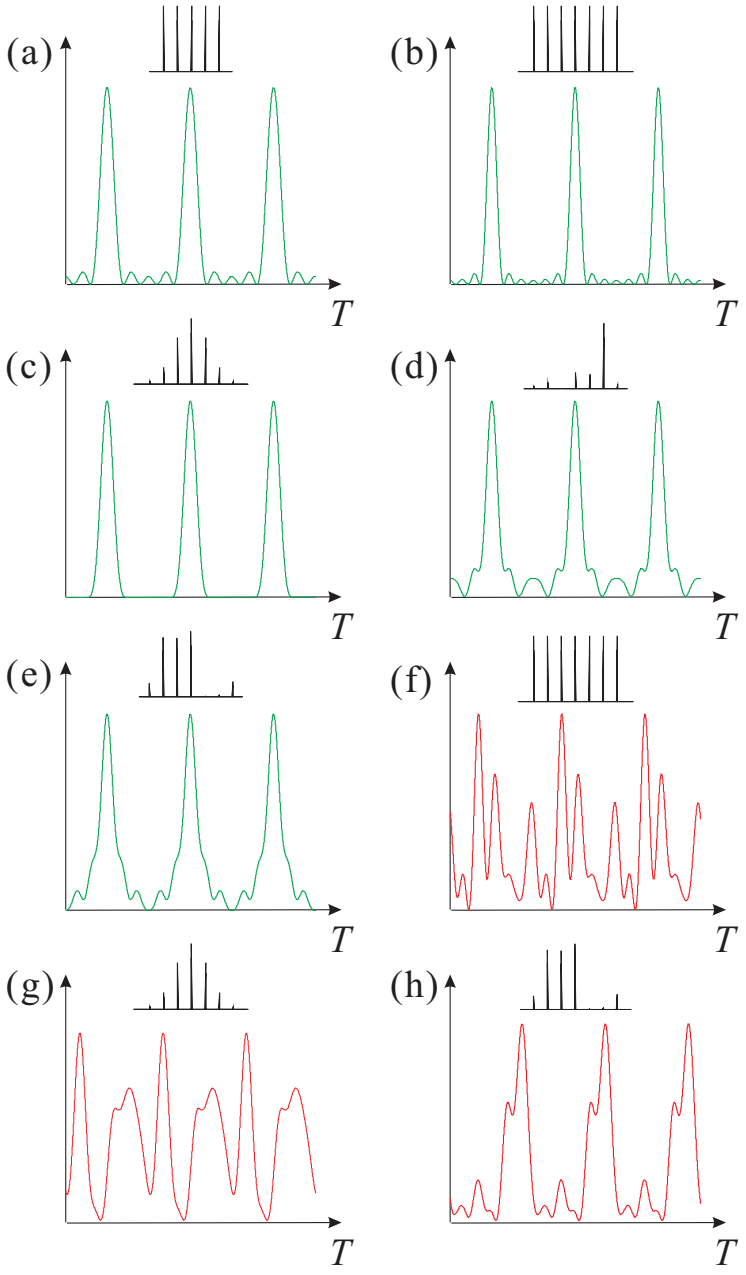

Figure 6.2: Influence of relative properties of axial modes on the synthesized temporal waveforms. (a) 5 axial modes with uniform amplitudes and coherent phase angles; (b) 7 axial modes with uniform amplitudes and coherent phase angles; (c) 7 axial modes with Gaussian envelope and coherent phase angles; (d) 7 axial modes with random amplitudes and coherent phase angles; (e) again, 7 axial modes with random amplitudes and coherent phase angles; (f) 7 axial modes with uniform amplitudes and random phase angles; (g) 7 axial modes with Gaussian envelope and random phase angles; (h) 7 axial modes with random amplitudes and random phase angles.

laser modes, a set of equally spaced axial modes can always be synthesized into a periodic temporal signal, even a noisy-like signal, whose period T is inverse to the spacing between the adjacent axial modes, hence $T = 2L/c$ in the linear cavity, and $T = p/c$

in the ring cavity. All the axial modes, in some sense, are coupled together. In [102], this effect is referred to as *Mode-Coupling*. It follows that periodic, clean and short pulses can be obtained in the laser cavity as long as all the axial modes are in phase, no matter how the amplitudes are distributed over the axial modes. This is referred to as *Mode-Locking* by Siegman [102].
More technically, *Mode-Locking* is a method to generate ultrashort pulses through applying coherent phase angles to multiple axial modes excited in the laser cavity [103]. The coherent phase relationship between a set of axial modes is achieved by applying modulation, which is synchronous to the round-trip time, in the laser cavity. Depending on how the light is modulated in the laser cavity, active mode-locking and passive mode-locking are the two common mode-locking methods.

6.2.1.1 Active Mode-Locking

Mode-locking is considered to be active, when an external signal is used to modulate the light in the laser cavity. Most commonly, an amplitude modulator, driven by a sinusoidal electrical signal with frequency ω_m, is included in the cavity. In order to synchronize this signal with the light bouncing in the cavity, the driving frequency ω_m is required to be exactly the axial mode spacing $\Delta\omega_{ax}$, or one of its harmonics.
In the frequency domain, the effect of the included amplitude modulator is to generate sidebands at frequencies $\omega_n \pm k \times \omega_m$ around axial mode ω_n. As a consequence, each of these modulation sidebands of ω_n will overlap with one of the other axial modes excited in the laser cavity. The modulator couples each axial mode together with one or more of its neighbouring modes with a coherent phase relationship. In other words, the inclusion of the intra-cavity modulator allows the axial modes to be mode-locked.
In the time domain, at the very early stages of the laser oscillation, the laser signal will have a temporal waveform resulting from coupling of all the existing axial modes with both random amplitude and random phase relations, similar to what was shown in Figure 6.2h. Since the output of the modulator is the product of the laser signal with the sinusoidal transmission of the modulator, the signal passes through the modulator at the instant when the transmission of the modulator is at its maximum. Once the laser reaches its steady state, a short pulse will be circulating inside the laser cavity.
In conclusion, active mode-locking is accomplished by the intra-cavity electrooptic or acoustooptic modulator, the driven frequency of which is required to be exactly the same as the separation between adjacent axial modes, or one of its harmonics. In active mode-locking, the circulating pulse experiences less loss in passing through the modulator while it becomes shorter. This is occurring at least until the pulse has a temporal width comparable to the period of the modulator. This phenomenon can be referred to as the pulse shortening effect of the intra-cavity modulator [102]. In the frequency domain, this requires corresponding amount of axial modes to be excited. This can

eventually not exceed the bandwidth of the gain medium. As a result, the pulse width obtained in the scenario of active mode-locking is a balance between the pulse shortening effect of the intra-cavity modulator and the bandwidth limitation of the gain medium. It is noted that active mode-locking can also be achieved using an intra-cavity phase modulator [102, 103].

6.2.1.2 Passive Mode-Locking

In passive model-locking, the modulation of the light circulating inside the laser cavity is obtained using an intra-cavity saturable absorber (SA). The absorption of such a saturable element changes with the intensity of the signal. For low intensities, the absorption is constant and high [104]. As the intensity of the signal increases, the absorption decreases to lower values and gets saturated at a certain level of intensity. Therefore, the light inside the laser cavity is modulated by itself. As a consequence, the modulation is already inherently perfectly synchronized to the laser signal and dynamically adjusted together with the pulse formation [105].
I will next examine how a passively mode-locked pulse builds up in the laser cavity from noise. When the pumping process has just started, the gain is too small compared to absorption of the SA and the loss of the cavity to generate any signal. With increasing pumping power, the gain will keep increasing and ultimately it will exceed the loss and saturable absorption in the cavity, at which point laser oscillation will start to emerge from the noise. Within the period of the laser signal, it is reasonable to expect that there is one special peak which is stronger than all the other peaks in the noise distribution. As the laser oscillation keeps growing, the intensity of this special noise peak can saturate the absorption of the saturable absorber placed in the cavity. After this stage, since the intensities of other weaker noise peaks have not yet reached the threshold of the saturable absorber, the special peak will first begin to encounter much less loss per round trip than all the other opponents. Consequently, this special peak will be growing ahead of the other noise peaks. Eventually, under certain conditions, the saturable absorber induced passive mode-locking process will choose a single noise peak and direct the laser oscillation to have a form of a single short optical pulse circulating inside the laser cavity [102, 105].
There are several advantages of passive mode-locking over active mode-locking. Firstly, the synchronization between the modulation and laser signal does not require special care in the passive mode-locking due to the self-modulation of the light in the laser cavity. In active mode-locking, the synchronization between the modulation and the circulating signal in the cavity is achieved by a phase lock loop. Secondly, the self-modulation of the light induced from the saturable absorber becomes faster and stronger while the pulse gets shorter and shorter. This generally leads to much shorter circulating pulse than in the case of active mode-locking. Based on these advantages, passive mode-locking is

selected to be the mode-locking mechanism for the laser work reported in this thesis. In the following parts of this section, I briefly introduce various passive mode-locking techniques, and describe how a passively mode-locked fibre ring laser can be configured based on these techniques and their corresponding pulse shaping mechanisms.

6.2.2 Passive Mode-Locking Techniques

There are various techniques to achieve passive mode-locked lasers and some of them are widely applied in fibre lasers as well. In this part of the chapter, saturable absorption mode-locking, additive-pulse mode-locking, dissipative four-wave-mixing mode-locking and nonlinear polarization rotation mode-locking are described. This presentation forms the background to Chapter 6, where the operation of various types of passively mode-locked lasers will be studied numerically, with a view of applying adaptive pulse shaping inside their cavities.

6.2.2.1 Saturable Absorption Mode-Locking

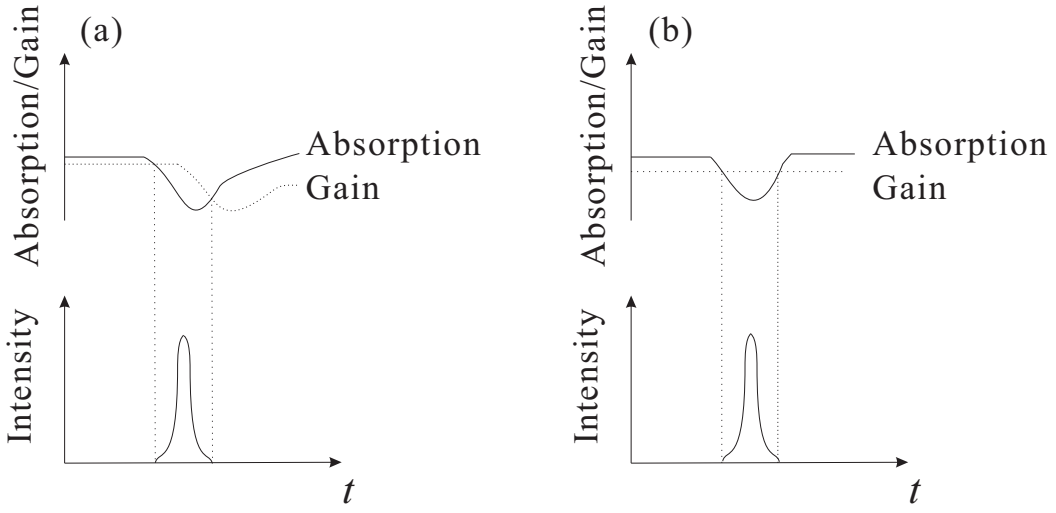

Figure 6.3: Slow (a) and fast (b) saturable absorbers.

Based on the description of passive mode-locking in Section 6.2.1.2, an element which has the property of saturable absorption is essential in a passively mode-locked laser. In this section, I first introduce the mode-locking technique based on saturable absorbers that exploits the properties of special optical materials. As shown in Figure 6.3, for most of the round-trip period, the saturable absorption is larger than the gain in the cavity. But due to the different change rates of the absorption and the gain, there exists a short time window in which the gain becomes higher than the saturable absorption and the net gain emerges. Within this time window, the initial noise in the cavity can evolve

into a short optical pulse, and passive mode-locking can be achieved [106]. Depending on the comparison between the recovery time of the absorber and the optical pulse duration, there are two categories of saturable absorber. If the time the absorber needs to recover to its initial absorption is longer than the pulse duration, then it is referred to as slow saturable absorber (Figure 6.3a). If the recovery time of an absorber is shorter than the pulse duration, it is a fast saturable absorber (Figure 6.3b). The fast saturable absorber is preferable as it is more stable in case of oversaturation of the absorber [107]. Theoretical studies of passive mode-locking using either fast or slow saturable absorbers can be found in [108] and [109], respectively.
Distinguished by the materials used to fabricate the saturable absorber, both semiconductor saturable absorbers and single-wall carbon nanotube saturable absorbers are commercially available. By using a semiconductor saturable absorber, S. Harun et al. [110] obtained a passively mode-locked EFRL emitting pulses with a width of $\sim 340 fs$. Combined with other optical fibre components and effects, lasers which are mode-locked by saturable absorption can exhibit additional features. By changing the pump power together with the fine adjustment of the cavity birefringence, C. Ouyang et al. [111] were able to double the period of the mode-locked EFRL, which means that the operating repetition rate was half of its fundamental frequency. Together with a cascaded sequence of FBGs, A. Luo [112] demonstrated a dual-wavelength passively mode-locked EFRL with a wavelength spacing of $12.49nm$. With single-wall carbon nanotube saturable absorber, N. Shahabuddin et al. [113] implemented a passively mode-locked EFRL emitting pulses with a width of $\sim 0.79ps$. X. Zhao et al. [114] obtained a $25nm$ spacing dual-wavelength operation of the EFRL by effectively controlling the gain profile through adjustment of cavity loss. H. Li et al. [115] achieved harmonic mode-locked EFRL up to seventh order by only adjusting the polarization in the cavity keeping the pump power fixed.

6.2.2.2 Additive-Pulse Mode-Locking

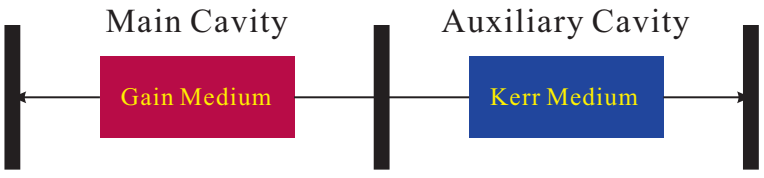

Figure 6.4: Typical structure of additive-pulse mode-locking.

Beside the special materials acting as saturable absorbers, inside a laser cavity, there are also several realizations of artificial absorbers using optical nonlinearities in a Kerr medium [105, 116]. Here, I first introduce additive-pulse mode-locking (APM). The most significant feature of an APM laser is the inclusion of an auxiliary cavity, as shown in Figure 6.4. In the APM, the gain medium is placed inside the main cavity, while the auxiliary cavity is used to contain the Kerr medium. The common mirror between the

main cavity and the auxiliary cavity is partially reflective. As a consequence, the light splits into two paths when it hits the common mirror. One path experiences gain when it circulates inside the main cavity. The other path is nonlinearly phase modulated in the auxiliary cavity. The lengths of these two cavities are required to be well matched to each other to ensure that the two portions of the light will overlap when they are back to the common mirror. When sufficient nonlinearities have been stimulated by the appropriate signal power in the auxiliary cavity, the central part of the recombined signal will be constructively interfered, while the two tails will be destructively interfered. Gradually, the initial long noise-like pulse will be compressed and passive mode-locking is achieved [105, 106].

APM can be implemented in an EFRL by adopting a figure-of-eight configuration [117]. As shown in Figure 6.5, a nonlinear amplifying loop mirror (NALM), comprising a $3dB$ optical coupler, the erbium doped fibre (EDF), and a wavelength division multiplexing coupler, is widely used as the nonlinear switch in the figure-of-eight configuration. It then forms the auxiliary cavity of the APM. Hence, unlike the traditional APM configuration, both the gain medium and the Kerr medium is in the auxiliary cavity in the figure-of-eight configuration. The output of the NALM is connected to an output coupler and then connected back to the input of the NALM through an optical isolator. The resulting ring is the main cavity of the APM. Passive mode-locking in a figure-of-eight laser is achieved through the reflection properties of the NALM [118]: The light propagates bi-directionally in the NALM. Since the EDF is placed asymmetrically in the NALM, the counter-propagating signals accumulate different amounts of nonlinear phase shift when they overlap again. Consequently, the pulse is shortened and amplified in the NALM. In the main loop, the pulse propagates uni-directionally because of the optical isolator.

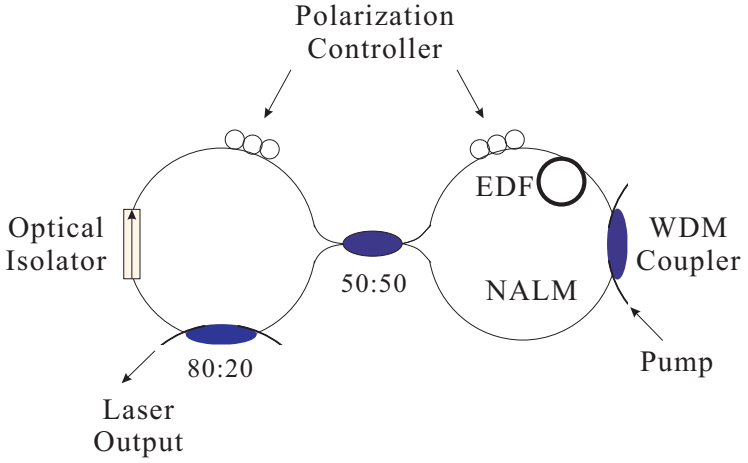

Figure 6.5: Configuration of figure-of-eight EFRL. EDF: Erbium-doped fibre. WDM: Wavelength division multiplexing. NALM: Nonlinear amplifying loop mirror.

The figure-of-eight configuration was extensively studied in 1990s. The performance and

properties of the figure-of-eight EFRL were explored by D. J. Richardson et al.. In 1991, their first paper reported both the emission of a $320fs$ wide pulse with lower pump power and the observation of square pulse generation in the case of higher pump power in the laser [19]. Meanwhile, harmonic mode-locking up to $10GHz$ was achieved by careful adjustment of both the pump power and the cavity birefringence. All these lasing regions were further clarified later in [119]. In 1992, the energy quantization effect of the figure-of-eight EFRL was studied [120]. By delivering the output pulse of the figure-of-eight EFRL into an external cavity including a pulse-compression amplifier, $30fs$ pulses were generated based on soliton self-frequency shifting and soliton compression effects [121]. Around the same time, the figure-of-eight configuration was also used by I. N. Duling, III in an EFRL to generate pulses as short as $\sim 2ps$ [20]. After a very short time, he managed to achieve shorter subpicosecond pulses with a width of $\sim 314fs$ by reducing the fibre length in the NALM from $30m$ to $1.2m$ [122]. In 1992, he achieved more stable mode-locking, further shortening the pulses to a width of $\sim 275fs$ and multipling the repetition rate in figure-of-eight EFRL by feeding the light rejected by the NALM back into the cavity [123]. Comprehensive theoretical studies of figure-of-eight EFRL using numerical simulations can be found in [124, 125, 126].

6.2.2.3 Dissipative Four-Wave-Mixing Mode-Locking

Dissipative four-wave-mixing (DFWM) mode-locking is a useful passive mode-locking technique that can yield pulses with as high a repetition rate as a few GHz. The key feature of DFWM mode-locked EFRLs is the inclusion of a dual-peak bandpass filter in the laser cavity [127]. The bandpass filter changes the net gain profile of the laser, such that only two axial modes experience net positive gain while all the others undergo net negative gain. Through the four-wave-mixing process, the two amplified peaks transfer energy to their neighbouring harmonics. Since the various harmonics have originated from a parametric process, their relative phases are inherently locked. According to the modelling results in [127, 128], the generated pulses are chirp-free. As the repetition rate of the laser is determined by the distance between the two distinct peaks of the filter, it is easy to achieve repetition rates in the order of GHz. It is finally worth to note that, in order to achieve mode-locking, the separation between the filter peaks is required to be equal to the axial mode spacing or one of its harmonics.
The first experimental demonstration of the DFWM mode-locked EFRL was reported by T. Sylvestre et al. [129] in 2001. In their experiment, a non-chirped FBG filter was used to generate the two distinct peaks. As a laser working in the normal dispersion region, an optical dark pulse train with a repetition rate of $80GHz$ was achieved [127]. They also pointed out that the performance of the laser can be improved by suppressing the supermode noise using a high-finesse intra-cavity Fabry-Perot filter. In 2009, J. Schröder et al. [130] implemented the intra-cavity spectral filter in a DFWM

mode-locked EFRL using a programmable optical processor for the first time. Based on the ability of reconfiguration of the programmable filter, they obtained a laser with a wavelength tuning range of $20nm$ and repetition rates between $40GHz$ and $640GHz$. In a subsequent publication, J. Schröder et al. [131] controlled the net cavity dispersion by applying different dispersion profiles into the programmable filter. Subsequently, they obtained both bright and dark soliton-like pulse train. Beside the spectral distance between the two peaks of the filter, the adjustment of the polarisation controller in the cavity can also alter the repetition rate of a DFWM mode-locked EFRL. In 2005, S. Zhang et al [132] showed that the repetition rate of the DFWM mode-locked EFRL can be tuned by adjusting the polarization controller in the cavity. They argued that the enhancement in the repetition rate originated from the birefringence in the cavity, which produced an extra periodic amplitude modulation in the cavity through a possible linear, wavelength-dependent polarization rotation. Using this technique, they obtained a repetition rate up to seven times the separation between the two original peaks from the FBG filter.

6.2.2.4 Nonlinear Polarization Rotation Mode-Locking

Nonlinear polarization rotation (NPR) mode-locking is based on the nonlinear birefringence induced by an intense pulse in the fibre. It is normally facilitated by the combination of a fibre and a polariser. The polarization evolution depends on the optical intensity in the fibre when the initial polarization is not along any of the polarization axes in the fibre. Then, the transmission of a signal is consequently intensity dependent. As a result, the low-intensity parts of the signal are blocked by the polariser while the high intensity part can go through. Hence, the shape of a signal can be modified by itself. This eventually leads to short pulse and subsequently mode-locking [133]. NPR is a widely used mode-locking technique in EFRL [106].
In 1992, V.J. Matsas et al. [21] demonstrated a self-staring, passively mode-locked EFRL using NPR. In the work, the threshold for self-starting mode-locking was determined and short pulses were obtained with a width of $\sim 1ps$. By adjusting the polarization controllers in the cavity, the dual-wavelength lasing was also achieved. In 1993, the same authors further characterized the laser with regard to its operation modes, cavity length and type of fibre used [134]. Depending on the pump power, the laser can either emit square or soliton pulses. They also found that the temporal width of the generated pulses had a $L^{1/2}$ dependence over the cavity length L. By comparing the self-starting ability, spectral quality and overall stability of the laser using both low-birefringence fibre and normal single mode fibre, the results with low-birefringence fibre were significantly better. The shortest pulse they obtained had a width of $700fs$ with a $3m$ long low-birefringence fibre in the cavity. Around the same time, J.R. Taylor's group in Imperial College reported a NPR based EFRL emitting $765fs$ [135] and $350fs$ [136] long

pulses. They also investigated the influence of the cavity length on the pulse width and obtained similar observations. Furthermore, they pointed out that in order to obtain short pulses, the average cavity dispersion should be kept small. Some theoretical study and numerical modelling of the EFRL based on NPR can be found in [137, 138].

6.2.3 Pulse Shaping Mechanism in Different Cavity Configurations

Distinguished by the net dispersion of the cavity, there are three main cavity configurations for passively mode-locked fibre ring lasers. These are all-anomalous dispersion, all-normal dispersion and dispersion-managed configurations. The pulse shaping mechanisms in these three kinds of configurations are introduced separately in this section, .

6.2.3.1 All-Anomalous Dispersion Cavity

All of the early experimental demonstrations of mode-locked EFRLs were based on all-anomalous dispersion cavities, regardless of the technique used to achieve mode-locking. The pulse shaping process in this kind of cavity is governed by the interplay between SPM and the anomalous GVD in the fibre. From the pulse propagation theory, it follows that soliton pulses are generated from an EFRL with all-anomalous dispersion cavity and sufficient gain [139].

The distinct feature of the pulses generated in an all-anomalous dispersion cavity is the existence of a series of discrete and symmetric, but unequally spaced sidebands on the spectrum. This phenomenon was carefully studied and explained by S. Kelly [140]. In a model of average soliton proposed in a subsequent publication [141], the pulse propagation after several round-trips in the ring cavity is considered to experience a gain profile with a period of z_a. Thus, if the soliton period z_0 is much larger than the amplification period z_a, the peak power of the generated soliton after several round-trips is averaged. Then, stable soliton propagation can only be achieved under the condition that the averaged soliton power $< P >$ equals to the fundamental soliton power P_{sol}. When z_0 is approaching z_a, the averaging process is no longer valid. The periodic change in the gain profile cannot be ignored. This leads to nonsoliton generation which is mixed with the original soliton generation. At certain values of z_0, the mixing process can be strengthened resonantly. It can be found that the position of the spectral sidebands Δf_n relative to the central frequency obeys Equation 6.4.

$$\Delta f_n = \pm \frac{1}{2\pi tp} \sqrt{1 + 8nz_0/z_a} \tag{6.4}$$

When n represents the order of the spectral sideband, and tp is the FWHM of the generated soliton. This result explains the unequal spacing between the spectral sidebands and indicates that the origin of these sidebands is not related to the modulation instability since the position of the sidebands does not scale with the power of the signal.

6.2.3.2 All-Normal Dispersion Cavity

The opposite extreme to an all-anomalous dispersion cavity is an all-normal dispersion cavity, which is constructed using only normal dispersion fibres. In such a cavity, depending on where the pulse formation occurs in the cavity, there are two operation mode. The laser is operated to produce dissipative soliton (DS) if the pulse is formed in the passive normal-dispersion fibre. On the other hand, active similaritons are generated when the self-similar evolution occurs in the active gain fibre [142]. In this section, I review the DS laser first and then the active similariton laser.
Similar to the pulse shaping mechanism in an all-anomalous dispersion cavity which is based on the balance between anomalous dispersion and nonlinearity, the DS pulses formed in an all-normal dispersion cavity require the balance between normal dispersion and nonlinearity. Additionally, dissipation (spectral filtering) is needed to avoid the optical wave breaking effect in the normal-dispersion fibre. A block diagram of an all-normal dispersion DS laser is shown in Figure 6.6.

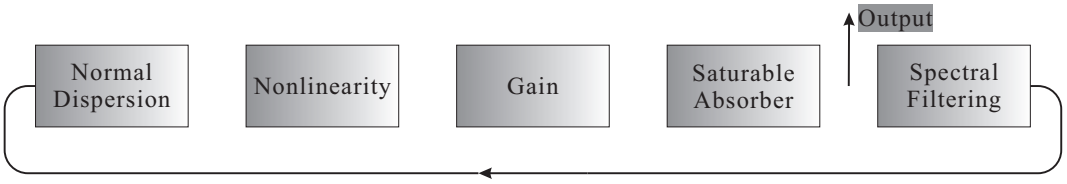

Figure 6.6: Schematic of an all-normal dispersion DS laser.

Figure 6.6 includes all the physical processes happening in an all-normal dispersion DS laser. Due to the normal dispersion, the temporal waveform is broadened. In the nonlinear section, the spectrum develops structures. The saturable absorber is used as the mode-locker of the laser. It can also slightly narrow the pulse down in both temporal and spectral domain. By contrast, the spectral filtering has much more influence on the pulse characteristics. It removes the spectral features and restores the pulse to its original duration as it is chirped. The saturable absorber and the spectral filter have little impact on the temporal phase. However, the accumulated nonlinear phase shift through SPM is compensated for by the normal dispersion. In summary, in a DS laser, the accumulated linear phase is balanced by the spectral filtering and the saturable absorber to restore the original pulse duration. Meanwhile, the nonlinear phase shift is cancelled out by the dispersion. It is worth noting that a chirped pulse acquire a negative linear

chirp in a normal-dispersion fibre. This is a critical feature in an all-normal dispersion DS laser.

Research on the DS lasers has been extensively carried out in F. Wise's group at Cornell University. They reported the first passive mode-locked all-normal dispersion fibre laser in 2006 [143]. This was an ytterbium-doped fibre ring laser working at $1030nm$, where the SMF has normal dispersion. The mode-locking technique was the NPR, which was implemented by a combination of two quarter-waveplates, a half-waveplate and a polarizing beamsplitter. The laser was capable of generating $1.4ps$ wide chirped pulses, which were further compressed to $170fs$ outside the cavity. The same group further studied the properties of an all-normal dispersion DS laser through both experiments and numerical modelling [144, 145]. They identified that the behaviour and properties of a DS laser are determined by the following three key parameters: the nonlinear phase shift accumulated by the pulse ϕ_{NL}, the bandwidth of the spectral filter BW and GVD. The dependence on Φ_{NL} is summarised as below: firstly, the pulse energy is nearly proportional to ϕ_{NL}. The pulse breathing ratio, which is the ratio between the maximum and minimum pulse durations inside the cavity, increases in the range from 1 to 4 as ϕ_{NL} increases. The chirp of the output pulse decreases as ϕ_{NL} increases. Same trends, as those observed when ϕ_{NL} is increased, are observed when either the BW or GVD is decreased. A detailed study on the influence of the spectral filter can be found in [146, 147].

In the case of active similariton, the pulse formation in the cavity is based on the fact that an arbitrary pulse would finally evolve into a parabolic pulse in a normal-dispersion gain fibre [14, 148]. Hence, the normal-dispersion gain fibre acts as a local nonlinear attractor to stabilize the pulse. The parameters of the output pulses are determined by the input pulse energy and the normal-dispersion gain fibre parameters. Spectral filtering is again important and crucial in this operation mode, as is responsible for restoring the original form of the pulses circulating in the cavity. A typical example of this operation mode was reported by Renninger et al. [149], in which a spectral filter is placed after the gain fibre to achieve the original pulse form.

6.2.3.3 Dispersion Managed Cavity

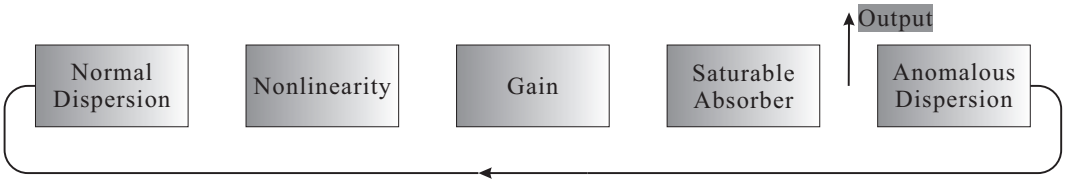

Figure 6.7: Schematic of a dispersion-managed fibre ring laser.

A dispersion-managed (DM) cavity consists of both normal and anomalous dispersion fibre segments, the relationship between the values of normal and anomalous dispersion

is referred to as the dispersion map. The net dispersion of a DM cavity is either near zero or largely normal. A block diagram of this kind of laser is shown in Figure 6.7. Compared to the all-normal dispersion fibre, the spectral filtering stage is replaced by an anomalous dispersion fibre segment. A comprehensive review of DM laser can found in [150].

As studied through numerical simulations in [142], there are two operation regimes in a DM laser distinguished by the nonlinearity of the normal-dispersion fibre segment. The passive self-similar (SS) operation exists when the nonlinearity of the normal-dispersion fibre segment is high. If the nonlinearity is lower than a certain critical point, the operation changes to produce stretched dissipative solitons (SDS).

In the passive SS mode, the pulses are always positively chirped and have a nearly parabolic profile. The temporal width of the pulses is monotonically increased during the propagation in the normal-dispersion fibre segment. These pulses are dubbed as similaritons, which are the asymptotic solutions of NLSE in the condition of only nonlinearity and normal GVD [16, 151]. The maximum pulse duration can been seen at the boundary between the normal-dispersion fibre segment and the anomalous-dispersion segment. The breathing ratio of the pulses in the passive SS mode can be up to 50. Then the anomalous-dispersion fibre section compresses the pulse back to its original duration. In the spectral domain, the spectrum broadens and acquires parabolic shapes during the propagation in the normal-dispersion fibre. Due to the gain filtering effects, the original form is restored after the gain fibre. This means that the dissipative effect also exists in a passive SS laser. Similar to the DS laser, the saturable absorber is responsible mainly for mode-locking and slightly contributes to the shortening of the broadened pulses after the normal-dispersion segments.

In the SDS operation mode, the pulses are narrowed in the normal-dispersion fibre segment and broadened in the anomalous-dispersion fibre segment. The pulse width monotonically evolves in each segments as in the passive SS mode. The gain filtering and saturable absorber plays a similar role as in the passive SS mode. The pulses are negatively chirped and can be nearly transform-limited at the end of the normal-dispersion section. It is important to note that the function of the anomalous-dispersion fibre segment is simply responsible for accumulating negative chirp. The solutions will be identical to an all-normal dispersion DS laser if it is removed from the cavity. Hence, the SDS operation mode is an extension of the DS laser with near zero net dispersion. The pulses in such a laser are DS with additional evolution determined by the dispersion map.

6.3 Simulation of an All-Anomalous Dispersion Cavity

This section presents the all-anomalous dispersion cavity. A figure-of-eight EFRL was used here as the laser configuration. This laser type was reviewed in Section 6.2.2.2.

6.3.1 Numerical Model for Figure-of-Eight Lasers

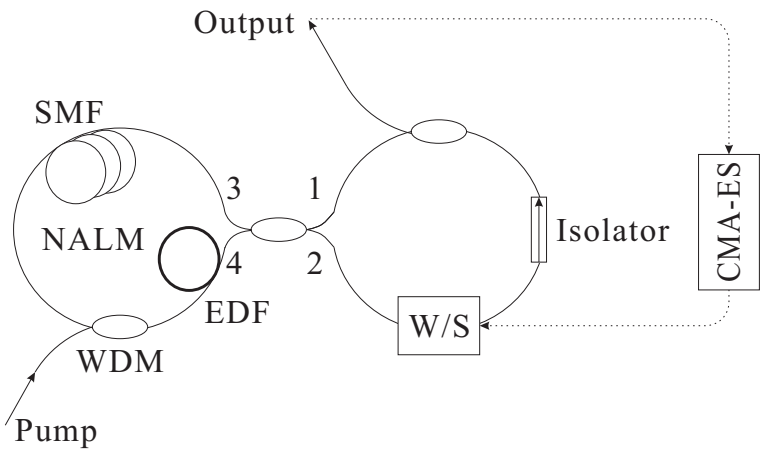

Figure 6.8: Figure-of-eight laser incorporated with adaptive pulse shaping system. The programmable filter W/S was placed in the isolator loop.

The simulation was carried out following the model described in [124]. As shown in Figure 6.8, a NALM, compromising a SMF with a length of L_2 and an EDF with a length of L_A was the nonlinear switch in the configuration. The isolator loop consists of a SMF with a length of L_1. The SMF and EDF in the configuration were assumed to have the same GVD β_2 and nonlinear coefficient γ. The programmable filter (assumed to be the Finisar W/S), was placed inside the isolator loop of the figure-of-eight laser. Then, the transfer function of the W/S was dynamically adjusted by the CMA-ES based on the comparison between the temporal shape of the output pulses and the target shape. In the NALM, there is a WDM coupler to provide the pump power for the EDF. It can be considered as transparent for the laser signal in the cavity. In the isolator loop, an output coupler exists with a coupling ratio of C_k. As a result, the power of signal is reduced by $1 - C_k$ after this coupler. The NALM and the isolator loop are connected by a coupler with a coupling ratio of C_r. Since all of its four ports are involved in the cavity, the general model of an optical coupler shown in Equation 6.5 below was used to determine the electrical field $E_i,\ i = 1, 2, 3, 4$ at each of its port:

$$\begin{bmatrix} E_3 \\ E_4 \end{bmatrix} = \begin{bmatrix} (1 - C_r)^{1/2} & jC_r^{1/2} \\ jC_r^{1/2} & (1 - C_r)^{1/2} \end{bmatrix} \cdot \begin{bmatrix} E_1 \\ E_2 \end{bmatrix} \tag{6.5}$$

where E_1 and E_2 represent the electric fields of incoming signal on one side of the coupler, and E_3 and E_4 the electric fields of outgoing signals on the other side. Since the operation of a fibre coupler is symmetric, the set of (E_1, E_2) and (E_3, E_4) are interchangable, in order to simulate the signals traversing the couple in the opposite direction.
In one round-trip of the figure-of-eight laser, the signal is propagating uni-directionally

in the isolator loop (therefore $E_2 = 0$), and then this signal is split into two counter-propagating components in the NALM according to Equation 6.5. In the NALM, the EDF is assumed to be placed very close to port 4. As a result, the clockwise direction experiences amplification before propagating in the SMF. Conversely, a low-power signal propagates in the SMF in the anticlockwise direction, before it is amplified in the EDF. Then, these two components are combined together at the coupler and coupled back to the isolator loop. In the isolator loop, the signal emerging at port 1 is suppressed by the isolator, leaving only the signal from port 2 to circulate in the cavity.
The signal propagation in the SMF was modelled using the NLSE shown in Equation 2.8, taking into account GVD, SPM and losses. For the signal propagation in the EDF, an extra gain term was required to be added to the loss term of Equation 2.8. This gain term was calculated according to [124].

$$g = g_0 exp(-E_p/E_{sat})[1 + (2|\omega|/\Delta\omega)^{2m}]^{-1} \tag{6.6}$$

In Equation 6.6, g_0 represents the small signal unsaturated gain, E_p is the pulse energy, while E_{sat} is the saturation energy of the EDF. $\Delta\omega$ stands for the $3dB$ bandwidth of the EDF and m is a parameter to determine the slope of the distributed chromatic gain profile. The SSFM was used to solve the NLSE.
Since the laser was expected to be self-starting, the noise should be assumed to be the initial seed for the pulse generation. In the figure-of-eight laser, the only noise source was the amplified spontaneous emission (ASE) from the EDF. In the simulation, it was modelled as a pseudorandom signal with a small mean power. In the frequency domain, it was a uniform signal with random spectral phase. The parameters used in the simulation are specified in Table 6.1.

Length of SMF in the isolator loop	L_1	$6m$
Length of SMF in the NALM	L_2	Varied from $32m$ to $61m$
Length of EDF in the NALM	L_A	$3m$
Small signal gain of EDF	g_0	$33dB$
$3dB$ bandwidth of EDF	$\Delta\omega$	$8.2rad \cdot THz$ $(10nm)$
Saturation power of EDF	E_{sat}	$10pJ$
Parameter to determine the slope of the distributed chormatic gain profile of EDF	m	1
GVD of SMF and EDF	β_2	$-10ps^2/km$
Nonlinear coefficient of SMF and EDF	γ	$2.2W^{-1}km^{-1}$
Central Wavelength	λ_0	$1550nm$
Coupling ratio of the coupler between NALM and the isolator loop	C_r	0.48
Coupling ratio of the output coupler	C_k	0.9

Table 6.1: Parameters for the simulation of a figure-of-eight laser.

A number of round-trip calculations were needed before the steady-state was reached.

Due to the random nature of the noise seed signal, the exact number of round-trips could vary with each execution of the simulation. In the following simulations, the steady-state was determined by comparing the temporal shape of the signal in the current round-trip with that in the previous round-trip. When the difference was relatively small, the steady-state was considered to have been reached. Alternatively, as a direct but less accurate judgement, the pulse energy can be used to determine the steady-state as well. As long as the pulse energy was stable in each round-trip, the laser could be safely considered to have reached its steady-state.
With the W/S in place inside the uni-directional isolator loop, the adaptive pulse shaping system was incorporated into the cavity. As a result, besides the propagation in the SMF segment, the pulses propagating in the isolator loop went through a spectral filtering stage. The shaping functions of both amplitude and phase were represented in the same way as described in Section 4.3.1. During the search process, they were blindly optimized by the CMA-ES. For each transfer function, the temporal shape of the pulses achieved in the steady-state was compared with the target shape. This difference was then quantified by the MF and used as the feedback signal for the CMA-ES.

6.3.2 Simulation Results and Discussion

At the beginning of the simulation, the model was executed without the adaptive pulse shaping system in place. In order to find out the shortest possible pulse width $\Delta\tau_{min}$, several values of length of SMF in the NALM L_2 in the range from $32m$ to $61m$ were tested. The length of $32m$ was the minimum requirement for the NALM to provide sufficient nonlinear phase difference to the counterpropagating signal through SPM. On the other side, the nonlinear phase difference would be greater than $\pi/2$ if the length of the SMF in the NALM is larger than $61m$. This would prevent the pulse generation and pulse shape stabilization in the laser cavity.

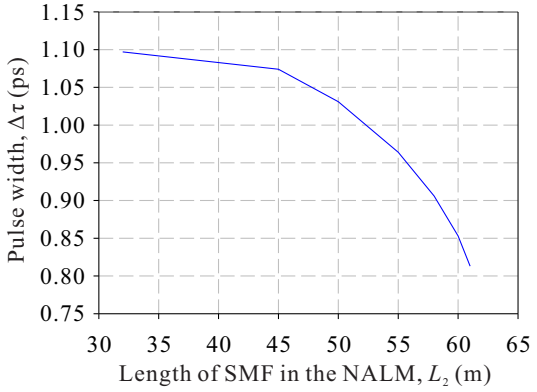

Figure 6.9: The dependence of the pulse width on the length of SMF in the NALM in a figure-of-eight laser.

The dependence of $\Delta\tau$ on L_2 is shown in Figure 6.9. As long as the steady-state can be reached, the shortest pulse width of $0.81ps$ occurs in the longest cavity with $61m$ SMF in the NALM. Since the pulses generated from an all-anomalous cavity are nearly transform-limited, the pulse with shortest pulse width also has the widest bandwidth, which is preferable for the pulse shaping process. Hence, in the following simulation with adaptive pulse shaping system, the length of SMF in the NALM was fixed to $61m$.

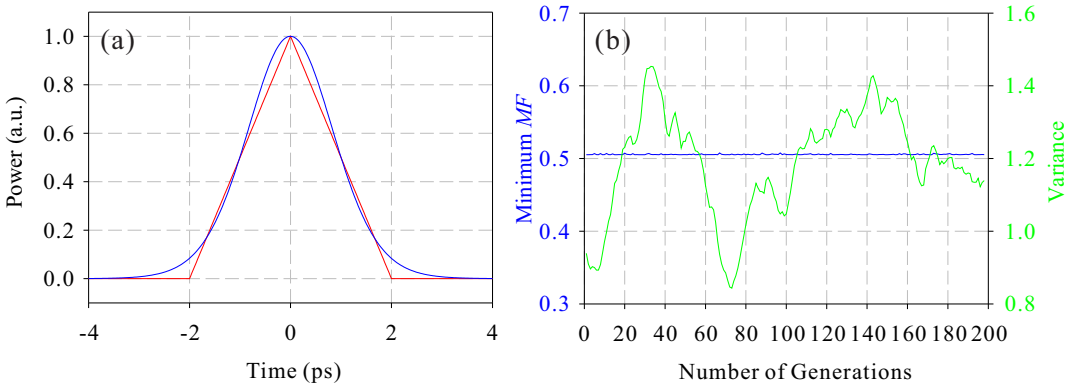

Figure 6.10: Simulation results of an all-anomalous dispersion cavity incorporated with adaptive pulse shaping system. (a) Comparison between the temporal shapes of generated pulse and target pulse. Red trace: target triangle pulse with a FWHM of $2ps$; blue trace: generated pulse. (b) Evolution of Minimum MF value and variance for each generation in CMA-ES.

The target waveform set here had a triangular shape and a FWHM of $2ps$. The simulation results are shown in Figure 6.10. The CMA-ES was allowed to run for 200 generations, which means that a large amount of the search space had been explored. By fitting the optimised waveform (blue trace in Figure 6.10a), the generated waveform had a shape of hyperbolic secant function and a FWHM of $2ps$. The adaptive pulse shaping system based on the CMA-ES was not able to alter the temporal shape of the generated pulses, but only forced the generated pulse to have a FWHM of $2ps$. Figure 6.10b shows that the variance for each generation in the CMA-ES experienced two rounds of significant fluctuations, but the minimum MF almost kept constant at a level of $\sim$0.5 during the process. This indicates that the CMA-ES had attempted to escape from the trapping from the current condition, however without success. This implies that the spectral filtering does not have significant influence on the pulse shaping mechanism in an all-anomalous dispersion cavity. The generated pulse was still a soliton.

6.4 Simulation of an All-Normal Dispersion Cavity

Although the attempt to change the temporal shape of the pulses generated from an all-anomalous dispersion cavity through adaptive pulse shaping was not successful, it is

still worth to try it out in an all-normal dispersion cavity where the pulse shaping mechanism is different. The spectral filtering has a greater impact on the pulse formation in such a cavity. In this section, the numerical efforts will be devoted to the combination of an all-normal dispersion cavity and the adaptive pulse shaping system, with the aim to change the temporal shape of the generated pulses.

6.4.1 Numerical Model for Active Similariton Lasers

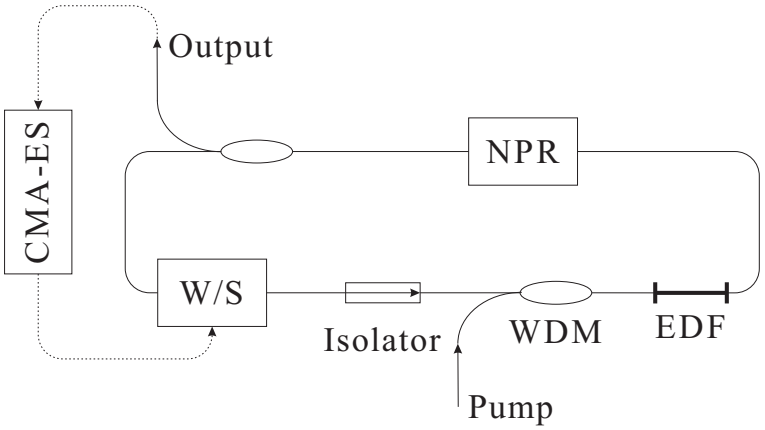

Figure 6.11: Active similariton laser incorporating an adaptive pulse shaping system.

Figure 6.11 shows the schematic diagram of the all-normal dispersion laser that I simulated, which included the adaptive pulse shaping system. In the model, the EDF and any other fibres in the ring cavity were lumped together into a single normal-dispersion gain fibre segment. Hence, the laser was operated in the mode of active similariton, which was reviewed in Section 6.2.3.2. The simulation then followed the model described in [149].

The mode-locking technique used in the laser was NPR, which was reviewed in Section 6.2.2.4. In order to make the simulation easier, the NPR based mode-locker was assumed to be implemented through a combination of a half-wave plate, a quarter-wave plate, a polariser with a second quarter-wave plate in sequence. In this way, all the polarization-dependent elements can be expressed by their corresponding standard Jones matrix in the simulation. Equations 6.7, 6.8 and 6.9 show the Jones matrices for a quarter-wave plate, a half-wave plate, and a polariser with orientations θ_{qwp}, θ_{hwp} and θ_{pol} (with respect to the x axis), respectively.

$$J_{qwp} = \begin{bmatrix} \frac{\sqrt{2}}{2}(1 + jcos2\theta_{qwp}) & \frac{\sqrt{2}}{2}jsin2\theta_{qwp} \\ \frac{\sqrt{2}}{2}jsin2\theta_{qwp} & \frac{\sqrt{2}}{2}(1 - jcos2\theta_{qwp}) \end{bmatrix} \tag{6.7}$$

$$J_{hwp} = \begin{bmatrix} cos2\theta_{hwp} & sin2\theta_{hwp} \\ sin2\theta_{hwp} & -cos2\theta_{hwp} \end{bmatrix} \tag{6.8}$$

$$J_{pol} = \begin{bmatrix} cos^2\theta_{pol} & cos\theta_{pol}sin\theta_{pol} \\ cos\theta_{pol}sin\theta_{pol} & sin^2\theta_{pol} \end{bmatrix} \tag{6.9}$$

The pulse propagation in the normal-dispersion gain fibre was modelled by the coupled NLSE taking into account the interaction between the two orthogonal polarization states, A_x and A_y:

$$\begin{aligned} \frac{\partial A_x}{\partial z} &= \frac{g}{2}A_x - j\frac{\beta_2}{2}\frac{\partial^2 A_x}{\partial T^2} + j\gamma(|A_x|^2 + \frac{2}{3}|A_y|^2)A_x, \\ \frac{\partial A_y}{\partial z} &= \frac{g}{2}A_y - j\frac{\beta_2}{2}\frac{\partial^2 A_y}{\partial T^2} + j\gamma(|A_y|^2 + \frac{2}{3}|A_x|^2)A_y, \end{aligned} \tag{6.10}$$

where z is the propagation distance, T is the retarded time frame, β_2 is the GVD of the fibre, γ is the nonlinear coefficient of the fibre. The gain parameter g is expressed as

$$g = \frac{g_0}{1 + \frac{\int[|A_x|^2 + |A_y|^2]dt}{E_{sat}}}, \tag{6.11}$$

where g_0 is the small-signal gain of the fibre and E_{sat} is the saturation energy of the fibre. The integral is used to calculate the pulse energy and should be done before the propagation. The SSFM was the numerical method employed in the simulation to solve the coupled NLSE Equation 6.10.

As the laser was expected to be self-starting, the initial field in the simulation was once again white noise with relatively low power. In one round-trip of the laser, the signal experienced nonlinear propagation in the normal-dispersion gain fibre, followed by the NPR-based mode-locker and the spectral filtering stage. A number of round-trips were required to reach the steady-state, which was determined using the method described in Section 6.3.1.

Length of normal-dispersion gain fibre	L	$3m$
Small signal gain of normal-dispersion gain fibre	g_0	$30dB$
Saturation power of normal-dispersion gain fibre	E_{sat}	$170pJ$
GVD of normal-dispersion gain fibre	β_2	$78ps^2/km$
Nonlinear coefficient of normal-dispersion gain fibre	γ	$7.2W^{-1}km^{-1}$
Central Wavelength	λ_0	$1550nm$
Orientation of half-wave plate	θ_{hwp}	$2.28rads$
Orientation of the first quarter-wave plate	θ_{qwp1}	$2.21rads$
Orientation of polariser	θ_{pol}	$\pi/2$
Orientation of the second quarter-wave plate	θ_{qwp2}	$0.59rads$
Coupling ratio of the output coupler	C_k	0.7

Table 6.2: Parameters for the simulation of an active similariton laser.

The output coupler with a coupling ratio of C_k was placed right after the NPR-based mode-locker. Once the steady-state was reached, the temporal shape of the output

pulse was compared with the target shape. After being quantified by the misfit function defined in Equation 3.9, this difference was fed into the CMA-ES, which then blindly adjusted both the amplitude and phase transfer functions of the programmable filter in the cavity. The parameters for the simulation are shown in Table 6.2.

6.4.2 Simulation Results and Discussion

Based on the previously described model, the goal here is to achieve flexible control of the temporal shape of the output pulse assisted by the intra-cavity adaptive pulse shaping system.

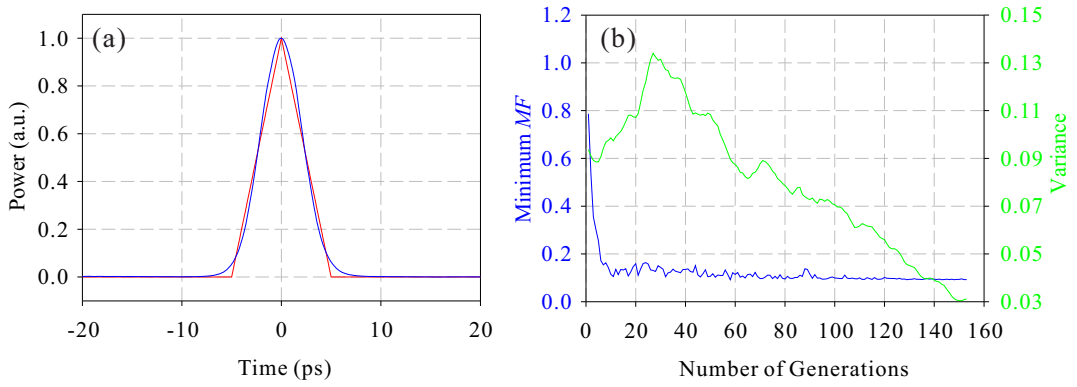

Figure 6.12: Simulation results of an active similariton laser incorporated with adaptive pulse shaping system targeting for a 5ps triangle pulse. (a) Comparison between the temporal shapes of generated pulse and target pulse. Red trace: target triangle pulse with a FWHM of 5ps; blue trace: generated pulse. (b) Evolution of Minimum MF value and variance for each generation in CMA-ES.

The first target I set for the laser was the generation of triangular pulses with a FWHM of 5ps. The optimum waveform obtained during the optimization is shown in Figure 6.12a. Similarly to the results obtained in an all-anomalous dispersion cavity, the optimized waveform had a similar width as the target shape, but acquired a Gaussian shape, rather than the desired triangular. From Figure 6.12b, it can be seen that the difference between the generated waveform and the target shape had been significantly reduced by the optimisation. This indicates that the CMA-ES based adaptive pulse shaping system did have an impact on the output of the laser. The failure to obtain triangular pulses may originate from the sharp top angle and the steep edges of this shape. It is then consequently worth to try and generate a temporal shape which has smoother top and edges.

A third-order super-Gaussian pulse with a FWHM of 5ps was selected as the second target for this study. From the simulation results shown in Figure 6.13, the best waveform achieved from the optimization process had good agreement with the target shape

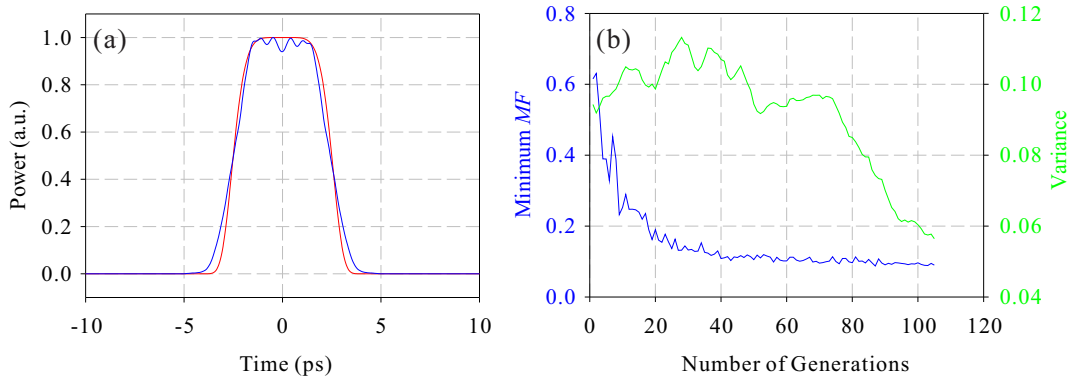

Figure 6.13: Simulation results of an active similariton laser incorporated with adaptive pulse shaping system targeting for a 5*ps* third-order super-Gaussian pulse. (a) Comparison between the temporal shapes of generated pulse and target pulse. Red trace: target third-order super-Gaussian pulse with a FWHM of 5*ps*; blue trace: generated pulse. (b) Evolution of Minimum MF value and variance for each generation in CMA-ES.

in spite of some small discrepancies on the top. The evolution of the minimum MF and variance in each generation of the CMA-ES shown in Figure 6.13b again demonstrated the effect of the adaptive pulse shaping system on the laser output. An obvious reduction of the difference between the generated waveform and the target shape was obtained after the optimization.

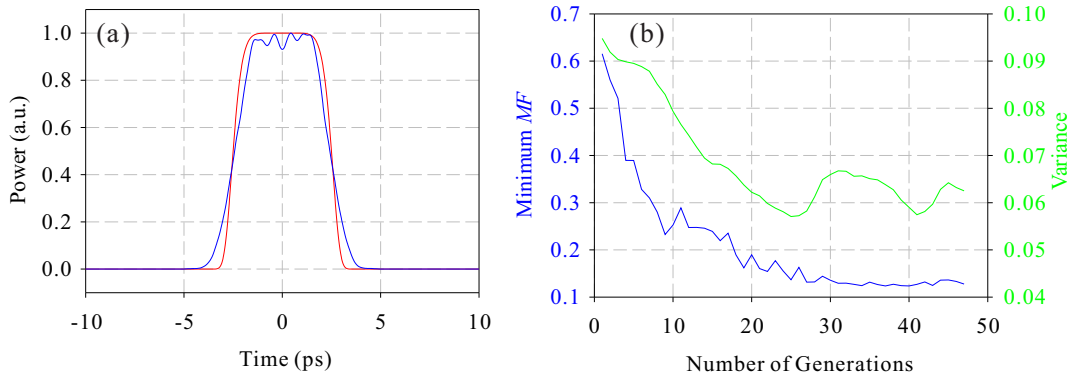

Figure 6.14: Simulation results of an active similariton laser incorporated with adaptive pulse shaping system targeting for a 5*ps* fourth-order super-Gaussian pulse. (a) Comparison between the temporal shapes of generated pulse and target pulse. Red trace: target fourth-order super-Gaussian pulse with a FWHM of 5*ps*; blue trace: generated pulse. (b) Evolution of Minimum MF value and variance for each generation in CMA-ES.

In order to increase the steepness of the edges of the target shape, fourth- and fifth-order super-Gaussian pulses with a FWHM of 5*ps* were also used as target shapes. The simulation results for these two cases are shown in Figures 6.14 and 6.15, respectively. Good agreement between the generated waveform and the target shape can still be seen

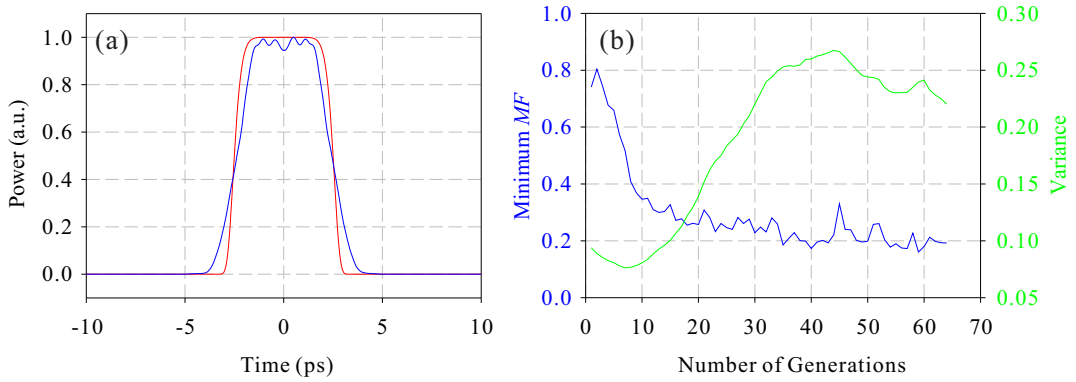

Figure 6.15: Simulation results of an active similariton laser incorporated with adaptive pulse shaping system targeting for a 5ps fifth-order super-Gaussian pulse. (a) Comparison between the temporal shapes of generated pulse and target pulse. Red trace: target fifth-order super-Gaussian pulse with a FWHM of 5ps; blue trace: generated pulse. (b) Evolution of Minimum MF value and variance for each generation in CMA-ES.

in both of these cases. Therefore, the intra-cavity adaptive pulse shaping system was able to change the characteristics of the generated waveform accordingly.

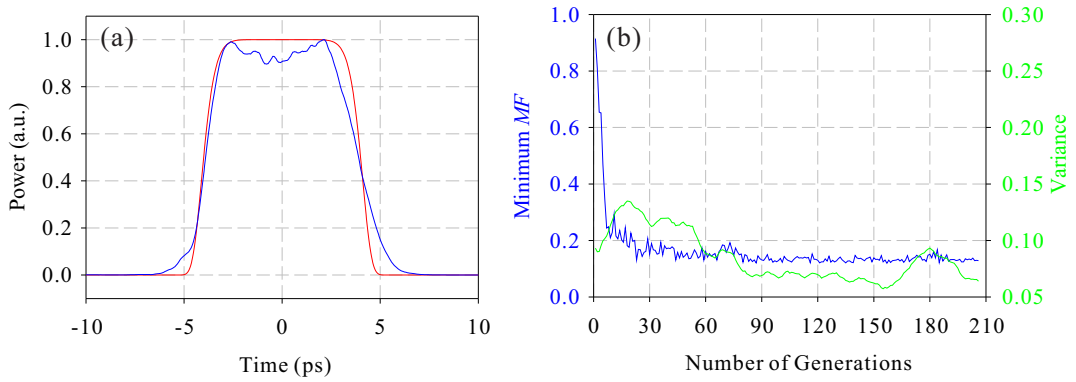

Figure 6.16: Simulation results of an active similariton laser incorporated with adaptive pulse shaping system targeting for a 8ps fifth-order super-Gaussian pulse. (a) Comparison between the temporal shapes of generated pulse and target pulse. Red trace: target fifth-order super-Gaussian pulse with a FWHM of 8ps; blue trace: generated pulse. (b) Evolution of Minimum MF value and variance for each generation in CMA-ES.

Then, the ability of the adaptive pulse shaping system was further tested by increasing the FWHM of the target shape. A fifth-order super-Gaussian pulse with a FWHM of 8ps was then in place as the target shape. The results presented in Figure 6.16 show good agreement between the two waveforms. Meanwhile, an improvement in the agreement between the generated waveform and the target shape was obtained (Figure 6.16b). The adaptive pulse shaping system once again exhibited its ability to alter the temporal waveform of the pulses generated in an active similariton laser.

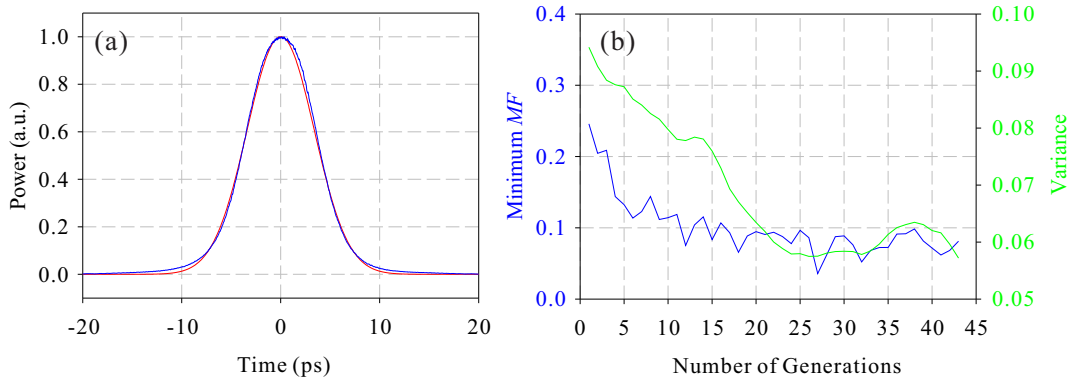

Figure 6.17: Simulation results of an active similariton laser incorporated with adaptive pulse shaping system targeting for a 8*ps* Gaussian pulse. (a) Comparison between the temporal shapes of generated pulse and target pulse. Red trace: target Gaussian pulse with a FWHM of 8*ps*; blue trace: generated pulse. (b) Evolution of Minimum MF value and variance for each generation in CMA-ES.

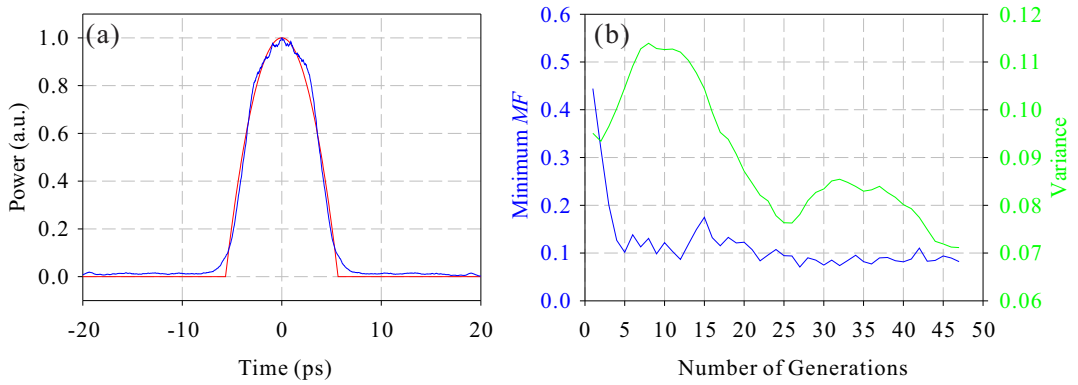

Figure 6.18: Simulation results of an active similariton laser incorporated with adaptive pulse shaping system targeting for a 8*ps* parabolic pulse. (a) Comparison between the temporal shapes of generated pulse and target pulse. Red trace: target parabolic pulse with a FWHM of 8*ps*; blue trace: generated pulse. (b) Evolution of Minimum MF value and variance for each generation in CMA-ES.

As the Gaussian profile is a widely used pulse shape and the parabolic profile is the nominal output from an active similariton laser, it is then interesting to wrap up the study here by setting a 8*ps* Gaussian pulse and a 8*ps* parabolic pulse as the target waveform for the laser. The results shown in Figures 6.17 and 6.18 indicate that both of these shapes can be generated. Through all these numerical attempts, the flexible control of the temporal waveform of the pulse generated from an active similariton laser was demonstrated.

6.5 Conclusion and Discussion

In this chapter, the theory of passively mode-locked EFRLs is thorougly reviewed in Section 6.2 and it is the foundation of the numerical simulations and the experimental work of this chapter and Chapter 7. Then, the flexible control over the temporal shape of the output of an EFRL through intra-cavity adaptive pulse shaping was investigated numerically. In an all-anomalous dispersion cavity, the intra-cavity spectral filtering has no influence on the temporal shape of the output pulses. Conversely, in an all-normal dispersion cavity, as the spectral filtering has strong impact, the temporal waveform of the generated pulses can be flexibly controlled. Through the search process of the adaptive pulse shaping system, the generation of super-Gaussian pulses up to the fifth order, Gaussian pulses and parabolic pulses was numerically simulated in such a cavity. In the next chapter, the implementation of an EFRL with normal-dispersion cavity is described, which was built to investigate the effect of intra-cavity spectral filtering.

Chapter 7

Dispersion-Managed Passively Mode-Locked Fibre Ring Laser

7.1 Introduction

In Chapter 6, the impact of adaptive pulse shaping on the temporal waveform of the output pulses from a passively mode-locked EFRL was studied using numerical simulations. In an all-anomalous dispersion cavity, soliton formation hinders effective shaping of the pulses using adaptive pulse shaping. Instead, in an all-normal dispersion cavity operated in the active similariton mode, flexible control over the characteristics of the output pulses through adaptive pulse shaping was demonstrated. The potential output waveforms range from the more traditional shapes of hyperbolic secant or parabolic to super-Gaussian profiles of different orders.

In this chapter, the influence of spectral filtering on a passively mode-locked EFRL will be investigated experimentally. A segment of (normal-dispersion) DCF is used in the ring cavity and a segment of EDF is the gain medium of the laser. Due to the SMF-pigtailed components used in the cavity, it is impossible to build an all-normal dispersion cavity. Instead, the implementation of a DM mode-locked EFRL is described in this chapter. As reviewed in Section 6.2.3.3, the original form and duration of the pulses circulating in the cavity are restored through the anomalous-dispersion fibre segment and the gain filtering effect in a DM laser. Although an additional spectral filtering is normally not included in the cavity of a DM laser for the purpose of pulse formation, it is still worth to investigate its impact on the characteristics of the laser output pulses. With a programmable pulse shaper included in the cavity, the laser response to different filter types of Gaussian, third-order super-Gaussian and sinc square function is demonstrated. On the other hand, the net dispersion of the laser cavity can be tuned by applying various amounts of dispersion on the pulse shaper. This consequently allows for the study of the laser performance with different amounts of net dispersion in the cavity. Both the

pulses before and after the pulse shaper are characterized in the experiment. The trends on how the pulse characteristics change with the filtering characteristics are summarized.

7.2 Laser Configuration

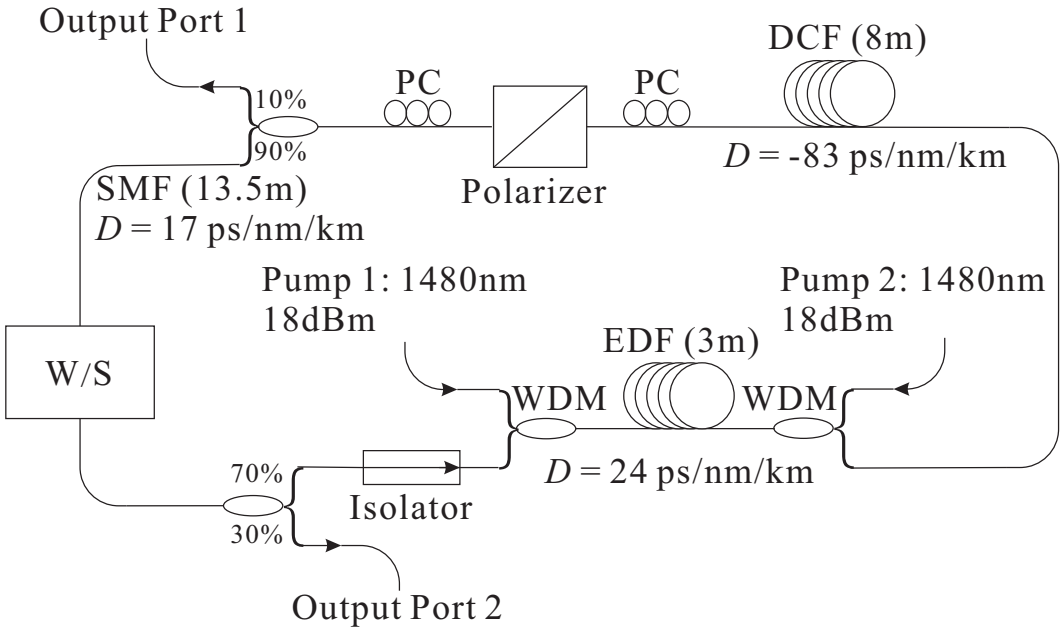

Figure 7.1: Schematic of a dispersion-managed passively mode-locked Er-doped fibre ring laser. W/S: Finisar Waveshaper. PC: Polarization Controller. DCF: Dispersion Compensating Fibre. EDF: Erbium-Doped Fibre. SMF: Single Mode Fibre. WDM: Wavelength Division Multiplexing.

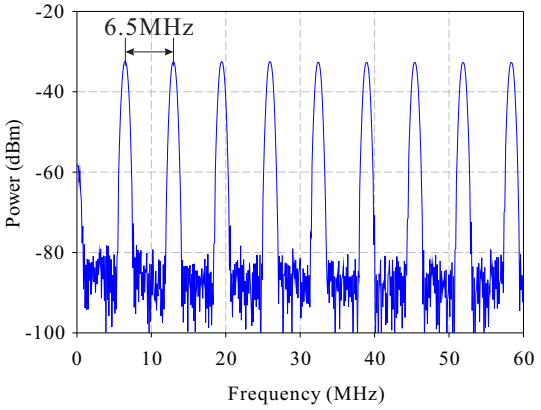

Figure 7.2: RF spectrum of the DM passively mode-locked EFRL.

Figure 7.1 shows the experimental setup of a DM passively mode-locked EFRL working at 1559nm. The mode-locking mechanism was NPR, facilitated through the inclusion of an $8m$ long DCF ($D = -83ps/nm/km$ and $\gamma = 7.2W^{-1}km^{-1}$) and a combination of two polarization controllers and a polariser. The polariser had an insertion loss of

$0.3dB$ and an extinction ratio of $67dB$. The EDF was $3m$ long ($D = 24ps/nm/km$ and $\gamma = 2.2W^{-1}km^{-1}$) and was pumped bi-directionally at $1480nm$ by two $18dBm$ pump lasers to ensure sufficient gain in the cavity. In this condition, the small signal gain of the EDF was $\sim 23dB$. Additional SMF sections ($D = 17ps/nm/km$ and $\gamma = 1.3W^{-1}km^{-1}$) associated with the various components of the laser cavity amounted to a length of $13.5m$. An isolator was used to ensure uni-directional propagation. A programmable phase and amplitude filter, the Finisar Waveshaper (W/S), was included right after the mode-locking mechanism. As shown in Figure 7.2, under mode-locking conditions, the laser operated at a repetition rate of $6.5MHz$. The laser pulses were observed at two points: the first was right after the normal-dispersion DCF segment, while the second was at the output of the W/S. Since the nonlinearity of the normal-dispersion DCF was high, the DM laser demonstrated here was working in the passive SS mode according to the review in Section 6.2.3.3.

The adaptive pulse shaping system was not included in the experimental configuration of Figure 7.1. This was due to some practical issues associated with the implementation of the laser. Firstly, an adaptive pulse shaping system required the laser to be self-adjusted once the transfer function was updated. This could not be guaranteed in all cases, since NPR was the mode-locking mechanism. Therefore, either the peak power or the state of polarisation would need to be continuously adjusted to ensure pulse operation. Secondly, the implementation of the feedback signal for the adaptive pulse shaping system was limited by the available devices. As the intention to employ adaptive pulse shaping in the system was to alter the temporal waveform of the output pulses, a spectral measurement using an OSA was not enough as the phase information was missing from such a measurement. The high speed OSO, which can be used to directly measure the short waveform, was not usable as it could not be synchronized to the $6.5MHz$ repetition rate. There was a linear FROG system available in the lab, but the measuring speed was low and its software package was too complicated to be included into the adaptive pulse shaping system. Also, my confidence on the capability of the FROG to reliably analyse shapes which varied substantially from conventional pulses was low. Finally, as a polarisation-dependent system, the laser system was prone to environmentally-induced random changes of birefringence. Therefore, it was not robust enough to support the time-consuming optimization process.

Although the adaptive pulse shaping was not implemented in the experiment due to the practical issues described above, the inclusion of the W/S was still the prominent feature of the cavity design. By taking advantage of the programming capability of the W/S, the characteristics of the output pulses could be manipulated through software control whilst keeping the laser configuration unchanged.

7.3 Laser Performance with Different Types of Filter Functions

The programmable filter placed inside the laser cavity allows for both amplitude and phase shaping of the optical pulses circulating in it. In this section, the influence of amplitude shaping on the characteristics of the pulses at the two output ports of the laser will be investigated when either a Gaussian or a third-order super-Gaussian transfer function is applied to the W/S. In the experiment, the pulses at the two output ports were characterized using an OSA (spectral measurement), an autocorrelator (indication of temporal width) and FROG (detailed temporal characteristics, including time-bandwidth product).

7.3.1 Gaussian Filters

In this section, I will first demonstrate the influence of Gaussian filters with different bandwidths on the characteristics of the output pulses of the laser. In the experiment, the Gaussian filters configured in the W/S were centred at $1559nm$. It was found that as long as the bandwidth (BW) remained in the range between $0.75nm$ and $9nm$, self-starting robust mode-locking of the laser could be observed.
Figure 7.3 shows the temporal characteristics of the pulses at output port 1. It can be seen from Figure 7.3a that with a narrower filter whose bandwidth is smaller than $5nm$, the FWHM of the autocorrelation trace of the pulses was around $6.5ps$. By further increasing the filter bandwidth to the upper limit of $9nm$, the FWHM of the autocorrelation traces increased from $6.3ps$ to $13.8ps$. The time-bandwidth product (TBP) of the pulses represented by the green line exhibited a similar trend as the FHWM of the autocorrelation traces. The maximum TBP of 9.3 was observed with a $9nm$ wide Gaussian filter and the minimum TBP of 2 occurred for a $0.75nm$ wide Gaussian filter. The high value of TBP indicates that the pulses at output port 1 were strongly chirped, which is due to their nonlinear propagation in a normal-dispersion fibre. In Figures 7.3b to 7.3d, the autocorrelation traces of the pulses generated with $0.75nm$, $4nm$ and $8nm$ filters are fitted to ideal shapes. It was found that the shape of the autocorrelation traces were closer to those of Gaussian pulses when the filter bandwidth was larger than $4nm$. For all the other filter bandwidths, the autocorrelation traces were more triangular-like.
Figure 7.4 summarizes the spectral properties of the pulses at output port 1. Figure 7.4a shows that the $3dB$ bandwidth of the spectrum of the pulses generally increased as the filter bandwidth increased from $0.75nm$ to $5nm$. Then, it decreased while the filter bandwidth was further increased to $9nm$. It is worth noting that all the spectra shown in Figure 7.4b had a flat top with fluctuations less than $1dB$.

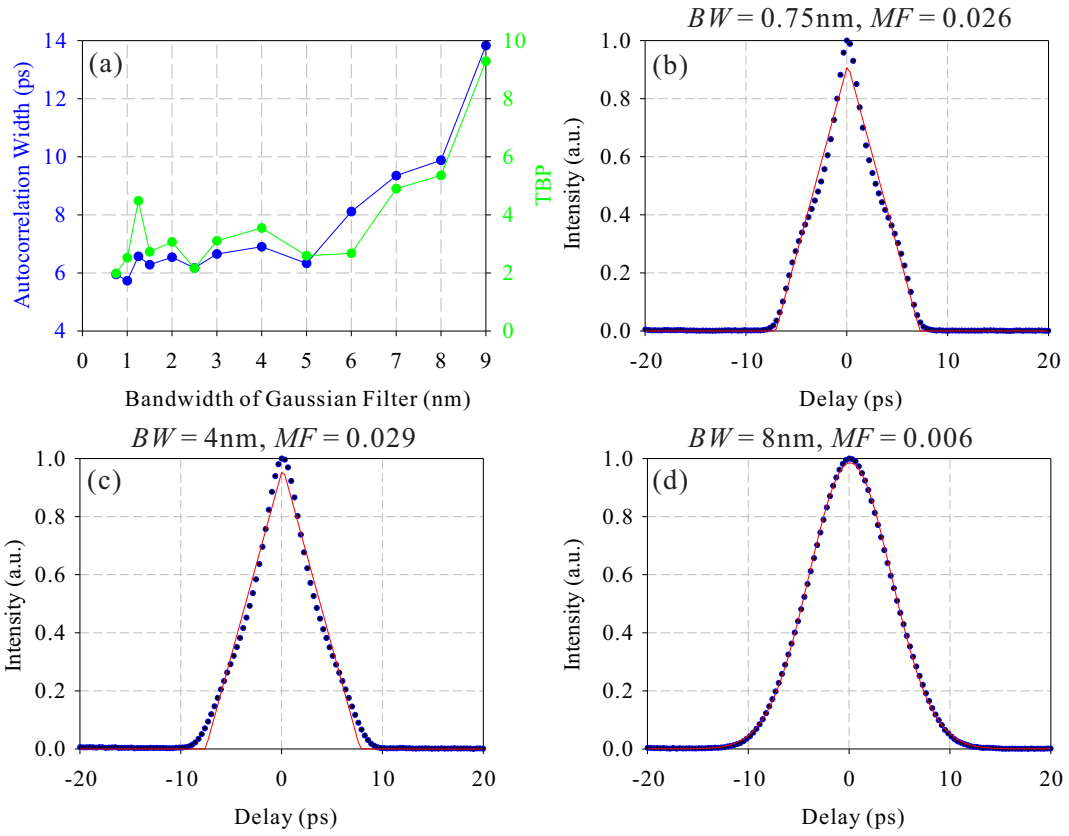

Figure 7.3: (a) Autocorrelation trace width (blue) and TBP (green) of the pulses at output port 1 vs bandwidth of the Gaussian filter. Autocorrelation traces measured at output 1 (blue dots) and its corresponding fitting (red solid line) for (b) $BW = 0.75nm$; (c) $BW = 4nm$; and (d) $BW = 8nm$.

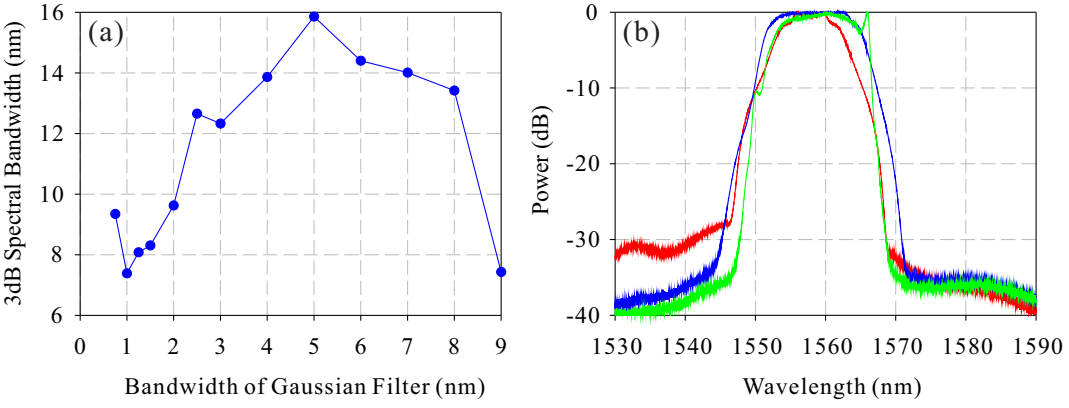

Figure 7.4: (a) $3dB$ spectral bandwidths of the pulses at output port 1 vs bandwidth of the Gaussian filter. (b) Spectra measured at output 1 for different bandwidths of the Gaussian filter. Red trace: $0.75nm$; Blue trace: $4nm$; Green trace: $8nm$.

Since the pulses were strongly and linearly chirped after propagation in the $8m$ long normal-dispersion DCF, it is reasonable to assume that the shape of the spectra could

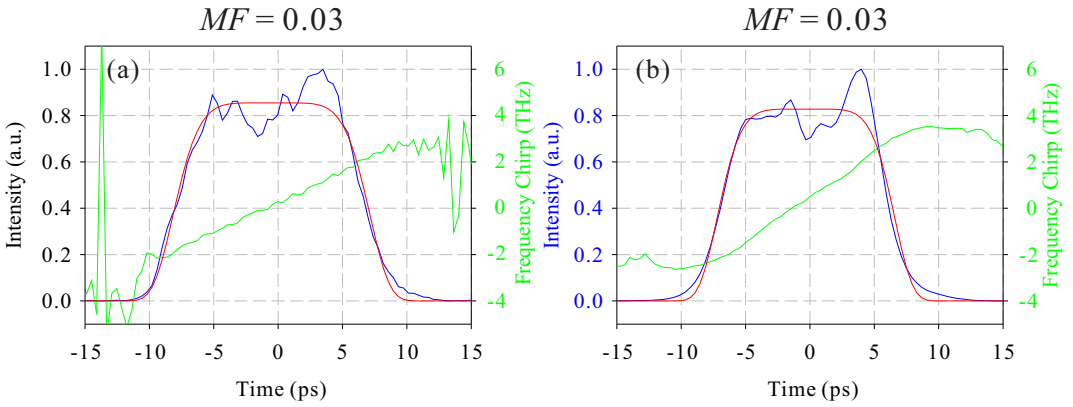

Figure 7.5: Pulse shape (blue solid line) and frequency chirp (green dashed line) of the pulses at output port 1 generated with (a) $4nm$ and (b) $5nm$ Gaussian filter. The red solid line represents the fitting of pulse shape to a super-Gaussian ($m = 3$) shape.

be transferred to the temporal domain. In other words, these pulses had the possibility to acquire a square temporal shape. FROG was then used to measure the pulses at output port 1. The temporal waveform and the frequency chirp of the pulses generated with (a) 4nm and (b) 5nm Gaussian filter are plotted in Figure 7.5. By fitting the waveform traces to a third-order super-Gaussian shape, these measurements confirmed that the pulses were close to super-Gaussian pulses and linearly chirped.

Taking the case of $4nm$ Gaussian filter as an example, the laser was then numerically studied to understand its operation and behaviour, especially the origin of the third-order super-Gaussian pulse shapes obtained at output port 1. As reviewed in Section 6.2.3.3, the pulses at output port 1 normally acquire the temporal shape of a parabolic function due to the self-similar propagation in the DCF. The length of the DCF (L_{DCF}) and the small signal gain of the EDF (g_0) were varied in the numerical simulations as they are crucial factors for the self-similar propagation in the laser. $L_{DCF} = 8m$ and $g_0 = 23dBm$ were the experimental parameters. In the simulation, the pulse shapes obtained at output port 1 were fitted to both third-order super-Gaussian and parabolic functions. Then the values of the MF of the fittings under various conditions were plotted in Figure 7.6. Figure 7.6a shows the comparison of the fitting when L_{DCF} was in the range between $6m$ and $12m$ with $g_0 = 23dBm$. It was found that the laser started to generate parabolic pulses only when L_{DCF} was larger than $8.5m$. This indicates that the $8m$ long DCF used in the experiment was not long enough to allow the pulses fully evolve into the similariton asymptotic solution. Figures 7.6b and 7.6c present the comparison of the fittings when g_0 was in the range between $18dB$ and $28dB$ and L_{DCF} was either $8m$ or $11m$. Through these two figures, the influence of g_0 on the generation of parabolic pulses in the laser can be investigated. It can seen from Figure 7.6b that the parabolic pulse cannot be generated in the laser by increasing g_0 when L_{DCF} was $8m$. Conversely, Figure 7.6c shows that, when L_{DCF} was $11m$, the parabolic pulses can always be generated even when g_0 was as low as $18dBm$. These findings from numerical

simulations imply that the length of the DCF was the key factor for the generation of parabolic pulses with temporal waveforms closer to third-order super-Gaussian function in my laser.

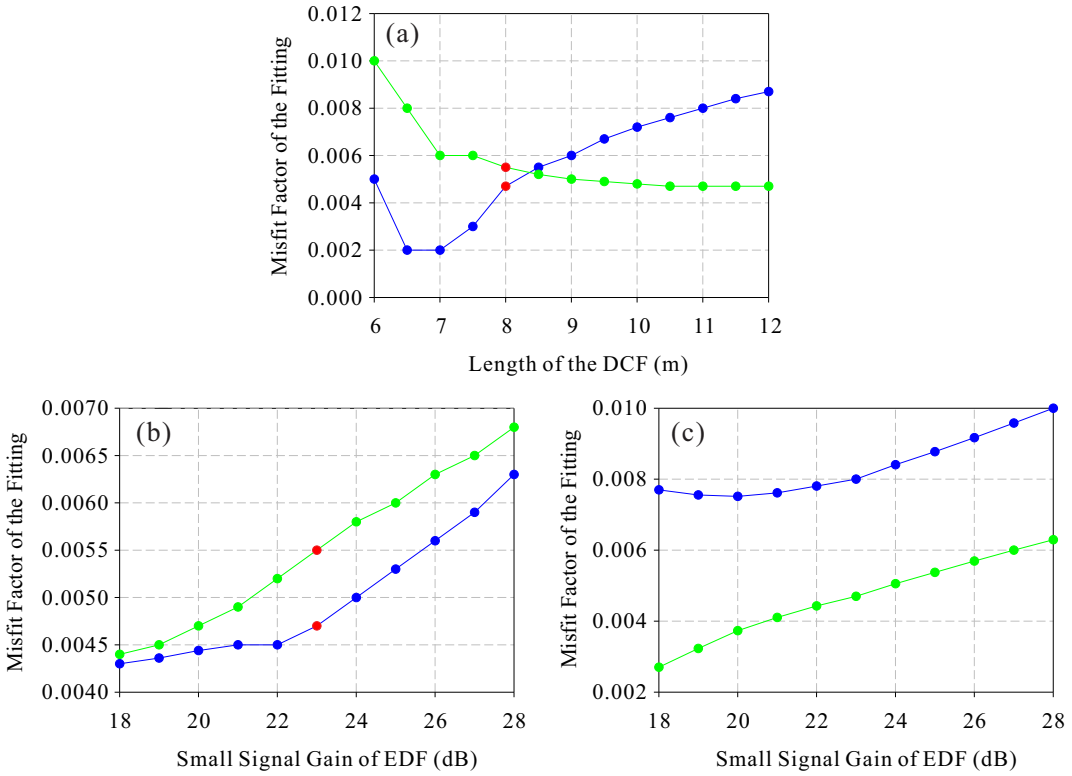

Figure 7.6: MF of the fitting of the pulse shapes at output port 1 to third-order super-Gaussian (blue) and parabolic (green) functions obtained from numerical simulations. (a) MF vs L_{DCF} with $g_0 = 23dBm$. MF vs g_0 in the conditions of (b) $L_{DCF} = 8m$ and (c) $L_{DCF} = 11m$. The red dots represent the experimental parameters of $L_{DCF} = 8m$ and $g_0 = 23dBm$.

Figure 7.7 shows the temporal properties of the pulses at output port 2. As shown in Figure 7.7a, both the FWHM of the autocorrelation trace and the TBP of the pulses exhibited an increasing trend with a increasing filter bandwidth. When the filter bandwidth was smaller than $2nm$, the values of the TBP of the pulses were close to 0.31, which is the value of a transform-limited hyperbolic secant pulse. The pulses became chirped again when the filter bandwidth went beyond $2nm$. This means that with a narrow filter, a relatively small amount of frequency components were allowed to pass through the filter and the spectral phases of those frequency components were similar to each other. As a result, chirp-free pulses were generated. On the other hand, when more frequency components were released due to a broader filter bandwidth, the chirp on the pulses gradually became more significant. Since the pulses at output port 2 acquired with the $9nm$ wide Gaussian filter were significantly broader than the other cases, the peak power of these pulses was low. Hence, they induced less nonlinearity in the DCF

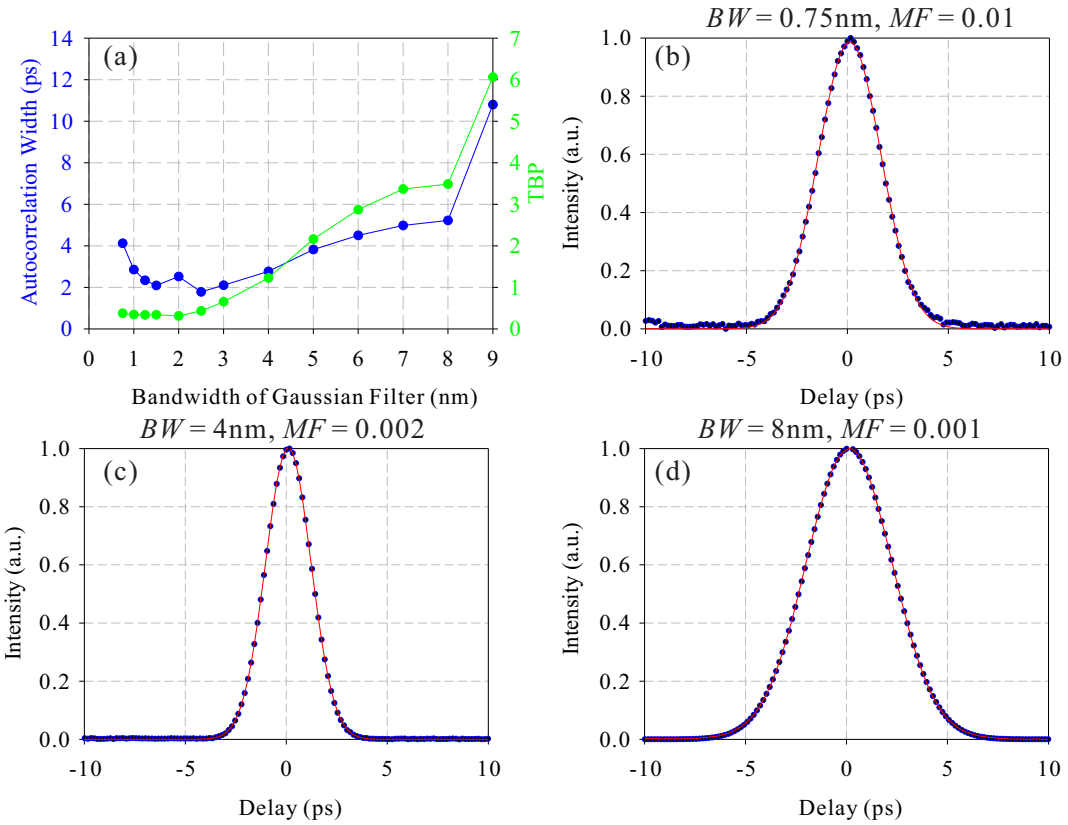

Figure 7.7: (a) Autocorrelation trace width (blue) and TBP (green) of the pulses at output port 2 vs bandwidth of the Gaussian filter. Autocorrelation traces measured at output 2 (blue dots) and its corresponding fitting (red solid line) for (b) $BW = 0.75nm$; (c) $BW = 4nm$; and (d) $BW = 8nm$.

and consequently led to a much narrower spectrum as indicated in Figure 7.4a. The autocorrelation traces and their fittings presented in Figures 7.7b - 7.7d show that they were closer to the Gaussian shape.

With more accurate FROG measurements at output port 2, some other features of the pulses are revealed. Figures 7.8 and 7.9 show (a) the FROG retrieved temporal characteristics of the pulses and (b) their fitting to either a Gaussian function or (c) a hyperbolic secant function with a $3nm$ and $4nm$ Gaussian filter, respectively. By comparing the fitting results of these pulses, it is found that the pulses generated with a $3nm$ Gaussian filter had a temporal shape of hyperbolic secant function. Instead, the pulses generated with a $4nm$ Gaussian filter possessed Gaussian shape. The filter bandwidth of $4nm$ was the critical point for the change in the pulse shape of the generated pulses. The spectral properties of the pulses at output port 2 are presented in Figure 7.10. It is shown that the spectral bandwidth of the pulses increased according to the filter bandwidth until a turning point was reached at around $8nm$. A sudden decrease in the bandwidth was observed beyond that point. This was due to the much narrower spectrum of the pulses at output port 1 when the $9nm$ wide Gaussian filter was in place. As shown in Figure 7.10b, in all cases, and especially those of a narrower filter bandwidth, the spectrum of the pulses followed closely the Gaussian shape of the filter.

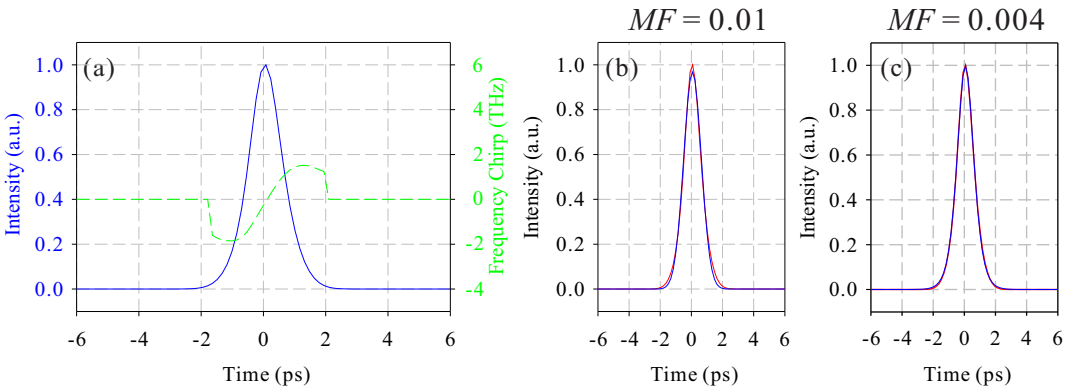

Figure 7.8: (a) Pulse shape (blue solid line) and frequency chirp (green dashed line) of the pulses at output port 2 generated with a $3nm$ Gaussian filter. (b) Gaussian fitting of the pulses. (c) Hyperbolic secant fitting of the pulses.

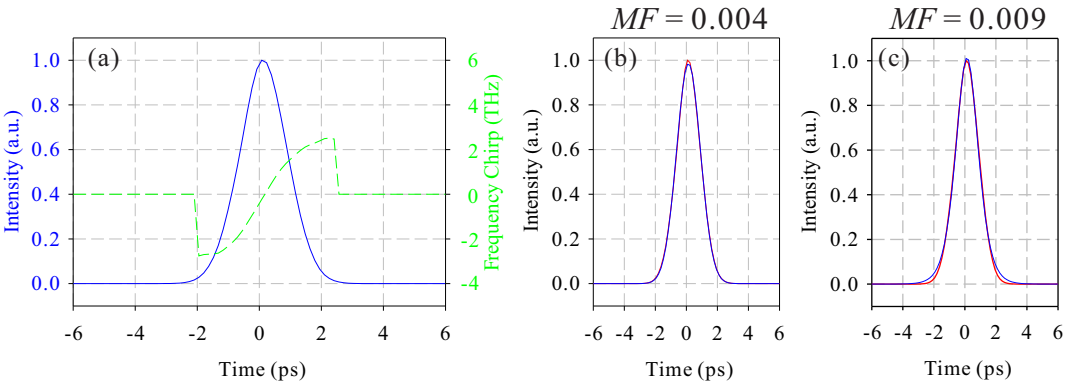

Figure 7.9: (a) Pulse shape (blue solid line) and frequency chirp (green dashed line) of the pulses at output port 2 generated with a $4nm$ Gaussian filter. (b) Gaussian fitting of the pulses. (c) Hyperbolic secant fitting of the pulses.

7.3.2 Third-Order Super-Gaussian Filters

Thanks to the ability of reconfiguration of the W/S, the impact of the third-order super-Gaussian filters on the generated pulse characteristics is probed in this section. As in the case described in the previous section, the third-order super-Gaussian filters were centred at $1559nm$. Robust mode-locking with third-order super-Gaussian filter shapes could be achieved when the filter bandwidth ranged between $0.5nm$ and $2.5nm$; this is clearly a much narrower range than in the previous case of Gaussian filters.

Figure 7.11 shows the temporal characteristics of the pulses at output port 1. It can be

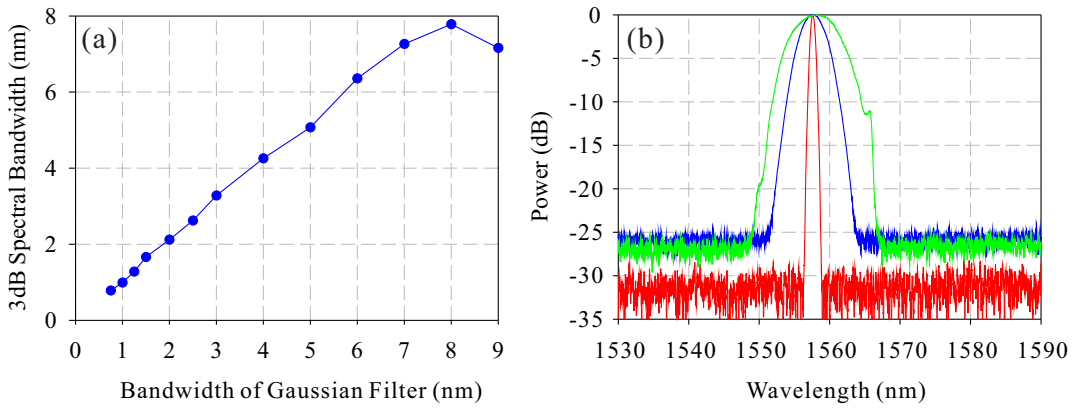

Figure 7.10: (a) $3dB$ spectral bandwidths of the pulses at output port 2 vs bandwidth of the Gaussian filter. (b) Spectra measured at output 2 for different bandwidths of the Gaussian filter. Red trace: $0.75nm$; Blue trace: $4nm$; Green trace: $8nm$.

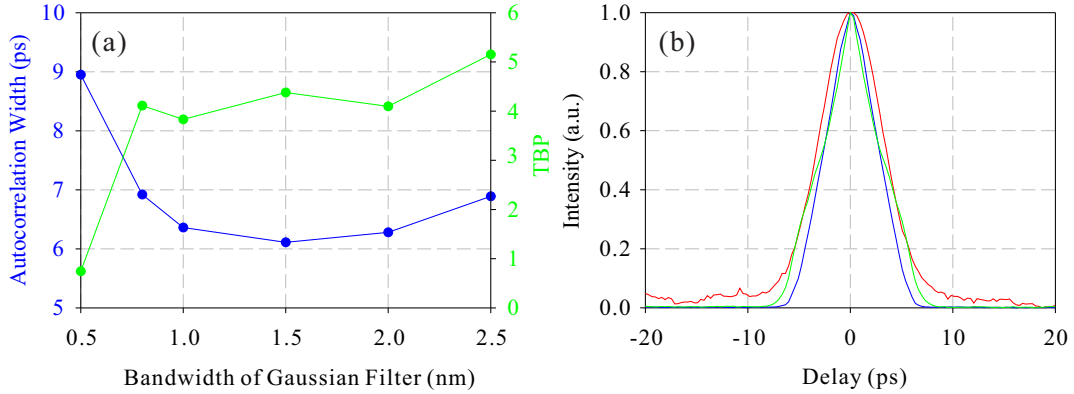

Figure 7.11: (a) Autocorrelation trace width (blue) and TBP (green) of the pulses at output port 1 vs bandwidth of the third-order super-Gaussian filter. (b) Autocorrelation traces measured at output 1 before the W/S for different bandwidths of the third-order super-Gaussian filter. Red trace: $0.5nm$; Blue trace: $1.5nm$; Green trace: $2.5nm$.

seen from the blue trace in Figure 7.11a that the FWHM of the autocorrelation trace of the pulse initially decreased as the filter bandwidth increased. This trend changed at filter bandwidths beyond $1.5nm$. This can also be observed from the autocorrelation traces plotted in Figure 7.11b. Apart from the autocorrelation trace of the pulse generated with the $0.5nm$ third-order super-Gaussian filter represented by the red trace, the other traces exhibited a similar width and a shape close to triangular. This indicates that the laser produced close to rectangular pulses (most probably of a super-Gaussian shape, following their spectral shape) once the filter bandwidth exceeded $0.8nm$. From the TBP of the pulses represented by the green trace in Figure 7.11b, the pulses generated with the $0.5nm$ wide filter had a TBP of 0.31, which was close to the value of the transform-limited hyperbolic secant pulses. With all the other filter bandwidths, the TBP of the pulses was between 3 and 6, implying that the pulses were strongly chirped in the DCF.

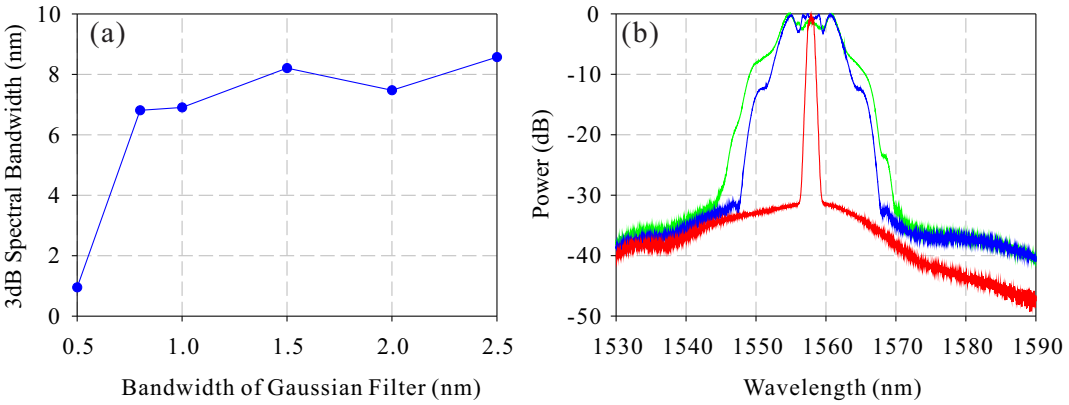

Figure 7.12: (a) $3dB$ spectral bandwidths of the pulses at output port 1 vs bandwidth of the third-order super-Gaussian filter. (b) Spectra measured at output 1 before the W/S for different bandwidths of the third-order super-Gaussian filter. Red trace: $0.5nm$; Blue trace: $1.5nm$; Green trace: $2.5nm$.

The spectral characteristics of the pulses at output port 1 are summarized in Figure 7.12. As plotted in Figure 7.12a, the $3dB$ bandwidth of the pulses shows itself an increasing trend as the filter bandwidth increased. A rapid increase was once more observed when the filter bandwidth increased from $0.5nm$ to $0.8nm$. When the filter bandwidth was larger than $0.8nm$, the bandwidth of the pulses varied slowly. The spectra depicted in Figure 7.12b show that the spectra exhibited the fluctuations less than $2dB$ on the top except the considerably narrow spectrum of the pulse generated while the $0.5nm$ wide filter was in place.

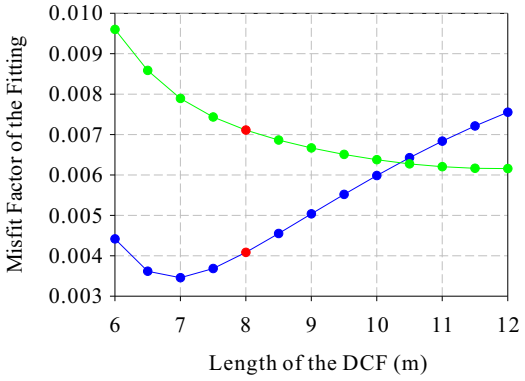

Figure 7.13: MF of the fitting of the pulse shapes at output port 1 to third-order super-Gaussian (blue) and parabolic (green) functions obtained from numerical simulations. MF vs L_{DCF} with $g_0 = 23dBm$. The red dots represent the experimental parameters of $L_{DCF} = 8m$ and $g_0 = 23dBm$.

The temporal and spectral characteristics of the pulses at output port 1 described above shows that the behaviour of the laser when the third-order super-Gaussian filter was applied to in the cavity was similar to the previous described case of Gaussian filters.

The numerical simulation procedure described previously was applied to the case of $1.5nm$ third-order super-Gaussian filter. Figure 7.13 shows that the minimum length of DCF for the laser to generate parabolic pulses was $10.5m$. Thus, similar to the case of Gaussian filters, the origin of the generation of pulses with a shape closer to third-order super-Gaussian function was that the normal-dispersion DCF was not long enough to allow a similariton asymptotic solution to fully develop.

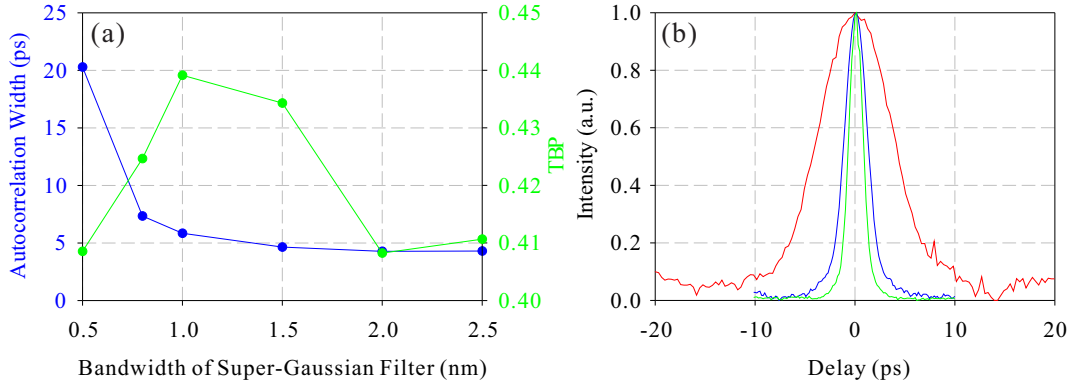

Figure 7.14: (a) Autocorrelation trace width (blue) and TBP (green) of the pulses at output port 2 vs bandwidth of the third-order super-Gaussian filter. (b) Autocorrelation traces measured at output 2 after the W/S for different bandwidths of the third-order super-Gaussian filter. Red trace: $0.5nm$; Blue trace: $1.5nm$; Green trace: $2.5nm$.

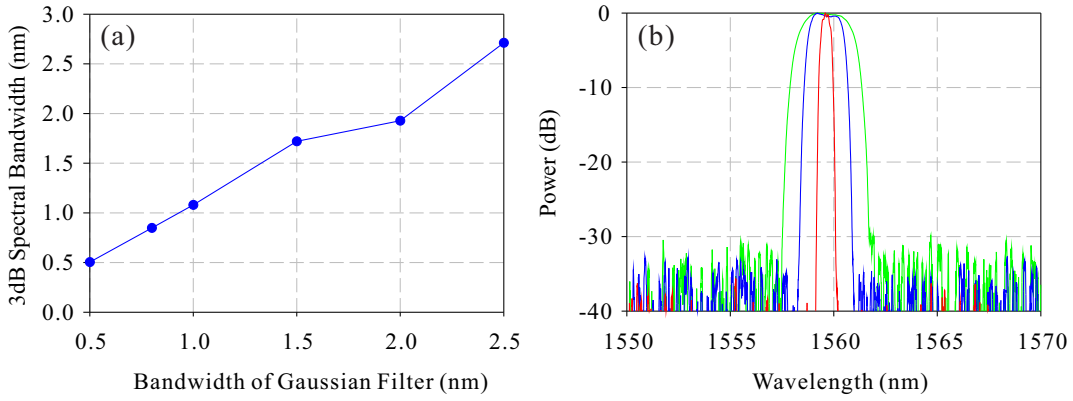

Figure 7.15: (a) $3dB$ spectral bandwidths of the pulses at output port 2 vs bandwidth of the third-order super-Gaussian filter. (b) Spectra measured at output 2 after the W/S for different bandwidths of the third-order super-Gaussian filter. Red trace: $0.5nm$; Blue trace: $1.5nm$; Green trace: $2.5nm$.

The temporal characteristics of the pulses at output port 2 are presented in Figure 7.14. The FWHM of the autocorrelation traces of the pulses represented by the blue trace in Figure 7.14a monotonically decreased with the filter bandwidth. This can also be observed from the autocorrelation traces plotted in Figure 7.14b. From the TBP represented by the green trace in Figure 7.14b, the TBP of the pulses showed small variations

around a value of 0.44, which is close to the value of transform-limited Gaussian pulses. Hence, the temporal width of the pulses at output port 2 can be accurately controlled by adjusting the filter bandwidth.
The spectral characteristics of the pulses at output port 2 are shown in Figure 7.15. Figure 7.15a presents that the $3dB$ bandwidth of the pulses took on a monotonical increasing as the filter bandwidth was increased. The spectra presented in Figure 7.15b followed closely the third-order super-Gaussian shape of the filter. This again indicated that the spectra of the pulses at output port 1 exhibited a flat central region.

7.3.3 Conclusion

In summary, the laser performance with amplitude shaping incorporated in the laser cavity was explored using both Gaussian and third-order super-Gaussian filter transfer characteristics. Under the mode-locking condition, at output port 1, a linearly chirped pulse with a temporal shape close to a super-Gaussian function and a flat-top spectrum can be generated from the laser. This is due to that the DCF in the cavity was not long enough to allow the pulses fully evolving into the similariton asymptotic solution. At output port 2, which was right after the W/S, nearly transform-limited pulses can be achieved if the filter bandwidth is narrow. The pulses become broader and chirped when the filter bandwidth is broad. The pulse characteristics can be controlled by adjusting the filter bandwidth. In the next section, I investigate the impact of spectral phase shaping on the laser performance.

7.4 Laser Performance Incorporating Dispersion Management

As reviewed in Section 6.2.3, dispersion management is essential to a laser cavity design, since it critically determines the pulse formation mechanism and consequently affects the characteristics of the pulses generated in the cavity. In the past, flexible control of intra-cavity dispersion could be achieved through the inclusion of grating pairs, prisms or simply physical changing the length of the fibre in the cavity [152, 153]. All these techniques however, require manual tuning of some physical parameters of the cavity. Relying on the phase shaping capability of the W/S, the net dispersion (ND) of the ring cavity could be manipulated purely through software control without any adjustment of the pump power or the layout of the laser cavity.
Since the GVD is the slope of the group delay with respect to the wavelength and the group delay is the first-order derivative of the spectral phase with respect to the angular frequency, control of the ND through the W/S was realized by applying different

parabolic phase profiles on the transfer function. In the experiment, the W/S was programmed to be a $4nm$ wide Gaussian filter centred at $1559nm$. Various parabolic phase profiles according to a range of dispersion values were then added to the transfer function of the W/S.

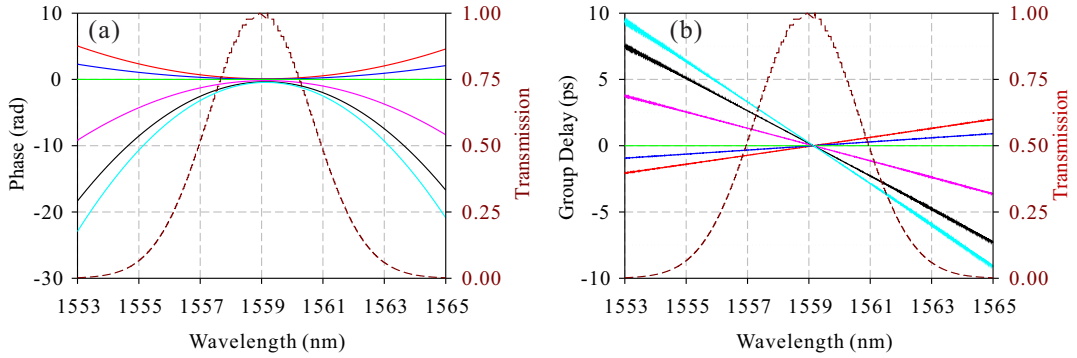

Figure 7.16: Transmission of the W/S and (a) the parabolic spectral phase profiles as well as (b) the group delay profiles corresponding to the dispersions applied into the W/S. Red trace: $\alpha = -0.55$; Blue trace: $\alpha = -0.25$; Green trace: $\alpha = 0$; Pink trace: $\alpha = 1$; Black trace: $\alpha = 2$; Cyan trace: $\alpha = 2.5$.

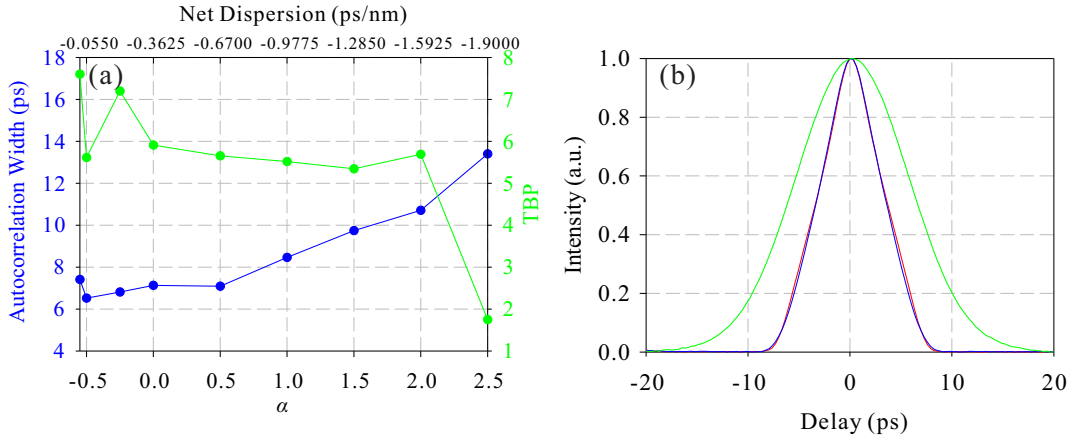

Figure 7.17: (a) Autocorrelation trace width (blue) and TBP (green) of the pulses at output port 1 vs different dispersion values. (b) Autocorrelation traces measured at output port 1 for different dispersion values. Red trace: $\alpha = -0.55$; Blue trace: $\alpha = 0$; Green trace: $\alpha = 2.5$.

When there was no phase shaping applied on the W/S, the cavity had an estimated ND of $\sim -0.363ps/nm$. In the experiment, the W/S was programmed to introduce a range of GVD values into the cavity. They can be expressed as αD_0, where $D_0 = -0.615ps/nm$ corresponding to the chirp on the pulses at output port 1 when no phase shaping was applied on the W/S and α was a scaling factor of the dispersion. Hence, the ND of the cavity could be calculated according to $-0.363 - 0.615\alpha$. The corresponding the group delay profiles and parabolic spectral phase profiles are shown in Figures

7.16a and 7.16b, respectively. In the experiment, it was found that robust mode-locking could be achieved as long as the value of α remained in the range -0.55 to 2.5 ($ND = -0.024ps/nm \sim -1.900ps/nm$).

The temporal characteristics of the pulses at output port 1 are summarized in Figure 7.17. Figure 7.17a shows that the FWHM of the autocorrelation traces of the pulses increased as the absolute value of ND increased. Coversly, the TBP of the pulses decreased. Figure 7.17b presents that when $\alpha < 0$, the autocorrelation traces acquired a triangular shape. In the other direction, the autocorrelation traces were closer to a Gaussian function.

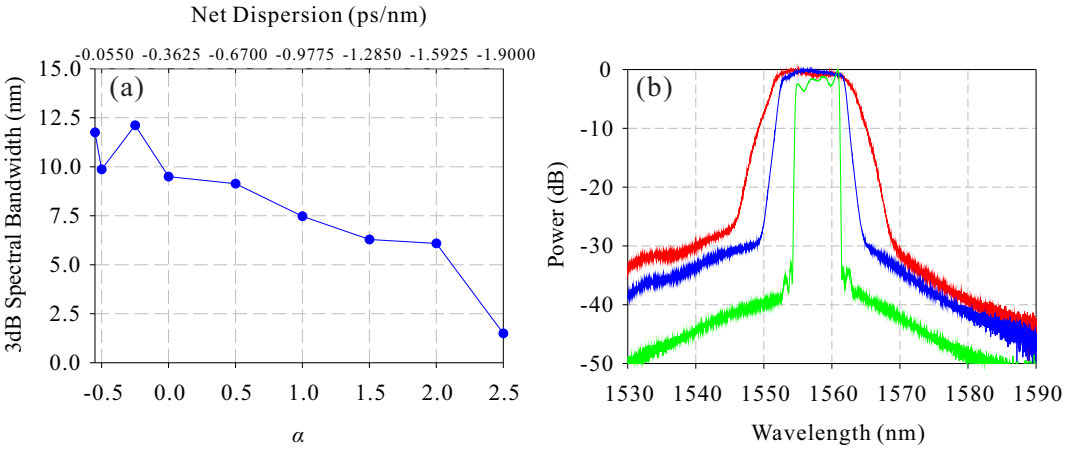

Figure 7.18: (a) $3dB$ spectral bandwidths of the pulses at output port 1 vs different dispersion values. (b) Spectra measured at output port 1 for different dispersion values. Red trace: $\alpha = -0.55$; Blue trace: $\alpha = 0$; Green trace: $\alpha = 2.5$.

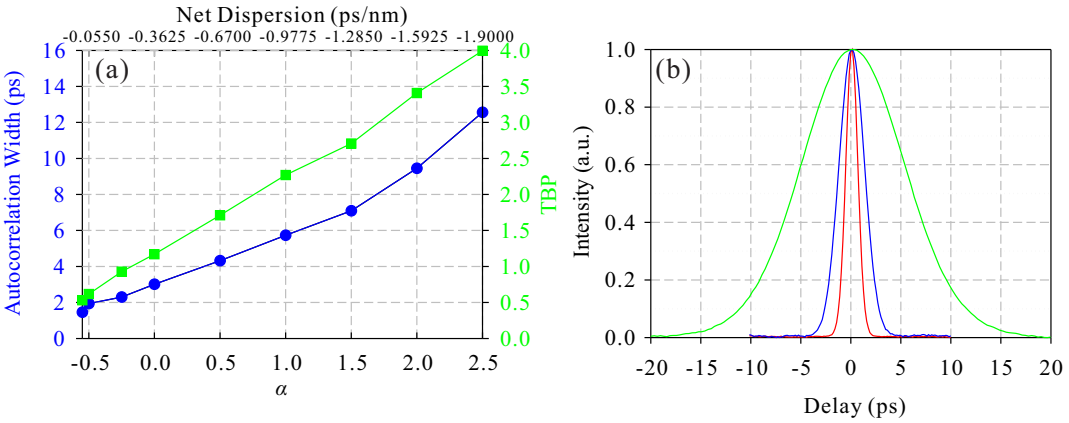

Figure 7.19: (a) Autocorrelation trace width (blue) and TBP (green) of the pulses at output port 2 vs different dispersion values. (b) Autocorrelation traces measured at output port 2 for different dispersion values. Red trace: $\alpha = -0.55$; Blue trace: $\alpha = 0$; Green trace: $\alpha = 2.5$.

Figure 7.18 presents the spectral characteristics of the pulses at output port 1. It was

found that the $3dB$ bandwidth decreased as the absolute value of ND increased. The spectra plotted in Figure 7.18b confirm this trend. This indicates that less nonlinearity was stimulated when the absolute value of the ND of the cavity was large.

From the temporal and spectral characteristics of the pulses at output port 1 summarized above, it is evident the manipulation of ND has a significant impact on the laser performance. When the ND of the laser cavity was tuned to be more normal, the pulses were less chirped. The generation of pulses with a flat-top spectrum required the ND of the cavity to be adjusted towards the zero dispersion.

The temporal characteristics of the pulses at output port 2 are presented in Figure 7.19. The FWHM of the autocorrelation traces of the pulses increased with the absolute value of ND. The TBP of the pulses exhibited an almost linear increase with the absolute value of ND. This can also be seen from the autocorrelation traces plotted in Figure 7.19b. Since the nonlinear propagation in the normal-dispersion DCF gave rise to positively chirped pulses, when some anomalous dispersion was applied on the W/S, the ND of the cavity was reduced and this resulted in shorter and less chirped pulses at the output of the filter. While propagating in the normal-dispersion DCF, pulses of a shorter width, hence a higher peak power, stimulated a larger nonlinear phase shift, in turn inducing a broader spectral bandwidth. This then explains the decreasing spectral bandwidth of the pulses at output port 1 when the absolute value of the ND of the cavity was increased.

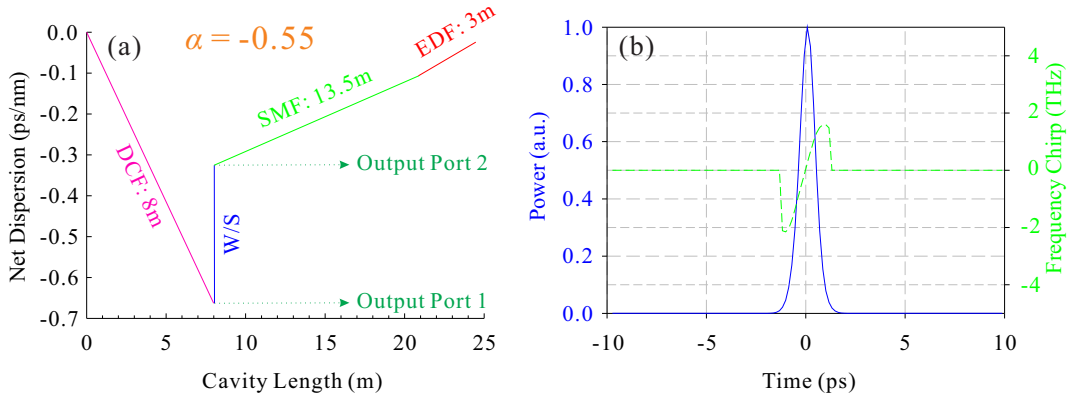

Figure 7.20: (a) Dispersion map of the cavity for $\alpha = -0.55$. (b) Pulse shape (blue solid line) and frequency chirp (green dashed line) of the pulses at output port 2.

The minimum TBP of 0.53 was observed for $\alpha = -0.55$, implying close to transform-limited pulses. The dispersion map of the cavity for this case is shown in Figure 7.20a. The W/S was programmed to provide anomalous dispersion. Thus, the net dispersion in the cavity was close to zero. Subsequently, a short and less chirped pulse with a duration of $\sim 1ps$, as shown in Figure 7.20b, was generated at output port 2 of the laser. The maximum TBP of 4 was observed for $\alpha = 2.5$, implying strongly chirped pulses. Figure 7.21a presents the dispersion map of the cavity for this case. The effect of the

spectral phase shaping programmed in the W/S was equivalent to adding a normal dispersion. Hence, the ND of the cavity was tuned to be more normal and generated a broader chirped pulse with a duration of $\sim 8.6ps$ (as shown in Figure 7.21b) at output port 2 of the laser. Numerical simulations show that this pulse can be further compressed to a transform-limited pulse with a duration of $\sim 1ps$ using $180m$ of SMF outside the cavity (Figure 7.21c).

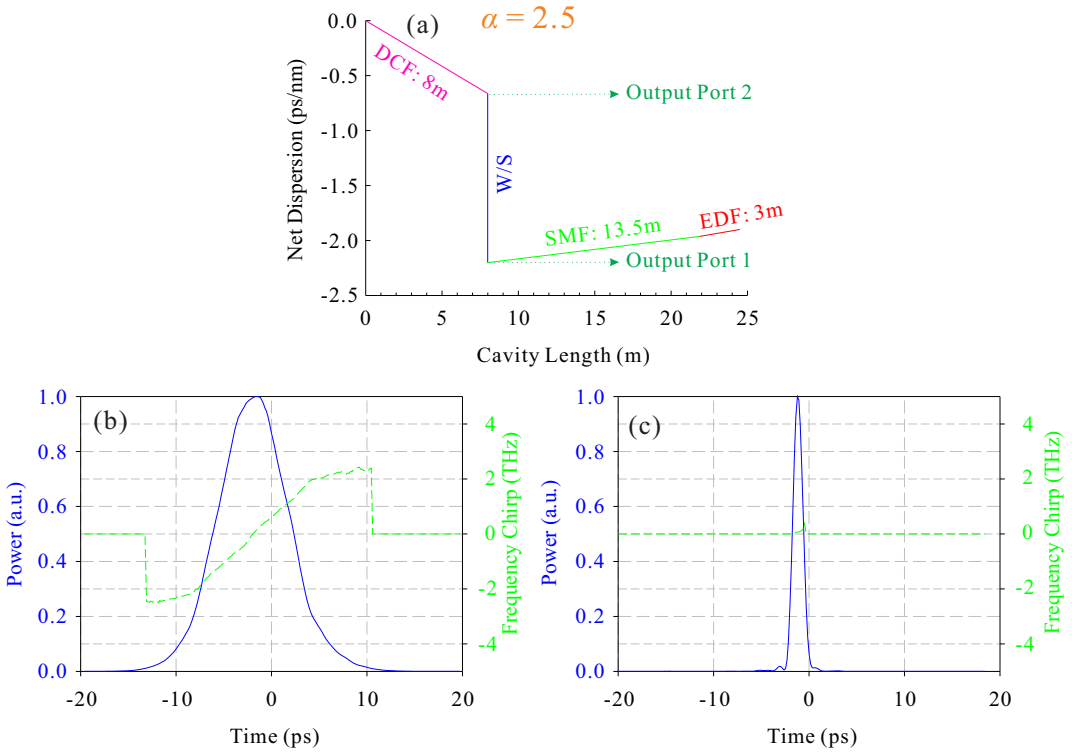

Figure 7.21: (a) Dispersion map of the cavity for $\alpha = 2.5$. (b) Pulse shape (blue solid line) and frequency chirp (green dashed line) of the pulses at output port 2. (c) Numerical calculated pulse shape (blue solid line) and frequency chirp (green dashed line) of the compressed pulse using a $180m$ long SMF.

Figure 7.22 presents the spectral characteristics of the pulses at output port 2. It can be seen that the spectral bandwidth of the pulses decreased as the absolute value of ND increased. This trend was identical to that of the pulses at output port 1. This was due to the fact that the filter bandwidth was kept constant at $4nm$ in the experiment.

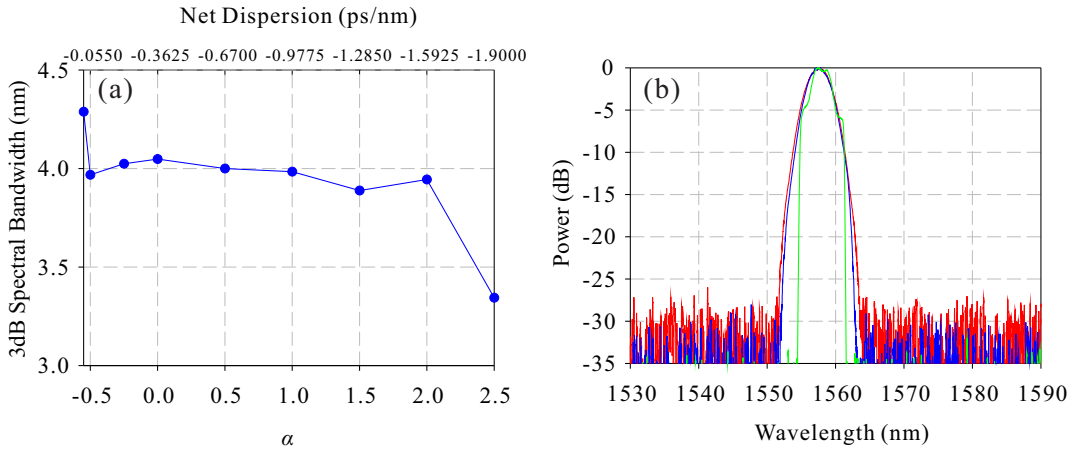

Figure 7.22: (a) $3dB$ spectral bandwidths of the pulses at output port 2 vs different dispersion values. (b) Spectra measured at output port 2 for different dispersion values. Red trace: $\alpha = -0.55$; Blue trace: $\alpha = 0$; Green trace: $\alpha = 2.5$.

7.5 Laser Performance with Sinc Square Filter

The generation of a flat-top spectrum was the common feature of the laser with different intra-cavity filtering characteristics described in the previous sections. Based on this observation, it is reasonable to expect the generation of rectangular pulses at output port 2 of the laser if the sinc square function is applied into the W/S. In this section, the impact of a sinc square filter function on the characteristics at output port 2 of the laser is investigated.

Although there are several pairs of sidelobes on a sinc square function, the $3dB$ bandwidth of the main lobe was used to represent the filter bandwidth as the first order sidelobe is already around $15dB$ down from the main lobe. In the experiment, it was found that as long as the filter bandwidth was in the range between $2nm$ and $6nm$, robust mode-locking of the laser could be achieved. A FROG measurement was used to obtain the characteristics of the pulses at output port 2.

Figures 7.23 to 7.25 show the pulse characteristics at output port 2 when a $6nm$, $5nm$ and $4nm$ wide sinc square filter was in place, respectively. As shown in Figures 7.23b to 7.25b, the common point for all these cases was that only the first-order sidelobe of the sinc square function could be genereted by the laser and the central lobe was well matched with the function. Unfortunately, this was not enough to obtain the rectangular pulses. The FROG traces shown in Figures 7.23a to 7.25a confirm that there were no rectangular pulses generated in the laser cavity.

Figures 7.26 and 7.27 present the characteristics of the pulses at output 2 when $3nm$ and $2nm$ wide sinc square function was applied on the W/S, respectively. From the spectra of the pulses plotted in Figures 7.26b and 7.27b, up to third- and fourth-order sidelobes were generated in the laser. But the discrepancy between the spectrum and sinc square function became larger as the order of sidelobe increased. Although the number

of sidelobes was enough to achieve the rectangular shape in the temporal domain, the spectrum did not fully agree with the sinc square function. As a result, the pulses could not acquire the rectangular shape in the temporal domain as shown in Figures 7.26a and 7.27a.

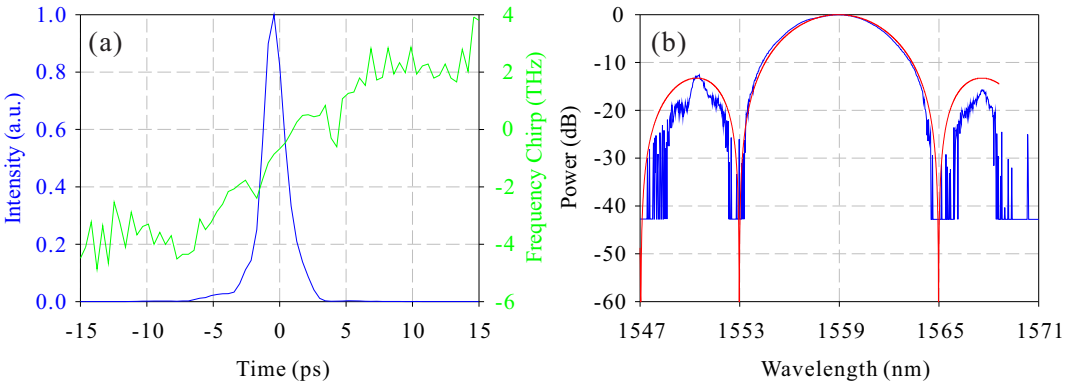

Figure 7.23: (a) Pulse shape (blue line) and frequency chirp (green line) of the pulses at the output of the W/S generated with a 6nm wide sinc square filter. (b) Comparison between the spectrum of the pulses (blue line) and the amplitude shaping function of the W/S (red line).

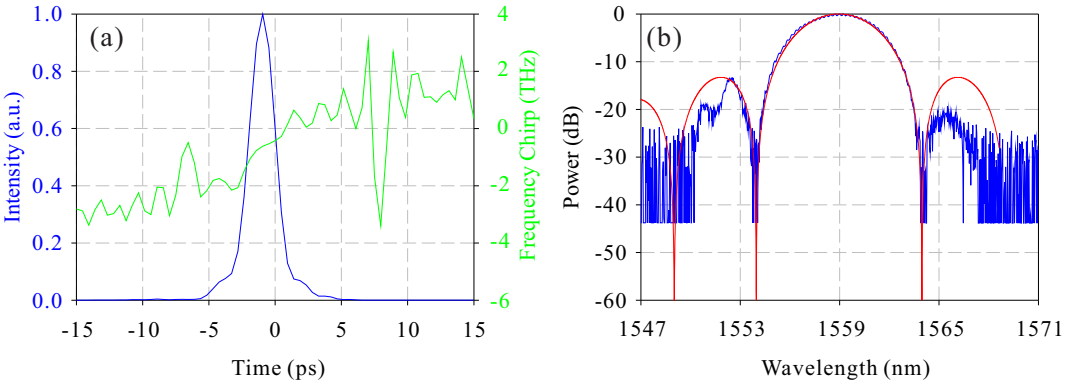

Figure 7.24: (a) Pulse shape (blue line) and frequency chirp (green line) of the pulses at the output of the W/S generated with a 5nm wide sinc square filter. (b) Comparison between the spectrum of the pulses (blue line) and the amplitude shaping function of the W/S (red line).

All the results described above were obtained when no spectral phase shaping was applied on the W/S. The Fourier transform of the rectangular function shows that there is a π phase shift at each sidelobe on the sinc square function. Thus, as the next attempt for the generation of rectangular pulses, it is worth programming the W/S to have the sinc square amplitude shaping function together with its corresponding π shift phase

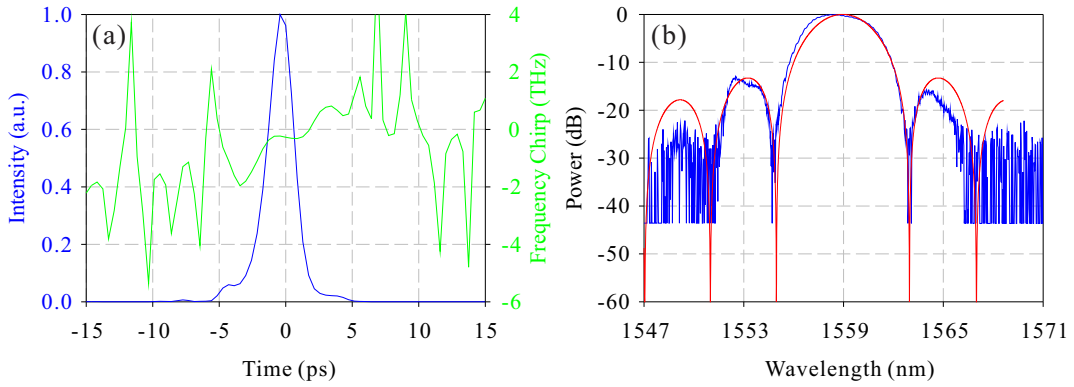

Figure 7.25: (a) Pulse shape (blue line) and frequency chirp (green line) of the pulses at the output of the W/S generated with a 4nm wide sinc square filter. (b) Comparison between the spectrum of the pulses (blue line) and the amplitude shaping function of the W/S (red line).

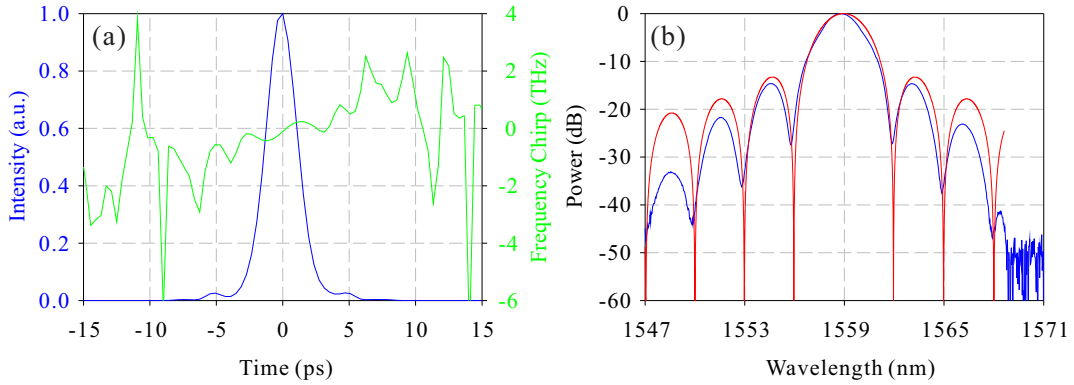

Figure 7.26: (a) Pulse shape (blue line) and frequency chirp (green line) of the pulses at the output of the W/S generated with a 3nm wide sinc square filter. (b) Comparison between the spectrum of the pulses (blue line) and the amplitude shaping function of the W/S (red line).

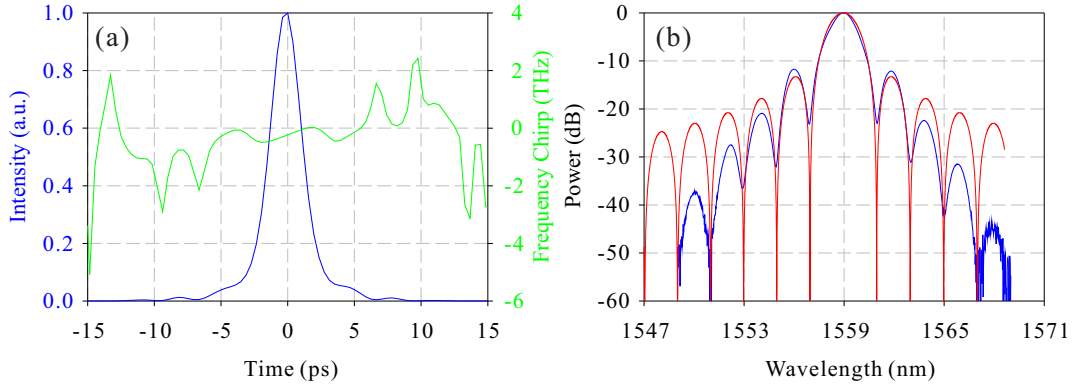

Figure 7.27: (a) Pulse shape (blue line) and frequency chirp (green line) of the pulses at the output of the W/S generated with a 2nm wide sinc square filter. (b) Comparison between the spectrum of the pulses (blue line) and the amplitude shaping function of the W/S (red line).

pattern.

When the π shift spectral phase profile was applied into the W/S, unfortunately, the mode-locking of the laser could be only achieved when the filter bandwidth was $6nm$. Figure 7.28 presents the characteristics of the pulses achieved in this scenario. The spectrum of the pulses plotted in Figure 7.28b was able to acquire the feature of the sinc square function with only the first-order sidelobes. The temporal characteristics of the pulses shown in Figure 7.28a indicates that no rectangular pulses were generated in the laser. As in the previously described cases, the number of sidelobes was not enough to produce rectangular pulses in the temporal domain.

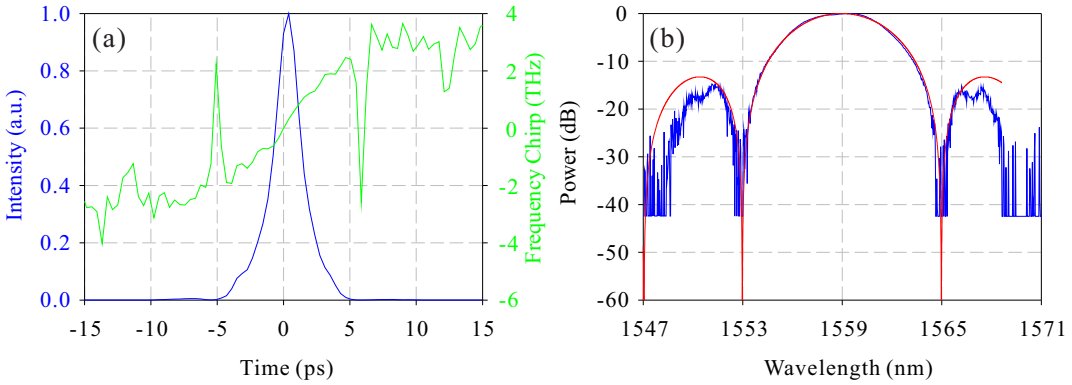

Figure 7.28: (a) Pulse shape (blue line) and frequency chirp (green line) of the pulses at the output of the W/S generated with a 6nm wide sinc square filter and its corresponding π phase shift pattern. (b) Comparison between the spectrum of the pulses (blue line) and the amplitude shaping function of the W/S (red line).

7.6 Conclusion

In this chapter, a DM passively mode-locked EFRL working around $1559nm$ with a repetition rate of $6.5MHz$ was developed and characterized. The laser was mode-locked by NPR, facilitated by the combination of a segment of DCF and a combination of two polarisation controllers and a polariser. The prominent feature of this laser was the inclusion of the programmable pulse shaper (Finisar, the W/S) in the cavity, which allows for both intra-cavity amplitude shaping and dispersion management without changing the layout of the laser.

By making use of the ability of reconfiguration of the pulse shaper, the influence of either Gaussian or third-order super-Gaussian filter functions on the laser performance was investigated. It was found that the pulses with a temporal shape close to a super-Gaussian function and a flat-top spectrum could be achieved at output port 1 of the laser. This was because the DCF included in the cavity was not long enough to fully develop the

similariton asymptotic solution. With a narrow band filter, nearly transform-limited pulses could be achieved at output port 2. Moreover, the characteristics of the pulses could be controlled by adjusting the filter bandwidth.
Then the pulse shaper was used to manipulate the ND of the cavity by applying different GVD profiles. Nearly transform-limited pulses with a duration of $1ps$ was achieved at output port 2 when the ND was tuned to be close to zero.
Based on the fact that the spectra of the pulses at output port 1 of the laser often acquire a flat top, sinc square filter functions with different bandwidths were applied on the W/S with the aim to generate rectangular pulses at output port 2 of the laser. Unfortunately, the attempt was failed due to that the spectrum generated in the laser could not fully agree with the sinc square function. In the future, thorough numerical simulations of the laser are required to seek for the appropriate filtering characteristics for the generation of the rectangular pulses in the laser.

Chapter 8

Conclusions and Future Work

In this thesis, I have presented the technique of pulse-shaping assisted nonlinear optical signal generation in fibres. Linear pulse shaping is the key element to achieve precise and flexible control over the characteristics of the optical signals generated in a nonlinear fibre optic system. There are two applications for this technique reported in this thesis. One of them is the pulse shaping assisted nonlinear spectral broadening. The characteristics on either the top or the edges of the generated broadband spectrum are manipulated by the linear pulse shaping process placed prior to the nonlinear broadening stage. The other one is the intra-cavity spectral amplitude and phase shaping in a passively mode-locked EFRL. The characteristics of laser pulses are controlled by the intra-cavity shaping parameters, e.g. filter shape, filter bandwidth, the amount of dispersion trimming through spectral phase shaping.

As a first step, I have presented an arbitrary spectral synthesis technique based on the adaptive pulse shaping. It allows for the dynamic adjustment of the filtering characteristics of the pulse shaper according to the quality of the generated spectrum. It is a powerful tool to overcome the limitations imposed by the uncertainties in the system which are difficult to be manually calibrated. In my experiments, the arbitrary spectral synthesis played a vital role.

The generation of flat-top spectrum was the first target for the adaptive pulses shaping assisted nonlinear broadening. A numerical simulation procedure was established to find out the appropriate filtering characteristics for the pulse shaper. In a proof-of-principle experiment, the filtering characteristics obtained from numerical simulations was applied to the W/S. A spectral lobe was developed at the centre of the spectrum. The quality of the generated spectrum was then significantly improved by employing the arbitrary spectral synthesis. The generated spectrum exhibited a $3dB$ bandwidth of $12nm$ and a central region of $8nm$ where the fluctuations were less than $0.4dB$. By further increasing the power level at the input of the HNLF, a frequency comb covering the full C-band was successfully generated. The comb exhibited a $3dB$ bandwidth of $35nm$ and a central region of $30nm$, where the fluctuations were less than $1dB$. A $20dB$

optical signal to noise ratio uniformly across the full spectrum was observed through high resolution OSA measurement. With further noise characterization of the comb, it was found that there was no noticeable difference between the noise characteristics of the generated spectrum and the seed pulse emitting from the commercial mode-locked laser. This observation indicated that both the linear pulse shaping process and the nonlinear spectral broadening would not deteriorate the noise performance of the seed signal.

The second target for the adaptive pulse shaping assisted nonlinear broadening was the generation of broadband spectra with symmetric and linear edges. The generated spectrum exhibited a $3dB$ bandwidth of $11nm$ as well as symmetric and linear edges with slopes of different steepness. It was then found that the arbitrary spectral synthesis had better performance when the target spectrum had a weaker steepness. Similar results were obtained from two different HNLFs in the experiment.

In summary, the adaptive pulse shaping assisted nonlinear spectral broadening has the following advantages: Firstly, it is no longer tied directly to the characteristics of either the pulse source or the HNLF. Therefore in principle, several different spectral shapes can be generated without changing the hardware of the system. Secondly, it is power-efficient since there is no power loss once the signal has been amplified prior to the nonlinear element. Meanwhile, it can be used to control the optical spectrum over ranges that greatly exceed the operating bandwidth of the pulse shaper itself.

In terms of the future directions of the adaptive pulse shaping assisted nonlinear broadening, it would be interesting to control the number and depth of the ripples in the oscillatory structure on the top of the spectrum, which is typical of SPM. Moreover, it would be also promising to target the generation of a spectrum with two distinct peaks, which is the SPM-induced spectrum of triangular pulses.

The intra-cavity filtering in a passively mode-locked EFRL was the second application of the technique of pulse shaping assisted signal generation in fibres. It was first investigated through numerical simulations. It was found that the adaptive pulse shaping cannot effectively shape the pulses due to the solition formation in an all-anomalous dispersion cavity. Instead, in an all-normal dispersion cavity operated in the active similariton mode, the adaptive pulse shaping system was capable of manipulating the characteristics of output pulses. It was shown that the potential waveforms of the laser pulses range from the more traditional shapes of hyperbolic secant and parabolic to super-Gaussian of different orders.

In the experiment, a dispersion-managed passively mode-locked EFRL with a repetition rate of $6.5MHz$ working around $1559nm$ was built and characterized. The mode-locking mechanism of the laser was NPR. A programmable spectral filtering stage was included right after the normal-dispersion fibre segment in the cavity. It performed both the intra-cavity amplitude shaping and the control of the net dispersion of the cavity. With either Gaussian filter or third-order super-Gaussian filter, the pulses before the pulse shaper exhibited a flat-top spectrum and a temporal-shape close to super-Gaussian functions.

The reason for this was that the length of the normal-dispersion fibre included in the cavity was not long enough to allow the asymptotic similariton solution to be fully developed. The characteristics of the pulses after the pulse shaper can be controlled by changing the filter bandwidth. With narrow-band filter, nearly transform-limited pulses can be achieved. Then, the net dispersion of the cavity was adjusted by applying different amount of dispersion to the filter. This was realized by the spectral phase filtering. The characteristics of the pulses after the pulse shaper can be manipulated by adjusting the amount of dispersion trimming provided by it. Nearly chirp-free pulse can be achieved when the net dispersion was tuned to be close to zero. The pulses before the pulse shaper acquired a flat-top spectrum as well. Sinc square filter was applied on the pulse shaper with the purpose to obtain rectangular pulse after it. This attempt was failed because the pulses generated in the laser cannot fully acquire the characteristics of the sinc square function.

In future, the dispersion-managed passively mode-locked laser with intra-cavity spectral filtering needs to be thoroughly modelled. With an accurate numerical model, the influence of intra-cavity filtering in such a laser can be deeply understood. Then together with the adaptive pulse shaping system, it is possible to find the appropriate transfer functions of the pulse shaper for the generation of rectangular pulses and pulses with other exotic shapes directly from the laser.

List of Publications

Journal Papers

1. **X. Yang**, D. J. Richardson, and P. Petropoulos, "Nonlinear Generation of Ultra-Flat Broadened Spectrum Based on Adaptive Pulse Shaping," Journal of Lightwave Technology, vol. 30, no. 12, pp. 1971-1977, 2012.

2. **X. Yang**, D. J. Richardson, and P. Petropoulos, "Broadband, Flat Frequency Comb Generated Using Pulse Shaping-Assisted Nonlinear Spectral Broadening," IEEE Photonics Technology Letters, vol. 25, no. 6, pp. 543-545, 2013.

3. D. Hillerkuss, R. Schmogrow, M. Meyer, S. Wolf, M. Jordan, P. Kleinow, N. Lindenmann, P. C. Schindler, A. Melikyan, **X. Yang**, S. Ben-Ezra, B. Nebendahl, M. Dreschmann, J. Meyer, F. Parmigiani, P. Petropoulos, B. Resan, A. Oehler, K. Weingarten, L. Altenhain, T. Ellermeyer, M. Moeller, M. Huebner, J. Becker, C. Koos, W. Freude, and J. Leuthold, "Single-Laser $32.5 Tbit/s$ Nyquist WDM Transmission," Journal of Optical Communications and Networking, vol. 4, no. 10, pp. 715-723, 2012.

4. David J. Thomson, Frederic Y. Gardes, S. Liu, H. Porte, L. Zimmermann, J-M Fedeli, Y. Hu, M. Nedeljkovic, **X. Yang**, P. Petropoulos and G. Z. Mashanovich, "High Performance Mach Zehnder Based Silicon Optical Modulators," Journal of Selected Topics in Quantum Electronics (Invited and Accpeted).

Conference Submissions

1. **X. Yang**, D. J. Richardson, and P. Petropoulos, "Pulse Shaping-Assisted Nonlinear Spectral Broadening," 2011 Conference on Lasers & Electro-Optics Europe & 12th European Quantum Electronics Conference CLEO EUROPE/EQEC, p. CI2.1, 2011.

2. **X. Yang**, D. J. Richardson, and P. Petropoulos, "Nonlinear Generation of Ultra-Flat Broadened Spectrum Based on Adaptive Pulse Shaping," 2011 37th European Conference and Exhibition on Optical Communication (ECOC 2011), p. We.7.A.2, 2011.

3. **X. Yang** and P. Petropoulos, "An Ultra-Flat Frequency Comb Generated Using Nonlinear Broadening and Adaptive Pulse Shaping," in Optical Fibre Communication Conference and Exposition (OFC/NFOEC), 2012 and the National Fibre Optic Engineers Conference, p. OW4H.5, 2012.

4. P. Petropoulos and **X. Yang**, "Nonlinear Sculpturing of Optical Spectra," 2012 14th International Conference on Transparent Optical Networks (ICTON), p. We.D1.2, 2012. (Invited)

5. **X. Yang**, K. Hammani and D. J. Richardson, and P. Petropoulos, "Passively Mode-Locked Fibre Laser Incorporating Adaptive Filtering and Dispersion Management," 2013 Conference on Lasers and Electro-Optics, p. CI1I.1, 2013.

References

[1] J. Toulouse, "Optical Nonlinearities in Fibers: Review, Recent Examples, and Systems Applications," *Journal of Lightwave Technology*, vol. 23, no. 11, pp. 3625–3641, 2005.

[2] B. B. Tiwari, V. Prakash, V. Tripathi, and N. Malaviya, "Nonlinear Effects in Optical Fiber Transmission System," *IETE Technical Review*, vol. 16, no. 5-6, pp. 461–479, 1999.

[3] E. H. Lee, K. H. Kim, and H. K. Lee, "Nonlinear Effects in Optical Fiber: Advantages and Disadvantages for High Capacity All-Optical Communication Application," *Optical and Quantum Electronics*, vol. 34, no. 12, pp. 1167–1174, 2002.

[4] S. B. Poole, D. N. Payne, R. J. Mears, M. E. Fermann, and R. I. Laming, "Fabrication and Characterization of Low-Loss Optical Fibers Containing Rare-Earth Ions," *Journal of Lightwave Technology*, vol. 4, no. 7, pp. 870–876, 1986.

[5] S. L. Hansen, K. Dybdal, and C. C. Larsen, "Gain Limit in Erbium-Doped Fiber Amplifiers Due to Internal Rayleigh Backscattering," *IEEE Photonics Technology Letters*, vol. 4, no. 6, pp. 559–561, 1992.

[6] R. Laming, M. N. Zervas, and D. N. Payne, "Erbium-Doped Fiber Amplifier with 54dB Gain and 3.1dB Noise Figures," *IEEE Photonics Technology Letters*, vol. 4, no. 12, pp. 1345–1347, 1992.

[7] F. A. Flood, "L-band Erbium-Doped Fiber Amplifiers," in *Optical Fiber Communication Conference, 2000*, vol. 2, pp. 102–104 vol.2, 2000.

[8] G. P. Agrawal, "Fibers with Silica Cladding," in *Nonlinear Fibre Optics*, pp. 434–436, Sinagpore: Elsevier (Sinagpore) Pte Ltd., 2009.

[9] B. J. Eggleton, C. Kerbage, P. S. Westbrook, R. S. Windeler, and A. Hale, "Microstructured Optical Fiber Devices," *Optics Express*, vol. 9, no. 13, pp. 698–713, 2001.

[10] P. S. J. Russell, "Photonic-Crystal Fibers," *Journal of Lightwave Technology*, vol. 24, no. 12, pp. 4729–4749, 2006.

[11] J. M. Dudley, G. Genty, and S. Coen, "Supercontinuum Generation in Photonic Crystal Fiber," *Reviews of Modern Physics*, vol. 78, no. 4, pp. 1135–1184, 2006.

[12] J. M. Dudley and S. Coen, "Coherence Properties of Supercontinuum Spectra Generated in Photonic Crystal and Tapered Optical Fibers," *Optics Letters*, vol. 27, no. 13, pp. 1180–1182, 2002.

[13] J. M. Dudley and S. Coen, "Fundamental Limits to Few-Cycle Pulse Generation from Compression of Supercontinuum Spectra Generated in Photonic Crystal Fiber," *Optics Express*, vol. 12, no. 11, pp. 2423–2428, 2004.

[14] M. E. Fermann, V. I. Kruglov, B. C. Thomsen, J. M. Dudley, and J. D. Harvey, "Self-Similar Propagation and Amplification of Parabolic Pulses in Optical Fibers," *Physical Review Letters*, vol. 84, no. 26, pp. 6010–6013, 2000.

[15] V. I. Kruglov, A. C. Peacock, and J. D. Harvey, "Exact Self-Similar Solutions of the Generalized Nonlinear Schrödinger Equation with Distributed Coefficients," *Physical Review Letters*, vol. 90, no. 11, 2003.

[16] T. Hirooka and M. Nakazawa, "Parabolic Pulse Generation by Use of a Dispersion-Decreasing Fiber with Normal Group-Velocity Dispersion," *Optics Letters*, vol. 29, no. 5, pp. 498–500, 2004.

[17] F. Parmigiani, C. Finot, K. Mukasa, M. Ibsen, M. A. F. Roelens, P. Petropoulos, and D. J. Richardson, "Ultra-Flat SPM-Broadened Spectra in a Highly Nonlinear Fiber Using Parabolic Pulses Formed in a Fiber Bragg Grating," *Optics Express*, vol. 14, no. 17, pp. 7617–7622, 2006.

[18] P. J. Almeida, P. Petropoulos, M. Ibsen, and D. J. Richardson, "Generation of Ultra-Flat SPM-Broadened Spectra in a Highly Nonlinear Fiber Using Pulse Pre-Shaping in a Fiber Bragg Grating," *2005 Optical Fiber Communications Conference*, p. paper OThA4, 2005.

[19] D. J. Richardson, R. I. Laming, D. N. Payne, M. W. Phillips, and V. J. Matsas, "320fs Soliton Generation with Passively Mode-Locked Erbium Fiber Laser," *Electronics Letters*, vol. 27, no. 9, pp. 730–732, 1991.

[20] I. N. Duling, "All-Fiber Ring Soliton Laser Mode-Locked with a Nonlinear Mirror," *Optics Letters*, vol. 16, no. 8, pp. 539–541, 1991.

[21] V. J. Matsas, T. P. Newson, D. J. Richardson, and D. N. Payne, "Self-Starting Passively Mode-Locked Fiber Ring Soliton Laser Exploiting Nonlinear Polarization Rotation," *Electronics Letters*, vol. 28, no. 15, pp. 1391–1393, 1992.

[22] X. Yang, D. J. Richardson, and P. Petropoulos, "Pulse Shaping-Assisted Nonlinear Spectral Broadening," *2011 Conference on Lasers & Electro-Optics Europe & 12th European Quantum Electronics Conference CLEO EUROPE/EQEC*, p. CI2.1, 2011.

[23] X. Yang, D. J. Richardson, and P. Petropoulos, "Nonlinear Generation of Ultra-Flat Broadened Spectrum Based on Adaptive Pulse Shaping," *Journal of Lightwave Technology*, vol. 30, no. 12, pp. 1971–1977, 2012.

[24] X. Yang, D. J. Richardson, and P. Petropoulos, "Nonlinear Generation of Ultra-Flat Broadened Spectrum Based on Adaptive Pulse Shaping," *2011 37th European Conference and Exhibition on Optical Communication (ECOC 2011)*, p. We.7.A.2, 2011.

[25] X. Yang and P. Petropoulos, "An Ultra-Flat Frequency Comb Generated Using Nonlinear Broadening and Adaptive Pulse Shaping," in *Optical Fiber Communication Conference and Exposition (OFC/NFOEC), 2012 and the National Fiber Optic Engineers Conference*, p. OW4H.5, 2012.

[26] X. Yang, D. J. Richardson, and P. Petropoulos, "Broadband, Flat Frequency Comb Generated Using Pulse Shaping-Assisted Nonlinear Spectral Broadening," *IEEE Photonics Technology Letters*, vol. 25, no. 6, pp. 543–545, 2013.

[27] D. Hillerkuss, R. Schmogrow, M. Meyer, S. Wolf, M. Jordan, P. Kleinow, N. Lindenmann, P. C. Schindler, A. Melikyan, X. Yang, S. Ben-Ezra, B. Nebendahl, M. Dreschmann, J. Meyer, F. Parmigiani, P. Petropoulos, B. Resan, A. Oehler, K. Weingarten, L. Altenhain, T. Ellermeyer, M. Moeller, M. Huebner, J. Becker, C. Koos, W. Freude, and J. Leuthold, "Single-Laser 32.5$Tbit/s$ Nyquist WDM Transmission," *Journal of Optical Communications and Networking*, vol. 4, no. 10, pp. 715–723, 2012.

[28] X. Yang, K. Hammani, D. Richardson, and P. Petropoulos, "Passively Mode-Locked Fiber Laser Incorporating Adaptive Filtering and Dispersion Management," *2013 Conference on Lasers and Electro-Optics*, p. CI1I.1, 2013.

[29] G. P. Agrawal, "Pulse-Propagation Equation," in *Nonlinear Fibre Optics*, pp. 31–41, Sinagpore: Elsevier (Sinagpore) Pte Ltd., 2009.

[30] R. W. Boyd, "The Coupled-Wave Equations for Sum-Frequency Generation," in *Nonlinear Optics*, p. 64, Sab Diego: Academic Press Limited, 1992.

[31] A. D. Polyanin, *Handbook of Linear Partial Differential Equations for Engineers and Scientists*. Boca Raton: Chapman & Hall/CRC Press, 2002.

[32] G. W. Stewart, *Matrix Perturbation Theory*. Academic Press, 1990.

[33] G. P. Agrawal, "Different Propagation Regimes," in *Nonlinear Fibre Optics*, pp. 51–53, Sinagpore: Elsevier (Sinagpore) Pte Ltd, 2009.

[34] G. P. Agrawal, "Dispersion-Induced Pulse Broadening," in *Nonlinear Fibre Optics*, pp. 53–62, Sinagpore: Elsevier (Sinagpore) Pte Ltd, 2009.

[35] G. P. Agrawal, "SPM-Induced Spectral Changes," in *Nonlinear Fibre Optics*, pp. 79–89, Singapore: Elsevier (Singapore) Pte Ltd., 2009.

[36] G. P. Agrawal, "Effect of Group-Velocity Dispersion," in *Nonlinear Fibre Optics*, pp. 89–100, Sinagpore: Elsevier (Sinagpore) Pte Ltd., 2009.

[37] A. Hasegawa and F. Tappert, "Transmission of Stationary Nonlinear Optical Pulses in Dispersive Dielectric Fibers .2. Normal Dispersion," *Applied Physics Letters*, vol. 23, no. 4, pp. 171–172, 1973.

[38] D. Anderson, M. Desaix, M. Lisak, and M. L. Quirogateixeiro, "Wave Breaking in Nonlinear-Optical Fibers," *Journal of the Optical Society of America B-Optical Physics*, vol. 9, no. 8, pp. 1358–1361, 1992.

[39] Y. Takushima, F. Futami, and K. Kikuchi, "Generation of over 140-nm-Wide Super-Continuum from a Normal Dispersion Fiber by Using a Mode-Locked Semiconductor Laser Source," *IEEE Photonics Technology Letters*, vol. 10, no. 11, pp. 1560–1562, 1998.

[40] D. Anderson, M. Desaix, M. Karlsson, M. Lisak, and M. L. Quirogateixeiro, "Wave-Breaking-Free Pulses in Nonlinear-Optical Fibers," *Journal of the Optical Society of America B-Optical Physics*, vol. 10, no. 7, pp. 1185–1190, 1993.

[41] L. E. Hooper, P. J. Mosley, A. C. Muir, W. J. Wadsworth, and J. C. Knight, "All-Normal Dispersion Photonic Crystal Fiber for Coherent Supercontinuum Generation," *2010 Conference on Lasers and Electro-Optics (CLEO)*, p. 2 pp., 2010.

[42] A. M. Clarke, D. G. Williams, M. A. F. Roelens, and B. J. Eggleton, "Reconfigurable Optical Pulse Generator Employing a Fourier-Domain Programmable Optical Processor," *Journal of Lightwave Technology*, vol. 28, no. 1, pp. 97–103, 2010.

[43] K. Kashiwagi, H. Ishizu, Y. Kodama, S. Choi, and T. Kurokawa, "Highly Precise Optical Pulse Synthesis for Flat Spectrum Supercontinuum Generation with Wide Mode Spacing," *2010 36th European Conference and Exhibition on Optical Communication (ECOC 2010)*, p. 3 pp., 2010.

[44] G. P. Agrawal, "Split-Step Fourier Method," in *Nonlinear Fibre Optics*, pp. 41–45, Sinagpore: Elsevier (Sinagpore) Pte Ltd., 2009.

[45] S. Shuxian, K. Demarest, and C. Allen, "Numerically Reversing the Nonlinear Wave Propagation in Single-Mode Optical Fiber," *1999 IEEE LEOS Annual Meeting Conference Proceedings. LEOS'99. 12th Annual Meeting. IEEE Lasers and Electro-Optics Society 1999 Annual Meeting (Cat. No.99CH37009)*, p. 10.1109/LEOS.1999.811876, 1999.

[46] O. V. Sinkin, R. Holzlohner, J. Zweck, and C. R. Menyuk, "Optimization of the Split-Step Fourier Method in Modeling Optical-Fiber Communications Systems," *Journal of Lightwave Technology*, vol. 21, no. 1, pp. 61–68, 2003.

[47] A. Weiner and A. Kan'an, "Femtosecond Pulse Shaping for Synthesis, Processing, and Time-to-Space Conversion of Ultrafast Optical Waveforms," *Selected Topics in Quantum Electronics, IEEE Journal of*, vol. 4, no. 2, pp. 317–331, 1998.

[48] A. M. Weiner, "Femtosecond Pulse Shaping Using Spatial Light Modulators," *Review of Scientific Instruments*, vol. 71, no. 5, pp. 1929–1960, 2000.

[49] A. M. Weiner, "Ultrafast Optical Pulse Shaping: A Tutorial Review," *Optics Communications*, vol. 284, no. 15, pp. 3669–3692, 2011.

[50] A. M. Weiner, D. E. Leaird, J. S. Patel, and J. R. Wullert, "Programmable Shaping of Femtosecond Optical Pulses by Use of 128-Element Liquid-Crystal Phase Modulator," *IEEE Journal of Quantum Electronics*, vol. 28, no. 4, pp. 908–920, 1992.

[51] M. M. Wefers and K. A. Nelson, "Analysis of Programmable Ultrashort Waveform Generation Using Liquid-Crystal Spatial Light Modulators," *Journal of the Optical Society of America B-Optical Physics*, vol. 12, no. 7, pp. 1343–1362, 1995.

[52] M. M. Wefers and K. A. Nelson, "Generation of High-Fidelity Programmable Ultrafast Optical Wave-Forms," *Optics Letters*, vol. 20, no. 9, pp. 1047–1049, 1995.

[53] M. E. Fermann, V. Dasilva, D. A. Smith, Y. Silberberg, and A. M. Weiner, "Shaping of Ultrashort Optical Pulses by Using an Integrated Acoustooptic Tunable Filter," *Optics Letters*, vol. 18, no. 18, pp. 1505–1507, 1993.

[54] C. W. Hillegas, J. X. Tull, D. Goswami, D. Strickland, and W. S. Warren, "Femtosecond Laser-Pulse Shaping by Use of Microsecond Radiofrequency Pulses," *Optics Letters*, vol. 19, no. 10, pp. 737–739, 1994.

[55] P. Petropoulos, M. Ibsen, A. D. Ellis, and D. J. Richardson, "Rectangular Pulse Generation Based on Pulse Reshaping Using a Superstructured Fiber Bragg Grating," *Journal of Lightwave Technology*, vol. 19, no. 5, pp. 746–752, 2001.

[56] Q. Ye, R. Huang, Q. F. Xu, H. W. Cai, R. H. Qu, and Z. J. Fang, "Numerical Investigation of Ultrashort Complex Pulse Generation Based on Pulse Shaping Using a Superstructure Fiber Bragg Grating," *Journal of Lightwave Technology*, vol. 27, no. 13, pp. 2449–2456, 2009.

[57] D. J. Richardson, P. Petropoulos, F. Parmigiani, P. J. Almeida, C. Tian, T. T. Ng, Z. Zhang, and M. Ibsen, "Advances in Fibre Based Pulse Shaping Technology

and its Applications in Optical Communications," *2007 International Conference on Transparent Optical Networks*, pp. 176–9, 2007.

[58] D. J. Richardson, F. Parmigiani, M. Ibsen, and P. Petropoulos, "High Performance Optical Processing Systems Incorporating Grating Based Pulse Shaping," *2009 IEEE/LEOS Winter Topicals Meeting Series (WTM 2009)*, pp. 266–267, 2009.

[59] F. Parmigiani, P. Petropoulos, M. Ibsen, T. T. Ng, and D. J. Richardson, "OTDM Add-Drop Multiplexer Using a Saw-Tooth Pulse Shaper," *2008 34th European Conference on Optical Communication (ECOC 2008)*, p. 2 pp., 2008.

[60] F. Parmigiani, T. T. Ng, M. Ibsen, P. Petropoulos, and D. J. Richardson, "Timing Jitter Tolerant All-Optical TDM Demultiplexing Using a Saw-Tooth Pulse Shaper," *IEEE Photonics Technology Letters*, vol. 20, no. 21-24, pp. 1992–1994, 2008.

[61] F. Parmigiani, P. Petropoulos, M. Ibsen, P. J. Almeida, T. T. Ng, and D. J. Richardson, "Time Domain Add-Drop Multiplexing Scheme Enhanced Using a Saw-Tooth Pulse Shaper," *Optics Express*, vol. 17, no. 10, pp. 8362–8369, 2009.

[62] F. Parmigiani, P. Petropoulos, M. Ibsen, and D. J. Richardson, "All-Optical Pulse Reshaping and Retiming Systems Incorporating Pulse Shaping Fiber Bragg Grating," *Journal of Lightwave Technology*, vol. 24, no. 1, pp. 357–364, 2006.

[63] F. Parmigiani, L. K. Oxenlowe, M. Galili, M. Ibsen, D. Zibar, P. Petropoulos, D. J. Richardson, A. Clausen, and P. Jeppesen, "All-Optical 160$Gbit/s$ RZ Data Retiming System Incorporating a Pulse Shaping Fibre Bragg Grating," *33rd European Conference and Exhibition on Optical Communication - ECOC 2007*, p. 4 pp., 2007.

[64] F. Parmigiani, L. K. Oxenlowe, M. Galili, M. Ibsen, D. Zibar, P. Petropoulos, D. J. Richardson, A. T. Clausen, and P. Jeppesen, "All-Optical 160 − $Gbit/s$ Retiming System Using Fiber Grating Based Pulse Shaping Technology," *Journal of Lightwave Technology*, vol. 27, no. 9, pp. 1135–1141, 2009.

[65] F. Parmigiani, P. Petropoulos, M. Ibsen, and D. J. Richardson, "Pulse Retiming Based on XPM Using Parabolic Pulses Formed in a Fiber Bragg Grating," *IEEE Photonics Technology Letters*, vol. 18, no. 5-8, pp. 829–831, 2006.

[66] Y. Park, M. H. Asghari, T. Ahn, and J. Azaña, "Transform-Limited Picosecond Pulse Shaping Based on Temporal Coherence Synthesization," *Optics Express*, vol. 15, no. 15, pp. 9584–9599, 2007.

[67] D. Krčmařík, R. Slavík, Y. Park, and J. Azaña, "Nonlinear Pulse Compression of Picosecond Parabolic-Like Pulses Synthesized with a Long Period Fiber Grating Filter," *Optics Express*, vol. 17, no. 9, pp. 7074–7087, 2007.

[68] R. Slavík, Y. Park, and J. Azaña, "Long-Period Fiber-Grating-Based Filter for Generation of Picosecond and Subpicosecond Transform-Limited Flat-Top Pulses," *IEEE Photonics Technology Letters*, vol. 20, no. 10, pp. 806–808, 2008.

[69] G. Baxter, S. Frisken, D. Abakoumov, H. Zhou, I. Clarke, A. Bartos, and S. Poole, "Highly Programmable Wavelength Selective Switch based on Liquid Crystal on Silicon Switching Elements," *2006 Optical Fiber Communication Conference/National Fiber Optic Engineers Conference, Vols 1-6*, pp. 94–96, 2006.

[70] K. M. Johnson, D. J. Mcknight, and I. Underwood, "Smart Spatial Light Modulators Using Liquid-Crystals on Silicon," *IEEE Journal of Quantum Electronics*, vol. 29, no. 2, pp. 699–714, 1993.

[71] B. Costa, D. Mazzoni, M. Puleo, and E. Vezzoni, "Phase-Shift Technique for the Measurement of Chromatic Dispersion in Optical Fibers Using LEDs," *IEEE Journal of Quantum Electronics*, vol. 18, no. 10, pp. 1509–1515, 1982.

[72] T. Baumert, T. Brixner, V. Seyfried, M. Strehle, and G. Gerber, "Femtosecond Pulse Shaping by an Evolutionary Algorithm with Feedback," *Applied Physics B-Lasers and Optics*, vol. 65, no. 6, pp. 779–782, 1997.

[73] D. Meshulach, D. Yelin, and Y. Silberberg, "Adaptive Real-Time Femtosecond Pulse Shaping," *Journal of the Optical Society of America B-Optical Physics*, vol. 15, no. 5, pp. 1615–1619, 1998.

[74] D. Zeidler, S. Frey, K. L. Kompa, and M. Motzkus, "Evolutionary Algorithms and Their Application to Optimal Control Studies," *Physical Review A*, vol. 64, no. 2, pp. art. no.–023420, 2001.

[75] A. Rundquist, A. Efimov, and D. H. Reitze, "Pulse Shaping with the Gerchberg-Saxton Algorithm," *Journal of the Optical Society of America B-Optical Physics*, vol. 19, no. 10, pp. 2468–2478, 2002.

[76] R. Mizoguchi, K. Onda, S. S. Kano, and A. Wada, "Thinning-out in Optimized Pulse Shaping Method Using Genetic Algorithm," *Review of Scientific Instruments*, vol. 74, no. 5, pp. 2670–2674, 2003.

[77] F. G. Omenetto, B. P. Luce, and A. J. Taylor, "Genetic Algorithm Pulse Shaping for Optimum Femtosecond Propagation in Optical Fibers," *Journal of the Optical Society of America B-Optical Physics*, vol. 16, no. 11, pp. 2005–2009, 1999.

[78] D. J. Kane and R. Trebino, "Characterization of Arbitrary Femtosecond Pulses Using Frequency-Resolved Optical Gating," *IEEE Journal of Quantum Electronics*, vol. 29, no. 2, pp. 571–579, 1993.

[79] C. Iaconis and I. A. Walmsley, "Spectral Phase Interferometry for Direct Electric-Field Reconstruction of Ultrashort Optical Pulses," *Optics Letters*, vol. 23, no. 10, pp. 792–794, 1998.

[80] T. Bäck and H.-P. Schwefel, "An Overview of Evolutionary Algorithms for Parameter Optimization," *Evol. Comput.*, vol. 1, no. 1, pp. 1–23, 1993.

[81] T. Bäck, U. Hammel, and H. P. Schwefel, "Evolutionary Computation: Comments on the History and Current State," *IEEE Transactions on Evolutionary Computation*, vol. 1, no. 1, pp. 3–17, 1997.

[82] K. A. De Jong, *Evolutionary Computation: A Unified Approach.* The MIT Press, Cambridge, Massachusetts, 2006.

[83] J. H. Holland, *Adaptation In Natural And Artificial Systems.* The MIT Press, Cambridge, Massachusetts, 1975.

[84] G. Syswerda, "Uniform Crossover in Genetic Algorithms," *Proceedings of the 3rd International Conference on Genetic Algorithms*, pp. 2–9, 1989.

[85] K. Spears, W.; De Jong, "On the Virtues of Parameterized Uniform Crossover," *Proceedings of the 4th International Conference on Genetic Algorithms*, pp. 230–236, 1991.

[86] J. H. Holland, "Outline for a Logical Theory of Adaptive Systems," *J. ACM*, vol. 9, no. 3, pp. 297–314, 1962.

[87] K. A. De Jong, *An Analysis of the Behavior of a Class of Genetic Adaptive Systems.* PhD thesis, University of Michigan, 1975.

[88] L. Fogel, "Autonomous automata," *Ind. Res.*, vol. 4, pp. 14–19, 1962.

[89] L. Fogel, *On the Organization of Intellect.* PhD thesis, University of California, Los Angeles, 1964.

[90] H. P. Schwefel, *Kybernetische Evolution als Strategie der Exprimentellen Forschung in der Strmungstechnik.* PhD thesis, Technical University of Berlin, 1965.

[91] I. Rechenberg, *Evolutionsstrategie: Optimierung Technischer Systeme nach Prinzipien der Biologischen Evolution.* PhD thesis, Technical University of Berlin, 1971.

[92] H.-P. P. Schwefel, *Evolution and Optimum Seeking: The Sixth Generation.* New York, NY, USA: John Wiley & Sons, Inc., 1993.

[93] H. G. Beyer and H. P. Schwefel, "Evolution Strategies - A Comprehensive Introduction," *Natural Computing*, vol. 1, no. 1, pp. 3–52, 2002.

[94] H. P. Schwefel, *Evolutionsstrategie und Numerische Optimierung.* PhD thesis, Technical University of Berlin, 1975.

[95] N. Hansen and A. Ostermeier, "Completely Derandomized Self-Adaptation in Evolution Strategies," *Evolutionary Computation*, vol. 9, no. 2, pp. 159–195, 2001.

[96] H. G. Beyer, "Toward a Theory of Evolution Strategies: Self-Adaptation," *Evolutionary Computation*, vol. 3, no. 3, pp. 311–347, 1995.

[97] T. Morioka, K. Mori, and M. Saruwatari, "More Than 100-Wavelength-Channel Picosecond Optical Pulse Generation from Single Laser Source Using Supercontinuum in Optical Fibers," *Electronics Letters*, vol. 29, no. 10, pp. 862–864, 1993.

[98] D. Hillerkuss, R. Schmogrow, T. Schellinger, M. Jordan, M. Winter, G. Huber, T. Vallaitis, R. Bonk, P. Kleinow, F. Frey, M. Roeger, S. Koenig, A. Ludwig, A. Marculescu, J. Li, M. Hoh, M. Dreschmann, J. Meyer, S. Ben Ezra, N. Narkiss, B. Nebendahl, F. Parmigiani, P. Petropoulos, B. Resan, A. Oehler, K. Weingarten, T. Ellermeyer, J. Lutz, M. Moeller, M. Huebner, J. Becker, C. Koos, W. Freude, and J. Leuthold, "26 $Tbits^{-1}$ Line-Rate Super-Channel Transmission Utilizing All-Optical Fast Fourier Transform Processing," *Nature Photonics*, vol. 5, no. 6, pp. 364–371, 2011.

[99] J. Kim, O. Boyraz, and M. N. Islam, "150^{+} Channel Ultra-DWDM Source with $N \times 10GHz$ Spacing Utilizing Longitudinal Mode Slicing of Supercontinuum," *2000 Optical Fiber Communication Conference*, pp. 5–7 vol.3, 2000.

[100] E. Yamada, H. Takara, T. Ohara, K. Sato, T. Morioka, K. Jinguji, M. Itoh, and M. Ishii, "150 Channel Supercontinuum CW Optical Source with High SNR and Precise $25GHz$ Spacing for $10Gbit/s$ DWDM Systems," *Electronics Letters*, vol. 37, no. 5, pp. 304–306, 2001.

[101] D. von der Linde, "Characterization of the Noise in Continuously Operating Mode-Locked Lasers," *Applied Physics B-Photophysics and Laser Chemistry*, vol. 39, no. 4, pp. 201–217, 1986.

[102] A. Siegman, *Lasers*. University Science Books, 1986.

[103] H. A. Haus, "Mode-Locking of Lasers," *IEEE Journal of Selected Topics in Quantum Electronics*, vol. 6, no. 6, pp. 1173–1185, 2000.

[104] M. Hercher, "An Analysis of Saturable Absorbers," *Applied Optics*, vol. 6, no. 5, pp. 947–54, 1967.

[105] E. P. Ippen, "Principles of Passive-Mode Locking," *Applied Physics B-Lasers and Optics*, vol. 58, no. 3, pp. 159–170, 1994.

[106] C. C. Yang, D.-W. Huang, C.-W. Hsu, S.-Y. Liang, C.-W. Lay, and M.-S. Lin, "Passive Mode-Locking Techniques of Lasers," *International Journal of High Speed Electronics and Systems*, vol. 08, no. 04, pp. 599–619, 1997.

[107] F. X. Kärtner, J. A. D. Au, and U. Keller, "Mode-Locking with Slow and Fast Saturable Absorbers - What's the Difference?," *IEEE Journal of Selected Topics in Quantum Electronics*, vol. 4, no. 2, pp. 159–168, 1998.

[108] H. A. Haus, "Theory of Mode-Locking with a Fast Saturable Absorber," *Journal of Applied Physics*, vol. 46, no. 7, pp. 3049–3058, 1975.

[109] H. A. Haus, "Theory of Mode-Locking with a Slow Saturable Absorber," *IEEE Journal of Quantum Electronics*, vol. 11, no. 9, pp. 736–746, 1975.

[110] S. W. Harun, R. Akbari, H. Arof, and H. Ahmad, "Mode-Locked Bismuth-Based Erbium-Doped Fiber Laser with Stable and Clean Femtosecond Pulses Output," *Laser Physics Letters*, vol. 8, no. 6, pp. 449–452, 2011.

[111] C. M. Ouyang, H. H. Wang, P. Shum, S. N. Fu, J. H. Wong, K. Wu, D. R. C. S. Lim, V. K. H. Wong, and K. E. K. Lee, "Properties of a Vector Soliton Laser Passively Mode-Locked by a Fiber-Based Semiconductor Saturable Absorber Operating in Transmission," *Optics Communications*, vol. 284, no. 2, pp. 619–624, 2011.

[112] A. P. Luo, Z. C. Luo, and W. C. Xu, "Switchable Dual-Wavelength Passively Mode-Locked Fiber Ring Laser Using SESAM and Cascaded Fiber Bragg Gratings," *Laser Physics*, vol. 21, no. 2, pp. 395–398, 2011.

[113] N. S. Shahabuddin, H. Mohamad, M. A. Mahdi, Z. Yusoff, H. Ahmad, and S. W. Harun, "Passively Mode-Locked Soliton Fiber Laser Using a Combination of Saturable Absorber and Nonlinear Polarization Rotation Technique," *Microwave and Optical Technology Letters*, vol. 54, no. 6, pp. 1430–1432, 2012.

[114] X. Zhao, Z. Zheng, L. Liu, Y. Liu, Y. X. Jiang, X. Yang, and J. S. Zhu, "Switchable, Dual-Wavelength Passively Mode-Locked Ultrafast Fiber Laser Based on a Single-Wall Carbon Nanotube Modelocker and Intracavity Loss Tuning," *Optics Express*, vol. 19, no. 2, pp. 1168–1173, 2011.

[115] H. F. Li, S. M. Zhang, J. Du, Y. C. Meng, Y. P. Hao, and X. L. Li, "Passively Harmonic Mode-Locked Fiber Laser with Controllable Repetition Rate Based on a Carbon Nanotube Saturable Absorber," *Optics Communications*, vol. 285, no. 6, pp. 1347–1351, 2012.

[116] H. A. Haus, J. G. Fujimoto, and E. P. Ippen, "Structures for Additive Pulse Mode-Locking," *Journal of the Optical Society of America B-Optical Physics*, vol. 8, no. 10, pp. 2068–2076, 1991.

[117] H. A. Haus, E. P. Ippen, and K. Tamura, "Additive-Pulse Modelocking in Fiber Lasers," *IEEE Journal of Quantum Electronics*, vol. 30, no. 1, pp. 200–208, 1994.

[118] M. E. Fermann, F. Haberl, M. Hofer, and H. Hochreiter, "Nonlinear Amplifying Loop Mirror," *Optics Letters*, vol. 15, no. 13, pp. 752–754, 1990.

[119] D. J. Richardson, R. I. Laming, D. N. Payne, V. J. Matsas, and M. W. Phillips, "Pulse Repetition Rates in Passive, Selfstarting, Femtosecond Soliton Fiber Laser," *Electronics Letters*, vol. 27, no. 16, pp. 1451–1453, 1991.

[120] A. B. Grudinin, D. J. Richardson, and D. N. Payne, "Energy Quantisation in Figure Eight Fiber LasLa," *Electronics Letters*, vol. 28, no. 1, pp. 67–68, 1992.

[121] D. J. Richardson, A. B. Grudinin, and D. N. Payne, "Passive, All-Fiber Source of $30fs$ Pulses," *Electronics Letters*, vol. 28, no. 8, pp. 778–779, 1992.

[122] I. N. Duling, "Subpicosecond All-Fiber Erbium Laser," *Electronics Letters*, vol. 27, no. 6, pp. 544–545, 1991.

[123] M. L. Dennis and I. N. Duling, "High Repetition Rate Figure Eight Laser with Extracavity Feedback," *Electronics Letters*, vol. 28, no. 20, pp. 1894–1896, 1992.

[124] V. Tzelepis, S. Markatos, S. Kalpogiannis, T. Sphicopoulos, and C. Caroubalos, "Analysis of a Passively Mode-Locked Self-Starting All-Fiber Soliton Laser," *Journal of Lightwave Technology*, vol. 11, no. 11, pp. 1729–1736, 1993.

[125] I. N. Duling, C. J. Chen, P. K. A. Wai, and C. R. Menyuk, "Operation of a Nonlinear Loop Mirror in a Laser Cavity," *IEEE Journal of Quantum Electronics*, vol. 30, no. 1, pp. 194–199, 1994.

[126] M. Salhi, A. Haboucha, H. Leblond, and F. Sanchez, "Theoretical study of figure-eight all-fiber laser," *Physical Review A*, vol. 77, no. 3, p. 033828, 2008.

[127] M. Quiroga-Teixeiro, C. B. Clausen, M. P. Sorensen, P. L. Christiansen, and P. A. Andrekson, "Passive Mode Locking by Dissipative Four-Wave Mixing," *Journal of the Optical Society of America B-Optical Physics*, vol. 15, no. 4, pp. 1315–1321, 1998.

[128] J. G. Caputo, N. Flytzanis, and M. P. Sorensen, "Ring Laser Configuration Studied by Collective Coordinates," *Journal of the Optical Society of America B-Optical Physics*, vol. 12, no. 1, pp. 139–145, 1995.

[129] T. Sylvestre, S. Coen, O. Deparis, P. Emplit, and M. Haelterman, "Demonstration of Passive Modelocking through Dissipative Four-Wave Mixing in Fibre Laser," *Electronics Letters*, vol. 37, no. 14, pp. 881–882, 2001.

[130] J. Schröder, T. D. Vo, and B. J. Eggleton, "Repetition-Rate-Selective, Wavelength-Tunable Mode-Locked Laser at up to 640 GHz," *Optics Letters*, vol. 34, no. 24, pp. 3902–3904, 2009.

[131] J. Schröder, S. Coen, T. Sylvestre, and B. J. Eggleton, "Dark and Bright Pulse Passive Mode-Locked Laser with in-Cavity Pulse-Shaper," *Optics Express*, vol. 18, no. 22, pp. 22715–22721, 2010.

[132] S. M. Zhang, F. Y. Lu, X. Y. Dong, P. Shum, X. F. Yang, X. Q. Zhou, Y. D. Gong, and C. Lu, "Passive Mode Locking at Harmonics of the Free Spectral Range of the Intracavity Flter in a Fiber Ring Laser," *Optics Letters*, vol. 30, no. 21, pp. 2852–2854, 2005.

[133] G. P. Agrawal, "Nonlinear Phase Shift," in *Nonlinear Fibre Optics*, pp. 187–189, Sinagpore: Elsevier (Sinagpore) Pte Ltd, 2009.

[134] V. J. Matsas, D. J. Richardson, T. P. Newson, and D. N. Payne, "Characterization of a Self-Starting, Passively Mode-Locked Fiber Ring Laser that Exploits Nonlinear Polarization Evolution," *Optics Letters*, vol. 18, no. 5, pp. 358–360, 1993.

[135] D. U. Noske, N. Pandit, and J. R. Taylor, "Subpicosecond Soliton Pulse Formation from Self-Mode-Locked Erbium Fiber Laser Using Intensity Dependent Polarization Rotation," *Electronics Letters*, vol. 28, no. 23, pp. 2185–2186, 1992.

[136] N. Pandit, D. U. Noske, and J. R. Taylor, "$350fs$ Pulse Generation from an Erbium Fiber Ring Laser Mode-Locked Using Nonlinear Polarization Rotation," *Journal of Modern Optics*, vol. 41, no. 1, pp. 11–14, 1994.

[137] C.-W. Chang and S. Chi, "Passive Mode-Locking through Nonlinear Polarization Rotation in Low-Birefringence Fibers," *Optical Communications*, vol. 134, pp. 218–222, 1997.

[138] K. M. Spaulding, D. H. Yong, A. D. Kim, and J. N. Kutz, "Nonlinear Dynamics of Mode-Locking Optical Fiber Ring Lasers," *Journal of the Optical Society of America B-Optical Physics*, vol. 19, no. 5, pp. 1045–1054, 2002.

[139] O. E. Martinez, R. L. Fork, and J. P. Gordon, "Theory of Passively Mode-Locked Lasers Including Self-Phase Modulation and Group-Velocity Dispersion," *Optics Letters*, vol. 9, no. 5, pp. 156–158, 1984.

[140] S. M. J. Kelly, "Characteristic Side-Band Instability of Periodically Amplified Average Soliton," *Electronics Letters*, vol. 28, no. 8, pp. 806–807, 1992.

[141] S. M. J. Kelly, K. Smith, K. J. Blow, and N. J. Doran, "Average Soliton Dynamics of a High-Gain Erbium Fiber Laser," *Optics Letters*, vol. 16, no. 17, pp. 1337–1339, 1991.

[142] W. H. Renninger, A. Chong, and F. W. Wise, "Pulse Shaping and Evolution in Normal-Dispersion Mode-Locked Fiber Lasers," *IEEE Journal of Selected Topics in Quantum Electronics*, vol. 18, no. 1, pp. 389–398, 2012.

[143] A. Chong, J. Buckley, W. Renninger, and F. Wise, "All-Normal-Dispersion Femtosecond Fiber Laser," *Optics Express*, vol. 14, no. 21, pp. 10095–10100, 2006.

[144] A. Chong, W. H. Renninger, and F. W. Wise, "Properties of Normal-Dispersion Femtosecond Fber Lasers," *Journal of the Optical Society of America B-Optical Physics*, vol. 25, no. 2, pp. 140–148, 2008.

[145] W. H. Renninger, A. Chong, and F. W. Wise, "Dissipative Solitons in Normal-Dispersion Fiber Lasers," *Physical Review A*, vol. 77, no. 2, 2008.

[146] B. G. Bale, J. N. Kutz, A. Chong, W. H. Renninger, and F. W. Wise, "Spectral Filtering for Mode Locking in the Normal Dispersive Regime," *Optics Letters*, vol. 33, no. 9, pp. 941–943, 2008.

[147] B. G. Bale, J. N. Kutz, A. Chong, W. H. Renninger, and F. W. Wise, "Spectral Filtering for High-Energy Mode-Locking in Normal Dispersion Fiber Lasers," *Journal of the Optical Society of America B-Optical Physics*, vol. 25, no. 10, pp. 1763–1770, 2008.

[148] V. I. Kruglov, A. C. Peacock, J. M. Dudley, and J. D. Harvey, "Self-Similar Propagation of High-Power Parabolic Pulses in Optical Fiber Amplifiers," *Optics Letters*, vol. 25, no. 24, pp. 1753–1755, 2000.

[149] W. H. Renninger, A. Chong, and F. W. Wise, "Self-Similar Pulse Evolution in an All-Normal-Dispersion Laser," *Physical Review A*, vol. 82, no. 2, 2010.

[150] S. K. Turitsyn, B. G. Bale, and M. P. Fedoruk, "Dispersion-Managed Solitons in Fibre Systems and Lasers," *Physics Reports-Review Section of Physics Letters*, vol. 521, no. 4, pp. 135–203, 2012.

[151] F. O. Ilday, J. R. Buckley, W. G. Clark, and F. W. Wise, "Self-Similar Evolution of Parabolic Pulses in a Laser," *Physical Review Letters*, vol. 92, no. 21, 2004.

[152] R. Gumenyuk, I. Vartiainen, H. Tuovinen, S. Kivisto, Y. Chamorovskiy, and O. G. Okhotnikov, "Dispersion Compensation Technologies for Femtosecond Fiber System," *Applied Optics*, vol. 50, no. 6, pp. 797–801, 2011.

[153] M. A. Chernysheva, A. A. Krylov, A. A. Ogleznev, N. R. Arutyunyan, A. S. Pozharov, E. D. Obraztsova, and E. M. Dianov, "Transform-Limited Pulse Generation in Normal Cavity Dispersion Erbium Doped Single-Walled Carbon Nanotubes Mode-Locked Fiber Ring Laser," *Optics Express*, vol. 20, no. 21, pp. 23994–24001, 2012.